

**Measurement and Modelling of Phase Stability,
Thermophysical Properties and Recrystallization
Behavior of Advanced Austenitic Steels**

By

Haraprasanna Tripathy

Enrolment No.: **PHYS 02 2012 04 016**

Indira Gandhi Centre for Atomic Research

Kalpakkam - 603102, India

*A thesis submitted to the
Board of Studies in Physical Sciences*

*In partial fulfillment of requirements
for the Degree of*

DOCTOR OF PHILOSOPHY

of

HOMI BHABHA NATIONAL INSTITUTE

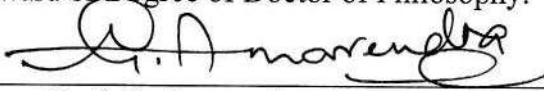
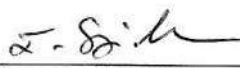


April 2018

Homi Bhabha National Institute

Recommendations of the Viva Voce Committee

As members of the Viva Voce Committee, we certify that we have read the dissertation prepared by Mr. Haraprasanna Tripathy entitled "Measurement and Modelling of Phase Stability, Thermophysical Properties and Recrystallization Behavior of Advanced Austenitic Steels" and recommend that it may be accepted as fulfilling the thesis requirement for the award of Degree of Doctor of Philosophy.

	Aug 21, 2018
Chairman – Prof. G. Amarendra	Date:
	21/08/2018
Guide / Convener – Prof. Saroja Saibaba	Date:
	21/8/18
Examiner - Prof. Indradev S. Samajdar	Date:
	21/8/2018
Member 1- Prof. A. K. Bhaduri	Date:
	21/8/18
Member 2- Prof. N. V. Chandrasekhar	Date:
	21/8/18
Technology Advisor- Dr. S. Raju	Date:

Final approval and acceptance of this thesis is contingent upon the candidate's submission of the final copies of the thesis to HBNI.

I/We hereby certify that I/we have read this thesis prepared under my/our direction and recommend that it may be accepted as fulfilling the thesis requirement.

Date: August 21, 2018

Place: IGCAR, Kalpakkam


Signature of Guide

Acknowledgements

It is a genuine pleasure to convey my deep sense of thanks and gratitude to all of those, whose support and encouragement assisted me in preparing this PhD thesis. My humble acknowledgement is as follows;

I would like to express my deep sense of gratitude to my guide, Dr. Saroja Saibaba, Associate Director, Material Characterization Group, IGCAR for her invaluable guidance, inspiration and support throughout this project.

I am extremely grateful to Dr. S. Raju, Head, Physical Metallurgy Division, whose persistent guidance and indispensable technical support assisted me for the completion of my PhD work.

I am thankful to my doctoral committee, Chairman- Dr. G. Amarendra and members- Dr. A. K. Bhaduri, Dr. N. V. Chandrasekhar, for their insightful suggestions for the progress of the research work at various DC meetings.

I would like to thank Dr. C. Sudha, Head, CMMS, IGCAR for her support in preparing my PhD thesis. I am grateful to her for her help during final redacting of the thesis.

I would like to thank Dr. R. Mythili, SAMS, IGCAR for carrying out TEM characterization on my samples and useful discussions in analyzing the results.

My heartfelt acknowledgements go to my colleagues Dr. Arun Kumar Rai (currently at RRCAT, Indore), Mr. Raj Narayan Hajra and Mrs. N. Vijayashanthi for their timely help in the laboratory works and useful discussions. Further, I extend my thanks to all PMD members for providing the experimental facilities and their support during the course of this research work.

I would like to express my deep appreciation to my school teacher Mr. Fagu Patra, whose faith on me has been an everlasting source of encouragement for me.

I owe my sincere gratitude to my parents and sisters for their persistent moral support and faith on me. I thank my late mother who taught me the power of knowledge and ethics which made me to come up in my life. I owe every bit of my existence to her. I am extremely thankful to my beloved wife *Madhu* for taking care of most of my domestic responsibilities and encouraging me to carry out my research work. Finally my God gifted angel, my daughter (*Tanu*) who has been a persistent source of inspiration for me.

At the end, I thank the Divine Master for giving me the strength, ability and opportunity to undertake this research study.



Dedicated
To
My Mother (late)

Who taught me the power of knowledge and ethics.

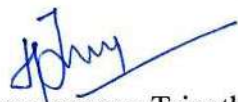
List of Publications arising from the thesis

Journal

1. Thermal stability and thermal property characterization of Fe–14.4Cr–15.4Ni–2.4Mo–2.36Mn–0.25Ti–1.02Si–0.042C–0.04P–0.005B (mass%) austenitic stainless steel (Alloy D9I), **Harapasanna Tripathy**, Subramaniam Raju, Arun Kumar Rai, G.Paneerselvam, & T. Jayakumar, *Nucl.Engg.Design* **2013**, 255, 86-96
2. A Calorimetric Study of Recovery and Recrystallization in Fe–14.4 Cr–15.4 Ni–2.4Mo–2.36 Mn–0.25 Ti–0.04 C–0.05 P (mass %) Austenitic Stainless Steel. **Harapasanna Tripathy**, Subramaniam Raju, Arun Kumar Rai, and Tamanna Jayakumar, *Steel Res. Int.*, **2013**, 84, 1046-1059
3. Calorimetric Investigation of Thermal Stability of SS304H Cu (Fe-17.7Cr-9.3Ni-2.95Cu-0.91Mn-0.58Nb-0.24Si-0.1C-0.12N- wt. %) Austenitic Stainless Steel, **Harapasanna Tripathy**, Subramaniam Raju R. N. Hajra, A. K Rai, R. Mythili, S. Saroja & T. Jayakumar, *Metall Mater Trans E*, **2016**, 3, 234-249.
4. High Temperature Thermophysical Properties of 18Cr-9Ni-2.95Cu-0.58 Nb-0.1C (Wt. %) Austenitic Stainless Steel. **Harapasanna Tripathy**, Arun Kumar Rai, Raj Narayan Hajra, N. Vijaya Shanthi, Subramaniam Raju and Saroja Saibaba, *J. Therm Analysis and Calorimetry*, **2018**, 131, 2749-2761
5. The Role of Nucleation Mode on the Kinetics of Static Recrystallization and Microstructure Evolution: Simulation and Experiments. **Harapasanna Tripathy**, Arun Kumar Rai, Raj Narayan Hajra, Subramaniam Raju and Saroja Saibaba, Communicated to *Metall Mater Trans A*.

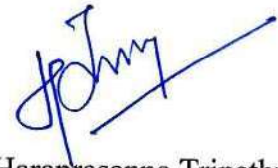
Conference Proceedings

1. Design-Principles of Super austenitic 304H Cu Stainless Steel: An Integrated Approach Involving Key Experiments and Thermo- Kinetic Modelling. **Harapasanna Tripathy**, S. Raju, Arun kumar Rai, S. Saroja and T. Jayakumar. MRSI-2013, *Theme Symposium on Advanced Materials for Energy Applications*, February **2013**, IGCAR, Kalpakkam
2. Modelling the Role of Nucleation on Recrystallization Kinetics: A Cellular Automata Approach. **Harapasanna Tripathy**, Arun Kumar Rai, Raj Narayan Hajra, Subramaniam Raju & Saroja Saibaba, *AIP Conference Proceedings* 1731, 030009 (2016); doi: 10.1063/1.4947614. (Presented in DAE Solid state physics Symposium, 2015)
3. Measurement of High Temperature Elastic Moduli of an 18Cr-9Ni-2.95 Cu-0.58 Nb-0.1C (Wt. %) Austenitic Stainless Steel. **Harapasanna Tripathy**, Raj Narayan Hajra, C. Sudha, S. Raju, Saroja Saibaba. *AIP Conference Proceedings* 1951, 020009 (2018); doi: 10.1063/1.5031717 (presented in National Conference on Thermophysical Properties, 2017)


(Harapasanna Tripathy)

DECLARATION

I, hereby declare that the investigation presented in the thesis has been carried out by me. The work is original and has not been submitted earlier as a whole or in part for a degree / diploma at this or any other Institution / University.

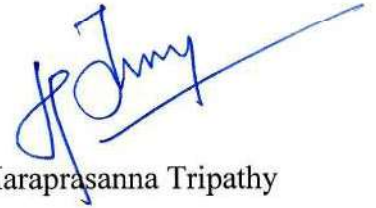


Harapasanna Tripathy

STATEMENT BY AUTHOR

This dissertation has been submitted in partial fulfillment of requirements for an advanced degree at Homi Bhabha National Institute (HBNI) and is deposited in the Library to be made available to borrowers under rules of the HBNI.

Brief quotations from this dissertation are allowable without special permission, provided that accurate acknowledgement of source is made. Requests for permission for extended quotation from or reproduction of this manuscript in whole or in part may be granted by the Competent Authority of HBNI when in his or her judgment the proposed use of the material is in the interests of scholarship. In all other instances, however, permission must be obtained from the author.



Haraprasanna Tripathy

7.2	Experimental study	192
7.2.1	Estimation of activation energy	192
7.3	Simulation method	197
7.3.1	Setup of the deformed microstructure	197
7.3.2	Algorithm for simulation of static recrystallization	199
7.3.3	Evaluation of actual and extended transformed fraction	201
7.3.4	Accuracy of the algorithm	201
7.4	Results	203
7.4.1	Evaluation of kinetic parameters from simulation	203
7.5	Analysis of kinetic parameters under different nucleation modes	206
7.5.1	Site saturation and continuous nucleation mode	206
7.5.2	Mixed nucleation mode	207
7.5.3	Avrami nucleation mode	208
7.6	Simulated and experimental grain size distribution: A comparison	210
7.7	Discussion	214
7.8	Summary and conclusions	217

Chapter 8

Summary and Further Avenues of Research

220-224

8.1	Summary of the present study	221
8.2	Further avenues of research	223

Appendix

Appendix-A: Algorithm for the generation of initial Microstructure	225
--	-----

References

226-241

5.5	Discussion	156
5.6	Conclusion	157

Chapter 6

Investigation of Recovery and Recrystallization Processes in IFAC-1 & SS 304H Cu Stainless Steels using Dynamic Calorimetry

158-188

6.1	Introduction	159
6.2	Experimental detail	161
6.3	Results	162
6.3.1	The deformed state	162
6.3.2	DSC investigation of recovery and recrystallization in IFAC-1 SS	163
6.3.3	The effect of heating rate on recovery and recrystallization	167
6.3.4	Microhardness variation and microstructural evolution during strain energy relaxation in IFAC-1	169
6.3.5	DSC investigation of recovery and recrystallization in SS 304 H Cu	171
6.3.6	Microhardness variation and microstructural evolution during strain energy Relaxation in SS 304 H Cu	174
6.4	Discussion	176
6.4.1	Calorimetry and the strain energy relaxation process	176
6.4.2	The stored energy release during annealing	177
6.4.3	Kinetics of recovery and recrystallization in IFAC-1 and SS 304 H Cu	180
6.5	Conclusion	187

Chapter 7

Role of Nucleation Mode on Kinetics of Static Recrystallization & Grain Structure Development: A Mesoscopic Simulation Approach

189-219

7.1	Introduction	190
-----	--------------	-----

4.2.2	<i>Thermocalc</i> [®] simulation of phase stability & solidification behavior of IFAC-1 SS	97
4.2.3	DSC investigation of phase stability and solidification behavior in IFAC-1 SS	101
4.2.4	<i>Thermocalc</i> [®] simulation of phase stability & solidification behavior in SS 304H Cu:	105
4.2.5	DSC investigation of phase stability in SS 304 H Cu	108
4.2.6	Effect of cooling rate on solidification in SS 304 H Cu	113
4.2.7	Stability of second phase carbides in SS 304 H Cu	117
4.3	Discussion	120
4.3.1	Cr/Ni equivalent and solidification of austenitic stainless steels	120
4.3.2	Effect of Cu on solidification mode in SS 304 H Cu	122
4.4	Conclusions	123

Chapter 5

Measurement and Modelling of High Temperature Thermophysical Properties of IFAC-1 & 304H Cu Stainless Steels

		125-157
5.1	Introduction	126
5.2	Experimental details	126
5.3	Results	127
5.3.1	Enthalpy increment measurements and specific heat as function of temperature	127
5.3.2	Thermal expansion and density	131
5.3.3	Thermal diffusivity	139
5.3.4	Measurement of dynamic elastic moduli	142
5.4	Integrated modelling of thermophysical properties by Debye-Grüneisen formalism	148
5.4.1	Estimation of elastic Debye temperature and Grüneisen parameter	148
5.4.2	Correlation of molar volume and enthalpy	150
5.4.3	Estimation of heat capacity and thermal expansivity	152

3.5.2	Instrument details	63
3.5.3	Drop calorimetry experimental procedure	66
3.5.4	Calibration of drop calorimeter	68
3.5.5	Estimation of enthalpy	69
3.6	Thermo mechanical analyzer/ dilatometer: Basic principles	70
3.6.1	Instrument details	70
3.6.2	Measurement details	73
3.6.3	The baseline correction in push rod dilatometer	74
3.7	Laser flash thermal diffusivity	76
3.7.1	Instrumental details	76
3.7.2	Measurement details	78
3.8	Impulse excitation technique	80
3.8.1	Instrument details	80
3.8.2	Estimation of elastic moduli	81
3.8.3	Measurement details	83
3.9	Optical metallography	84
3.10	Micro-hardness measurement	85
3.11	X-Ray diffraction (XRD)	85
3.12	Scanning electron microscopy (SEM) Study	86
3.12.1	Analysis of microstructural parameters	86
3.13	Transmission electron microscopy	87
3.13.1	Phase analysis using electron diffraction pattern	88

Chapter 4

Investigation of Phase Stability in IFAC-1 and SS 304 H Cu Stainless Steels

89-124

4.1.	Introduction	90
4.2	Results	91
4.2.1	Structural and microstructural characterization of initial alloys	91

2.6.2	Growth during recrystallization	30
2.6.3	Effect of particles on recrystallization behavior	31
2.7	Grain growth	32
2.8	Kinetics of phase transformation	33
2.9	Isothermal and non-isothermal transformation	35
2.10	Mechanisms of diffusional transformations	36
2.10.1	Nucleation mode	36
2.10.2	Growth mode	38
2.10.3	Mode of impingement	39
2.11	Modeling solid state transformation kinetics	40
2.12	Isokinetic methods	41
2.12.1	Kolmogorov-Johnson-Mehl-Avrami (KJMA) model for isothermal and non-isothermal transformations	41
2.12.2	Microstructural path method	44
2.13	Model-free isoconversional methods	45
2.13.1	Kissinger-Akahira-Sunose (KAS) method	46

Chapter 3

Experimental Methodology

		48-88
3.1	Introduction	49
3.2	Alloy preparation, compositional analysis and heat treatment	50
3.3	Calorimetry: Basic principles	52
3.4	Dynamic or differential scanning calorimetry (DSC)	53
3.4.1	Setaram® Setsys 1600 DSC	54
3.4.2	DSC experimental Procedure	57
3.4.3	Determination of phase transformation temperature	58
3.4.4	Temperature calibration in DSC	60
3.4.5	Determination of phase transformation enthalpy	60
3.5	Principle of drop calorimeter	61
3.5.1	Inverse drop calorimetry	63

CONTENTS

Synopsis		VII
List of Figures		XIII
List of Tables		XXI
Chapter 1		
Introduction		1-15
1.1	Efficient energy production process: Need for advanced materials	2
1.2	Advanced austenitic stainless steel for fast breeder reactor core applications	5
1.3	Development of austenitic stainless steel for AUSC thermal power plants	7
1.4	Materials design for high temperature applications	9
1.5	Genesis of this study	12
1.6	Scope of this study	12
1.7	Organization of thesis	13
Chapter 2		
Literature Survey		16-47
2.1	Stainless steels: General introduction	17
2.2	Austenitic stainless steels	18
2.2.1	Role of alloying elements	20
2.2.2	Classification of austenitic stainless steels	21
2.3	Phase stability and thermophysical properties of austenitic stainless steels	22
2.4	Work hardening	27
2.5	Recovery	27
2.6	Recrystallization	29
2.6.1	Role of deformation on recrystallization behavior	30

Chapter-8: Summary and Further Avenues of Research

Chapter 8 presents a summary of the salient features of the experimental and modeling studies carried out in this thesis; and also identifies few potential avenues for further research. The key issues identified may be explored for furthering the frontiers of knowledge on advanced austenitic stainless steels.

elastic properties in the temperature range of 300-1273 K, as measured using impulse excitation technique and a critical analysis of these data in terms of existing literature are also presented. On the modeling front, measured enthalpy, hence heat capacity and thermal expansion, for both the steels are analyzed in terms of quasiharmonic Debye-Grüneisen formalism.

Chapter- 6: Investigation of Recovery and Recrystallization Processes in IFAC-1 & SS 304H Cu Stainless Steels using Dynamic Calorimetry

The results of dynamic calorimetric investigation of 85% cold worked IFAC-I and SS304H Cu are presented and discussed in this chapter. The peak recovery (815 K) and recrystallization temperatures (1070 K) for IFAC-1 SS and SS304H Cu (826 & 986 K) have been identified. The averaged estimates of the total stored energy release ($9.4 \pm 1.4 \text{ J g}^{-1}$ in IFAC-1; $17.3 \pm 1.4 \text{ J g}^{-1}$ SS304H Cu) have also been obtained. For annealing temperatures exceeding 1273 K, partial dissolution of TiC particles in IFAC-1 SS resulted in secondary recrystallization. Similarly Cu-precipitation in SS304H Cu is found to influence recrystallization. The kinetics of static recovery and recrystallization steps have been modeled using Kolmogorov-Johnson-Mehl-Avrami (KJMA) schemes. The effective activation energies for recovery and recrystallization steps for (IFAC-1: $198 \pm 7 \text{ kJ mol}^{-1}$ and $336 \pm 9 \text{ kJ mol}^{-1}$; SS304 H Cu: 144 ± 14 and $192 \pm 12 \text{ kJ mol}^{-1}$) have been evaluated.

Chapter-7: Role of nucleation mode on kinetics of static recrystallization & Grain structure development: A Mesoscopic Simulation Approach

Following the kinetic results obtained in Chapter - 7, a geometrical simulation approach has been adopted to model the time evolution of grain structures in IFAC 1. The activation energies derived from dynamic calorimetry results served as input parameters for the computer model. The entire simulation code has been written in the laboratory using MATLAB. From the simulation, the kinetic parameters of KJMA and microstructural path method (MPM) are explicitly evaluated for pure site saturation (SSN), continuous nucleation (CN), mixed nucleation (MN) and Avrami nucleation (AN) modes. It is found that the results of simulation for Avrami nucleation mode are in agreement with the experimental results of a decreasing Avrami exponent with transformation progress. The grain size distribution due to static recrystallization is found to be sensitive to the nucleation mode.

diffusivity (LFTD) and impulse excitation technique (IET) are described in adequate detail. The experimental schedules, calibration, and error limits associated with each experimental technique are also described in this chapter.

Chapter-4: Investigation of Phase Stability in IFAC-1 and SS 304 H Cu Stainless Steels

This chapter begins with characterization of IFAC-1 and SS304H Cu using X-ray diffraction, optical and electron microscopy techniques in order to establish the existence of different phases in these alloys. Together with equilibrium *Thermocalc* based simulations the presence of $M_{23}C_6$, MX and Cu rich metallic precipitates in SS304 H Cu is established. The effect of non equilibrium conditions that prevails upon cooling the liquid has been simulated with Scheil-Gulliver scheme. IFAC-1 SS is found to contain only a small fraction of MX type TiC precipitates, in addition to γ -austenite. It is found that small fraction of δ -ferrite phase can also form from the liquid phase in highly alloyed austenitic steels, such as 304HCu, due to non-equilibrium segregation or enrichment of interdendritic liquid with Cr and Nb. Following thermodynamic simulations, the results of scanning calorimetry investigation on temperature induced phase changes in these alloys have been described. The entire sequence of on-heating and cooling transformations, together with associated enthalpy effects (where they are measurable) are enumerated for both IFAC 1 and SS304H Cu. Depending on the capabilities of calorimeter, the effect of cooling rate variation on solidification has also been monitored to a limited extent. It is found that under slow cooling like (3 K per minute) both IFAC-1 and SS304HCu exhibit, Liquid \rightarrow Liquid + austenite \rightarrow L + austenite + ferrite; mode of solidification. Further, in the case of IFAC-1 SS the observed temperature domain for δ -ferrite formation is found to be narrow as compared to SS304H Cu. The amount of δ -ferrite formed in SS304HCu is appreciable. The effect of Cu on solidification and also the kinetics of dissolution of second phase precipitates in SS304H Cu have also been discussed in this chapter.

Chapter-5: Measurement and Modelling of High Temperature Thermophysical Properties of IFAC-1 & 304H Cu Stainless Steels

In this chapter, data on enthalpy increment measured using drop calorimetry in the temperature range 300-1273 K are presented and discussed for both the alloys . Further, bulk thermal expansion and thermal diffusivity and their temperature variation as measured using dilatometer and laser flash diffusivity technique respectively, are presented. The variation of

Chapter-1: Introduction

This chapter begins with a description on the potential requirements of high temperature structural materials for liquid metal cooled fast breeder reactors (LMFBR) and AUSA fossil power plants. This is followed by a brief introduction of two important candidate materials namely, the austenitic stainless steel IFAC-1 SS (LMFBR) and SS304H Cu (AUSA). This chapter also includes a brief discussion on the systems engineering approach involved in the modern design of materials for advanced engineering systems in order to highlight the importance of generating fundamental knowledge or data base on various metallurgical aspects of advanced engineering materials.

Chapter-2: Literature Survey

Chapter 2 focuses on the literature survey on thermal stability and thermophysical properties of advanced austenitic stainless steels for power plant applications. This description serves as a prelude for the high temperature calorimetry studies carried out on IFAC 1 and SS304H Cu. This chapter also includes a brief description on the present understanding in literature on the recovery and recrystallization phenomena of advanced austenitic stainless steels. The kinetic aspects of stored energy relaxation of a severely cold worked (85% thickness reduction) system through interface and diffusion mediated phase transformations, specifically transformations mediated through nucleation and growth are important from the point of view of analyzing calorimetry data. In the light of this the isokinetic and isoconversional methods of analyzing the scanning calorimetry measurements and the Kolmogorov-Johnson-Mehl-Avrami (KJMA) formalism, one of the common methodologies adopted for interpreting diffusional transformation kinetics. This provides the theoretical background used for the computer simulation of static recrystallization phenomenon using geometrical simulation approach in the present thesis.

Chapter-3: Experimental Methodology

In this chapter the experimental methodology employed in this thesis is presented in detail. Brief descriptions on alloy preparation, compositional characterization and annealing treatments are followed by structural characterization techniques namely X-ray diffraction, metallography, scanning and transmission electron microscopy. More importantly, descriptions on specific instrumentation techniques like inverse drop calorimetry (IDC), differential scanning calorimetry (DSC), high temperature dilatometry, laser flash thermal

Further, a joint mission oriented materials development programme has been initiated at IGCAR (BHEL, NTPC being other partnering agencies), India, for establishing efficient *Advanced ultra supercritical (AUSC)* coal based technology. One of the effective ways to increase the efficiency of coal utilization is to increase the steam temperature and pressure. Over the years, the steam parameters has seen improvement from that of a subcritical system (455 °C and 22 MPa) with efficiency under 37% to supercritical systems (563 °C and 25 MPa), where the efficiency has been raised up to 42%. Eventually, the next generation coal based power plants are planned to operate with steam temperature of 700 to 760 °C and at a pressure of 35 MPa. This would get a net efficiency up to 50% with an emission of 35% less carbon dioxide. In reality, the attainment of maximum steam parameters are limited by current materials capabilities; as only few materials can operate at these plant conditions for a practical service lifetime of about 40 years without failure. Therefore, it becomes necessary to develop newer materials capable of dealing with high temperature, high pressure combination in an optimized thermodynamic cycle. In this regard, it is known that the boiler tubes are the key components of an AUSC power plant where the steam generated is further heated to increase the temperature. Besides the demands of meeting severe operating conditions, the secondary objective of introducing newer materials into the coal combustion cycle in AUSC power plants, is towards economizing the overall plant cost. In this scenario, advanced austenitic stainless steels having good creep strength and corrosion resistance are potential choices for the boiler tube applications in advanced AUSC plants. Accordingly, the indigenous production of a high temperature corrosion resistant austenitic stainless steel, based on commercial SS304H Cu composition (wt.%): Fe-17.7Cr-9.3Ni-2.95Cu-0.91Mn-0.58Nb-0.24Si-0.1C-0.12N is currently pursued at IGCAR. Being an indigenous variant of the popular SS 304H Cu austenitic steel, a comprehensive investigation on the phase stability and thermophysical properties for this alloy is essential.

In view of the above, the present thesis deals with investigations on two indigenously developed austenitic stainless steels, namely, IFAC-1 SS and SS304H Cu. The scope of the thesis includes study on thermal stability, thermophysical properties, and recovery and recrystallization behavior of these advanced steels employing both experimental and modeling tools. This thesis report contains eight (8) chapters in all. The organization of the thesis is given below.

SYNOPSIS

It is a well known fact that availability of reliable knowledge-base on various thermodynamic and thermophysical properties and the kinetic aspects of associated structural transformations are essential for the robust design and fabrication of many engineering components. In the case advanced fossil fuel and nuclear power plants this requirement is of paramount importance for the appropriate selection of structural materials for, performance under demanding service conditions like high pressure, high temperature and intense neutron irradiation. In the Indian energy scenario, where about 60% of the total electricity is still generated from fossil fuel reserves, there is a huge expectation and demand on alternate energy sources to provide for long term energy security with a concomitant need to reduce the overall CO₂ emission and mitigate other adverse environmental issues. Sustained efforts are being made in this direction in India towards building power plants based on advanced ultra supercritical (AUSC) and nuclear fast reactor technology.

In the early design of fast reactors 316 austenitic stainless steel in 20% cold worked condition was used as core structural material for cladding and wrapper. However, the achievable fuel burn up was often limited to about 50 dpa (displacement per atom), which is mainly due to the high swelling rates of 316 SS at higher dpa. Appropriate tailoring of composition of SS316 with respect to Chromium, Nickel, Titanium and Carbon contents, resulted in the development of a swell resistant austenitic stainless steel variant, namely *Alloy D9*. The nominal chemical composition of Alloy D9 (wt.%) is: *15Cr-15Ni-0.05C-1.65Mn-2Mo-0.3Ti-0.5Si-0.02P-0.01S*. Based on extensive in-pile testing, this composition is found to possess enhanced irradiation swelling resistance, along with good high temperature creep strength. Alloy D9 served as the base candidate alloy for making in-core components like clad and wrappers for the first 500MWe fast breeder reactor in India. Recently, a further optimized version of Alloy D9 with a **Ti/C** content of about **6**, together with **1.02 wt.% Si**, and **0.04 wt% P**, has been developed at IGCAR, Kalpakkam. This modified grade is found to possess improved swelling resistance with comparable creep properties over standard Alloy D9 composition and has been designated as ***IFAC-1 SS (Indian Fast Reactor Advanced Cladding-1)***. Since this is a fully indigenous effort, fundamental data on thermal stability and thermophysical properties of IFAC 1 need to be generated accurately.

Table 5.2	The fit coefficients appearing in <i>Eq. (5.3)</i> of measured dilatational strain as a function of temperature for IFAC-1 and SS 304H Cu.	133
Table 5.3	Values of enthalpy increment, specific heat, linear thermal expansion coefficient and density for IFAC-1 are tabulated as a function of temperature	137
Table 5.4	Values of enthalpy increment, specific heat, linear thermal expansion coefficient and density for SS304 H Cu are tabulated as a function of temperature.	138
Table 5.5	Measured thermal diffusivity and estimated thermal conductivity data for IFAC-1 and SS 304H Cu are tabulated for different temperatures	141
Table 5.6	Fit parameters obtained from nonlinear least square fitting of the temperature variation of elastic modulus data to <i>Eq. (5.8)</i> .	147
Table 5.7	List of input parameters used in Debye–Grüneisen model of thermal properties	153
Table 6.1	Tabulation of kinetic parameters for the recovery and recrystallization processes for IFAC-1 and SS 304 H Cu obtained in this study under different heating rates (β)	184
Table 7.1	Experimentally measured kinetic parameters (n , Q_{eff} and k_0) for static recrystallization in IFAC-1 at different annealing temperatures in accordance with KJMA model	194
Table 7.2	Numerical value of the parameters in <i>Eq. (2.3-2.7)</i> and <i>Eq. (2.13)</i> used in the computer simulation [119, 126]. The activation energy for nucleation (Q_N) and growth (Q_G) is estimated from the experimental data	196
Table 7.3	The variation of kinetic parameters calculated from the simulation using KJMA and MPM model [Hom. Rxtn. (Homogeneous Recrystallization), Het. Rxtn. (Heterogeneous Recrystallization)]	206
Table 7.4	The fit parameters obtained from the grain size distribution fits (<i>Eq. (7.10 & 7.11)</i>) for simulated (different nucleation modes) and experimental microstructures	213

List of Tables

Table No.	Table Captions	Page No.
Table 1.1	Nominal composition (Wt. %) of austenitic steels for core structural material applications in fast breeder reactors	7
Table 1.2	Nominal composition (Wt.%) of selected 18Cr-8Ni austenitic steels for boiler applications in thermal power plants	9
Table 2.1	Classification of stainless steels	18
Table 2.2	Chemical composition (Wt. %) of some popular AISI 300 grade austenitic stainless steels	21
Table 2.3	List of Secondary phases observed in austenitic stainless steels and their characteristics	23
Table 2.4	Theoretical values of kinetic parameters under isothermal and isochronal transformations	43
Table 3.1	Chemical composition (wt. %) of IFAC-1 SS and SS304H Cu steels	51
Table 4.1	The <i>Thermocalc</i> [®] predicted phase transformation sequence and the transformation temperature for IFAC-1 SS	99
Table 4.2	Measured transformation temperatures for IFAC-1 using slow scan DSC experiments	105
Table 4.3	<i>Thermocalc</i> [®] predicted phase transformation sequence and corresponding temperature for SS 304H Cu	107
Table 4.4	Experimentally determined transformation sequence, transformation temperatures and solidification enthalpy for SS 304H Cu	113
Table 4.5	The transformation start (T_s), peak (T_p) and finish (T_f) temperature along with transformation enthalpy for two separate DSC solidification peaks for SS 334H Cu	116
Table 4.6	The calculated values of $[Cr_{eq} / Ni_{eq}]$ ratio for IFAC-1 SS and SS 304H Cu	120
Table 5.1	Fit parameters of measured enthalpy data as a function of temperature for IFAC-1 and SS 304 H Cu.	130

- Fig. 7.13** Variation of Avrami exponent for varying (λ_0) in the Avrami nucleation mode with heterogeneous recrystallization. ($\lambda_0=6.4 \times 10^8$ Nuclei m^{-2}) 209
- Fig. 7.14** Snapshots of microstructure evolution in (a) Site saturation (SSN) (b) continuous nucleation (CN) (c) Mixed nucleation (MN) and (d) Avrami Nucleation (AN) mode for heterogeneous recrystallization 211
- Fig. 7.15** A comparison of grain size distribution in the fully recrystallized microstructure from simulation and experiment for different nucleation modes.(a) Site saturation (b) Continuous nucleation (c) Mixed nucleation (d) Avrami nucleation.(e) from experiment. The grain size is normalized to the average grain size of the corresponding deformed microstructure for both simulation (R) and experiment (R_0).The solid lines in (a) is fitted to *Eq. (7.10)* and for (b), (c), (d) and (e) is fitted to *Eq.(7.11)*. 212

- The solid line represents the fitted curve according to *Eq. (7.2)*
- Fig. 7.5** (a) The initial microstructure generated using the present algorithm (b) 198
The 70% rolled microstructure generated from microstructure shown in (a) by uniform compression in one direction
- Fig. 7.6** Time evolution of number of nuclei per unit volume for different 202
nucleation modes considered in the present simulation
- Fig. 7.7** The time evolution of recrystallized fraction as calculated from the 202
microstructure evolution from the simulation for different nucleation modes in homogeneous recrystallization. The solid lines represent the transformed fraction calculated from KJMA model
- Fig. 7.8** Variation of Avrami exponent with transformed fraction for different 204
nucleation modes (a) homogeneous recrystallization (b) heterogeneous recrystallization
- Fig. 7.9** Variation of Grain boundary area per unit volume as a function of 204
transformed fraction estimated from the simulation for different nucleation modes. (a) homogeneous recrystallization (b) heterogeneous recrystallization
- Fig. 7.10** Plots of $\ln(S_v/(1-f))$ vs $\ln(-\ln(1-f))$ for different nucleation modes 205
under (a) homogeneous recrystallization (b) heterogeneous grain boundary recrystallization. The slope of the plots (q) is estimated using *Eq. (2.24)* excluding the nonlinear region observed at the end of the transformation. The q values are listed in the figure for corresponding nucleation modes
- Fig. 7.11** Plots of $\ln(S_v/(1-f))$ vs $\ln(t)$ for different nucleation modes under (a) 205
homogeneous recrystallization (b) heterogeneous grain boundary recrystallization. The slope of the plots (m) is estimated using *Eq. (2.23)* excluding the nonlinear region observed at the end of the transformation. The m values are listed in the figure for corresponding nucleation modes
- Fig. 7.12** Variation of Avrami exponent for varying nucleation rate (N_0) in the 208
mixed mode nucleation for heterogeneous recrystallization. ($N_0=2.1 \times 10^{16}$ Nuclei m^{-2})

deformation in order to avoid the simultaneous precipitation and recrystallization in this steel.

- Fig. 6.9** Variation of micro hardness in SS 304H Cu for 30 minutes of annealing at different temperatures. The temperature domains of recovery, recrystallization and grain growth is noted 174
- Fig. 6.10** The evolution of microstructure in deformed SS304H Cu samples as a function of annealing temperature for 30 min annealing time 175
- Fig. 6.11** Histogram showing the measured stored energy release during recovery and recrystallization for (a) IFAC-1 SS and (b) SS 304 H Cu 178
- Fig. 6.12** The fractional extent of (a) recovery and (b) recrystallization registered as a function of temperature under different heating rates for 85% cold work IFAC-1 SS 181
- Fig. 6.13** The fractional extent of (a) recovery and (b) recrystallization registered as a function of temperature under different heating rates for 85% cold work SS 304H Cu 181
- Fig. 6.14** Kissinger linearization plots of (a) recovery (b) recrystallization for IFAC-1 SS. T_p represents the peak temperature corresponding to the exothermic hump obtained using DSC 183
- Fig. 6.15** Kissinger linearization plots of (a) recovery (b) recrystallization for SS 304 H Cu 183
- Fig. 7.1** (a) The optical micrograph for 70% rolled austenitic stainless steel showing elongated grains in the rolled direction. (b). Nucleation of strain-free grains along the grain boundary of the deformed austenitic stainless steel after annealing for 240 s at 1073 K (c) microstructure showing complete recrystallization for annealing time 600 s at 1073 K 193
- Fig. 7.2** Variation of microhardness and the recrystallized fraction with annealing time for IFAC-1 austenitic stainless steel at annealing temperature 1073 K 194
- Fig. 7.3** The Avrami plot for isothermal static recrystallization at four different temperatures 195
- Fig. 7.4** Effective activation energy (Q_{eff}).as a function of Avrami exponent. 196

Fig. 5.15	Linear correlation between enthalpy increment and specific volume for IFAC-1 SS and SS 304H Cu	150
Fig. 5.16	The Debye- Grüneisen model C_p values obtained for IFAC-1 SS are co-plotted with the experimental low temperature data for SS 316 by Corson et al. The measured and model estimated volume thermal expansivity is also shown as an inset to the figure.	155
Fig. 5.17	The Debye- Grüneisen model C_p values obtained for SS 304 H Cu are co-plotted with the experimental low temperature data for SS 316 by Corson et al. The measured and model estimated volume thermal expansivity is shown as an inset to the figure	155
Fig. 6.1	Optical microstructure for 70% deformed (a) IFAC-1 (b) SS304 H Cu austenitic stainless steel	162
Fig. 6.2	(a) Three successive heating DSC traces of 85 % cold rolled IFAC-1 obtained on same sample under identical experimental conditions. (b) The expanded view of the on-heating DSC thermogram for the 1st cycle shown in (a). Distinct thermal arrests due to recovery and recrystallization events are seen.	164
Fig. 6.3	Optical micrograph of the IFAC-1 sample annealed at 1323 K for 15 minutes in DSC and fast cooled to room temperature. The part of the microstructure outlined by the dotted rectangle bears evidence for secondary recrystallization	166
Fig. 6.4	Variation of recovery and recrystallization peak temperatures with heating rate for 70 and 85% cold worked IFAC-1 specimens.	167
Fig. 6.5	Variation of microhardness with annealing temperature for the 85% cold worked IFAC-1.	170
Fig. 6.6	The microstructure evolution during annealing of cold rolled IFAC-1 SS as observed through optical microscopy	170
Fig. 6.7	DSC thermogram for the 85% cold rolled SS 304H Cu specimen. The three consecutive runs for the same specimen are denoted as 1st, 2nd and 3rd cycle.	172
Fig. 6.8	DSC thermogram for 85% rolled SS 304H Cu for different heating rates. The samples were aged at 923 K for 150 h duration prior to	172

Fig. 5.2	Enthalpy variation with temperature for SS 304H Cu	128
Fig. 5.3	Comparison of measured heat capacity (C_p) values of IFAC-1 and SS304H Cu with the reported data on the related 300 grade austenitic stainless steels [54, 55]	130
Fig. 5.4	Temperature variation of measured dilatational strain for IFAC-1 SS	132
Fig. 5.5	Temperature variation of measured dilatational strain for SS 304H Cu. The inset portrays the enlarged region in the temperature domain 850-1200 K along with the temperature derivative of the dilatational strain. A subtle variation in apparent linear expansion coefficient is observed in this region.	132
Fig. 5.6	Comparison of measured linear thermal expansion coefficients of IFAC-1 and SS 304H Cu austenitic stainless steel with literature data on 300 grade austenitic stainless steels	135
Fig. 5.7	Density versus temperature data on IFAC-1 SS and SS 304H Cu compared with literature values on related austenitic stainless steels	136
Fig. 5.8	Temperature variation of measured thermal diffusivity for IFAC-1 and SS 304 H Cu	140
Fig. 5.9	Thermal conductivity for IFAC-1 and SS 304H Cu obtained in the present study are compared with literature data on other related austenitic stainless steels	140
Fig. 5.10	Variation of flexural and torsion mode frequency with temperature for IFAC-1 SS	143
Fig. 5.11	Variation of flexural and torsion mode frequency with temperature for SS 304H Cu	143
Fig. 5.12	Temperature variation of measured Young's modulus (E), Shear Modulus (G), Bulk Modulus (K) and Poisson's ratio (μ) for IFAC-1 SS	145
Fig. 5.13	Temperature variation of measured Young's modulus (E), Shear Modulus (G), Bulk Modulus (K) and Poisson's ratio (μ) for SS 304H Cu	145
Fig. 5.14	Young's modulus and Shear modulus for IFAC-1 and SS 304H Cu obtained in the present study are compared with literature data on other related austenitic stainless steel	146

expanded view of the melting and solidification region. In contrast to slow 3 K min^{-1} cooling, only one peak is observed under fast cooling condition

- Fig. 4.10** *Thermocalc*[®]-based calculated vertical section as a function of Ni- 106
content for SS 304H Cu. The vertical dotted line corresponds to the Ni
content in the steel
- Fig. 4.11** (a)Temperature variation of phase fraction for different phases 106
estimated from *Thermocalc*[®] for SS 304H Cu (b) Magnified view of
(a), showing phases with low volume fraction
- Fig. 4.12** Scheil simulation of the solidification in SS 304H Cu 108
- Fig. 4.13** (a) The DSC heating profile obtained at 3 K min^{-1} heating rate, 110
showing various thermal arrests due to phase changes. (b) The
expanded view around melting regime
- Fig. 4.14** (a)The cooling cycle DSC profile obtained at 3 K min^{-1} , showing 111
various thermal arrests due to phase changes. (b) The expanded view
around solidification regime.
- Fig. 4.15** DSC solidification thermal arrests obtained at different cooling rates 115
for SS 304H Cu
- Fig. 4.16** Optical micrographs of samples that are cooled from liquid at different 115
rates. The inset in 7 K min^{-1} cooled sample marks the intragranular
 M_{23}C_6 phase
- Fig. 4.17** Microstructural evolution depicting the dissolution of second-phase 118
precipitates as a function of time after annealing at 1413 K ($1140 \text{ }^\circ\text{C}$).
- Fig. 4.18** Estimated percentage area of M_{23}C_6 precipitates plotted (a) as a 119
function of temperature, for 30 min. annealing time; (b) as a function of
time, at an annealing temperature 1413 K ($1140 \text{ }^\circ\text{C}$) (c) Fraction of
precipitates as a function of time during annealing at 1413 K ($1140 \text{ }^\circ\text{C}$).
The solid line represents the fit to KJMA model equation (*Eq. (2.15)*)
- Fig. 4.19** *Thermocalc*[®]-based vertical sections for various copper contents 122
ranging from 0 to 5 wt. % are collated. The vertical line in each denotes
the Ni composition for SS 304 H Cu.
- Fig. 5.1** Enthalpy variation with temperature for IFAC-I SS 128

Fig. 3.10	Schematic representation of a vertical push rod dilatometer	72
Fig. 3.11	Experimental set up for <i>Setaram</i> [®] <i>setsys</i> Evolution TMA 16	72
Fig. 3.12	Calibration of push rod dilatometer using sapphire standard	74
Fig. 3.13	Schematic representation of a laser flash diffusivity measurement system	77
Fig. 3.14	Experimental set up for the <i>Linseis</i> [®] laser flash Apparatus	77
Fig. 3.15	The experimental set up for the impulse excitation technique	82
Fig. 4.1	Room temperature X-ray diffraction pattern of (a) IFAC-1 SS and (b) SS 304H Cu showing the diffraction peaks for different phases	92
Fig. 4.2	Optical micrograph of IFAC-1 SS solution annealed at 1323 K	93
Fig. 4.3	Optical micrograph of SS 304H Cu solution annealed at 1473K for 2h	94
Fig. 4.4	Secondary electron micrograph and associated EDX spectra of a slow-cooled solution-treated SS 304H Cu sample	94
Fig. 4.5	(a) Bright field TEM micrograph of the solution annealed SS 304H Cu showing Nb rich MX phase in austenite matrix (b) SAD pattern from MX phase and austenite matrix in the solution annealed steel (c) TEM image of the aged steel showing M ₂₃ C ₆ precipitation along the austenite grain boundary (d) SAD pattern of M ₂₃ C ₆ carbide shown in (c) (e) TEM micrograph showing the dense Cu rich metallic precipitates in the aged sample (f) EDX spectrum corresponding to Cu rich phase (g) EDX spectrum of austenite matrix	96
Fig. 4.6	(a) <i>Thermocalc</i> [®] -based calculated vertical section for IFAC-1 steel as a function of Ni-content. The vertical dotted line corresponds to the Ni content in the steel (b) The mole fraction of different phases as a function of temperature	98
Fig. 4.7	<i>Thermocalc</i> [®] -based Scheil simulation of the solidification process for IFAC-1 SS	100
Fig. 4.8	(a) The on-heating and cooling DSC profile of IFAC-1 taken at 3 K min ⁻¹ . (b) The expanded view of DSC on-heating thermogram around the melting region (c) The expanded view of cooling cycle DSC profile in the solidification region	102
Fig. 4.9	DSC profile obtained at 99 K min ⁻¹ for IFAC-1 SS. The insets give the	104

List of Figures

Figure No.	Figure Captions	Page No.
Fig. 1.1	Step by step organization of materials design for high temperature applications	10
Fig. 2.1	Isothermal section of Fe-Cr-Ni ternary phase diagram at 1073 K calculated using <i>Thermocalc</i> [®] . The positions of typical 15Cr-15Ni and 18Cr-9Ni (wt. %) steels are marked in the figure which lies in the γ -austenite region.	19
Fig. 2.2	Successive stages in recovery during annealing of a deformed material [68]	28
Fig. 2.3	A schematic of different possible kinetic paths for the same phase transformation from the state α to β for three different cooling rates. The path A stands for an isothermal transformation whereas the path B represents the same under linear cooling rate. The path C depicts a stepwise cooling with small incremental isothermal holds.	34
Fig. 3.1	The experimental set up for Heat flux DSC used in the present study	55
Fig. 3.2	(a) <i>Setaram</i> [®] high temperature DSC furnace (b) Heat flux DSC plate-rod	56
Fig. 3.3	Typical cooling cycle DSC thermogram for the solidification of SS 304H Cu alloy from liquid. The two separate exothermic peaks indicates two transformation thermal arrests	59
Fig. 3.4	Temperature calibration in DSC with Copper and Aluminum	59
Fig. 3.5	Schematic of the temperature variation of enthalpy increment	62
Fig. 3.6	The experimental setup for inverse Drop calorimeter used in the present study	64
Fig. 3.7	(a) High temperature furnace with cabinet (b) Measurement head	65
Fig. 3.8	Snapshot of the signal output from the drop calorimeter	67
Fig. 3.9	Illustration of the temperature variation of Q for a typical experimental schedule and calibration constant (inset)	68

Chapter 6: This chapter deals with a dynamic calorimetric investigation of recovery and recrystallization in IFAC-1 and SS 304H Cu austenitic stainless steels. The chapter begins with a short description on the microstructural features of the deformed state of these alloys which is followed by a dynamic calorimetric investigation of recovery and recrystallization temperature and the associated stored energy release in IFAC-1 SS. Further the effect of heating rate on the recovery and recrystallization kinetics is discussed. The dynamic calorimetry results are further supported by micro hardness measurements and metallography results. The results of similar investigations on SS 304H Cu are also presented. Finally the estimation of kinetic parameters individually for recovery and recrystallization based on inputs from calorimetry is presented using analytical formalisms of Kissinger as well as Kolmogorov-Johnson-Mehl-Avrami (KJMA) model.

Chapter 7: Following the kinetic results obtained in Chapter 6, a geometrical simulation approach has been adopted to model the kinetics of static recrystallization and time evolution of grain structures in IFAC-1. The activation energies derived from experimental results served as input parameters for the computer model. From the simulation, the kinetic parameters are explicitly evaluated for pure site saturation (SSN), continuous nucleation (CN), mixed nucleation (MN) and Avrami nucleation (AN) modes using KJMA approach. The grain size distribution of simulated microstructures is obtained and compared with the experiment. The role of nucleation mode on the kinetics of static recrystallization and grain structure development is analyzed.

Chapter 8: This chapter summarizes the salient features of this thesis, highlights the important conclusions and outlines further avenues of research for future.

alloys. Finally structural characterization techniques like X-ray diffraction, optical and electron microscopy techniques are also described in brief.

Chapter 4: This chapter begins with the preliminary characterization of the alloys using X-ray diffraction, optical and electron microscopy techniques in order to examine the possible phases present in these alloys. This is followed by an equilibrium *Thermocalc*[®] simulation of phase equilibria in both the alloys which is intended to identify the temperature domain of stability of possible phases. The effect of non-equilibrium cooling on the solidification from liquid alloy has also been simulated with Schiel-Guliver non equilibrium module using *Thermocalc*[®] [33-34]. Following this a detailed dynamic calorimetry investigation on the phase stability and the effect of cooling on the solidification has been described. Finally the effect of Cu on the solidification and the kinetics of dissolution of second phase precipitates in SS 304H Cu have been described in detail.

Chapter 5: In this chapter the measurement and modelling of thermophysical properties of IFAC-1 and SS 304H Cu has been discussed. The chapter begins with the measurement of enthalpy increment in the temperature range 473 K to 1273 K and the estimation of temperature dependant heat capacity. This is followed by the results of dilatational strain measurement using TMA and the estimation of linear thermal expansivity. This is followed by the measurement of thermal diffusivity using laser flash technique and the estimation of thermal conductivity for both the steels. Following this the estimation of elastic moduli from room temperature to 1273 K using impulse excitation technique is presented. Finally the enthalpy data obtained in the present study for both the steels are modeled using quasi harmonic Debye-Grüneisen formalism. The modeling exercise yielded dilatational contribution to heat capacity, and a consistent estimate of temperature dependent volume thermal expansivity for both the alloys.

1.7. Organization of thesis

The thesis is divided into eight chapters of which the present chapter (**Chapter 1**) outlines the issues related to the design of advanced materials for the power sector. A brief description of the basic architecture behind the materials design protocol is also discussed in this chapter.

Chapter 2: This chapter focuses on the literature survey on thermal stability and thermophysical properties of advanced austenitic stainless steels for power plant applications. This description serves as a prelude for the high temperature calorimetry studies carried out on IFAC-1 and SS 304H Cu. This chapter also includes a brief description on the present understanding in literature on the recovery and recrystallization phenomena of advanced austenitic stainless steels. The kinetic aspects of stored energy relaxation of a severely cold worked (85% thickness reduction) system through interface and diffusion mediated phase transformations, specifically transformations mediated through nucleation and growth are important from the point of view of analyzing calorimetry data. In the light of this, the isokinetic and isoconversional methods have been adopted to analyze the kinetics of recovery and recrystallization in these advanced austenitic steels.

Chapter 3: In this chapter the experimental methodology adopted in the present study is described in detail. The chapter begins with a brief description of the alloy preparation and heat treatments adopted for the present alloys. This is followed by a detailed discussion of the instrumentation, calibration and experimental procedure for major experimental techniques employed in this study. The experimental techniques include the static and dynamic calorimetry for the estimation of phase stability and heat capacity, Thermo mechanical analyzer (TMA) for the evaluation of linear thermal expansivity, Laser flash thermal diffusivity for the temperature dependant thermal conductivity and Impulse excitation technique for the measurement of temperature variation of elastic moduli in these

recrystallization. Therefore a detailed database starting from the phase stability, thermo physical and mechanical properties as well as an extensive knowledge on the microstructure evolution during recovery and recrystallization is of major importance for the advanced materials design protocol. Once a comprehensive knowledge is established, an optimization procedure is generally adopted to obtain a microstructure suitable to achieve the desired properties of the final product for demanding engineering applications.

1.5. Genesis of this study

As the in core structural material in the case of sodium cooled fast reactors and the boiler components for advanced AUSC thermal power plants are exposed to very stringent service conditions, this draws special attention on the material selection in addition to design and fabrication of components. This thesis is focused towards the second stage of the materials design process which involves generation of a comprehensive knowledgebase on phase stability, thermophysical properties and recovery, recrystallization aspects of indigenously developed IFAC-1 SS and SS 304H Cu advanced austenitic stainless steels.

1.6. Scope of this study

The scope this study may be mentioned as follows:

“Measurement and modelling of phase stability, Thermophysical properties and the recrystallization behavior of advanced austenitic steels”

The study is focused towards the elucidation of thermal stability, thermophysical properties as well as the strain energy relaxation phenomena occurring during the process of static recovery and recrystallization. This study has both experimental and modelling components; and these are outlined in the following subsections dealing with the scope of individual thesis chapters.

The initial stage in the materials design calls for the material selection criteria. This step involves compositional control considering several factors like the demand from service environment, property requirements as well as the issues related to fabricability of components etc [28]. In addition to these, the overall life cycle cost and the safety and environmental issues also play a major role in the material selection criteria. Once the material is selected based on these inputs, the next step is to identify different possible phases and their temperature domain of stability. In case of materials for high temperature application, evaluation of thermal stability is an inevitable step, where the comprehensive knowledgebase on the thermodynamics and the kinetics of the phase transformation is absolutely essential in order to optimize the process parameters [26, 27-28]. This information further helps in the refinement of the microstructure suitable for service environment. The next step is to understand, how the microstructure can be controlled by the phase transformation. The correlation between the microstructure and the material property is of central importance in advanced materials design and a majority of worldwide research activities are presently focused on understanding the linkage between materials chemistry, physics and mechanics [26, 29-32]. The main challenge in determining microstructure–property relationships is that any variation in microstructure inevitably changes a host of properties. This limitation is due to the fabrication methods, which do not permit completely independent variation of just one microstructural feature. At some stage or the other during processing, engineering materials undergo hot working, cold working, annealing etc. These processes which involve recrystallization phenomena in one form or another need to be carefully controlled to obtain the desired grain size, shape, distribution, and orientation, which dictates their physical, and mechanical properties. *It is worth to mention here that austenitic steels do not involve phase transformation unlike ferritic therefore its microstructure can only be altered by means of thermo mechanical treatment which involve*

achieved deliberately by subjecting them to thermal activation in a predefined temperature and time domain i.e., heat treatment. Besides heat treatment, mechanical (plastic deformation and subsequent recrystallization) as well as chemical (metal-gas reactions) methods are also employed in order to achieve desired microstructures since it determines a variety of structural and functional properties of the materials [27]. Whether it be austenite to ferrite / martensite transformation in ferritic steels or precipitation of secondary phases in

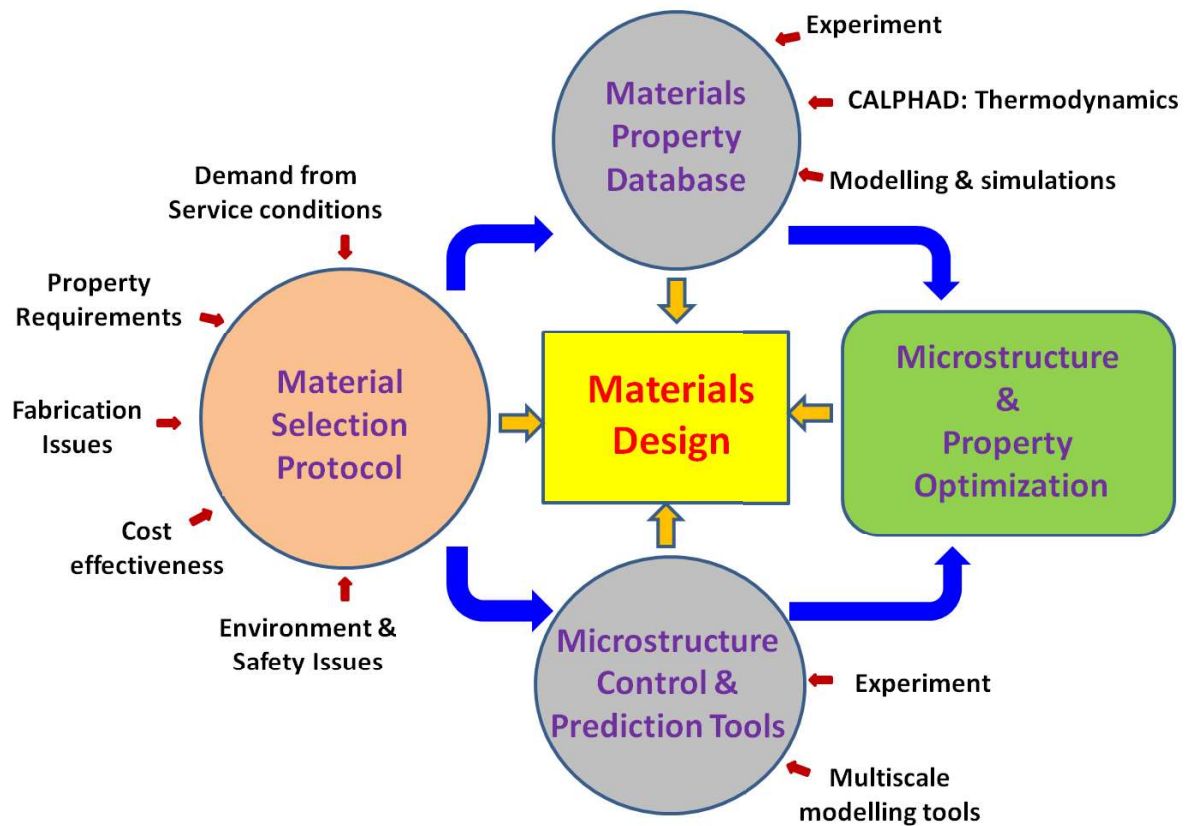


Fig.1.1. Step by step organization of materials design for high temperature applications

Al base and Ni base alloys, the mechanical properties are greatly enhanced by the phase transformation [27]. The enhancement of the properties of engineering alloys by employing phase transformation can be realized in several ways. A stepwise organization of materials design process is depicted in **figure 1.1.**

aging. This further enhances the creep strength of the steel and is a direct outcome of poor solubility of Cu in the γ -austenite phase.

In the context of setting up India's maiden AUSC power plant, an in-house development of an austenitic stainless steel of nominal composition (wt.%): Fe-17.7Cr-9.3Ni-2.95Cu-0.91Mn-0.58Nb-0.24Si-0.1C-0.12N, has been pursued. This material meant for boilers and super heater tubes of AUSC is an indigenous variant of the popular SS 304H Cu austenitic stainless steel. In the present study the basic physical metallurgy of this steel is investigated with respect to its thermal stability, the thermophysical properties in addition to the recovery and recrystallization aspects after plastic deformation.

Table 1. 2

Nominal composition (*Wt. %*) of selected 18Cr-8Ni austenitic steels for boiler applications in thermal power plants [14]

Material	Cr	Ni	C	Mn	Nb	Si	Others	Fe
TP304 H	18.0	8.0	0.08	1.6	--	0.6		Bal
Super 304 H	18.0	9.0	0.1	0.8	0.4	0.2	3.0 Cu, 0.1 N	Bal
TP321H	18.0	10.0	0.08	1.6	--	0.6	0.5 Ti	Bal
Tempaloy A-1	18.0	10.0	0.12	1.6	--	0.6		Bal
TP316H	16.0	12.0	0.08	1.6	--	0.6	2.5 Mo	Bal
TP347H	18.0	10.0	0.08	1.6	0.8	0.6		Bal
TP347 HFG	18.0	10.0	0.08	1.6	0.8	0.6		Bal

1.4. Materials design for high temperature applications

Materials design plays a central role in the development of advanced engineering alloys by optimization of the composition for tailoring the microstructure and vis-a-vis the properties [26]. Many industrial materials undergo phase transformations during the manufacturing process where the microstructure of the parent phase is replaced partly or fully by the product phase with a new microstructure. In engineering materials this is often

temperature as well as steam pipes which carry the steam from the boiler to the turbine [14, 15]. In general the steam piping operate at a relatively lower temperature compared to the SH and RH tubes. In addition to this, these components demand fatigue strength due to thermal fatigue conditions prevailing during operation. Generally ferritic and martensitic steels are preferred for this application which provides an extended fatigue life cycle in comparison to austenitic steels. However, due to poor high temperature creep strength as well as poor oxidation resistance ferritic steels cannot be used for components operating at temperatures exceeding 873 K [10,11]. The RH, SH and the furnace wall tubes in the AUSC plant demand for far enhanced creep strength as well as oxidation and corrosion resistance at operating temperatures exceeding 973 K. Hence advanced austenitic stainless steels with improved high temperature creep strength have been proposed as the candidate materials for the SH, RH tube components. In the recent evaluation of the steam conditions, various advanced grades of austenitic stainless steels have been developed meeting the requirements of enhanced creep strength as well as oxidation resistance. **Table 1.2** lists selected austenitic stainless steels developed for boiler applications in coal fired thermal power plants in the temperature range 923-973 K [14]. In order to increase the corrosion resistance in a harsh corrosive environment, a higher Cr content ($> 20 \text{ wt. } \%$) is generally preferred [14]. Extensive investigation on the effect of alloying elements in austenitic steels revealed that, the presence of stable precipitates largely enhances the creep properties as well as corrosion resistance [20, 25]. Elements like Ti and Nb were found to stabilize the steel by the formation of stable carbides [25]. Further the addition of Ti and Nb were controlled in order to obtain a uniform distribution of the secondary phases which is responsible for the creep strength in this class of materials [14-15, 25]. Recently copper has been identified as a beneficial alloying element which forms ultrafine metallic precipitates during long term

Beyond the regular functional requirements, the selection of materials for nuclear applications is generally realized by an optimized overall life cycle cost and also needs approval from the safety and environmental issues. In order to finalize the candidate material for a specific component in a fast reactor and to predict its long term behavior, a broad spectrum of material knowledgebase is highly essential. For example, the thermal stability of materials calls for both thermodynamic and kinetic databases under in-reactor service as well as transient conditions. This needs extensive experimental inputs as well as modeling in order to achieve a fundamental understanding of the basic physical metallurgy in these alloys.

Table 1.1

Nominal composition (*Wt. %*) of austenitic steels for core structural material applications in fast breeder reactors [10]

Steel	Cr	Ni	C	Mn	M	Ti	Si	P	S	B	Fe
316 SS	18	8.0	0.05	1.6	--	--	0.6	--			Bal
Alloy D9	13.5 - 14.5	14.5 - 15.5	0.035 - 0.05	1.65 - 2.35	2 - 2.5	5xC - 7.5xC	0.5 - 0.75	0.02 max	0.01 max		Bal.
IFAC-1	13.5 - 14.5	14.5 - 15.5	0.04 - 0.05	1.65 - 2.35	2 - 2.5	0.25	0.7 - 0.9	0.025 - 0.04	0.5x Ti	0.004 - 0.006	Bal.

1.3. Development of austenitic stainless steel for AUSC thermal power plants

It is widely accepted that the major enabling technology for the AUSC plants is the design of advanced materials with enhanced creep strength and corrosion resistance apart from its economic viability [13-19]. The key component in the AUSC plant design is the boiler which will operate with steam temperature in the range of 700 to 760 °C and pressure 35 MPa [14-15, 18]. The function of a boiler is to convert water into superheated steam, which is then delivered to a steam turbine. The boiler constitutes furnace wall tubes, super heater (SH) and reheater (RH) tubes where the steam is generated with high pressure and

rather than the fuel, limits the achievable fuel burn up in sodium cooled fast reactors [10-12, 21]. Therefore continuous R&D efforts have been in place towards the development of materials with improved radiation resistance with an objective to enhance the fuel performance and hence the overall life cycle cost. In this regard, the chemical composition of type 316 SS has been modified with higher nickel and lower chromium contents in comparison to the standard grade [10-11]. Further compositional tailoring with respect to minor alloying additions like titanium, silicon, phosphorous, boron and carbon has also been carried out as these elements play a dominant role in controlling the void swelling and creep resistance [10-12, 21-22]. These efforts led to the development of *Alloy D9* (15Cr-15Ni-Mo-Ti-C) with specifically tailored composition, with respect to titanium and carbon content, which is found to possess enhanced void swelling resistance in addition to creep strength [21-22]. Alloy D9 in 20% cold worked condition has been chosen for the in core structural materials for the 500MWe Prototype Fast Breeder Reactor (PFBR) presently under commissioning. It was further observed that, the composition of minor alloying elements like silicon, titanium and phosphorous have substantial influence on the void swelling behavior of alloy D9 [23-24]. Extensive experimental investigations have been carried out to study the void swelling behavior using both ion and neutron irradiation for varying compositions of Si, Ti, and P. Based on these studies, an optimized D9 alloy with Ti/C = 6, 0.75 wt. % Si, and 0.04 wt. % P has been developed at IGCAR which is found to have improved swelling resistance as well as creep strength [10, 22]. This alloy designated as *IFAC-1 (Indian Fast Reactor Advanced Cladding-1)* is the proposed in-core structural material for the future cores of PFBR as well as future FBRs in India with a target burn-up of ~150 dpa [10]. **Table 1.1** lists the compositions of the austenitic steels for purpose of in core structural material applications.

Considering the demand from both the fast breeder nuclear reactors and advanced A-USC coal fired thermal power plants, there has been a continuous indigenous effort to develop high temperature grades of austenitic stainless steels with improved thermo mechanical and thermophysical properties to meet the demands of service conditions as well as being economically realizable.

1.2. Advanced austenitic stainless steel for fast breeder reactor core applications

The selection of materials for nuclear applications is considerably more arduous than for other conventional energy systems. Under operating conditions of sodium cooled fast breeder reactors, materials used for various components experience different temperatures and gradients, load as well as neutron irradiation [8, 10-11]. For example, components like reactor vessels and intermediate heat exchangers which constitute “the out of core” structural materials are exposed to hot sodium coolant and therefore compatibility with hot sodium is the prime requirement [10-11]. However, the in-core structural materials consisting of fuel clad and hexagonal wrapper tubes, experience severe neutron irradiation, in addition to the high temperature and sodium environment [8-12]. The intense neutron irradiation leads to unique material problems like void swelling, irradiation creep, and irradiation embrittlement which gradually deteriorate the physical and mechanical properties of these materials [10-12]. Therefore resistance to irradiation induced changes in properties as well as high temperature strength are essential criteria for the choice of “in core” structural materials. Although ferritic steels have better radiation resistance as compared to austenitic steels, they are not found to be suitable for the in core applications due to their poor high temperature creep strength and high ductile to brittle transition temperature (DBTT) [10]. Type 316 austenitic stainless steel in 20% cold worked condition has been used as cladding and wrapper in early fast reactors [10-12]. But the achievable burn up was limited to only 50dpa [10-12]. It is a widely accepted fact that, the core structural materials (cladding and wrapper)

[15-16]. Eventually, the next generation of power plants namely Advanced Ultra Supercritical (AUSC) are planned to operate with steam temperature in the range of 700 to 760 °C and pressure of 35 MPa to obtain net efficiencies up to 50% and emit nearly 35% less carbon dioxide than conventional coal-fired power plants [15-16]. The achievement of enhanced efficiency in AUSC power plants not only helps in reduced fuel cost but also in reduced off plant costs due to less transportation, less waste disposal, emission controls as well as less cooling water consumption. However, the maximum steam parameters are again limited by materials that can operate at these conditions for a service lifetime without failure [14-18]. Therefore, it is essential to develop materials that can withstand high temperature and high pressure in addition to optimized thermodynamic cycles. The boiler tubes are the key components of an AUSC power plant where steam is generated and further heated to increase the temperature [14-15, 17, 19]. In addition to high temperature and high pressure, the boiler tubes are also exposed to fireside corrosion and steam side oxidation which are also important criteria for the selection of materials [14-15, 17, 19]. Ferritic steels are generally preferred as boiler materials for sub critical as well as super critical units due to their higher thermal conductivity and lower coefficient of thermal expansion (CTE). However, use of ferritic steels is limited to 873 K as they undergo a linear rate of oxidation as well as a substantial reduction in creep strength at higher temperatures [18-20]. Besides the demands of actual operating conditions, the secondary objective of introducing newer materials into the coal combustion cycle in AUSC power plants also needs to be in tune to meet the purpose of economizing the overall plant cost. In this context, although Nickel base super alloys fulfill the requirements of a boiler material they are relatively expensive. Therefore, advanced austenitic stainless steels with improved creep strength and corrosion resistance are promising materials for the advanced AUSC power plants.

the second stage and is an important milestone in the three stage nuclear power programme as they will not only help in the rapid growth of nuclear power capacity but also enable the conversion of thorium into fissile U_{233} , which will fuel the reactors in the third stage of the programme thus utilizing the large reserves of Th in the country [6-8]. There has been a continuous effort to design fast reactors with higher burn up in order to increase the effective fuel utilization [6-9]. However, with the increase in burn up, the in-core structural materials are subjected to a very demanding environment of high energy neutron flux ($\sim 10^{15}$ n $\text{cm}^{-2}\text{s}^{-1}$) in addition to high temperature [7-11]. The effective fuel burn up or in other words the residence time of fuel elements is determined by the performance of the reactor core components which in turn is dictated by the high temperature phase stability, mechanical properties and radiation resistance of the structural materials [8,10-12]. In this context, development of advanced materials with improved radiation resistance and high temperature mechanical properties play a vital role for the safe and economical fast reactor technology. Austenitic stainless steels with good high temperature mechanical properties along with low absorption coefficient for fast neutrons and corrosion resistance in sodium makes them excellent choice for the in core structural materials in the present generation of Fast Breeder reactors (FBRs) [10-12].

Parallely a mission oriented materials development programme has been initiated at IGCAR, India, for the high efficiency *Advanced ultra supercritical (AUSC)* coal fired thermal power plants. The most effective way to increase the efficiency of coal fired thermal power plants is to increase the steam temperature and pressure [13-16]. The conventional power plants which operated with the steam temperature and pressure up to 455 °C and 22 MPa, respectively (subcritical condition) resulted in efficiencies under 37% [15-16]. Continuous improvements on the steam temperature and pressure have resulted in supercritical systems (563 °C and 25 MPa) where the efficiency has increased up to 45%

1.1. Efficient energy production Process: Need for advanced materials

Global warming is an important point of concern and has a huge impact on the world's environment. The most significant contribution to global warming arises from the increasing concentration of CO₂ gas in the earth's atmosphere. Although this arises from several sources, the primary reason for CO₂ emission is the extensive use of coal and oil for the generation of heat and electricity [1- 4]. Coal fired thermal power plants are the prime source for worldwide electricity production. Easy availability and economic viability, makes usage of coal nearly 40 % of the world's energy supplies [5], which causes a major concern on the CO₂ emission due to heavy carbon content per unit energy release [5]. In the context of Indian energy scenario, the energy consumption and demand has grown substantially over the last few decades. Coal is the primary source of India's energy supply contributing to nearly 60% of the total electricity generation in 2014 [2]. Although alternative energy sources are being pursued with vigour for the long term energy security, coal utilization is expected to rise in the near future to meet the huge demand of electricity. Hence, it is necessary to evolve a strategy to either reduce the CO₂ emission from conventional thermal power plants or to rapidly facilitate green energy sources such as nuclear or solar energy. With this background, considerable R & D activities are being pursued in India for the development of advanced coal fired thermal plant as well as nuclear power technologies.

After successful commissioning of a large number of commercial pressurized Heavy Water Reactors (PHWRs) in the first stage of the three stage nuclear programme, India has designed and constructed the first sodium cooled 500MWe Fast Breeder Reactor (FBR) which is now in an advanced stage of commissioning. The fast breeder reactors constitute

Chapter 1

Introduction

$$\ln \frac{\beta}{T^2} = \ln \left(\frac{k_0 R}{Eh(f)} \right) - \frac{Q_{eff}}{RT} \quad (2.28)$$

The slope of the plot of $\ln (\beta/T^2)$ vs $1/T$ from the above equation leads to the value of the effective activation energy for the transformation. *Eq. (2.28)* is most popularly known as Kissinger equation which is widely used to study the kinetics of structural phase transformations.

It is important to mention here that, isoconversional methods are known to accurately estimate the effective activation energy for non-isothermal experiments as these methods do not assume any reaction model for the rate equation. However these methods are limited to the estimation of only one kinetic parameter, namely the effective activation energy. Therefore it is practically difficult to predict the transformation mechanism i.e. the nucleation, growth and impingement by adopting isoconversional methods. In this regard, the most efficient way for the estimation of the kinetic parameters is to use estimated values of effective activation energy from Kissinger method and using this value in the KJMA model equation to evaluate the growth exponent (n) and the rate constant (k_0). This approach is followed in the present study for the estimation of kinetic parameters for recovery and recrystallization in the austenitic stainless steels.

Eq. (2.26) again deals with the same temperature integral for which the exact solution is not available. There have been numerous attempts to obtain an approximate solution to the temperature integral to evaluate the kinetic parameters which resulted in multitude of methods. The isoconversional methods are broadly classified into two categories: (1) *isothermal methods* (2) *non-isothermal methods*. The non-isothermal methods are further classified as differential and integral methods based on the use of differential or integral form of the rate equation. Ozawa, Flynn and Wall used Doyle's approximation [151-154] to simplify the temperature integral to obtain a linear equation for the estimation of effective activation energy. The isoconversional method suggested by Friedman [155] uses a differential form of the rate equation. Another method suggested by Li and Tang [156] suggests an analytical approach for the determination of activation energy without approximating the temperature integral. The details of various isoconversional methods and their applicability under different transformation mechanisms are discussed by Starink [138]. Out of all these methods used, the most popular and widely adopted approach is the Kissinger-Akahira-Sunose method or more popularly called Kissinger method [157, 158] which is discussed below.

2.13.1. Kissinger-Akahira-Sunose (KAS) method

This method adopts the approximation of Murray and White [159] for the temperature integral in Eq. (2.20) to obtain an expression for the reaction model. As per this approximation the temperature integral in Eq. (2.20) can be expressed as:

$$\int_0^T \exp\left(-\frac{Q_{eff}}{RT}\right) dT = \frac{\exp\left(-\left(\frac{Q_{eff}}{RT}\right)^2\right)}{\left(\frac{Q_{eff}}{RT}\right)^2} \quad (2.27)$$

Using the above approximation (Eq. (2.27)) in Eq. (2.26) and rearranging the terms:

for treating the heterogeneous nucleation using Cahn's approach [146]. The parameters S_v and f are measured experimentally and the values of q and m are estimated from the slope of the plots of $\ln(S_v/(1-f))$ vs $\ln(-\ln(1-f))$ and $\ln(S_v/1-f)$ vs $\ln(t)$ using Eq.(2.24) & Eq.(2.23) respectively. The kinetic parameters q and m contains explicit information about the nucleation and growth mechanisms of the transformation similar to the Avrami exponent in the KJMA approach. The observed values of q , m , and the Avrami exponent n can be compared with the theoretical values to predict the nature of nucleation and growth during the transformation [148, 149]. A critical analysis of the MPM method has been made by Goetz and Seetharaman using CA approach, for pure site saturated and continuous nucleation modes in heterogeneous recrystallization [150].

2.13. Model-free isoconversional methods

The isoconversional methods are primarily based on the fundamental equation that governs the transformation kinetics which is expressed as follows:

$$\frac{df}{dt} = k(T) g(f) \quad (2.25)$$

Where $k(T)$ is the rate constant as given in Eq. (2.16) and $g(f)$ is the reaction model. The primary difference between the isokinetic and isoconversional methods arises due to the reaction model $g(f)$ which assumes certain functional form for isokinetic methods. In case of KJMA model, the $g(f)$ is expressed by Eq. (2.17). However for isoconversional methods, the effective activation energy is estimated without assuming any function form for the reaction model for which these methods are popularly known as model-free isoconversional methods.

Eq. (2.25) can be expressed in the integral form as follows:

$$h(f) = \int_0^f \frac{df}{g(f)} = \frac{k_0}{\beta} \int_0^T \exp\left(-\frac{Q_{eff}}{RT}\right) dT \quad (2.26)$$

dimensionality of growth. Further, the expressions for the overall, effective activation energy, Q_{eff} , given in **table 2.4** can be represented by a single equation, incorporating the exponent n , the ratio of the number of growth dimensions and the growth mode, d/m , and the individual activation energies for nucleation, Q_N , and for growth, Q_G , as follows [126, 134, 137].

$$Q_{eff} = \frac{\frac{d}{m_G} Q_G + \left(n - \frac{d}{m_G} \right) Q_N}{n} \quad (2.22)$$

Eq. (2.22) is valid under isothermal and isochronal transformations.

2.12.2. Microstructural path method

Another successful method called microstructural path method (MPM) was developed by Vandermeer and co-workers to study the kinetics of transformation that are governed by nucleation and growth processes [144-149]. The model defines a microstructural path function S_v , as a function of transformed volume fraction f , which contains implicit information on nucleation and growth characteristics of the transformation. The parameter S_v stands for the interfacial area per unit volume between the transformed and untransformed regions. In case of recrystallization, S_v basically serves the role of a quantifiable stereological measure of recrystallized fraction. Incorporating the isothermal KJMA as given in Eq. (2.15) into MPM formalism, the parameter S_v can be expressed as a function of annealing time (t) and transformed fraction (f) by the following equations [146].

$$S_v = C_1 (1 - f) t^m \quad (2.23)$$

$$S_v = C_2 (1 - f) \left[\ln \frac{1}{(1 - f)} \right]^q \quad (2.24)$$

Here, C_1 , C_2 , m and q are constants. Although the method was originally proposed in line with the basic tenets of KJMA model, appropriate modifications were incorporated later on,

Eq. (2.21) can be used to fit the experimental transformed fraction data with the help of method of least squares to obtain the kinetic parameters Q_{eff} , n and k_0 .

It is important to mention here that, based on the degree of transformation, explicit analytical equations for n , Q_{eff} and k_0^n for both isothermal and isochronal transformations can be derived using specific nucleation and growth models [119]. For pure site saturation and for pure continuous nucleation or both in combinations with growth, KJMA like equations can be obtained following Eq. (2.21) which are listed in **table 2.4** [119].

Table 2.4

Theoretical values of kinetic parameters under isothermal and isochronal transformations [119]

Transformation mode	Isothermal	Isochronal
<i>Continuous nucleation</i>		
n	$d/m+1$	$d/m+1$
Q_{eff}	$\frac{\left(\frac{d}{m}\right)Q_G + Q_N}{n}$	$\frac{\left(\frac{d}{m}\right)Q_G + Q_N}{n}$
K_0	$\left(\frac{gN_0G_0^{d/m}}{n}\right)^{1/n}$	$\left(\frac{gN_0G_0^{d/m}}{n}\right)^{1/n} C$
<i>Site saturation nucleation</i>		
n	d/m	d/m
Q_{eff}	Q_G	Q_G
K_0	$(gN^*G_0^{d/m})^{1/n}$	$(gN^*G_0^{d/m})^{1/n}$

In **table 2.4** the parameter C in the expression for K_0 for isochronal annealing under continuous nucleation is the correction factor arising due to the unequal contribution of Q_N and Q_G towards the Q_{eff} as the growth exponent n varies continuously with temperature [119]. The parameter m decides the mechanism of transformation. For interface controlled growth, $m= 1$ and for diffusion controlled process $m=2$. The second term d is the

In the above equation Q is the effective activation energy for the overall transformation. For the rest of the thesis *Eq. (2.15)* will be referred to KJMA isothermal relation. Differentiation of *Eq. (2.15)* results in the well-known KJMA rate equation.

$$\frac{df}{dt} = n k (1-f) [-\ln(1-f)]^{\frac{n-1}{n}} \quad (2.17)$$

Eq.2.17 constitutes the basis for analyzing non isothermal transformations as the transformation rate is dependent on the temperature (through k) and the transformed fraction [126-128, 139-143]. For non-isothermal experiments the temperature at any instant can be expressed as a function of heating/cooling rate (β) and time (t) as follows:

$$T = T_s \pm \beta t \quad (2.18)$$

Where T_s is the onset temperature. Substituting *Eq. (2.18)* in *Eq. (2.15)* and *Eq. (2.16)*, the transformed fraction during a non-isothermal case can be stated as:

$$f = 1 - \exp \left[- \frac{k_0}{\beta} \int_{T_s}^T \exp \left(- \frac{Q_{eff}}{RT} \right) dT \right]^n \quad (2.19)$$

It is important to mention here that, there is no unique solution for the temperature integral appearing in *Eq. (2.19)*. Several attempts have been made before to obtain accurate approximations to the temperature integral in *Eq. (2.19)*. The approximate solution is stated below [141-142].

$$\int_{T_s}^T \exp \left(- \frac{Q_{eff}}{RT'} \right) dT' \cong T \exp \left(- \frac{Q_{eff}}{RT} \right) \sum_{p=1}^{\infty} \left(\frac{RT}{Q_{eff}} \right)^p (-1)^{p-1} p! \quad (2.20)$$

Retaining only the first term ($p=1$) in the approximation to temperature integral and using in *Eq. (2.19)*, the transformed fraction during a non-isothermal case can be expressed as:

$$f = 1 - \exp \left[- \left\{ \frac{k_0 R (T - T_s)^2}{\beta Q_{eff}} \exp \left(- \frac{Q_{eff}}{RT} \right) \right\}^n \right] \quad (2.21)$$

2.12. Isokinetic methods

Most of the isokinetic models developed to study the kinetics of phase transformations mediated through nucleation and growth are based on **KJMA** model [126-128, 139, 140].

2.12.1. Kolmogorov-Johnson-Mehl-Avrami (KJMA) model for isothermal and non-isothermal transformations

This model, assumes spatially random and homogeneous nucleation and constant isotropic growth during the transformation [126-128, 139, 140]. In this model, the transformed fraction (f) is expressed in terms of an extended volume fraction as per the following equation.

$$f = 1 - \exp(-f_{ext}) \quad (2.14)$$

In the above equation, f_{ext} stands for the extended transformed volume fraction and f is the actual transformed volume fraction. The extended volume is defined as the ratio of total volume of all the product phase to that of the volume of the parent phase, neglecting the role of impingement between the product phases. Following standard developments of the KJMA model that are extensively discussed in literature [128, 139-140]; Eq. (2.14) may be simplified as follows.

$$f = 1 - \exp(-(kt)^n) \quad (2.15)$$

Where, n represents Avrami exponent and k is the rate constant, which usually exhibit Arrhenius temperature dependence as

$$k = k_o \exp\left(\frac{-Q}{RT}\right) \quad (2.16)$$

described in literature they are not practically suitable for many general applications [129-131].

2.11. Modeling solid state transformation kinetics

A solid state phase transformation generally proceeds through three independent processes, namely nucleation, growth and impingement. The kinetic parameters obtained from the analysis of experimental data depend mainly on two factors; namely (a) mode of experiment (i.e. isothermal or non-isothermal) and (b) kinetic models adopted to analyze the experimental data. There are several methods available for the analysis of the kinetic data [117, 132], which can be broadly categorized into two namely:

(a) Isokinetic methods, (b) Model-free Isoconversional methods

Isokinetic methods are based on the assumption that the transformation mechanism (nucleation, growth, impingement etc.) remains the same throughout the transformation. Therefore the kinetic parameters are assumed to be constant throughout the transformation irrespective of time and temperature [133-137]. On the other hand isoconversional methods which are generally adopted for non-isothermal transformations assume that the transformation rate for a fixed extent of transformation is a function of temperature [138]. Therefore the kinetic parameters in this case are no more constants but a function of time and temperature. In case of many thermally activated solid state transformations including those for static recovery and recrystallization, the transformation mechanism is quite complex and involves multistep nucleation and growth. Therefore the activation energy in principle cannot be purely a constant which is contrary to the isokinetic hypothesis. Notwithstanding the limitations of isokinetic approach, this method is widely used for the analysis of kinetic parameters for several solid state transformations.

phase per unit time. The jump of atoms is determined by the difference in the Gibb's free energy for an atom between parent and product phase. However, the transfer of the atom is inhibited due to the formation of a new interface, which in turn creates an energy barrier for the jump of atoms across the interface. If Q_G is the net free energy difference between parent and product phases, then the net flux of atoms jumping across the interface from the parent to the product phase can be approximated as follows [67, 118].

$$J = J_0 \exp\left(-\frac{Q_G}{RT}\right) \quad (2.11)$$

Here J_0 is the pre-exponential factor. Further, the volume of the growing particle in case of interface controlled growth is expressed as:

$$G_v = g \left(\int J dt \right)^d \quad (2.12)$$

Therefore for interface controlled growth the growth velocity (G_v) can be represented by

$$G_v(T) = G_o \exp\left(-\frac{Q_G}{RT}\right) \quad (2.13)$$

Where, G_o represents the interface velocity independent of temperature and Q_G is the activation energy for growth.

2.10.3. Mode of impingement

The growth of the nuclei calculated from Eq. (2.13) evaluates the transformed volume considering independent growth of each nucleus without taking into account the impingement from the surrounding nuclei. In real systems, the particles do not grow into an infinitely large parent phase and suffer impingement either due to the geometrical obstruction caused by the surrounding particles (hard impingement) or due to the overlapping fields (soft impingement) of the growing particles. Although a few specific analytical and numerical approaches to model the effect of impingement have been

2.10.2. Growth mode

The growth mode can be either *interface controlled* or *diffusion controlled* depending on the mechanism of diffusion [67]. Interface controlled growth involves short range diffusion and the composition of the product phase does not change compared to the parent phase. On the other hand diffusion controlled growth involves long range diffusion wherein the composition of the product phase is different than that of the parent phase [67,118].

In the case of diffusion controlled growth, the diffusion length, R_d is proportional to square root of time and can be expressed in the following form [67,118]

$$R_d = (Dt)^{1/2} \quad (2.8)$$

Where the parameter D is called the diffusion coefficient and is constant at a fixed temperature. Under non-isothermal conditions the diffusion coefficient is a function of temperature and can be described as per the following equation [118].

$$D(T(t)) = D_0 \exp\left(-\frac{Q_G}{RT}\right) \quad (2.9)$$

In the above equation, D_0 is the pre-exponential factor and Q_G is the activation energy for diffusion or growth. The volume of the growing particle in case of diffusion controlled growth is expressed in terms of diffusion length by the following expression.

$$G_v = g(R_d)^d \quad (2.10)$$

Here G_v is the growth velocity, g is the geometrical factor with respect to the particle growth and d is the dimensionality of growth.

In interface controlled growth, the growth of the particle is governed by the mobility (velocity normalized to driving force) of the interface between product and parent. The velocity of the interface is decided by the net jump of atoms from the parent to the product

For transformations under large undercooling, (where the thermodynamic driving force can be neglected) the nucleation rate is governed by the rate of diffusion of atoms between the parent and the product phase. In this case, the nucleation occurs continuously and the nucleation rate is expressed by an Arrhenius term.

$$\dot{N}(T(t)) = N_o \exp\left(\frac{-Q_N}{RT}\right) \quad (2.4)$$

Where N_o is the pre-exponential constant, independent of temperature, Q_N is the activation energy for nucleation and R is the gas constant. This is called *continuous nucleation mode (CN)*.

Under certain experimental conditions, nucleation can occur with finite quenched in nuclei at $t=0$ and subsequent continuous nucleation upon further annealing [120-122]. This mode is called (one of) the *mixed nucleation mode (MN)* and is expressed as a linear combination of both site saturation and continuous nucleation mode [123-125].

$$\dot{N}(T) = N^* \delta(t-0) + N_o \exp\left(\frac{-Q_N}{RT}\right) \quad (2.5)$$

Where N^* is the number of preexisting nucleation sites.

In case of *Avrami nucleation mode (AN)*, the nucleation rate varies continuously with time in a manner, proposed originally by Avrami [126-128]. For AN mode, the rate of nucleation under isothermal conditions can be expressed by the following expression.

$$\dot{N}(t) = \bar{N} \lambda \exp(-\lambda t). \quad (2.6)$$

Where, \bar{N} represents the pre-exponential factor and λ is the rate constant, which again follows Arrhenius temperature dependence.

$$\lambda = \lambda_o \exp\left(\frac{-Q_N}{RT}\right). \quad (2.7)$$

during the non-isothermal transformation can be estimated from the sum of the transformations during the isothermal steps from state α to β .

2.10. Mechanisms of diffusional transformations

There have been several efforts in the past to understand the fundamental mechanism of phase transformations that ultimately decides the kinetics. In the classical treatment, the Kolmogorov-Johnson-Mehl-Avrami (KJMA) approach plays a central role in the kinetics of phase transformations. This phenomenological approach is based on the transformation mechanism which initiates with the homogeneous nucleation of product phase in the parent phase matrix that subsequently grows into the parent phase and suffers impingement by the other growing grains. The mode of nucleation, growth and impingement are responsible to drive the transformation and hence decides the transformation kinetics. The detailed discussion on the kinetic formulation of nucleation, growth and impingement effects in a solid state transformation is well documented in literature [118-119]. In view of this, only a brief account on different nucleation and growth modes for isothermal annealing conditions is presented here.

2.10.1. Nucleation mode

The term *site saturated nucleation (SSN)* is often used in cases where all potential nuclei already preexist in the parent phase at $t=0$; and for $t > 0$, the nucleation rate is zero; hence no more nucleation is allowed. Therefore, the condition of site saturation can be expressed mathematically in the following form.

$$\dot{N}(T) = N' \delta(t - 0) \quad (2.3)$$

Where, $\dot{N}(T)$ is the nucleation rate per unit volume at temperature T (K), N' represents the number of preexisting nucleation sites per unit volume and $\delta(t)$ stands for the Dirac delta function.

strength [110-111] etc., that are brought upon by collective defect reorganization processes [68, 70]. Generally, one or many of these techniques are employed in conjunction with detailed microstructural characterization using advanced microscopy and quantitative microstructural enumeration techniques [112-115] so that a comprehensive knowledge of the micromechanics of the stored energy driven lattice relaxation is obtained [68, 70, 72, 116]. In the present study, heat flux differential scanning calorimeter is used to study the kinetics of recovery and recrystallization under non-isothermal conditions.

2.9. Isothermal and non-isothermal transformation

In case of an isothermal transformation, the sample is held at a fixed temperature for a finite time where the transformation rate is decided by the magnitude of absolute temperature and time which governs the available driving force for the atomic diffusion and hence the extent of transformation (path A in **figure 2.3**). Non-isothermal processes involve continuous heating and cooling as a function of time (path B in **figure 2.3**). In general non-isothermal experiments are performed easily with minimal expenditure of time; but there are serious computational difficulties associated with the kinetic analysis [117]. Under practical situations, most of the industrial heat treatments are carried out under a mixture of isothermal and non-isothermal conditions which demand a detailed understanding of the transformation kinetics under both the conditions. The ultimate goal is to adopt the best method to analyze the kinetic data (under isothermal and nonisothermal conditions) not only to estimate the kinetic parameters but also to achieve a fundamental understanding of the processes responsible for the transformation kinetics. In general a non-isothermal continuous heating or cooling kinetic path can be assumed to be a sum of isothermal steps (path C of **figure 2.3**) where the transformation occurs only during the isothermal steps. If the number of steps for a linear heating or cooling schedule goes to infinite, the total transformation

rates play an important role as the kinetic variable decides the final microstructure in many engineering alloys. In the context of recrystallization although there is no structural phase change during the transformation from parent phase to the product phase (strain free grains), a complete new grain structure evolves mediated through the process of nucleation of strain free grains in the deformed state and subsequently grows to consume the deformed microstructure by the diffusion of atoms. There are several kinetic path variables such as the mode of deformation, the deformed state, the heating rate etc which drives the transformations into different kinetic paths. Therefore, it is desired to estimate the kinetic parameters in order to control the kinetics of recovery and static recrystallization which

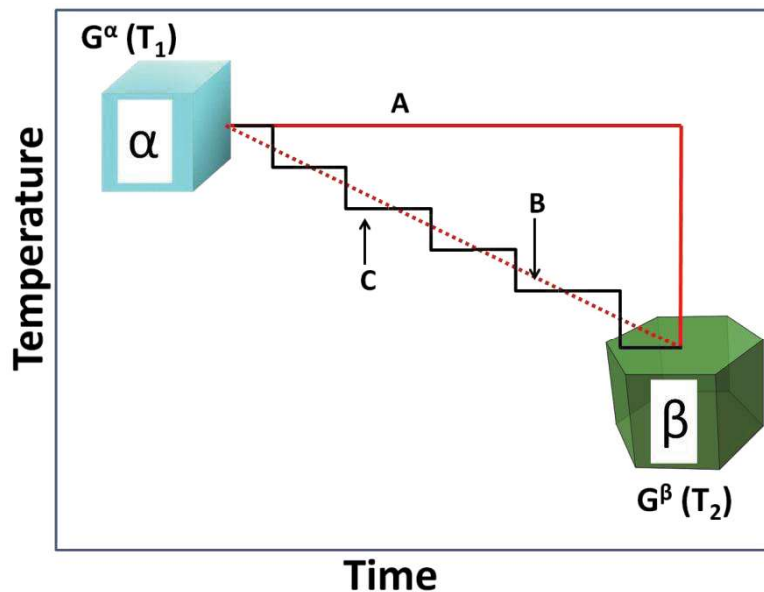


Fig.2.3. A schematic of different possible kinetic paths for the same phase transformation from the state α to β for three different cooling rates. The path A stands for an isothermal transformation whereas the path B represents the same under linear cooling rate. The path C depicts a stepwise cooling with small incremental isothermal holds.

ultimately decides the final microstructure, for the optimization of physical and mechanical properties in engineering alloys. In general the dynamics of recovery and recrystallization have been studied by monitoring as a function of time (for isothermal) or temperature (non-isothermal) the changes in physical properties such as resistivity [101-103], heat capacity [104-105], magnetization [106], X-ray line profile analysis [107, 108], hardness [109], yield

size distribution is referred to the cases where a few selective grains grow preferentially and consume the smaller grains [97]. A bimodal size distribution is generally observed in case of abnormal grain growth.

2.8. Kinetics of phase transformation

Phase transformation which stands for the thermodynamic instability in a system is one of the most investigated areas in materials physics, chemistry and engineering. Any change in the thermodynamic variables like pressure, temperature or volume leads to a corresponding change in the Gibbs free energy of the system. The change in Gibbs free energy then results in a change in the structural details of the phase which is called *Phase Transformation*. While the phase transformation of the system is decided by the minimization of thermodynamic Gibbs free energy, the rate at which the transformation proceeds cannot be predicted purely from the thermodynamic grounds. A thermodynamic phase change is classified from the nature of discontinuity in appropriate susceptibility functions. The kinetic considerations further broaden these classifications [98-100]. In general the solid state phase transformations can proceed along a variety of kinetic paths depending on the path variable [98-100]. Let us consider a system undergoing a phase transformation from the parent phase α to the product phase β during cooling from high temperature. **Figure 2.3** illustrates the schematic of the path variable concept in studying the phase transformation kinetics where the cooling rate serves as the path variable [28]. From **figure 2.3** it can be clearly observed that, the system can choose three independent paths (A, B, C) which involve different time durations for the same transformation. There are several possible path variables for a solid state transformation which includes morphology of the material, the stress state (σ), the grain size, the irradiation level etc. All of these path variables can act separately or in combination with each other which determines the overall kinetics of transformation. In case of solid state transformations, the heating and cooling

nucleus [68, 70]. In case of precipitation strengthened steels, precipitation generally occurs before recrystallization which affect both recovery and recrystallization. F. J. Humphreys has observed that, the nucleation rate is higher in case of two phase alloys compared to a single phase system [94]. Further the nucleation rate in his study was found to be more for alloys containing large particles although the effect of particle size is found to be less on the growth. In essence the presence of second phase particles influence the recrystallization process in multiphase system either by change in nucleation mechanism / kinetics or a change in grain boundary pinning, or by changing the rate of work hardening.

2.7. Grain growth

After the primary recrystallization driven by the stored energy of deformation is complete, the stability of the microstructure cannot be ensured and further growth of the recrystallized grains may occur. This growth mechanism which is driven by the stored energy in the grain boundaries is generally referred to as grain growth [68, 70]. The driving force for grain growth is nearly two orders of magnitude less than that for primary recrystallization [68, 70]. Grain growth is of considerable importance as it plays a major role in controlling the grain size. For example, a small grain size is preferred for materials operating at relatively low temperatures in order to enhance the strength and toughness. However, a large grain size is preferred in case of structural materials operating under high temperature environment in order to improve the creep strength [95]. Therefore a prior knowledge on the grain growth kinetics helps in controlling the average grain size and hence in optimizing the desired mechanical properties depending on the operating environment.

In general grain growth is classified into two types, namely normal grain growth and abnormal grain growth or secondary recrystallization. Normal grain growth is a continuous process where the microstructure coarsens uniformly and results in a narrow distribution of grain sizes and shapes in the final microstructure [96]. On the other hand abnormal grain

$$v = m \times \Delta\tau \quad (2.1)$$

The mobility of the interface is a function of the misorientation between the deformed and the recrystallized state. The mobility of the interface is expressed by the following relationship [68].

$$M = M_o \left(-\frac{Q_b}{RT} \right) \left[1 - \exp \left\{ -5 \left(\frac{\Delta\theta}{15} \right)^4 \right\} \right] \quad (2.2)$$

Where M_o is the temperature independent mobility factor, Q_b is the activation energy of grain boundary migration and $\Delta\theta$ is the misorientation angle. The number 15 in the above expression stands for the limiting misorientation angle that differentiates the high angle and low angle grain boundaries.

2.6.3. Effect of particles on recrystallization behavior

It is well known that the second phase particles significantly influence the recrystallization process [68, 92-93]. The primary effect of small particles is to pin the grain boundaries often called as Zener-pinning [68, 70]. The influence of small particles on recrystallization actually depends on its appearance during deformation or during the subsequent anneal before recrystallization. However, large particles promote the nucleation process during annealing as these particles form deformation heterogeneities [92]. This is known as particle stimulated nucleation (PSN) [68, 92, 93]. The conditions under which PSN can occur are well documented in literature [68, 93]. The large particles also influence the deformation process as they do not undergo shear during deformation. Thus they form complex deformation heterogeneity around them which affects the recrystallization kinetics [70]. During the deformation of an alloy containing large particles, there exists a large strain gradient in the vicinity of the particle. This creates a region of high dislocation density and large orientation gradient which is an ideal site for the development of a recrystallization

boundaries. The driving force for the growth of these nuclei arises from the difference in dislocation densities across the high angle grain boundaries [70, 86].

2.6.1. Role of deformation on recrystallization behavior

It is a well-known fact that understanding recrystallization requires a detailed knowledge on the deformed microstructure [68, 70]. The nucleation during recrystallization is a direct outcome of the instability in the deformed state where the potential embryos already exist adjacent to high local misorientations. Unlike other transformations mediated through nucleation and growth, nucleation during recrystallization does not occur by atom by atom construction as explained by kinetic models. Nuclei rather appear during recrystallization from the recovered subgrains or cells that are already present in the deformed/ recovered matrix which ensures that the orientation of new strain free nuclei arises from the deformed / recovered matrix [88-90]. Similarly, the growth of the grains depends on the average stored energy [68] and the frequency of new grains appearing with orientations similar to the deformed state [89, 90]. A detailed qualitative microstructural investigation on the size and orientation of individual regions as well as a quantitative estimation of the average stored energy in the deformed state is absolutely necessary to understand in detail the mechanism of recrystallization.

2.6.2. Growth during recrystallization

The recrystallized nuclei by definition are the region in the recovered subgrains surrounded by high angle boundary which is able to migrate through the deformed microstructure causing the nucleus to grow. The high angle grain boundary gradually moves towards the deformed region where the stored energy acts as the driving force for recrystallization. The velocity (v) of these high angle boundaries is expressed by the product of mobility (m) and the driving force ($\Delta\tau$)

structure is consumed by the recrystallized strain free grains. Therefore the kinetics of recrystallization process in principle depend on the extent of recovery which is again dependant on the stacking fault energy of the material. Austenitic stainless steels generally have relatively low stacking-fault energies (less than 100 mJ m^{-2}) [83]. There is considerable evidence that the dislocation cell structure commonly observed in pure metals is suppressed in alloys with low stacking-fault energies due to difficulty in dislocation cross-slip during deformation [68, 84].

2.6. Recrystallization

Recrystallization is defined as the appearance of a new strain free grain structure in a deformed material by the formation and migration of high angle grain boundaries driven by the stored energy of deformation [70]. Recrystallization in general can be categorized into two types, namely static and dynamic recrystallization. Dynamic recrystallization refers to the evolution of new grain structure during hot deformation in contrast to static recrystallization where the new recrystallized grain structure appears during annealing at a suitable annealing temperature in a cold deformed material [85, 86]. The recrystallization temperature in case of static recrystallization is defined as the temperature at which 50% of the material is recrystallized during an annealing duration of one hour [68, 87]. The recrystallization temperature plays a vital role in material processing because the mechanical and physical properties of a product can be tuned by design of grain size, shape and the mean orientation or texture by appropriate selection of time and temperature of annealing [68, 70, 87]. Recrystallization initiates with the process of nucleation of strain free grains followed by growth where the defects and dislocations are absorbed by the moving high angle grain boundaries. The nucleus is a minute region of space inside the deformed subgrains which is separated from the rest of the deformed matrix by high angle grain

configuration consisting of dislocation walls or the subgrain boundaries which significantly reduce the stored energy due to the random dislocation network in a heavily deformed material. The formation of cells or subgrains occurs continuously and grows under thermal

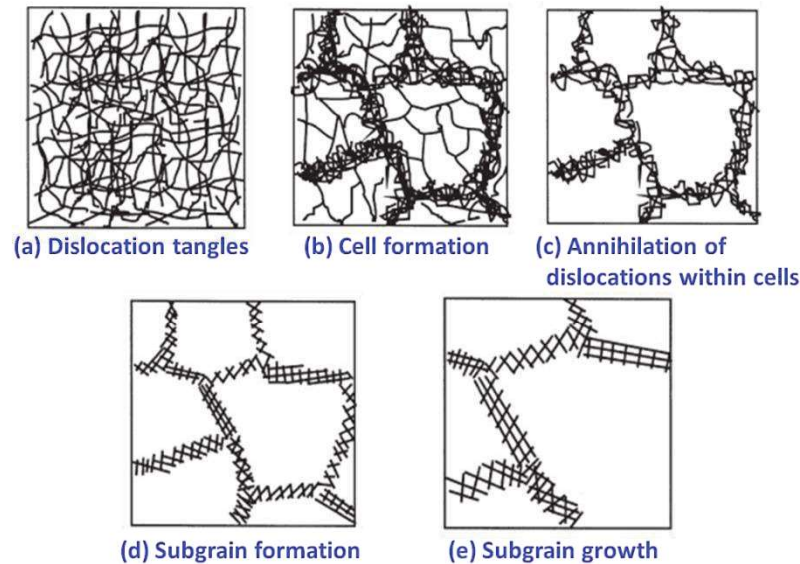


Fig.2.2. Successive stages in recovery during annealing of a deformed material [68]

activation (**figure 2.2(c) & (d)**). This process is popularly called polygonization [76]. The kinetics of recovery i.e. the rate at which the subgrain boundaries appear during recovery annealing depends on the mode and extent of deformation [68, 77]. The development of subgrains in the recovery stage has been well documented for pure elements like iron [78, 79], nickel [80] and aluminum [81, 82]. In the next step during recovery, the well-developed subgrains start to grow which further reduces the total stored energy. There are several factors such as high stacking fault energy, large strain energy as well as the temperature of deformation which favors easy subgrain formation during the recovery annealing [70]. In the case of metals with low stacking fault energy, the well-developed subgrain structure is not generally observed [68, 70]. It is instructive to note here that both recovery and recrystallization are driven by the stored energy of deformation and hence in real systems compete with each other. The recovery process continues till the complete deformed

2.4. Work hardening

Work hardening is one of the popular strengthening mechanisms which takes place due to formation and interaction of dislocations in crystals during plastic deformation [68, 69]. With increase in the extent of plastic deformation, the dislocation density and hence the interaction between them also increases continuously. This results in a decrease in the mobility of the dislocations resulting in increased strength of the material [69]. The plastic deformation introduced in a material at low temperatures in order to prevent the rearrangement of defect structure, is called cold working. In contrast the hot working refers to the process where the deformation is carried out at a relatively higher temperature where the formation and annihilation of defects takes place simultaneously [68]. A plastically deformed crystalline material is thermodynamically unstable due to the excess stored energy of deformation in the form of lattice defects. However, with adequate thermal activation, the material can reduce its free energy by subsequent rearrangement and annihilation of lattice defects [70-74]. The strain energy relaxation is generally categorized into three processes, namely recovery, recrystallization and grain growth.

2.5. Recovery

The recovery process is referred to all annealing processes occurring in a deformed material that do not involve the migration of high angle grain boundaries i.e. boundaries with a misorientation angle greater than $10-15^\circ$ [70]. Recovery occurs in several steps which initiates with the annihilation of point defects and the rearrangement of complex dislocation networks into low energy configurations [68, 75]. The different stages of recovery are schematically shown in **figure 2.2** [68]. The dislocation recovery actually proceeds through a series of micro mechanisms which starts with the formation of cells (subgrains) from random dislocation networks (**figure 2.2(b)**) [68, 70]. The dislocations in the cell interior annihilate leaving behind a dislocation free region (**figure 2.2(c)**). This forms a low energy

there is a paucity of robust database on the high temperature polycrystalline elastic modulus of austenitic stainless steels although a few measurements have been carried out for SS 304, SS 316 and SS 310 below room temperature [63-65].

It is needless to say that the high temperature strength is the major criteria in materials selection for power plant applications. The relatively higher strength of austenitic steels at high temperatures makes it attractive for numerous applications with a major thrust on continuous R& D activities to further improve the strength. Unlike ferritic steels the strength of the austenitic stainless steels are improved by adopting solid solution strengthening, precipitation strengthening and work hardening [66, 67]. Although precipitation hardening is one of the most common strengthening mechanisms for austenitic steels, the coarsening of precipitates under high temperature exposure for long times, leads to a decrease in strength. On the other hand, work hardening by introduction of plastic deformation can be adopted under several situations to enhance the strength. Moreover the formation of new strain free grains by recrystallization during controlled annealing after deformation is also a method used widely to obtain the desired grain size, shape and orientation with optimum physical and mechanical properties of materials [39, 68]. However both deformation response and the recrystallization behavior of a material is sensitive to various factors namely the alloying elements, the mode and extent of deformation, temperature and time of deformation/annealing, the presence of secondary phases and/or impurities etc. Therefore a fundamental understanding of these phenomena is an essential step in advanced materials design in order to control the microstructure to obtain specific desirable properties. The next section deals with the details of work hardening and the subsequent strain energy relaxation process during annealing.

case of indigenously developed advanced materials for specific high temperature applications; it becomes necessary to carry out a critical reappraisal of the available literature data on similar materials as well as fresh measurements with a view to provide a reliable data input to design engineers.

Although an extensive research activity is going on worldwide to design austenitic steels with improved mechanical properties, attention has also been paid towards the thermophysical property of these classes of materials. A comprehensive and critical literature review on the thermophysical properties from room temperature up to melting is reported by Bogard et. al on a few selected grades of steels [54]. Recommended values of thermodynamic and transport properties of low carbon versions of nuclear grade austenitic stainless steel (SS 304L, SS 316L) were reported by C. S. Kim from 300 K to melting temperature [55]. Further Mills et.al have proposed empirical equations for the estimation of heat capacity, thermal expansivity, thermal conductivity and resistivity, as well as the viscosity for both solid and liquid phase in a few austenitic, ferritic and precipitation strengthened stainless steels [56]. However, the measured data on 300 grade austenitic stainless steels differ appreciably in their investigations for steels of similar composition. Although a few investigations on thermophysical properties of 15Cr-15Ni austenitic steels have been carried out recently [57-59], most of the literature data are limited to 18Cr- 8Ni or 18Cr-12Ni based 300 grade austenitic stainless steels [54-56]. In addition, measurements on the high temperature thermophysical properties of any precipitation strengthened austenitic steels containing alloying elements like Cu and Nb is not found in literature. Besides the thermo-physical properties, the temperature dependent elastic moduli and Poisson's ratio play a central role in numerous metallurgical aspects of materials design as well as in understanding the basic nature of the interatomic forces in condensed matter. They share intrinsic interrelationship with the thermodynamic properties as well [60-62]. However,

	although it can form under normal aging conditions too. Si content of the steel greatly influences the G-Phase formation.	
σ -Phase	This is the common intermetallic phase (FeCr) in Fe-Cr system. It is observed to precipitate along triple points, incoherent twin boundaries and intragranular inclusions during long term aging.	40,48
Laves Phase	This phase is seldom found in austenitic steels. This is a minor constituent and forms as intragranular particles. Most commonly observed Laves phase in austenitic steels is Fe ₂ Nb.	40-41
χ -Phase	χ -Phase is often a minor intermetallic phase in austenitic steels found in AISI 316 at higher aging temperatures. A typical composition of this phase is Fe ₃₆ Cr ₁₂ Mo ₁₀ . Nucleation of this phase is observed to occur preferentially along the grain and twin boundaries.	49, 50
Cr ₂ N	Cr ₂ N is generally observed in steels containing high nitrogen content.	40-41
Cu precipitates	Addition of Cu in steels promotes the precipitation of metallic Cu due to its poor solubility in austenite. Normally the precipitation occurs homogeneously. The precipitation of Cu significantly enhances the creep rupture strength.	51-53

For sodium cooled fast reactors adequate heat capacity and thermal conductivity are important factors for the fuel cladding materials as they effectively transfer the heat from the core to the coolant [10]. This property is essential to prevent accidental conditions like core melt down by controlling any unusual increase in the temperature of fuel elements. Therefore a knowledge based design approach for the fabrication of engineering components especially those operating at high temperature conditions require a comprehensive understanding on the thermophysical, chemical and thermo-mechanical properties. In the

Besides the enhancement in the mechanical properties, the presence of second phase precipitates also influence the chemical and thermo-physical properties of the steels [41]. Thermophysical properties like heat capacity, thermal expansion and thermal conductivity of structural steels are of paramount importance in power industries. In case of AUSC fossil fuel power plants, the boiler tube components demand for a better thermal conductivity to reduce the heat loss as well as a higher thermal expansion coefficient to improve the fatigue resistance [14-16].

Table 2.3

List of Secondary phases observed in austenitic stainless steels and their characteristics

Secondary phases	Characteristics	References
$M_{23}C_6$	General notation for $Cr_{23}C_6$. Often Ni, Mo and Fe are found to substitute for Cr. Most commonly observed in austenitic steels and nucleated along the grain boundaries, twin boundaries and intra-granular sites.	40-43
MX	Forms when strong Carbide/Nitride formers (Ti, Nb, V, Ta) are added to the steels. MX precipitates generally form on dislocations in the matrix, stacking faults and grain boundaries.	40,41
M_6C	M_6C represents the phase where the composition varies appreciably. This phase is reported to be either Mo rich ($(Fe\ Cr)_{21} Mo_3 C_3$) or Nb rich (Fe_3Nb_3C). It is generally formed after long aging times.	41-43
Z-Phase	Z-phase is a complex carbo-nitride often observed in Nb stabilized austenitic steels with relatively higher nitrogen content. It generally forms on grain boundaries very rapidly although it can form on twin boundaries or even inside the matrix along the dislocation sites.	40,44-45
G-Phase	G-Phase is basically a silicide phase commonly observed in Ti and Nb containing stabilized steels under irradiation	40,46-47

temperature applications have a carbon content of about 0.08% to provide better creep strength. These steels are denoted with a symbol ‘H’. The symbol ‘N’ after the series number denotes the nitrogen addition to the steel. **Table 2.2** lists the nominal composition of most popular AISI 300 grade austenitic stainless steels.

2.3. Phase stability and thermophysical properties of austenitic stainless steels

Although AISI 300 series of austenitic stainless steels retain the parent fcc- austenite structure up to ambient temperatures, numerous secondary phases form as equilibrium phases in these classes of steels. In the case of creep resistant precipitation hardened steels, secondary precipitates are deliberately introduced in the austenite matrix in order to improve the mechanical properties. A detailed analysis of the precipitates that form in austenitic stainless steels is well documented in literature [40, 41]. In order to achieve the desired properties in these steels, prior knowledge on fundamental mechanisms and kinetics of formation, dissolution and coarsening of the second phase precipitates is necessary [40, 41]. The precipitation process is primarily based on the decrease in solubility of alloying elements with lowering temperature. In general, solution annealing at a suitable temperature and time domain is adopted to form a single austenite phase solid solution followed by quenching in order to form a supersaturated solid solution. Further aging of the austenite under in-service or appropriate thermal conditions promotes secondary precipitates by conventional nucleation and growth process aided by diffusion. The in-service precipitation of the secondary phases acts as obstacles for movement of dislocations and hence enhances the strength. However, the overall achievable creep strength depends on the type of precipitates, their shape and size, distribution in the bulk austenite matrix as well as their temperature domain of stability etc. **Table 2.3** lists the commonly observed precipitate phases in austenitic steel.

provides enhanced creep strength. Therefore Cu is generally used as an alloying element in creep resistant austenitic stainless steels.

- **Silicon** is basically a ferrite stabilizer and also improves the oxidation resistance of steels by forming a silicon oxide layer

2.2.2. Classification of austenitic stainless steels

The compositions of austenitic stainless steels cover a wide range. However, they are mostly referred by the compositions of the major alloying element, namely Cr and Ni. For example 18/8 grade stands for the austenitic stainless steel with 18 wt. % Cr and 8 wt. % Ni. The AISI designation for austenitic steels is well known with the number series 200 (Cr-Mn steels) and 300 (Cr-Ni steels) [36, 37]. The 300 series austenitic stainless steels are the larger subgroup due to its extensive use in various applications. Generally letter designations at the end of the number series indicate modifications to the composition. Steels that are used in corrosive environments should have low carbon content (≤ 0.03 wt %) to prevent corrosion [38, 39]. In the steel description, it is denoted with a symbol 'L'. Steels used for high

Table 2.2

Chemical composition (Wt. %) of some popular AISI 300 grade austenitic stainless steels

Steel grade	Cr	Ni	C max	Mn (Max)	Si (Max)	others
301	16-18	6-8	0.15	2.0	1.0	
302	17-19	7-10	0.15	2.0	1.0	
304	18-20	8-12	0.08	2.0	1.0	
310	24-26	19-22	0.25	2.0	1.0	
316	16-18	10-14	0.08	2.0	1.0	Mo (2-3)
321	17-19	9-12	0.08	2.0	1.0	Ti (5x%C)
347	17-19	9-13	0.08	2.0	1.0	Nb (10x%C)

2.2.1. Role of alloying elements

- **Mn** is one of the important secondary alloying elements in an austenitic stainless steel which is a strong austenite stabilizer. Although Mn is used as a substitute for Ni, Mn-steels lack in corrosion resistance compared to high Ni steels. Mn is also used as a sulfide scavenger in steels.
- **Carbon** provides excellent solid solution strengthening effect as these atoms occupies the interstitial sites of a FCC austenite structure. In case of stabilized steels C also acts as a precipitation strengthening element by the formation of carbide precipitates in the presence of Ti, Nb or V.
- **Nitrogen** is a strong austenite stabilizer which acts very similar to carbon with better solid solution strengthening effect compared to C. Addition of N is responsible for the enhancement of creep strength of austenitic stainless steels by promoting the precipitation of nitrides and carbo-nitrides.
- **Molybdenum** is another important constituent in most of the austenitic stainless steel which improves the creep properties by solid solution hardening. Mo is also believed to improve the resistance to pitting corrosion. Nevertheless Mo is a ferrite stabilizer and on long term thermal exposure, it promotes the formation of several detrimental phases like sigma and Laves phase.
- **Nb, Ti and V** are alloyed in few austenitic stainless steels (stabilized grades) for the precipitation of intragranular carbides and carbo-nitrides which provide improved high temperature creep strength in these classes of steels. However these elements are ferrite stabilizers.
- **Copper**, which is also an austenite stabilizer, promotes the precipitation of nano size metallic precipitates due to its extremely poor solubility in austenite and hence

15Cr-15 Ni and 18Cr- 9 Ni steels which lies in the austenite field are also marked in the same figure. The advantages of austenitic stainless steels are manifold. They can be made soft or hard depending on the requirement. The excellent corrosion resistance, ductility,

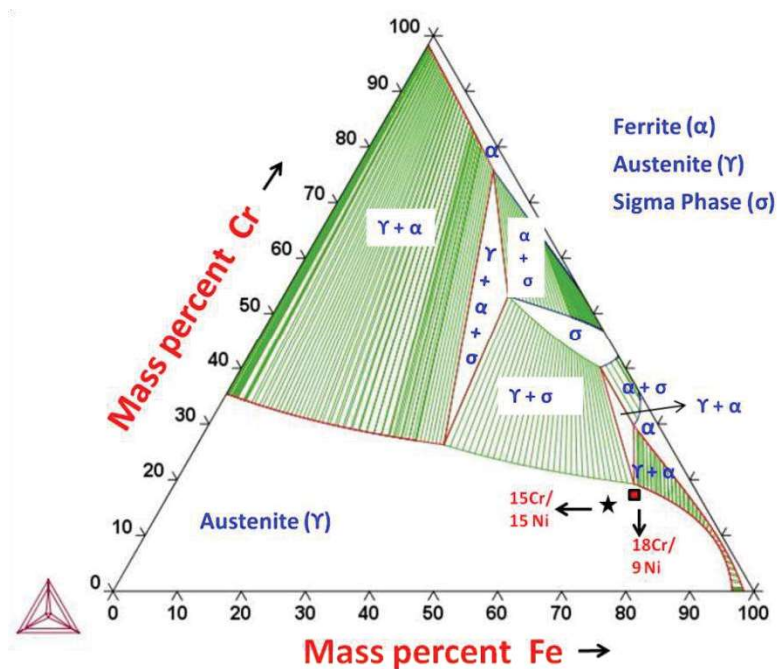


Fig.2.1. Isothermal section of Fe-Cr-Ni ternary phase diagram at 1073 K calculated using *Thermocalc*[®]. The positions of typical 15Cr-15Ni and 18Cr-9Ni (wt. %) steels are marked in the figure which lies in the γ -austenite region.

toughness, high temperature strength in addition to the easy formability and weldability of austenitic steels makes them the prime candidate in a wide range of applications such as chemical, petrochemical, power generation and allied industries. The motivation behind the continuous evolution of austenitic stainless steels has been improvements in mechanical and chemical properties as well as thermal stability considerations [36]. Besides being the primary substitutional alloying element which stabilizes the austenite phase Ni also improves the toughness, ductility and weldability of austenitic stainless steels [36, 37]. Ni is also believed to improve the resistance to pitting corrosion. The role of different alloying elements added to achieve desired properties in austenitic stainless steels is summarized in the following section [36, 37].

especially for high temperature applications [36-38]. **Table 2.1** summarizes the alloying elements and the applications of the five different classes of stainless steels with a goal to provide a brief background on the stainless steels.

Table 2.1
Classification of stainless steels

Stainless steel Category	Structure	Composition range for common alloying elements (Wt. %)				Other alloying elements	Properties
		Cr	Ni	C	Mo		
Austenitic	FCC	16-25	8-20	<0.08	0-7	Mn, Nb, Ti, Cu, N	Excellent corrosion resistance and good strength
Ferritic	BCC	10-30	0-4.5	<0.25	0-4.5	Mn, Si, Ti, Al, N	Low cost, Excellent formability
Martensitic	BCC/ BCT	10-18	0-7	.03-2.2	0-4	Mn, Si, V, N, Cu	Superior strength and hardness
Duplex	BCC+FCC	18-30	1-8	<0.05	1-5	Mn, Si, N, Cu, W	Excellent Corrosion resistance, work hardenability and toughness
Precipitation hardened	BCC/FCC	10-17	4.3-26	< 0.2	0-5	Mn, Si, Al, Ti, Nb, V, Cu, W	Superior high temperature strength and toughness

2.2. Austenitic stainless steels

Austenitic stainless steels are the most common and familiar grade of stainless steels which contain about 16-25 wt. % Cr , 8-20 wt. % Ni and 0.03-0.08 wt. % C and retains the austenite structure at ambient temperature. They are non-magnetic in nature and possess high strength at elevated temperatures unlike ferritic stainless steels [36-38]. Since Ni is the basic alloying element used to stabilize the austenite phase, the austenitic steels are generally considered as Fe-Cr-Ni ternary alloys. **Figure 2.1** illustrates an isothermal section of ternary Fe-Cr-Ni equilibrium phase diagram at 1073 K calculated using *Thermocalc*[®] with TCFE8 database. The austenite, ferrite and the sigma phase regions are shown in the figure. Typical

Literature Survey

2.1. Stainless steels: General introduction

The alloy steels which exhibit the stainless property and contain a minimum of 11% Cr are generally known as stainless steels. The minimum amount of Cr is adequate to produce a uniform, adherent and passive layer of Cr_2O_3 to prevent further oxidation and make the steel 'stainless'. Stainless steels are basically found in two crystallographic forms, namely body centered cubic (bcc) and face centered cubic (fcc). The crystal structure is dictated by the proportion of alloying elements. The alloying elements are classified as either ferrite stabilizers (those stabilizing bcc structure) or austenite stabilizers (those stabilizing fcc structure). Cr, higher than 11% by weight is the basic constituent in steels to impart corrosion resistance or stainless quality and is a ferrite stabilizer. Besides Cr, Ni and carbon are the primary alloying elements in a stainless steel and are strong austenite stabilizers. A number of other alloying elements added to the steel for different functions have different potentials to stabilize either the bcc ferrite or fcc austenite structures. The potential of individual alloying elements in stabilizing the bcc/ fcc phase are expressed either in terms of Cr-equivalent (for ferrite stabilizers) or Ni-equivalent (for austenite stabilizers). In practice, a preliminary idea on the crystallographic structure of any stainless steel with a specified composition can be obtained from its Cr and Ni equivalents using Schaeffler diagram although the diagram was primarily devised to predict the possible phases in a weld metal [35]. Depending on the crystallographic structure, stainless steels are categorized into various subgroups, namely (i) Ferritic, (ii) Austenitic, (iii) duplex (ferrite + austenite) and (iv) martensitic stainless steels [36, 37]. Further there is another special group of stainless steels called precipitation hardened which caters to the need of very high strength materials

Chapter 2

Literature Survey

from several regions of the specimen for a statistically meaningful analysis of the composition. For the quantification of EDS spectra the beam diameter and the tilt angle was kept 50 nm and 30° respectively.

3.13.1. Phase analysis using electron diffraction pattern

The indexing of electron diffraction patterns involve phase identification by the assignment of specific (hkl) indices to the individual spots and the determination of the beam direction which corresponds to the zone axis of the reflecting planes. To identify the (hkl) planes, the distance (d-spacings) from the diffracted spot to the transmitted spot and the angle between the diffracted spots and the transmitted spot are measured. The matched angles and d-spacings were attained with an error of 1° and 0.2 Å respectively.

and counting the number of times the line segments are intersected by grain boundary and finding the ratio of the intercepts to line length. Thus it is written as,

$$\text{Average grain size} = \text{line length} / N \times M. \quad (3.23)$$

where N = number of intercepts and M = magnification. The statistical scatter in grain size quantification from 50 measurements is of the order of $\pm 10\%$.

The volume fraction of the constituent phases was determined by estimating the area fraction of the phases. This quantification has been done by automated image analysis software (Image J[®]) [200]. The image thresholding option provided in Image J[®] software converts the gray scale image to binary images and delineates the contrast between features [200].

3.13. Transmission electron microscopy

TEM studies were carried out using a *CM200* Analytical Transmission Electron microscope equipped with Inca X-max with SDD detector for microstructural and micro-chemical analysis. The experiment was carried out at a voltage of 200 kV. Magnification calibration was carried out with a cross grating of 2160 lines/mm with a separation of 469 nm between two lines. Camera length was calibrated with standard nano-crystalline oriented gold in holey carbon film at different accelerating voltages. The high resolution test with a line resolution of 2.3 Å is performed by using same standard sample. Analysis of selected area diffraction (SAD) patterns and dark field microscopy were carried out to identify the presence of different phases. An aperture of 10 µm size was used for obtaining the SAD pattern and dark field images. Trace analysis was carried out after applying correction for rotation of SAD pattern w.r.t magnification using MoO₃ crystals. A spot size of ~50 nm was used to collect the characteristic X-rays from the constituent phases for determining the composition. In-hole spectra were collected periodically to ensure the absence of spurious X-ray sources in the column of the microscope. A large number of spectra were acquired

steels with a dimension of 10 mm×10 mm and thickness of about 2 mm using diamond saw. The sample is cut in such a way that it is easily leveled flat in a sample stage to avoid the height problem. Before loading, the samples have been ground well with 1000 grit paper to remove any unwanted particles sticking on to it. The voltage and the current level in X-ray tube are set as 40 kV and 30 mA. The wavelength used is of 1.5406 Å (Cu-K_α) fitted with nickel filter. The diffraction pattern for each sample is recorded for 1h duration. The diffractometer has been calibrated with annealed silicon powder (5000 Å) supplied by NPL, India. The peak positions, the full width at half maximum, and the *d*-spacings are recorded and are compared with the standard values suggested by NPL

3.12. Scanning electron microscopy (SEM) Study

The scanning electron microscopy studies are carried out with *Philips XL30 ESEM* attached with *EDS* facility. Secondary electron modes are used for the microstructural observations. The sample preparation procedure for SEM studies is similar to the one employed for optical microscopy studies. In order to prevent the electrostatic charge formation, conducting carbon tapes are used for the purpose of charge grounding. The magnification calibration is made with standard cross grating samples of 20 lines/mm and 2160 lines/mm. The high resolution calibration test is performed on a carbon film embedded with gold nanoparticles, whose spacing is of the order of 20 Å. Energy dispersive X-ray analysis is carried out using energy dispersive spectrometer for qualitative identification of elements with atomic number greater than 10. Energy calibration is carried out with a detector resolution of 132 eV at Mn-K_α.

3.12.1. Analysis of microstructural parameters

In this study, important microstructural parameters such as grain size and volume fraction of the constituent phases are measured. The grain size was measured using the intercept method [199]. It is obtained by drawing a set of line segments on the microstructure

discs. Finally the samples are alumina and diamond polished. This step is followed by washing in soap solution followed by methanol. Etching is done by gently swabbing the surface of the specimen with cotton bud soaked with the appropriate etchant. Etched samples are immediately washed with distilled water and methanol to protect from any further chemical attack. In this study the polished austenitic stainless steel samples are etched with oxalic acid solution for outlining the grain boundaries. Further in special circumstances of cold rolled and recovered samples, electrolytic etching has been carried out with dilute nitric acid (60% HNO₃:40 % H₂O) at 2 V for 1 min for revealing the grain interior.

3.10. Microhardness measurement

The hardness measurements have been carried out with *Leitz* Vickers micro hardness tester. All the measurements are taken with 50 and 100 g load. About eight to ten measurements are taken for each sample and the average value is reported here. A standard test block of known hardness with prescribed load of 100 g is used for calibration. The probable error calculated by taking 15 indentation measurements on the standard sample is found to be within $\pm 3\%$. The Vickers hardness number (VHN) is calculated using the following formula:

$$\text{VHN} = 1.854 \times (F/D^2). \quad (3.22)$$

In the above equation, F being the applied load (measured in kilograms-force) and D^2 , the area of the indentation (measured in square millimeters). The applied load is also specified when VHN is cited.

3.11. X-Ray diffraction (XRD)

The X-ray characterization is performed with *Inel* XRG 3000 -X-Ray Diffractometer which makes use of a curved position sensitive X-ray detector for detecting diffracted X-ray intensity. Such type of detectors can measure up to 120 degrees of 2θ simultaneously and have high speed of data acquisition. Thin slices of samples have been cut from respective

and Shear (G) modulus. The frequencies are measured during heating, holding and cooling cycles.

The key factors that decide the uncertainty in measurement in the impact excitation technique are the mass and dimension of the test-piece. A maximum of 0.05 % uncertainty in the measured mass, 0.1 % uncertainty in the measured length and 0.2 % uncertainty in the measured width and thickness of the sample leads to a 0.1% uncertainty in the calculated modulus values [197]. In addition to this, the frequency which enters in *Eq. (3.15)* and *Eq. (3.17)*, as the second power, should ideally be measured to better than 0.1%. The accuracy of the sound card attached to the computer for the measurement of the frequency in the present case is 0.05%. The mass of the samples has been measured using *Satorious®* semi micro balance where the uncertainty in the measured mass is 0.01%. Further, the dimensions are measured accurately using a vernier caliper with the measurement uncertainty is found to be 0.05 %. Therefore the calculated elastic modulus in the present case has an uncertainty of 1%. It is instructive to note that both K and μ are sensitive in a sense that these parameters are obtained as the ratio of two independent elastic modulus values, and hence any measurement error associated with E and G gets intensified in the indirectly estimated μ and K .

3.9. Optical metallography

The optical microscopy studies are carried out with the *Leica MeF4A®* optical microscope fitted with a Leica digital camera and associated proprietary software for image acquisition and treatment. The sample for optical metallography has been prepared using established metallography procedures [198]. Due care has been taken to ensure that it contains all the representative features present in the investigated material. Mounting of sample is usually done using cold setting resin (epoxy resin) and some samples through hot mounting press (thermosetting plastic – phenolic resin). Mounted specimens are grounded systematically from coarser to finer emery grades (wet silicon carbide paper) with rotating

$$G = \frac{4Lmf_{tor}^2}{bt} \left[\frac{B}{1+A} \right] \quad (3.17)$$

In the above expression, G is shear modulus in Pa, f_{tor} is the torsional frequency in Hz, l , b and t are length, breadth and thickness respectively of the bar sample in mm ; and A and B are the correction factors represented by the following equations [195, 196].

$$A = \left[\frac{0.5062 - 0.8776 \left(\frac{b}{t} \right) + 0.3504 \left(\frac{b}{t} \right)^2 - 0.0078 \left(\frac{b}{t} \right)^3}{12.03 \left(\frac{b}{t} \right) + 9.892 \left(\frac{b}{t} \right)^2} \right] \quad (3.18)$$

$$B = \left[\frac{\frac{b}{t} + \frac{t}{b}}{4 \left(\frac{t}{b} \right) - 2.52 \left(\frac{t}{b} \right)^2 + 0.21 \left(\frac{t}{b} \right)^6} \right] \quad (3.19)$$

Once the values of E and G are evaluated using *Eq. (3.15)* and *Eq. (3.17)*, the bulk modulus (K) and the Poisson ratio (μ) are estimated using following relations

$$K = \frac{EG}{3(3G - E)} \quad (3.20)$$

$$\mu = \frac{E}{2G} - 1 \quad (3.21)$$

3.8.3. Measurement details

In the present investigation, before commencement of an experimental run, the furnace is continuously flushed with pure Ar gas (6.6 litres per minute) to minimize sample oxidation at high temperatures. A heating rate of 7 K min^{-1} from room temperature (298 K/25°C) to 1273 K /1000°C is adopted. The sample is held at 1273 K /1000°C for about 5 minutes to acquire thermal equilibrium, before the cooling cycle at 3 K min^{-1} is initiated. The measured frequency spectrum at each temperature had at least one prominent flexural and torsional frequency components that were needed for estimating respectively the Young's (E)

$$E = 0.9465 \left(\frac{mf_{flx}^2}{b} \right) \left(\frac{L}{t} \right)^3 T_c \quad (3.15)$$

$$\text{Where } T_c = 1 + 6.858 \left(\frac{t}{L} \right)^2 \quad (3.16)$$

In Eq. (3.15), E is the elastic modulus in Pa; m is the mass of rectangular bar sample in g; b is the breadth; l is the length; t is the thickness of sample in mm; f_{flx} is the measured flexural resonance frequency in Hz; and finally T_c is the empirical correction factor represented by Eq. (3.16).

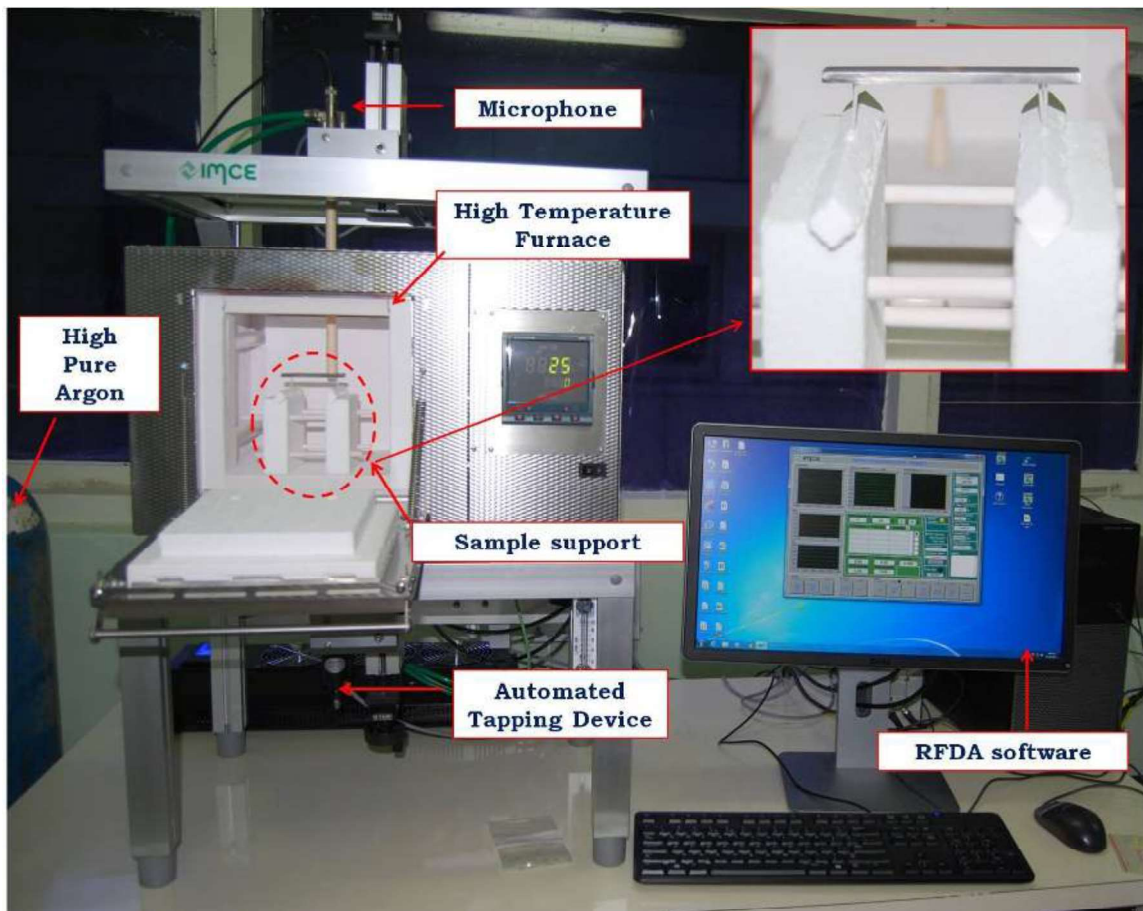


Fig. 3.15. The experimental set up for the Impulse excitation technique

In a similar manner, the relation connecting the fundamental torsional frequency f_t and shear modulus G of a rectangular bar specimen is given as follows [194-196].

support system) is put as an inset to the **figure 3.15** The sample is excited by providing a gentle mechanical impulse by firing a small ceramic hammer (placed bellow the sample) called automated tapping device at periodic intervals, and the excited resonance frequencies are picked up by a sensitive microphone, placed at an optimal position over the sample outside the furnace. The microphone is cooled continuously by a portable air cooled chiller. The automatic excitation source and the acoustic sensor are positioned precisely with respect to the sample in order to obtain the resulting frequency spectrum for both flexural and torsional mode of vibration at room temperature [189-192]. The suitability of this frequency spectrum for the purpose of estimating elastic constants is judged by inspecting as to whether the spectrum contains few prominent flexural or torsional modes, as the case may be.

3.8.2. *Estimation of elastic moduli*

The experimental acoustic spectrum obtained using an acoustic sensor is Fourier transformed and compared against a simulated one, using the RFDA software. The simulated spectrum is actually a superposition of exponentially damped sinusoidal waves of the following form [192].

$$x(t) = x_0 e^{-kt} \sin(2\pi f_r t + \varphi) \quad (3.14)$$

In Eq. (3.14), $x(t)$ is the amplitude at time t ; x_0 is the maximum amplitude, f_r is the flexural resonance frequency; k is the exponential decay parameter for the chosen frequency and ϕ is the phase factor. In the process of simulation, the quantities, k , f_r , x_0 and ϕ are iteratively determined by force fitting the measured frequency spectrum with Eq. (3.14). Once a convergent set of estimates are obtained for k , f_r , and other parameters, the Young's modulus ($E(T)$) at the measurement temperature T , may be estimated by the following analytical relation that is valid for a rectangular bar specimen [194, 195]

been shown to have a maximum uncertainty of $\pm 4\%$ at elevated temperatures [188]. The accuracy in the temperature measurement is observed to be ± 2 K.

3.8. Impulse excitation technique

IET is a versatile, nondestructive experimental technique for characterizing the dynamic elastic response or carrying out mechanical spectroscopy of engineering materials, including metals, alloys, ceramics and polymers [189-193]. It is well known that the resonance frequency of a sample that is set into vibration by suitable mechanical impulse, are dependent on its mass (m), dimensions and more importantly, the bulk elastic constants namely Young's modulus (E) and Shear modulus (G). For a sample of simple geometry, like that of a rectangular bar, well defined analytical relations (approximations) connecting bulk elastic moduli with appropriate resonance frequencies exist [189,191, 194-195]. These relations can be employed to obtain an accurate estimate of E , G and Poisson ratio (μ), including their temperature variations, if data on experimental resonance frequencies could be measured as a function of temperature [189-193]. In addition, the time dependent decay of the amplitude of the chosen resonance frequency, gives a measure of internal friction (Q^{-1}) or vibrational damping characteristics of the material, which is dependent on frequency [189]. In the present study, measurements have been made using commercial *IET* equipment, supplied by *IMCE*[®] Belgium, together with suitable high temperature furnace and proprietary RFDA (Resonant Frequency Damping Analyzer) data analysis software. The details of the measurement system are described below.

3.8.1. Instrument details

A rectangular bar specimen is suitably supported on a ceramic bridge (formed by alumina tubes) called the sample support system which is placed centrally inside a resistance heated muffle furnace. **Figure 3.15** depicts the experimental set up for the impulse excitation technique used in the present study. For a better clarity, the enlarged view of the (sample +

changed depending on the temperature dependence of electrical conductivity of the specimen. In case of stainless steels the absorptivity increases as the electrical conductivity goes down with increase in temperature [186]. However the absorptivity can be enhanced to a great extent using graphite coatings which gives the surfaces a near black body behavior [186, 187]. In addition, the measurements of diffusivity are carried out under vacuum which eliminate the possibility of gaseous convection of heat from the sample after it is exposed to the laser pulse. Under such situations, it is assumed that the incident laser energy is fully absorbed on the irradiated surface which ensures the adiabatic conditions. As soon as the back surface of the specimens is irradiated with the laser flash, the transient thermal energy is conducted through the thickness of the thin sample in a short time interval. This is detected at the back surface of the flat sample by the rise in temperature (ΔT) through the infrared detector. The measured temperature rise as a function of time (t) is recorded by a suitable electronic data collection and analysis protocol. The observed ΔT versus t variation is fitted to a standard predefined one dimensional conduction model through a thin metallic slab, which enables the precise estimation of the quantity $t_{1/2}$. Physically $t_{1/2}$ represents the time required for the back surface to reach half of the maximum measured temperature rise ($\Delta T/2$). Then it emerges that the thermal diffusivity of the sample is given by the following expression [187, 188].

$$\lambda = \frac{1.73 L^2}{\pi^2 t_{1/2}} \quad (3.13)$$

Where L is the thickness and λ is the thermal diffusivity of the sample. A minimum of five concordant measurements were carried out at 50 K temperature interval. The average of these five measurements at each temperature was taken as typical thermal diffusivity estimate at the measurement temperature. The accuracy of each measurement is found to be ± 5 %. In case of materials where the conduction is the mode of heat transmission, the flash method has

temperature (ΔT). The infrared detector is cooled with the help of liquid N_2 at regular intervals during an experimental schedule.

(iii) High temperature furnace

The high temperature SiC furnace is positioned inside the diffusivity set up. The maximum temperature achieved by the furnace is 1873 K. The heating rate can be varied from 2 K min^{-1} to 50 K min^{-1} depending on the experimental conditions. In the present investigation an optimal heating rate of 7 K min^{-1} has been chosen for the measurement of thermal diffusivity.

(iv) Sample holder

A fully motorized sample robot is placed at the center of the furnace which can carry up to 6 samples. There are three sample slots for square shaped (length- 10 mm) as well as circular disc shaped specimens (25.4 mm diameter). This design allows unbeaten sample throughput and sample size at the same time. Measurement of liquid samples can also be made in special containers.

(v) Gas, vacuum, chill-water circuit and controller

An external turbo molecular pump (10^{-5} mbar) attached to the furnace chamber is used for evacuating the furnace chamber. Furthermore a manual or automatic software controlled gas control box (2, 3 or 4 gases) is also attached to generate specific gas atmosphere. The recorded data from the IR detector is analyzed through the LFA software provided by *Linseis* which evaluates the thermal diffusivity by the selection of appropriate conduction model which best fits the measured time variation of temperature data.

3.7.2. Measurement details

Square shaped samples with length 10 mm, and thickness of about 2.3 mm was prepared for the diffusivity measurement. In order to ensure the maximum absorption of heat from the incident laser pulse, the sample was coated with a thin layer of graphite. It is noteworthy to mention here that, with increase in temperature, the absorptivity of laser is

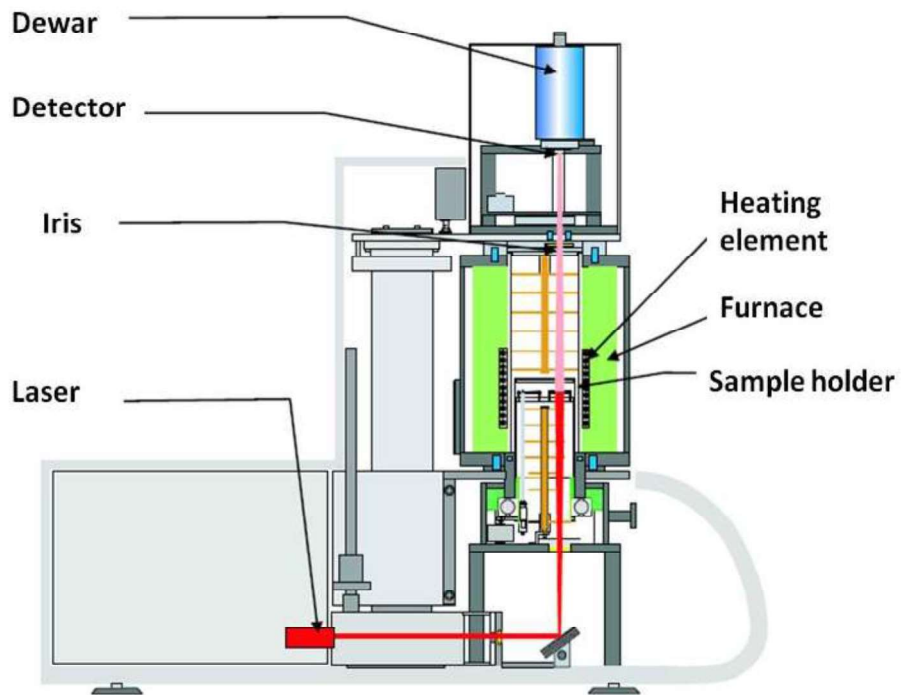


Fig. 3.13. Schematic representation of a laser flash diffusivity measurement system

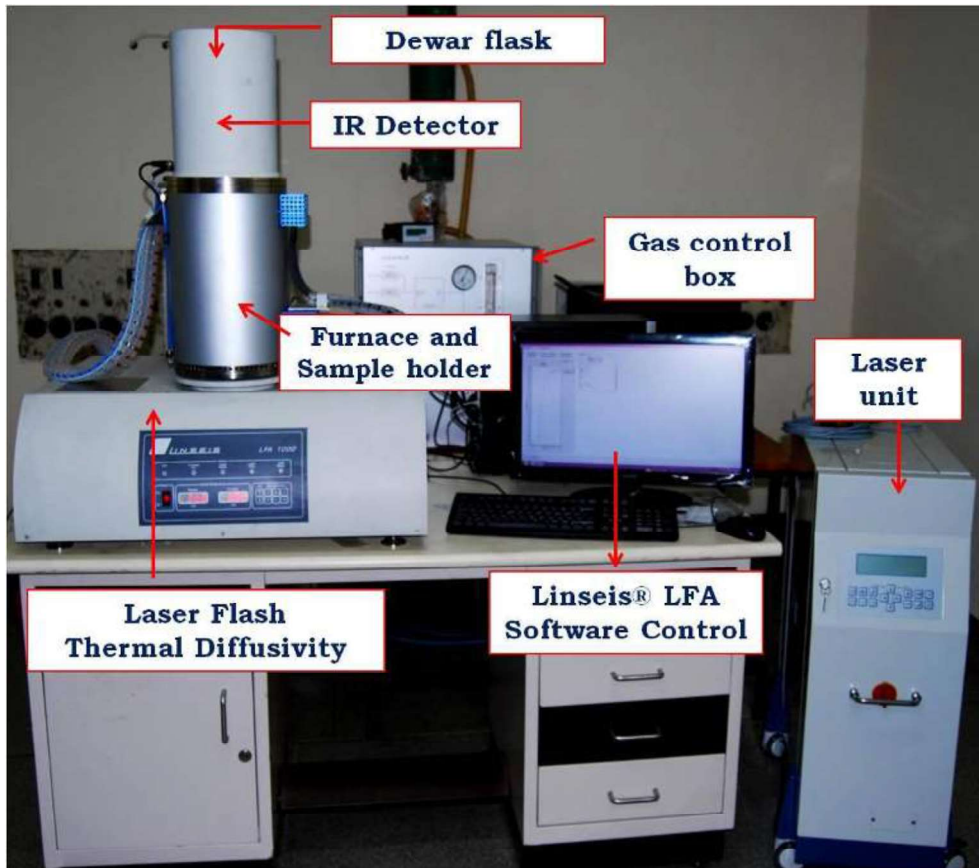


Fig. 3.14. Experimental set up for the *Linseis*® Laser flash Apparatus

3.7. Laser flash thermal diffusivity

The laser flash method is generally acknowledged as the standard and the most popular method for measuring thermal diffusivities of solid materials above room temperature [182, 183]. This is because the method employs non-contact, non-destructive temperature sensing to achieve high accuracy [184]. The basic principle of a laser flash thermal diffusivity is the measurement of the temperature rise of one surface of the specimen as a function of time when the other surface is irradiated with a programmed laser flash. The resulting measuring signal computes the thermal diffusivity. If the temperature dependences of density and specific heat (C_p) is known for the sample, the thermal conductivity of the sample is estimated from the measured thermal diffusivity values.

3.7.1. Instrumental details

In the present study the measurement of temperature dependant thermal diffusivities was carried out using a *Linseis*® laser flash apparatus (LFA). A schematic of the LFA is given in **figure 3.13** [185]. The experimental set up for the thermal diffusivity measurement carried out in this study is portrayed in **figure 3.14**. The major components of the LFA are described below.

(i) Laser source

The sample was irradiated with an Nd-YAG laser source with adjustable incident pulse energy and a pulse length of 300 μ s. The maximum pulse energy of the laser source is 25 J per pulse. Both the power and the pulse length can be easily adjusted by the controlling Software.

(ii) IR detector

The diffusivity system is equipped with one InSb infrared detector at the rear end of the sample. The transient thermal energy conducted through the thickness of the thin sample after the irradiation of laser flash is detected at the back surface of the flat sample by the rise in

$$\Delta l_{blank}(T) = \Delta l_{sampleholder}(T) + \Delta l_{pushrod}(T) \quad (3.7)$$

For the blank run, the extra length of the pushrod introduced inside the furnace due to the absence of the sample needs to be considered. The extra contribution from the (sample holder + pushrod) towards the dilatational strain in the blank run is an outcome of the extra length of the pushrod (equivalent to the length of the sample) introduced inside the furnace due to the absence of the sample. If α_{sample} and $\alpha_{push-rod}$ are the thermal expansion coefficient of sample and the push rod respectively, then the dilatational strain is represented as

$$\Delta l_{sample} = \Delta l_{sampleholder}(T) + L_{sample} \times \alpha_{sample}(T) \quad (3.8)$$

$$\Delta l_{Blank} = \Delta l_{sampleholder}(T) + L_{pushrod} \times \alpha_{pushrod}(T) \quad (3.9)$$

In a similar manner the temperature dependant dilation can be recorded for a reference specimen with known thermal expansion. The dilation in the reference can be written as:

$$\Delta l_{reference} = \Delta l_{sampleholder}(T) + L_{reference} \times \alpha_{reference} \quad (3.10)$$

Subtracting Eq. (3.9) from Eq. (3.10) and Eq. (3.10) from Eq. (3.8) one can obtain

$$\alpha_{sample}(T) = \frac{(\Delta l_{sample} - \Delta l_{blank} + L_{pushrod} \times \alpha_{pushrod}(T))}{L_{sample}} \quad (3.11)$$

$$\alpha_{pushrod}(T) = \frac{(L_{reference} \times \alpha_{reference}(T) - \Delta l_{reference} + \Delta l_{blank})}{L_{pushrod}} \quad (3.12)$$

Once the $\alpha_{push-rod}(T)$ is evaluated from Eq. (3.12) using known value of $\alpha_{reference}$ the dilation due to sample alone and the thermal expansion of the sample can be evaluated using Eq. (3.11). Sapphire standards (supplied by Setaram[®]) with known thermal expansion coefficients has been used as the reference in the present study.

purity iron (Sigma Aldrich iron with 80 mass ppm of impurities) under slow heating (5 K min⁻¹) conditions. The temperature accuracy was found to be ±2 K.

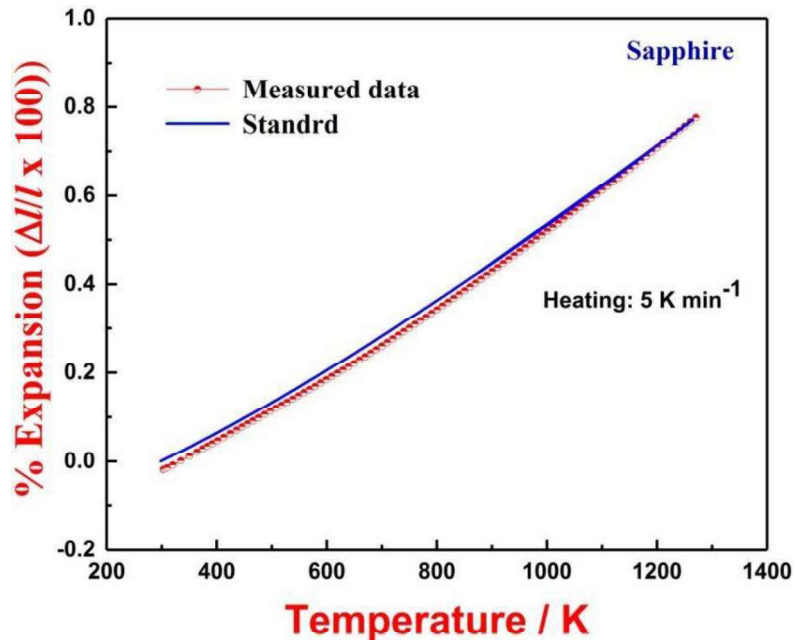


Fig. 3.12. Calibration of push rod dilatometer using sapphire standard

3.6.3. The baseline correction in push rod dilatometer

The recorded dilation in a push rod dilatometer for any specimen is the overall dilation due to the sample, the sample holder, as well as the push rod. In order to obtain the dilatational strain due to the sample alone, a baseline correction is essential in a push rod dilatometer. The details of baseline correction in a pushrod dilatometer have been documented in the literature [177, 180-181]. A brief account of the baseline correction method adopted in this study is presented here. For each experiment with the sample, one blank run (without sample) has been carried out to monitor the dilatational strain due to the sample holder and push rod assembly. The measured values of temperature dependent dilation (Δl) with the sample placed on the holder and without sample can be expressed by the following equations.

$$\Delta l_{sample}(T) = \Delta l_{sampleholder}(T) + \Delta l_{pushrod}(T) + \Delta l_{sample}(T) \quad (3.6)$$

(iii) Linear variable differential transformer (LVDT)

The LVDT is connected to the pushrod with a spring load configuration. The maximum range of displacement for the LVDT is ± 2 mm. The lower range resolution of the LVDT is 0.23 μm . The output signal (analog) from the LVDT is directly fed to the data analysis software in order to obtain a temperature and time variation of dilatational strain in the measured specimen.

(iv) Gas, vacuum, chill-water circuit and controller

An external rotary vacuum pump (EDWARDS) supplied by *Setaram*[®] is used for evacuating both the experimental and furnace chambers before starting the experiment. After the pressure inside the experimental chamber reaches 1×10^{-2} mbar, both the chambers were filled with high pure argon gas to maintain atmospheric pressure. An external chill water supply with controlled flow is provided for the furnace cooling. The heating schedule programming, the data acquisition and storage are performed through controller interfaced with the Calisto software through a personal computer.

3.6.2. Measurement details

Samples for dilatometry are taken in the form of small rectangular (20 x 20 mm) slices with smooth and flat surface. The starting thickness of the sample has been measured by a digital Vernier gauge with least count of ± 0.01 mm. The entire experiment has been carried out in flowing high purity Ar-gas atmosphere. Pure Sapphire supplied by *Setaram*[®] with known bulk thermal expansion values was used as calibration standard [179]. **Figure 3.12** portrays the measured dilation ($\Delta l/l$) observed for the sapphire standard supplied by *Setaram*[®] along with the reported values. The relative accuracy of the measured normalized dilatational strain in percentage ($\Delta l / l_{298}$) has been estimated to be 5%. The calibration of temperature has been carried out by measuring the allotropic transition (α -bcc $\rightarrow\gamma$ -fcc) of high

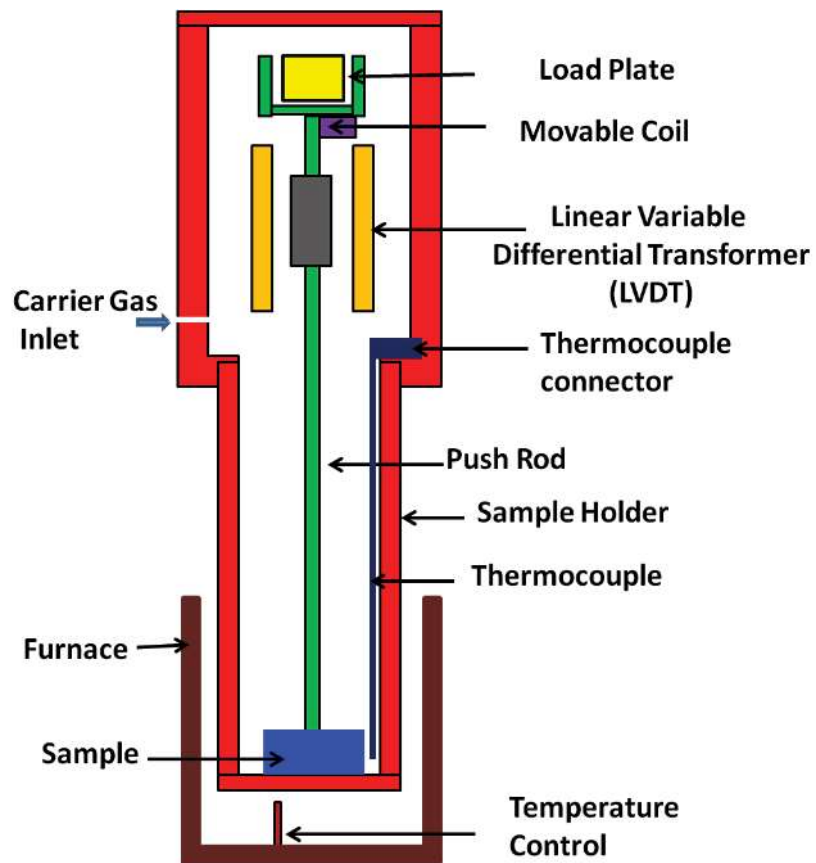


Fig. 3.10. Schematic representation of a vertical push rod dilatometer

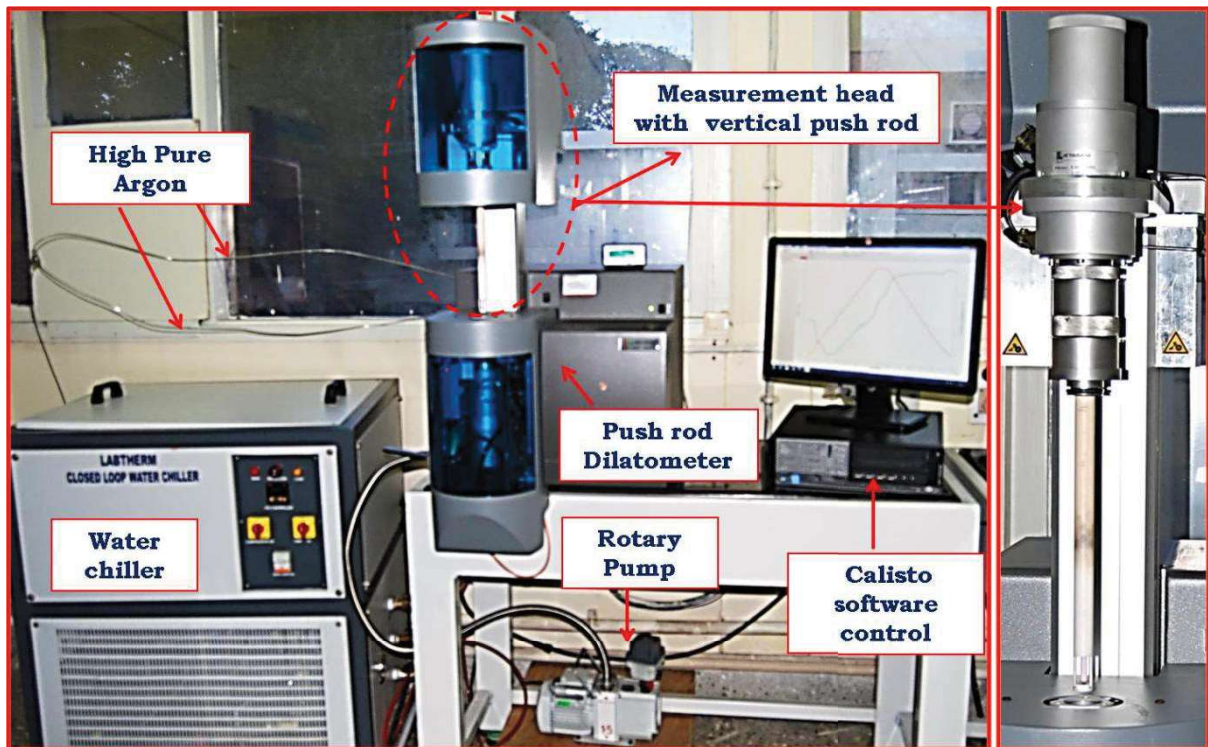


Fig. 3.11. Experimental set up for *Setaram*[®] setsys Evolution TMA 16

measuring the temperature induced linear dimensional strain ($\Delta l / l_0$) [178]. **Figure 3.11** depicts the experimental set up for the *Setaram[®] Setsys evolution TMA 16*.

(i) High temperature furnace

The high temperature furnace is made up of graphite tube which serves the purpose of heating element that surrounds the experimental chamber. A type-B thermocouple (PtRh 6% / PtRh 30%) was fixed along the wall of the sample holder tube to measure the furnace temperature. The temperature controller is placed below the sample holder tube mounted on the bottom of the furnace wall.

(ii) Sample holder and push rod assembly

The sample holder and the push rod assembly consist of a flat-ended recrystallized (RC) alumina sample holder tube and a RC alumina push rod with a hemispherical end. A rectangular cut was made at the bottom end of the sample holder tube to hold an RCA alumina plate over which the sample is positioned. The top end of sample holder tube was fixed with an aluminum support, which is connected to LVDT protective shell for vertical movement of the holder tube. The push rod used is mounted exactly at the center of the sample holder tube, and transmits the dilation signal to LVDT through a connected plunger. The bottom end of the push rod rested on the RCA alumina plate. The push rod is enabled to move up and down from the software control. When the pushrod is moved up, the sample is placed over the RCA alumina plate. Once the sample is placed properly, the pushrod is allowed to move down to touch the sample. For vertical movement of the sample holder and push rod assembly, a motor-controlled lifting mechanism has been positioned on the top. Once the sample is loaded, the entire assembly along with the sample is brought inside the furnace using the motor controller.

3.6. Thermo mechanical analyzer/ dilatometer: Basic principles

Thermo Mechanical Analyzer (TMA) or Dilatometry is a thermo-analytical technique for measuring the linear thermal dilation (expansion/shrinkage) of a solid material that is subjected to a programmed heating/cooling. The dilation that results from a specimen with change in temperature is mechanically detected by a pushrod in contact with the sample and is transmitted to a sensor which records the variation of dimension changes as a function of temperature. In general the push rod dilatometers are mounted in two different designs, namely (i) horizontal push-rod dilatometers and (ii) vertical push rod dilatometers. A horizontally mounted push rod dilatometer gives better temperature uniformity within the furnace although a small tracking force is always required for the push rod to ensure good contact between the sample and pushrod [177]. In contrast, components in a vertical dilatometer can remain in contact under their own weight, which may be at the expense of an inferior thermal gradient in the specimen due to furnace convection currents [177]. **Figure 3.10** portrays the schematic of a vertical push rod dilatometer. The push rod is thermally stabilized and insensitive to mechanical vibration. The specimen is positioned just below the push rod inside the furnace. The linear variable differential transformer (LVDT) which is insulated from the furnace is mounted over the push rod which measures the dimensional change in the sample. The thermocouple is placed very close to the sample in order to measure the specimen temperature precisely. In the present investigation, the dilatational strain has been measured using *Setaram[®] Setsys evolution TMA 16* equipment. A brief description on the equipment is what follows in the next section.

3.6.1. Instrument details

Setaram[®] Setsys evolution TMA 16 is a vertically mounted single pushrod type dilatometer equipped with a resistance heated graphite furnace and an LVDT sensor for

taken from more than 10 different experimental runs that have been carried out on alumina when used as the standard during enthalpy measurement. It is found that the standard deviation (σ) of Q is less than 5 Jg⁻¹ up to 810 K and is less than 15 Jg⁻¹ for higher temperatures.

3.5.5. Estimation of enthalpy

Assuming that quasi-adiabatic conditions are maintained in the experimental chamber, the heat energy transported ($Q_S(T)$) from the hot alumina bed to the cold sample can be written as:

$$Q_S(T) = C(T) \times (m_S/M_S) \times (H_T - H_{298.15})_S \quad (3.4)$$

In the above expression, m_S is the mass of the sample, M_S its molecular weight, $(H_T - H_{298.15})_S$ is the measured enthalpy increment with respect to the reference temperature 298.15 K (25^oC) and $C(T)$ is the temperature dependent calibration constant. The calibration constant can be obtained from the heat change $Q_R(T)$ recorded with the standard alumina reference drop, whose critically assessed enthalpy values are known from literature [176, 177]. Thus

$$Q_R(T) = C(T) \times (m_R/M_R) \times (H_T - H_{298.15})_R \quad (3.5)$$

In this equation, m_R is the mass of the reference and M_R its molecular weight which is taken to be 101.96 Kg m⁻³ [176]. It is worth noting that $C(T)$ remains the same in both expressions. Considering Eq. (3.4) and (3.5) together, it is clear that the quantities $Q_S(T)$, $Q_R(T)$, (heat flux transferred between the sample, reference and the alumina bed) are measured at each temperature, as the respective area under the peak (see **figure 3.8**). The quantity $C(T)$, the calibration constant is obtained by substituting in Eq. (3.5) the known enthalpy value $(H_T - H_{298.15})_R$ of standard reference for each temperature. This calibration constant, $C(T)$ is subsequently used to determine the unknown enthalpy $(H_T - H_{298.15})_S$ of the sample at each temperature.

3.5.4. Calibration of drop calorimeter

The temperature of the calorimeter has been calibrated with melting of pure element standards such as In, Sn, Al, Ag, Au, and Cu. The heat change (Q) calibration is made by dropping the α -alumina standard reference material. The performance of the thermocell has also been monitored by repeatedly observing the standard deviation of the value of heat change (Q) of the standard α - alumina in the temperature range 460 to 1373 K. The temperature variation of Q measured over one typical experimental schedule is graphically shown in **figure 3.9**. In this figure, an inset is shown for a typical sensitivity curve used for

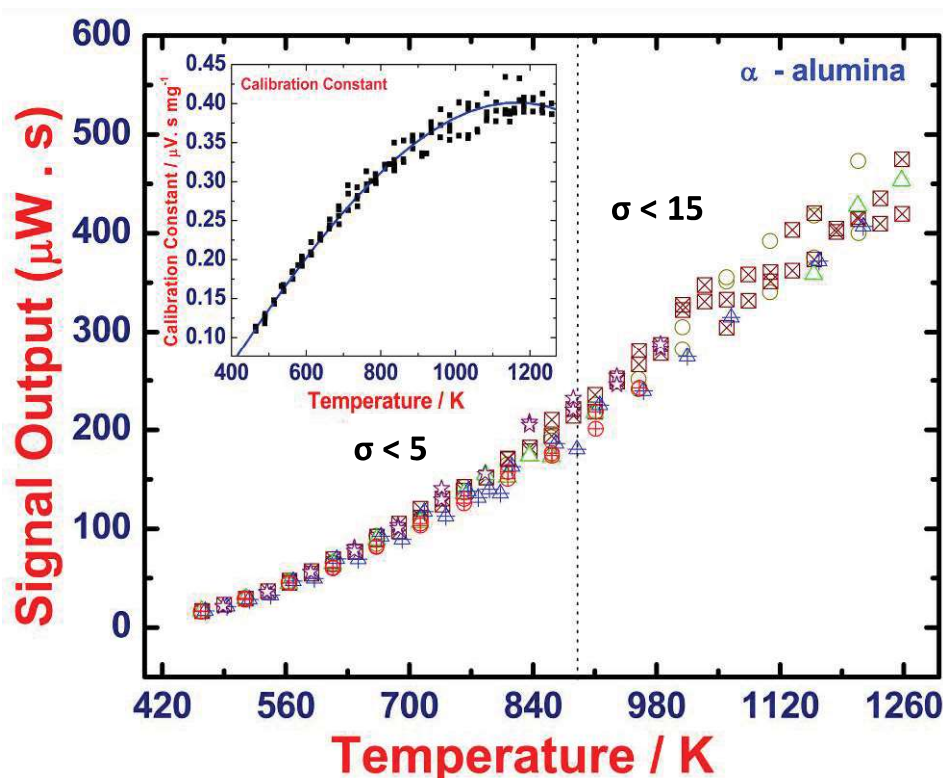


Fig. 3.9. Illustration of the temperature variation of Q for a typical experimental schedule and Calibration constant (inset)

enthalpy evaluation. The polynomial fit expression used is: $a + bT + cT^2 + dT^3$ and the fit coefficients obtained are: $a = 0.248 \pm 0.078$, $b = 7.84 \pm 2 \times 10^{-4}$, $c = 8.795 \pm 3 \times 10^{-8}$, $d = -2.5 \pm 1 \times 10^{-10}$. Different symbols in the figure correspond to different sets of data obtained at different instances of time with standard α -alumina. The individual data points of Q quoted here are

digital conversion. An identical experiment is carried out at the same temperature by dropping the known mass of calibration standard to quantify the heat flux, which is measured as area under the ΔV vs. *time* curve [175]. The typical time for the data acquisition is

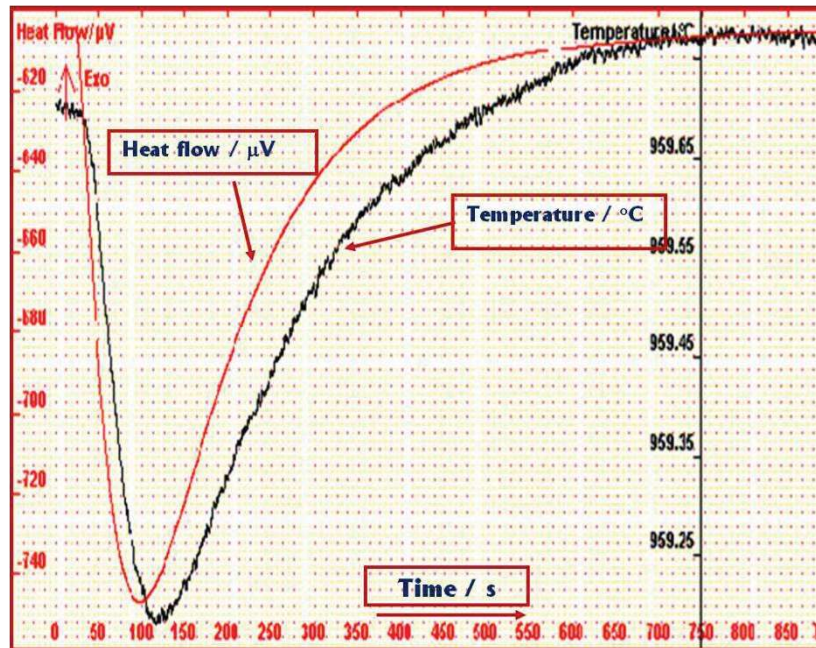


Fig. 3.8. Snapshot of the output signal from the drop calorimeter

maintained between 20 and 25 minutes for each drop and after each measurement a time of about 30 minutes is allowed to elapse between successive drops. Normally, about two drops are performed for each temperature in order to monitor the intrinsic scatter associated with the experiment at one temperature. A total of three experimental schedules covering the temperature range of 400 to 1273 K are conducted. Each experimental schedule consists of a series of successive drop experiments performed at prefixed discrete temperature steps (approximately 25 K). Before the measurement was carried out for the experimental specimens, the inverse drop calorimeter was calibrated using standard procedure which is discussed below.

pump (EDWARDS) supplied by *Setaram*[®] is used for evacuating both the experimental and furnace chambers before starting the experiment. An external chill water supply with controlled flow (*Julabo FC 1600 T*) is provided for the furnace cooling. The heating schedule programming, the data acquisition and storage are performed through the *RS 232* controller interfaced with the personal computer. In the following section, the procedure for performing inverse drop calorimetry experiment is discussed.

3.5.3. *Drop calorimetry experimental procedure*

Samples of dimension (2x2x2) mm and mass 50-75 mg were prepared and loaded in the specimen slots of the multi sample introducer of *Setaram*[®] multi HTC inverse drop calorimeter. Along with samples, the standard alumina (α -Al₂O₃) samples weighing 66.8 mg (supplied by *Setaram*[®]) are also loaded into respective vacant slots. The calorimeter bed onto which the sample is dropped is the one which contains the high pure alumina powder inside an alumina crucible. After loading the samples and setting the working crucible in its position, the experimental as well as the furnace chambers are evacuated followed by flushing both the chambers with high purity argon gas a few times, and continuing the process of evacuation and controlled argon gas leaking in an alternate manner. When the argon gas pressure level reaches one atmospheric pressure in both chambers, the chill water supply is switched on. Then the furnace is gradually heated to a desired experimental temperature at a rate of about 3–5 K min⁻¹. Once the pre-set value of the temperature of the alumina bed is attained to within an accuracy of ± 0.1 K, the respective samples are dropped from the corresponding slots in to the hot alumina bed through the guiding ceramic drop tube. The heat absorbed by the sample upon dropping produces a sudden change in the temperature of the alumina bed. The thermocell measures the temperature difference between the sample and reference and the typical integrated output is given as ΔV vs. time (t) which is shown in **figure 3.8**. The *RS 232* controller serially interfaced with the computer provides for this

(iii) Multi-sample introducer and the drop tube

The multi sample introducer equipped at the top portion of the experimental chamber shown in **figure 3.7(a)** provides 23 slots to load samples into it. Normally four to six samples are

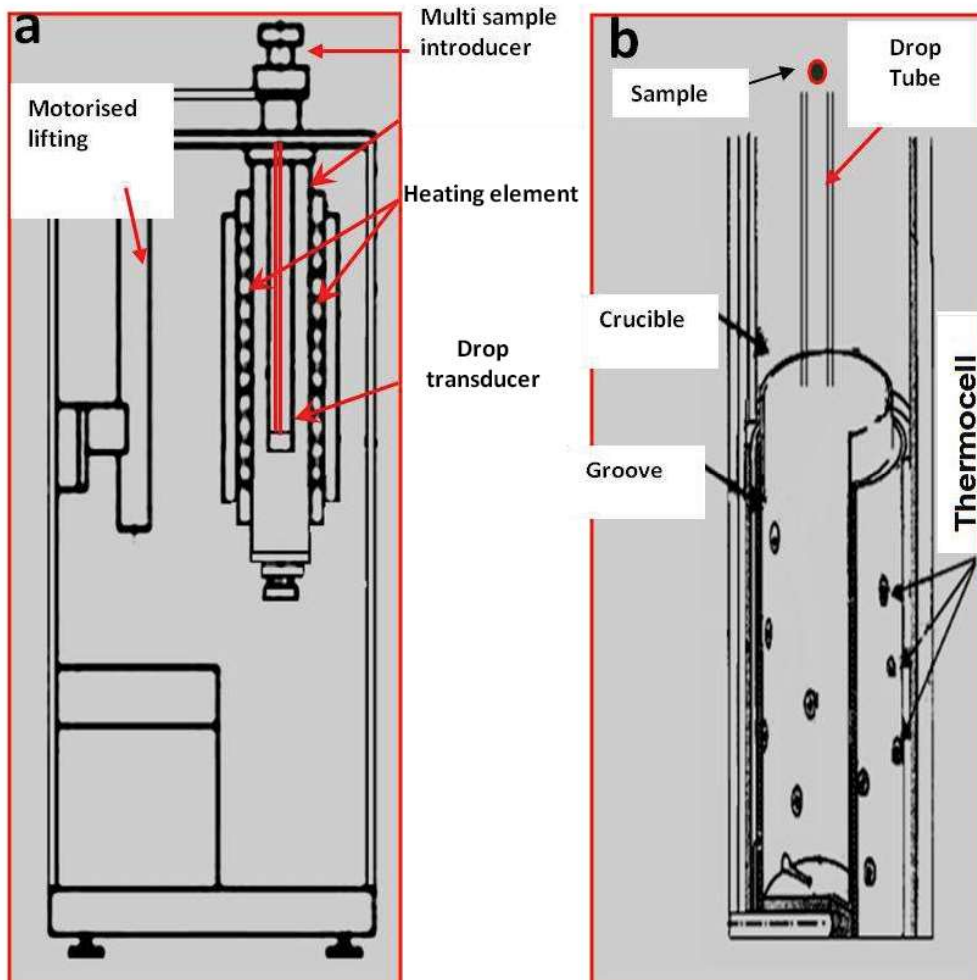


Fig. 3.7. (a) High temperature furnace with cabinet (b) Measurement head

loaded for each measurement. For each sample, a reference sample is also loaded into the adjacent slot. The drop tube called sample-guiding tube shown in **figure 3.6(b)**, guides the sample to fall exactly into the sample crucible during the course of the experiment.

(iv) Gas, vacuum, chill-water circuit and controller

The equipment contains two separate gas circuits, one for the furnace and another for the analysis chamber to maintain the required inert gas atmosphere. An external rotary vacuum

(ii) *Measurement head – Drop transducer*

The experimental chamber containing the transducer is usually called the drop transducer or detector whose cross sectional view is displayed in **figure 3.7(b)**. This measurement head itself is an integrated structure made of a cylindrical recrystallized alumina tube in which two grooves are cut at its bottom to introduce the sample crucible. The crucible has a working volume of 6.25 cm³ with dimensions 16.20 mm in diameter and 44.50 mm in height. The measuring crucible's temperature is monitored by a thermocell made up of 28 B-type



Fig. 3.6. The experimental setup for Inverse Drop calorimeter used in the present study

thermocouples distributed over the bottom and all over the side surface of the crucibles. Similarly a dummy reference crucible having an identical thermocell arrangement is kept underneath the sample crucible. This vertically aligned arrangement of both the sample and reference crucible is placed in the uniform temperature zone of the graphite furnace. Measurement of the sample and furnace temperatures is undertaken by two thermocouples of B type (PtRh-6% / PtRh-20%).

temperatures, although the enthalpy change accompanying phase changes are accurately given in drop calorimetry.

3.5.1. Inverse drop calorimetry

As the name suggests, in the inverse drop calorimeter mode, measurements are made in the inverse manner, namely the cold sample is dropped onto the hot calorimeter bed. The principal advantage of this inverse drop mode over the direct one is that the heat losses in the direct mode of dropping the hot sample are minimized by resorting to dropping of cold samples [174]. Inverse calorimetry has some advantages; namely it can easily adopt small sample size, avoid any metastable phase retention from high temperature excursion, ability to study many different types of chemical reactions *etc* [165]. The calorimeter used in the present study for the measurement of enthalpy increment is one of such inverse drop calorimeter which is described in the following section.

3.5.2. Instrument details

The drop calorimeter used in this study is manufactured by *Setaram*[®], France; - the actual model is the “Multi Detector *HTC Drop Calorimeter 96*”, functioning in inverse drop mode. **Figure 3.6** portrays the experimental setup for the drop calorimetry. The instrument details are pictorially depicted in **figure 3.7** [174].

(i) High temperature furnace

The high temperature furnace, supported by the drop calorimeter cabinet's top plate is displayed in **figure 3.7(a)**. The furnace is made out of graphite tube which acts as the heating element that surrounds the experimenting chamber containing the calorimeter. A sealed alumina tube running from the top portion of the furnace into the bottom separates the experimental chamber from the furnace atmosphere.

due to radiation are invariably present in any calorimetry set up. However the heat loss is minimized in a good calorimeter design. The net heat change Q is determined as:

$$Q = C(T) \Delta V \times \Delta t \quad (3.3)$$

Where $C(T)$ is the usual calibration constant which is determined by calibration with known enthalpy standards like α -alumina. The parameter ΔV (normally in microvolts) stands for the thermopile output which is continuously monitored with time until the thermal equilibration ($\Delta T \sim 0$) is complete. By determining $Q(T)$ as a function of temperature T , the curve of enthalpy versus sample temperature is readily obtained. A schematic of one such enthalpy curve or drop curve is shown in **figure 3.5** which indicates a sudden jump in the enthalpy that

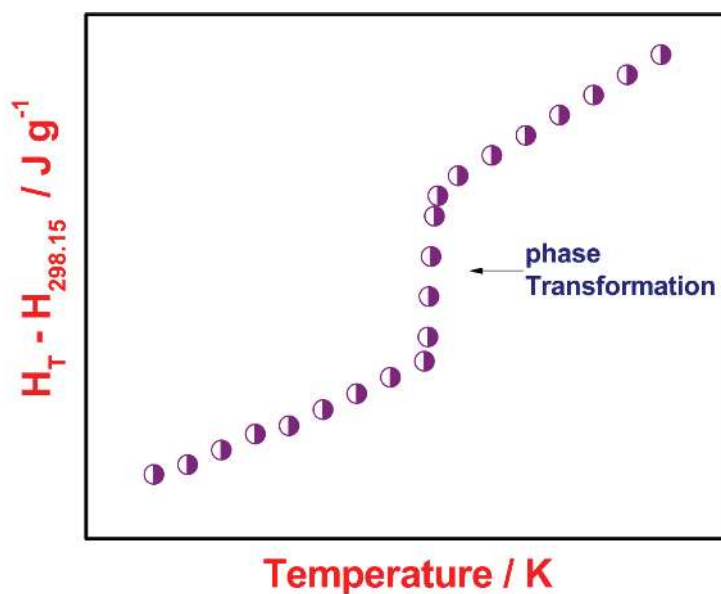


Fig. 3.5. Schematic of the temperature variation of enthalpy increment

is associated with a phase transformation event. In cases where the transformation occurs over a temperature domain, then the enthalpy exhibits a gradual change of slope. *A continuous enthalpy increment versus temperature data is not obtained through drop calorimetry. This has important bearing on the precise fixation of the transformation*

construction [170-173]. The conversion factor $k(T)$ is obtained by measuring the peak area recorded with the melting reactions of standards like pure aluminum, zinc, tin, copper and iron etc. of known enthalpy [170-173]. In case of metals it is a usual practice to estimate the calibration constants with small heating rates in order to avoid the effect of undercooling. In addition, it is also desirable to employ a calibrant that shares similar thermophysical characteristics with the alloy under investigation. In view of this, pure iron has been taken as the calibrant in the present study for characterizing accurately the enthalpy effects of steels.

It is instructive to note here that, with the adaptation of proper calibration procedure, a DSC can also be effectively used to get estimates of specific heat [170-173]. However in the present study, the specific heat has been estimated from the measured enthalpy increment using drop calorimeter which provides more reliable and accurate heat capacity as the measurements are carried out under near-equilibrium conditions. The details of the inverse drop calorimeter are presented in the ensuing section.

3.5. Principle of drop calorimeter

In a direct drop calorimeter the relative enthalpy of a specimen at a chosen temperature T is measured with respect to its value at the reference temperature (usually taken as 298.15 K). This is realized by heating the sample to a desired temperature and after equilibration at this temperature for some fixed time, is dropped in to a well-equilibrated calorimeter block or bed that is maintained at fixed reference temperature. The rise in temperature of the calorimeter bed due to the heat transferred from the sample to the calorimeter bed is measured maintaining near-adiabatic conditions. The experiment is usually repeated by dropping the reference or calibrating sample of known mass and known enthalpy under identical experimental conditions to evaluate the calorimeter constant. This calorimeter constant is used to calculate the enthalpy for the sample from the measured heat flow at a fixed temperature. It must be mentioned here that, some thermal loss mechanisms, such as

maximum inclination (inflection point of the peak); - their intersection is taken as the transformation temperature. This construction is also illustrated in **figure 3.3**.

3.4.4. Temperature calibration in DSC

The temperature calibration is carried out using the melting points of pure aluminum, zinc, tin, copper, silver, gold, and iron standards [168]. The onset value T_s of the melting point has been determined, based on the procedure explained above. These onset temperatures are determined for various heating rates such as 1, 3, 5, 7, 10, 15, 20, 30 $K\ min^{-1}$ etc., and the resulting data are plotted in **figure 3.4**. In order to obtain the so-called equilibrium onset temperature, generally the plot in **figure 3.4** is extrapolated to hypothetical heating rate of $0\ K\ min^{-1}$ [169, 170].

These values are compared with the standard literature values in order to estimate the correction to be employed for obtaining the true transformation temperatures. The temperature accuracy in case of low heating rate experiments ($1\text{--}30\ K\ min^{-1}$) is found to be $\pm 2\ K$ for samples of mass up to $50\text{--}100\ mg$; while, it is $\pm 4\ K$ for high heating rates ($99\ K\ min^{-1}$). The extrapolated melting temperature of Cu and Al is compared with literature values and the deviation is found to be within $\pm 4\ K$. The degree of reproducibility is also checked with repeat runs and the error in temperature measurement is found to be $\pm 1\ K$.

3.4.5. Determination of phase transformation enthalpy

From a standard non-isothermal DSC scan exhibiting a peak due to distinct phase transformation; it is generally assumed that the heat of phase transformation is directly proportional to the peak area after suitable baseline normalization. Thus,

$$\Delta H_{tr} = k(T) \times (\text{Peak Area}) \quad (3.2)$$

ΔH_{tr} is the enthalpy change accompanying phase transformation, $k(T)$ is the temperature dependent calibration constant. Peak area is the total area under the transformation peak which is readily obtained by the data processing software after appropriate baseline

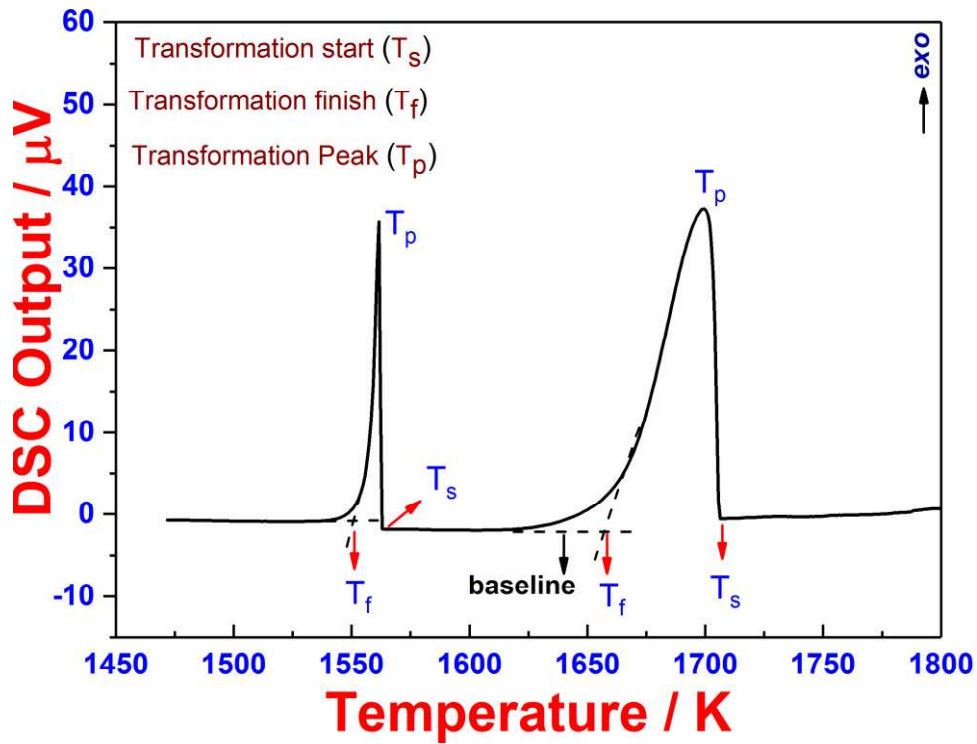


Fig. 3.3. Typical cooling cycle DSC thermogram for the solidification of SS 304H Cu alloy from liquid. The two separate exothermic peaks indicates two transformation thermal arrests

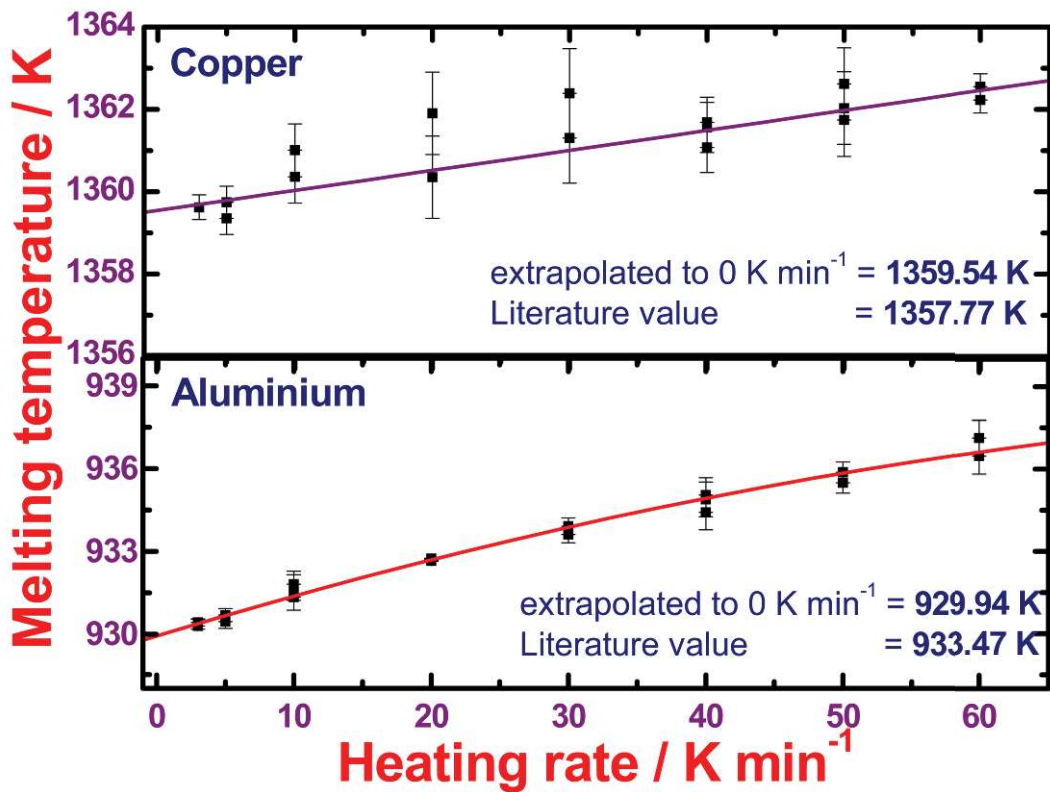


Fig. 3.4. Temperature calibration in DSC with Copper and Aluminium

IFAC-1 and SS304H Cu were studied by heating the samples from 473 to 1773 K, equilibrated at this temperature for about 15 minutes and then cooled to 473 K at the same scan rate. The heating and cooling rates adopted are in the range 1-99 K min⁻¹. Fresh samples are employed for each individual run and a few repeat runs are also performed for select heating rates (10 and 100 K min⁻¹) in order to ensure the reproducibility at either end of the scan rate spectrum. In general DSC is employed for following studies:

- (i) Accurate determination of solidus, liquidus and other phase transformation temperatures
- (ii) Estimation of heat effects accompanying phase changes
- (iii) Estimation of the kinetic parameters of phase transformation
- (iv) Estimation of specific heat

The measurement details of the transformation temperature, enthalpy of transformation as well as the estimation of kinetic parameters are described in the following section.

3.4.3. Determination of phase transformation temperature

A typical cooling cycle DSC thermogram for SS 304H Cu is shown in **figure 3.3** where the alloy is cooled from the liquid state. When the sample experiences no phase change, the basic DSC signal is a smooth baseline (parallel to the x- axis) without any characteristic features. However, in a heat flux DSC, mild deviation from horizontal base line is generally observed, due to the slight difference in thermal character of apparently the same set of crucibles. However, when there occurs a phase transformation in the sample, the differential heat flow due to the latent heat of transformation which is transported across the heat flux resistor results in the production of a distinct thermal arrest which is seen as a peak in the baseline plot. This is illustrated in **figure 3.3**. The phase transformation onset (T_s) and finish temperatures (T_f) are determined by drawing a tangent to the baseline from the point of

which is hung from the top balancing plate. The DSC probe is always kept within the uniform temperature zone of the water cooled graphite furnace.

(iii) Vacuum Circuit, Gas Circuit, Chill water Cooling Circuit

A rotary vacuum pump serves the purpose of evacuating both analysis and furnace chamber. A separate chiller (*Julabo FC 1600 T*) for water circulation is connected to cool the graphite furnace. The vacuum and the water supply operations are done through an electro valve command option. The programming and temperature control of the furnace is done by the controller which is integrated with the CPU.

3.4.2. DSC experimental procedure

Samples of dimension $2 \times 2 \times 2$ mm were cut for DSC study using a diamond saw in order to reduce the mechanical damage and stress due to cutting. The sample mass is kept nearly identical to about 80-100 mg. Further, the samples are polished to obtain a flat surface to ensure better heat conduction. In the present study, an empty cylindrical alumina crucible with a volume of $100 \mu\text{L}$ is taken as reference and another identical crucible is loaded with the sample. Before starting the experiment, the experimental chamber consisting of DSC probe and the furnace is evacuated and purged with pure argon gas with a flow rate of about 50 ml per minute. The flow rate is maintained by means of electronic mass flow controller (MFC) throughout the experiment. An argon pressure of about 1300 mbar is maintained in the graphite furnace chamber.

In the first step of the experimental schedule, the furnace temperature is gradually raised to 473 K at a heating rate of 5 or 10 K min^{-1} and is allowed to stabilize at this temperature for about 15 minutes. This leads to a smooth baseline which ensures the attainment of thermal equilibrium of the system before starting any measurement, which is essential for quantitative DSC experiments. Following this step, suitable heating and cooling programmes are adopted as per the requirement. For example, the thermal stability and solidification behavior of

crucibles are made of recrystallized alumina having nearly identical mass of about 240–250 mg and a volume of about 100 μL . The metallic plate consists of an embedded thin wire of highly conductive platinum that serves the purpose of *heat resistor* between sample and the reference. The differential thermocouple of B-type (PtRh 6%/PtRh 30%) is positioned exactly below the DSC plate and the gap between them is less than 2 mm. In addition, the central section of the DSC plate sensor contains a thermocouple of B- type that measures the sample temperature directly. The whole set up comprising DSC plate, sample and reference crucibles, thermocouples, guiding alumina tube together make up the heat flux DSC probe

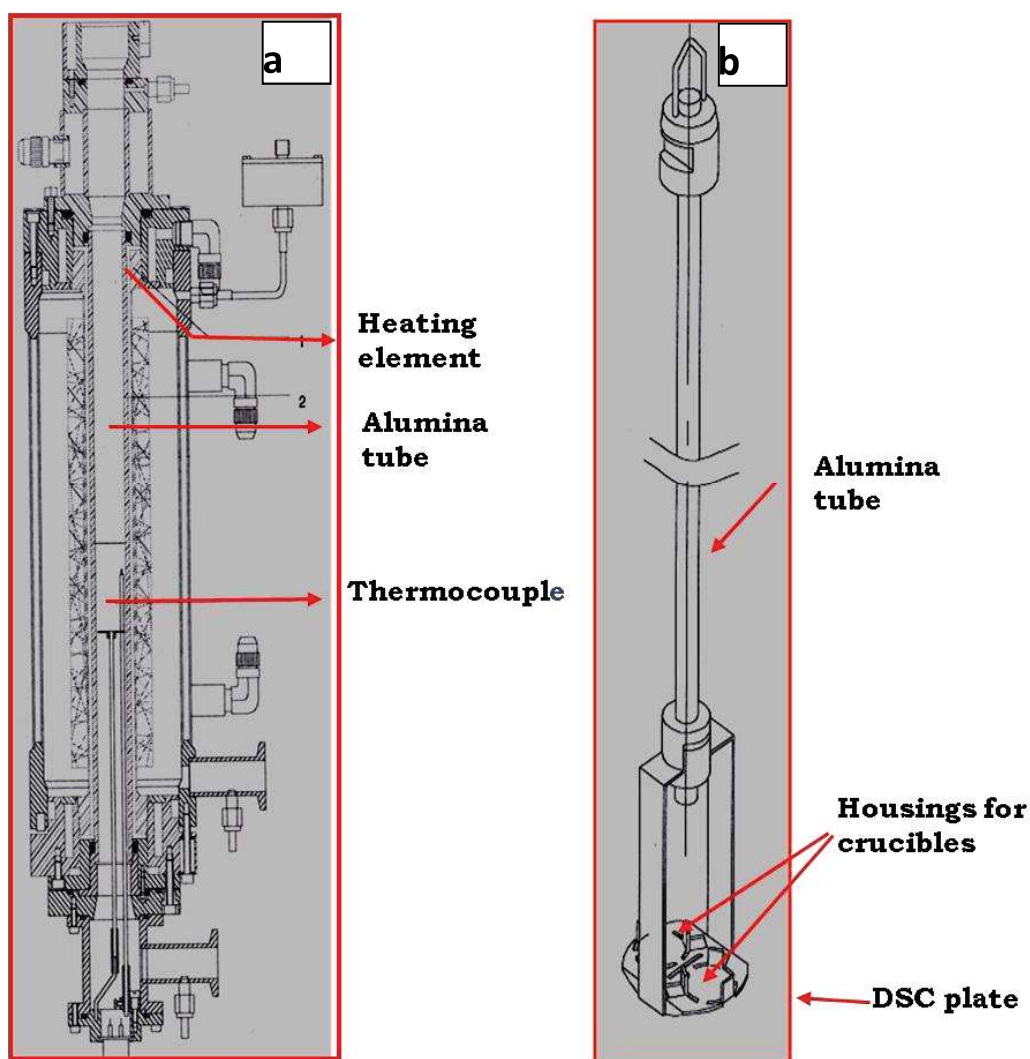


Fig. 3.2. (a) *Setaram*[®] high temperature DSC furnace (b) Heat flux DSC plate-rod

made through the proprietary software that is interfaced with the equipment. The essential components of this DSC are as follows [167].

(i) High Temperature Furnace

The high temperature furnace shown in **figure 3.2(a)** is of cylindrical shape with a graphite tube heating element. An inert gas atmosphere is always maintained at the furnace chamber to avoid carbon evaporation at higher temperature. A thermocouple of B-type (PtRh 6%/30%) is placed in the analysis chamber and furnace chamber for respective temperature measurement.

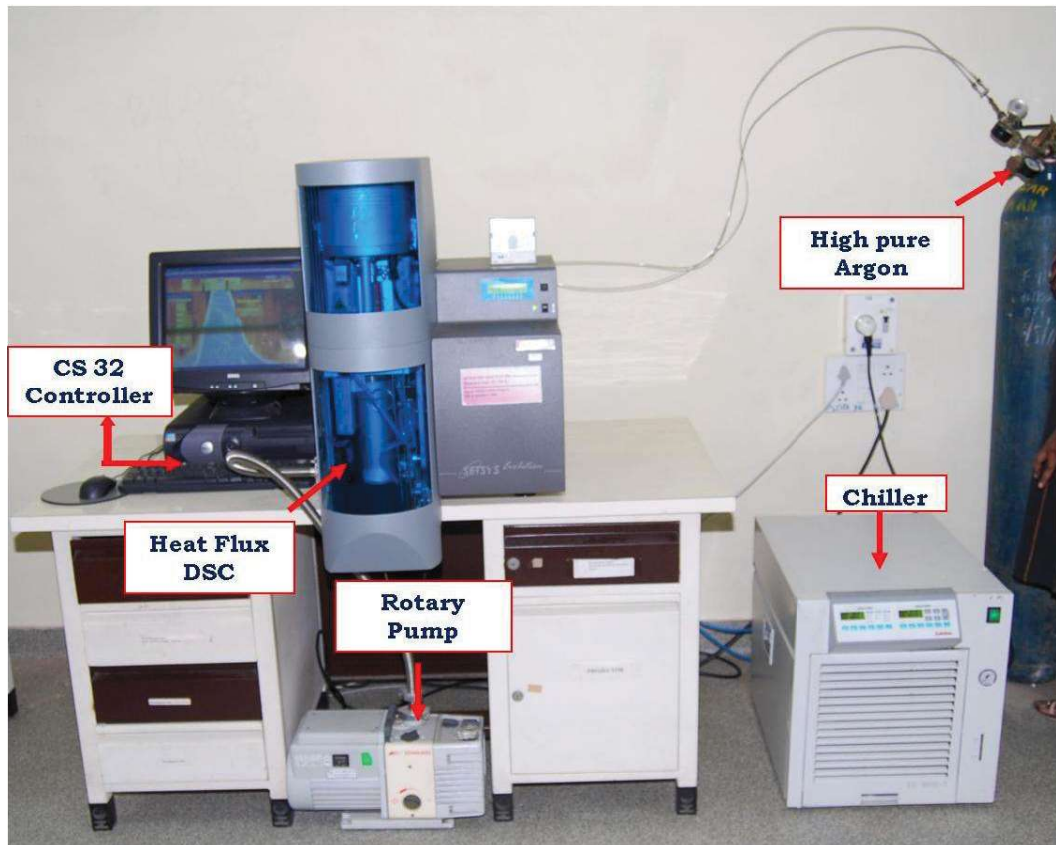


Fig. 3.1. The experimental set up for heat flux DSC used in the present study

(ii) Measurement Head – DSC Probe

The DSC – plate is called the measurement head which is displayed in **figure 3.2(b)**. This is a machined metallic plate made of platinized copper-constantan containing two housings for the sample and reference crucible fitted to a narrow alumina rod. The sample and reference

In *heat flux DSC*, the test specimen *S* and reference material *R* (usually an empty sample pan + lid) are enclosed in the same furnace together with a metallic block of high thermal conductivity that ensures a good heat-flow path between *S* and *R*. Further, the enthalpy or heat capacity changes in the specimen *S* leads to a temperature difference between both *S* and *R* pans which results in a finite heat-flow between the sample and the reference. The temperature difference ΔT between *S* and *R* is recorded and further related to the enthalpy change in the specimen using calibration experiments. The heat-flux DSC system is thus a slightly modified DTA system with a good heat-flow path between the specimen and reference crucibles. The radiation loss at high temperature is same for both sample and reference materials and hence the heat flow between the sample and reference is not affected due to the radiation loss. The instrument used in the present investigation is a heat-flux type differential scanning calorimeter (*Setaram*[®] *Setsys 1600*), which is described below.

3.4.1. *Setaram*[®] *Setsys 1600 DSC*

Figure 3.1 portrays the heat flux DSC used in the present study (*Setaram*[®] *Setsys 1600*). The heat flux calorimeter consists of two pans, one for sample and the other for reference. The two pans are connected by a low resistance heat flow path, with the thermocouple meant to sense the differential temperature positioned exactly underneath and midway connecting sample and reference. The accuracy of results obtained with DSC is slightly inferior at high temperature, notwithstanding the possibility of ensuring adequate experimental precaution [166].

The *Setaram*[®] *Setsys 1600* heat flux differential scanning calorimeter is basically a single structure integrated unit, wherein furnace, measurement head, mass flow controller, gas circuits and the controller are housed on a single mount. The control of equipment is

conditions which can be put to effective use for studying a variety of non-equilibrium phenomenon, such as phase transitions, relaxation phenomena etc. [164].

The static calorimetry technique on the other hand is useful in studying the time dependent stability at a fixed temperature which is suited for making equilibrium thermodynamic property measurements of a stable phase as a function of temperature. The major characteristics of many different versions of static and dynamic calorimetry techniques are adequately summarized by Cezairliyan *et al* [165]. In this thesis, the description is confined to only drop and scanning calorimetry techniques. The detailed discussion on the differential scanning calorimetry technique is taken up first in the following section.

3.4. Dynamic or differential scanning calorimetry (DSC)

The principle behind DSC is the comparison of the heat flow to the sample and to an inert reference material when both are heated or cooled at a fixed rate. Phase changes that are associated with heat absorption or evolution induce a commensurate change in the differential heat flow between sample and reference, which in effect appears as an uncompensated temperature differential ΔT , spread over the transformation event. Two types of DSC systems are commonly in use and that are *power compensating* type and *heat flux* type.

In a *power compensated DSC*, both sample and reference materials are heated by two separate identical furnaces at equal heating rate. Any change in the sample or reference temperature is being compensated by means of an electric power from external source to maintain the temperature difference (ΔT) between the sample and reference material either zero or constant. The compensating heating power is linearly proportional to the temperature difference ΔT between sample and reference. However the use of this type of DSC at high temperature (above 700 °C) is limited because the heat loss is more prominent at high temperature due to radiation.

were further subjected to an aging treatment for 150 h at 873 K (600 °C). The aging treatment was carried out to promote the precipitation of nano-scale coherent Cu-precipitates in γ -austenite matrix [160,161].

3.3. Calorimetry: Basic principles

The basic principle of calorimetry is based on an accurate quantitative measurement of the temperature or its differential in terms of the heat transfer between a sample and a reference under thermal equilibrium [162]. The heat transferred from a body at a higher temperature to a body at lower temperature under adiabatic conditions is directly proportional to the temperature difference between the two bodies. The relationship between the heat (Q) that is transferred and the change in temperature (ΔT) is given as

$$Q = C(T) \Delta T \quad (3.1)$$

In the above equation the parameter $C(T)$ is the calorimeter constant which is a function of temperature. The calorimeter constant is generally evaluated using suitable standards with known heat capacity which represents the heat capacity of the sample as well as the heat transfer characteristics of the entire calorimetry cell, including ambience, gas flow rate *etc.* In practice, the constant $C(T)$ is estimated, by performing the experiment with a suitable standard of known Q or enthalpy under identical and reproducible conditions.

The actual methodology employed in calorimetry calibration is dependent on the type of calorimeter used, which in turn is decided by the choice of material systems, and the temperature range of interest and the nature of physical problem studied [163, 164]. While there are many designs of static calorimeters, in which the experiment and measurement are done under constant temperature or probably at *near-equilibrium* conditions, there are also dynamic techniques in which the thermal response of a system is monitored as a function of time, during which the temperature of the sample is continuously changed. Therefore in a dynamic or scanning technique, the measurement is often carried out under *non-equilibrium*

optical emission spectroscopy (ICP-OES) at MIDHANI India and the details are listed in **table 3.1**.

Table 3.1

Chemical compositions (*wt. %*) of IFAC-1 SS and SS304H Cu steels

Element	Cr	Ni	Mn	Mo	Cu	Ti	Nb	C	N	Si	P	S	Al	B	Fe
IFAC-1	14.4	15.4	2.36	2.4	--	0.25	--	0.042	0.008	1.02	0.040 max	0.01 max	--	0.005	Bal
SS 304H Cu	17.7	9.3	0.91	--	2.95	--	0.58	0.1	0.12	0.24	0.030 max	0.01 max	0.003	0.002 to 0.006	Bal

The chemical composition of the steels has been carefully chosen to meet the intended long term application under the service environments. For example the ratio of (Ti/C) in IFAC-1 is deliberately chosen as 6 to facilitate enough TiC precipitation for enhanced void swelling resistance under intense neutron irradiation in the core of fast breeder reactors. On the other hand a higher concentration of C with the addition of required amount of Cr and Nb is desired in SS 304H Cu in order to precipitate out the $M_{23}C_6$ and MX which enhances the high temperature creep strength under elevated temperature and pressure in the coal fired advanced ultra supercritical thermal power plant. It is also noteworthy to mention that the composition of minor alloying elements has been controlled during the steel making to achieve desired properties for these alloys.

The as received IFAC-1 samples, were solution annealed for two hours at 1323 K (1050 ° C), followed by furnace cooling to room temperature for homogenization and to relieve the stresses if any in the specimen. For SS 304H Cu, the samples were annealed at 1250 ° C (1523 K), followed by furnace cooling to room temperature. The choice of time and temperature of annealing is to obtain a strain free homogeneous microstructure with the complete dissolution of Cu and $M_{23}C_6$ precipitates. A part of the above annealed specimens

have also been measured using impulse excitation techniques which estimate the bulk elastic moduli of the present alloys. These fundamental quantities not only provide a handy database for the design engineers but also help in understanding the underlying physics of these multi-component alloys.

Beside these major experimental tools, other supplementary techniques such as optical microscopy, scanning electron microscopy (SEM), transmission electron microscopy (TEM), microhardness testing and X-ray diffraction (XRD) are also employed for the structural and microstructural characterization in these alloys

The present chapter deals with a brief description of the alloy preparation, details on composition and heat treatments of the specimens. This is followed by a detailed description on the static and dynamic calorimetry, dilatometry and laser flash thermal diffusivity techniques employed for the measurement of high temperature thermophysical properties. Following this section the details of impulse excitation techniques employed for the measurement of thermomechanical properties is elucidated. Finally a short account on the structural characterization techniques such as optical microscopy, SEM, TEM, hardness tester and X-ray diffraction (XRD) is provided.

3.2. Alloy preparation, compositional analysis and heat treatment

The alloy systems investigated in this study i.e. IFAC-1 and SS 304H Cu mainly belong to two different compositions of AISI300 grade austenitic stainless steel. Both the alloys were developed indigenously by IGCAR in collaboration with Mishra Dhatu Nigam Ltd (MIDHANI) and Nuclear Fuel Complex (NFC), Hyderabad India. The steels were melted using vacuum induction melting and hot forged to different shapes. The IFAC-1 steel was obtained in the form of 25mm thick plates whereas SS 304H Cu was received in the form of tubes with 30 mm inner diameter and 53 mm outer diameter respectively. The chemical composition of steel samples was analyzed using inductively coupled plasma

Experimental Methodology

3.1. Introduction

In recent times, with the development of Multiscale computational tools, it is possible to predict the phase stability and thermophysical properties of the materials with reasonable degree of accuracy. However, the assessment based on these computational techniques is limited to binary or ternary systems. For multi component alloys like steels, accurate prediction of the phase stability, thermophysical and mechanical properties is practically impossible using only computational tools. This calls for reliable and reproducible experiments by which accurate measurements on thermo-chemical, thermo-physical and thermo-mechanical data can be obtained.

In the present investigation, several measurement techniques as well as modelling tools have been employed for the measurement of phase stability, thermophysical and mechanical properties of two advanced austenitic stainless steels namely IFAC-1 SS and SS 304H Cu. The major experimental technique employed for thermodynamic and kinetic measurements is static and dynamic calorimetry. Static calorimetry is a useful tool in measuring the enthalpy increment under near equilibrium conditions, while dynamic calorimetry is employed under non-isothermal conditions to study the kinetic aspects of phase transformations that occur during continuous heating and cooling cycles. Besides the calorimetry techniques, thermomechanical analyzer (TMA) /dilatometry techniques have also been employed for the measurement of temperature dependant dilation in order to estimate the linear thermal expansivity. Further the measurement of thermal diffusivity is carried out using laser flash thermal diffusivity technique and the temperature dependence of thermal conductivity has been evaluated. In addition, high temperature thermomechanical properties

Chapter 3

Experimental Methodology

(1047°C) respectively. The enthalpy of precipitation of Cu+ $M_{23}C_6$ is found to be $20 \pm 2 \text{ J g}^{-1}$.

- V. For IFAC-1, the liquidus and solidus temperatures are found to be 1684 K (1411 °C) and 1631 K (1358 °C) respectively under 3 K min^{-1} cooling rate. The latent heat of solidification is $190\text{--}220 \pm 15 \text{ J kg}^{-1}$. Similarly for SS 304H Cu the observed liquidus and solidus temperature are 1723 K (1450 °C) and 1607 K (1334 °C) respectively.
- VI. The standard annealing temperature above 1323 K (1050 °C) for IFAC-1 makes it only reasonably homogeneous, since the complete dissolution of TiC precipitates in IFAC-1 occurs only above the solidus temperature 1323 K (1050 °C). For the dissolution of Cu and $M_{23}C_6$ in SS 304H Cu, solution-annealing temperature of about 1413 K (1140 °C) is adequate. However for the complete dissolution of $M_{23}C_6$, longer annealing times is required. On the other hand the Nb rich MX precipitates in SS 304H Cu dissolve just below the solidus temperature of 1607 K (1334 °C).

Thermocalc[®] predicts primary ferrite or, $L \rightarrow \delta \rightarrow L + \delta + \gamma$, type solidification sequence. In fact, the 3-wt % Cu composition sits just at the transition zone of primary ferrite to austenite+ferrite mode of solidification. Thus, the observed A–F mode of solidification in the current steel having 2.95 Cu and 0.58Nb appears well supported on thermodynamic grounds.

4.4. Conclusions

The high temperature phase stability has been investigated using differential scanning calorimetry with supporting *Thermocalc*[®] simulation for two advanced austenitic stainless steels namely IFAC-1 and SS 304H Cu. The major results obtained in the present investigation are summarized below.

- I. The initial microstructure in IFAC -1 is γ -austenite with fine scale TiC precipitates. In the case of SS 304H Cu, the initial microstructure consists of a mix of (γ -austenite + MX+ $M_{23}C_6$ + Cu).
- II. Under slow cooling conditions, IFAC-1 is found to follow austenite + ferrite (AF) mode of solidification with a narrow domain for δ -ferrite solidification. The small amount of δ -ferrite formed during slow cooling again transforms into γ -austenite just below the solidus. In contrast to IFAC-1, SS 304H Cu also undergoes a mixed austenite + ferrite mode (AF) of solidification. However the amount of δ -ferrite formed is appreciable.
- III. The *Thermocalc*[®] Scheil-Gulliver solidification strongly supports the formation of δ -ferrite during slow cooling for both steels.
- IV. The homogenization of IFAC-1 is found to be initiated at 1323 K (1050 °C), with an endothermic heat effect of 16 ± 2 J g⁻¹. Similarly the dissolution of Cu and $M_{23}C_6$ precipitates in SS 304H Cu is found to initiate at 1167 K (894 °C) and 1320 K

4.3.2. Effect of Cu on solidification mode in SS 304H Cu

The austenitic-ferritic mode of solidification observed in SS 304H Cu has been supported by empirical deductions based on Cr_{eq}/Ni_{eq} ratio. As mentioned before, the primary reason behind the A-F mode of solidification in this steel is the non-equilibrium segregation of ferrite stabilizers (Cr and Nb) in the inter-dendritic liquid after the nucleation of austenite. However the effect of Cu on the solidification behavior of austenitic stainless

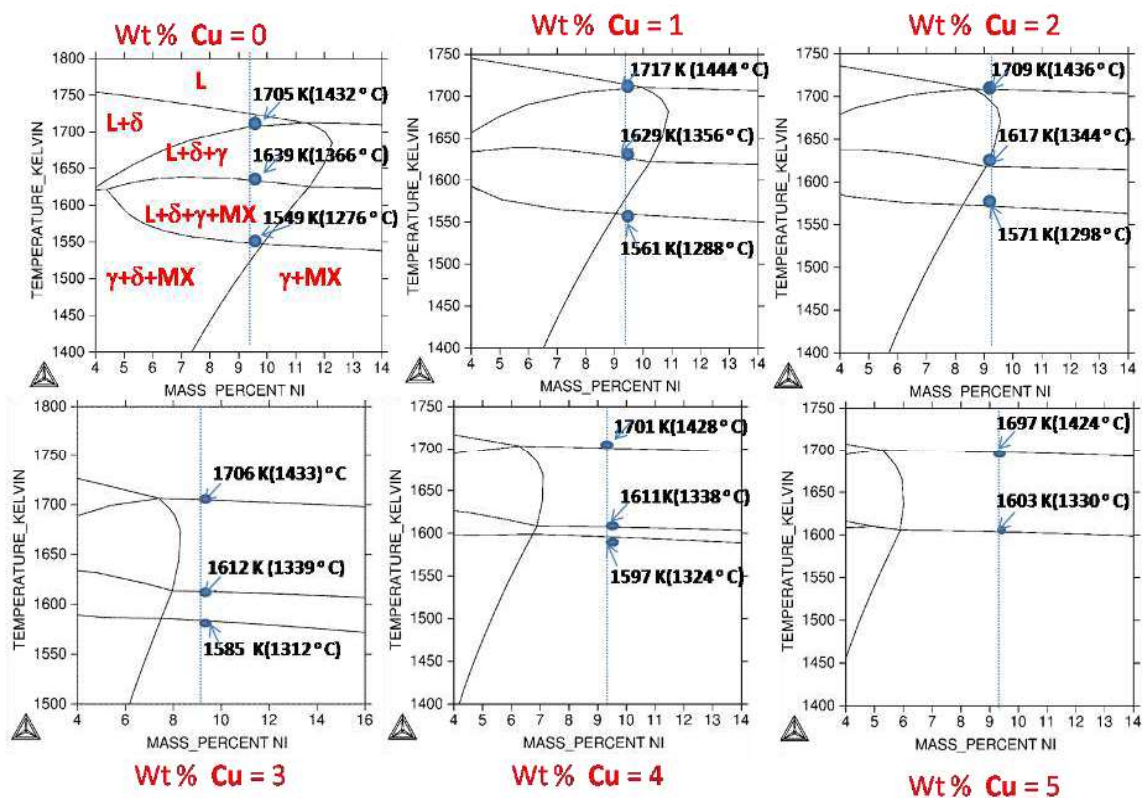


Fig. 4.19. *Thermocalc*[®]-based vertical sections for various copper contents ranging from 0 to 5 wt. pct are collated. The vertical line in each denotes the Ni composition for SS 304H Cu

steel has not been investigated before as Cu is not a common alloying element in austenitic steels. In this regard an investigation on the effect of Cu on the primary solidification mode in SS 304H Cu using equilibrium *Thermocalc*[®] simulation has been attempted. **Figure 4.19** depicts a collage of calculated vertical sections for various Cu contents (0, 1, 2, 3, 4, 5 wt %) in the solidification domain of the steel. It is readily seen that for low copper concentration

basis of non-equilibrium solidification under finite cooling rate in experimental situations. Upon solidification, if the first nuclei of γ -austenite do not form through a massive mode (composition invariant solidification to yield γ that has the same composition as the parent liquid), then it emerges that liquid adjacent to the freshly nucleated γ -austenite grains will be relatively enriched with ferrite stabilizing elements. Thus, as solidification proceeds, the inter-dendritic liquid becomes progressively more ferritic than what is stipulated by the starting alloy composition. This change in composition of the coexisting liquid towards enriched ferrite stabilizer's content, is conducive to the formation of δ -ferrite phase [209, 210]. Thus precipitation of δ ferrite ensues after the initial formation of γ austenite, until the liquid is relieved of the thermodynamic excess Cr and Mo [210]. In case of IFAC-1, it is the Cr and Mo which is segregated to the inter-dendritic liquid and primarily responsible for the non-equilibrium solidification of δ -ferrite. However as the Ni composition of this steel is high, the amount of δ -ferrite formed is very small and it eventually transforms into γ -austenite below the solidus point. On the other hand in case of SS 304H Cu containing Nb, the lack of full thermodynamic equilibrium prevailing at the liquid/solid interface under practical, finite cooling rate conditions would result in appreciable segregation of Nb to the liquid/ γ -interface. The 0.58 wt. % of Nb in SS 304H Cu is appreciable, as compared to that of SS 304 or SS 316 etc. [214, 224]. Because of this, the effective composition of liquid after initial γ -austenite + MX nucleation will be still higher in effective (Cr_{eq} / Ni_{eq}) ratio, than what is given by the actual alloy composition. Thus, the conditions prevailing at L/ γ interface are kinetically conducive for the secondary formation of δ -ferrite from liquid. The δ -ferrite so formed is obviously metastable, and must eventually transform to γ -austenite through subsequent solid state transformation route, namely, $\gamma + \delta \rightarrow \gamma$, if kinetic conditions are favorable for facilitating necessary solid state diffusion [219, 224].

4.3. Discussion

4.3.1. Cr/Ni equivalent and solidification of austenitic stainless steels

The solidification mode plays an important role in steel design. Generally the solidification mode is strongly dictated by the effective $[Cr_{eq}/Ni_{eq}]$ ratio. This ratio is estimated by evaluating the Cr_{eq} and Ni_{eq} of steels which are reported in the literature by several groups [216, 219, 220, 222]. The most popular expressions for evaluating the Cr_{eq} and Ni_{eq} for austenitic steels and the calculated values for the present steels due to Brooks et. al and Hammar et.al are listed in **table 4.6**. The parameter W_i in **table 4.6** stands for the weight fraction of the alloying element i . Notwithstanding the difference between these two

Table 4.6

The calculated values of $[Cr_{eq}/Ni_{eq}]$ ratio for IFAC-1 SS and SS 304H Cu

Reference	Expression for Cr_{eq} and Ni_{eq}	Cr_{eq}/Ni_{eq}	
		IFAC-1 SS	SS 304H Cu
J.A. Brooks et. al [216]	$Cr_{eq} = W_{Cr} + W_{Mo} + 1.5W_{Si} + 0.5W_{Nb}$ $Ni_{eq} = W_{Ni} + 30W_C + 0.5W_{Mn} + 30W_N$	1.016	1.122
O. Hammar et. al [223]	$Cr_{eq} = W_{Cr} + 1.37W_{Mo} + 1.5W_{Si} + 2W_{Nb} + 2W_{Ti}$ $Ni_{eq} = W_{Ni} + 22W_C + 0.31W_{Mn} + 14.2W_N + 1W_{Cu}$	1.14	1.169

empirical recommendations of estimating Cr_{eq} and Ni_{eq} , many studies on the solidification behavior of austenitic stainless steels reveal that for $[Cr_{eq}/Ni_{eq}] \leq 1.5$ or nearby either fully austenitic or austenite+ ferrite mode of solidification is preferred [209, 215, 223]. Following the results of Elmer et al [215], steels with $Cr_{eq}/Ni_{eq} \leq 1.25$, the solidification mode is anticipated to be fully austenitic. In view of this, the ratio Cr_{eq}/Ni_{eq} in the present case suggests a primary austenitic mode of solidification for both IFAC-1 and SS 304H Cu. However the DSC investigation as well as the non-equilibrium Scheil solidification using *Thermocalc*[®] suggests the formation of δ -ferrite in both steels. This can be rationalized on the

for temperatures above 1398K (1125 °C), the kinetics are accelerated. From **Figure 4.18 (b)**, it is clear that at 1413 K, the dissolution of $M_{23}C_6$ carbides reaches near completion only after 3 hours of annealing. In **figure 4.18 (c)** the time evolution of the fractional carbide area has been portrayed which reveals the behavior of a typical diffusion limited phenomena. In view of this, a numerical fit to the following Kolmogorov–Johnson–Mehl–Avrami (KJMA) type functional form is attempted (*see chapter 2, Eq. (2.15)*).[118, 126-128, 139, 140]

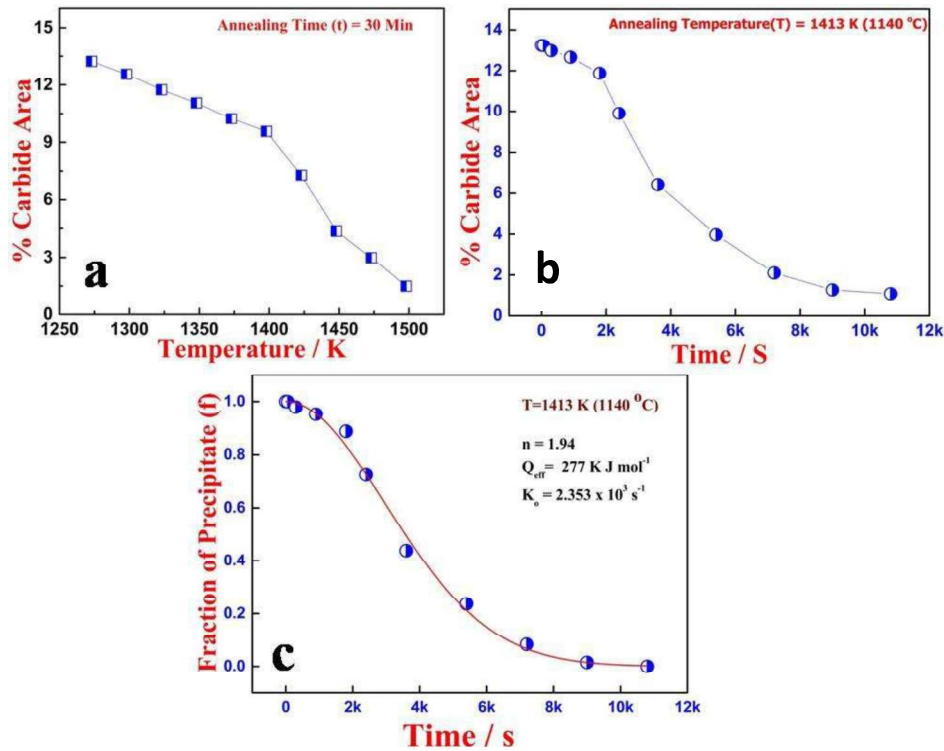


Fig. 4.18. Estimated percentage area of $M_{23}C_6$ precipitates plotted **(a)** as a function of temperature, for 30 min. annealing time; **(b)** as a function of time, at an annealing temperature 1413 K (1140 °C) **(c)** Fraction of precipitates as a function of time during annealing at 1413 K (1140 °C). The solid line represents the fit to KJMA model equation (*Eq. 2.15*).

The solid line in **figure 4.18 (c)** represents the fit to KJMA kinetics expression. The estimated values of kinetic parameters (k_0 , Q_{eff} , n) are found to be $2.35 \times 10^3 \text{ s}^{-1}$, 277 kJmol^{-1} and 1.94 respectively. It is interesting to note that the estimated effective activation energy is close to the activation energy for bulk diffusion of Nb in austenite.

scanning electron microscopy and the fraction of carbides were estimated from the microstructure in terms of percentage carbide area with the help of *Image-J* software. The accurate quantification of the carbide area fraction was achieved by setting a suitable gray-level threshold depending on the contrast difference between the matrix and the second-phase $M_{23}C_6$ precipitates. This procedure is repeated over three different images of the same sample and then averaged out for the estimation of final area fraction of the second-phase carbides.

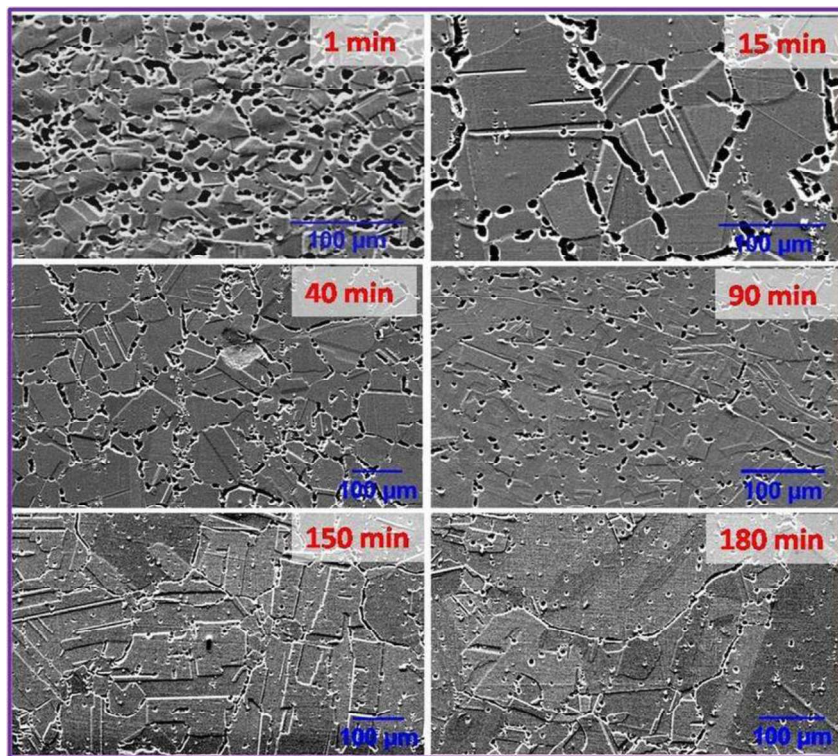


Fig. 4.17. Microstructural evolution depicting the dissolution of second-phase precipitates as a function of time after annealing at 1413 K (1140 °C).

The microstructures of samples annealed at 1413 K (1140 °C) for different durations of time are presented in **figure 4.17**. The results of *Image-J* semi-quantitative analysis are plotted in **figure 4.18 (a) and (b)** respectively, for isochronal [fixed time of 30 minutes, 1273 K to 1498 K (1000 °C to 1225 °C)] and isothermal (1213 K (940 °C); 0 to 3 hours) annealing experiments. It emerges from **figure 4.18 (a)** that the dissolution proceeds rather slowly from 1273 K to 1498 K (1000 °C to 1225 °C), which is suggestive of sluggish kinetics. However,

cooling rates above 50 K min^{-1} clear evidence of the presence of δ -ferrite is observed in microstructure. The typical microstructure obtained for 60 K min^{-1} cooled sample contains what are known as skeletal δ -ferrite [214].

4.2.7. *Stability of second phase carbides in SS 304H Cu*

In SS 304H Cu, the major second phase precipitates are the MX type carbo-nitrides, $M_{23}C_6$ and the elemental Cu precipitates. This fact has been conformed from the *Thermocalc*[®] (See section 4.2.4) as well as our electron microscopy investigation (see section 4.2.1). As a candidate material for AUSC applications, SS 304H Cu is desired to have adequate mechanical properties by suitable choice of heat treatments. Therefore the temperature domain of stability of second phase precipitates and their dissolution kinetics play a major role in the overall phase stability of the material. The nano-sized Cu rich precipitates, which share a coherent interface with γ -austenite matrix, [51, 160] have a very small phase fraction of about 0.02 mole % at the maximum (*Thermocalc*[®]). Upon heating, their dissolution into γ -matrix is fairly quick, once a temperature of about 1167 K (894 °C) is reached. From the on heating DSC thermogram shown in **figure 4.12 (a)**, the onset of $M_{23}C_6$ (~0.018 mol. %) dissolution starts around 1320 K (1047 °C); but the dissolution occurs over a wider temperature domain and the complete dissolution is realized only above 1373 K (1100 °C). On the other hand dissolution of MX (~0.015 mol. %) precipitates occurs at comparatively high temperatures, near about melting. To identify a suitable time temperature window for the solution treatment, a first set of samples of SS 304H Cu are aged at 1413 K (1140 °C), for various time durations, starting from 1 minute to 3 hours. The choice of this annealing temperature is based on our prior knowledge of the dissolution temperatures of Cu and $M_{23}C_6$. In the second set of experiments, fresh samples were isothermally annealed for 30 minutes at varying temperatures with 25 K interval, starting from 1273 K to 1498 K (1000 °C to 1225 °C). The microstructures of all these annealed samples were characterized using

Table 4.5

The transformation start (T_s), peak (T_p) and finish (T_f) temperature along with transformation enthalpy for two separate DSC solidification peaks for SS 334 H Cu

Cooling Rate K min ⁻¹	L→L+ γ				L+ γ +MX→ γ +MX+ δ			
	T_s K (°C)	T_p K (°C)	T_f K (°C)	Enthalpy (J g ⁻¹)	T_s K (°C)	T_p K (°C)	T_f K (°C)	Enthalpy (J g ⁻¹)
3	1706 (1433)	1705 (1432)	1678 (1405)	77.5	1634 (1361)	1633 (1360)	1630 (1357)	5.8
7	1697 (1424)	1696 (1423)	1696 (1423)	158.9	1620 (1347)	1619 (1346)	1615 (1342)	17.1
10	1718 (1445)	1711 (1438)	1641 (1368)	237.7	1563 (1290)	1561 (1288)	1556 (1283)	30.6
20	1718 (1445)	1708 (1435)	1651 (1378)	400.8	1612 (1339)	1609 (1336)	1598 (1325)	50.2
30	1706 (1433)	1699 (1426)	1635 (1362)	731	1563 (1290)	1561 (1288)	1546 (1273)	112.9
50	1711 (1438)	1691 (1418)	1620 (1347)	935.3	1620 (1347)	1617 (1344)	1596 (1323)	141.3
60	1709 (1436)	1688 (1415)	1626 (1353)	1194.9	1626 (1353)	1623 (1350)	1594 (1321)	192.7
70	1702 (1429)	1674 (1401)	1610 (1337)	1273.4	1610 (1337)	1607 (1334)	1574 (1301)	208.4
80	1694 (1421)	1668 (1395)	1601 (1328)	1341.9	1601 (1328)	1597 (1324)	1562 (1289)	214.3
99	1708 (1435)	1676 (1403)	1571 (1298)	1945.9	1571 (1298)	1564 (1291)	1518 (1245)	306.1

The optical micrographs of the samples subjected to different rates of cooling are collated together in **figure 4.16**. It is readily observed that for low cooling rates the microstructure consists of broad austenite grains with dispersed carbide precipitates. This is anticipated as the slow cooling provides enough time for the diffusion driven precipitation of $M_{23}C_6$ and MX carbides along the grain boundary and within the austenite grain respectively. The inset shown in 7 K min⁻¹ microstructure represents a typically coarse $M_{23}C_6$ particle. For

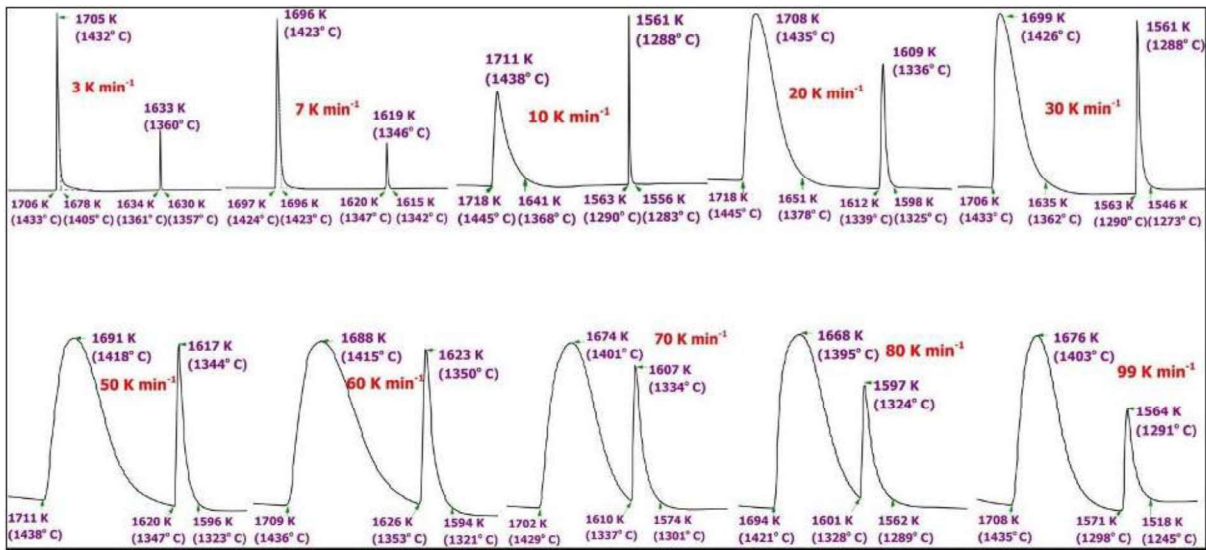


Fig. 4.15. DSC solidification thermal arrests obtained at different cooling rates for SS 304H Cu

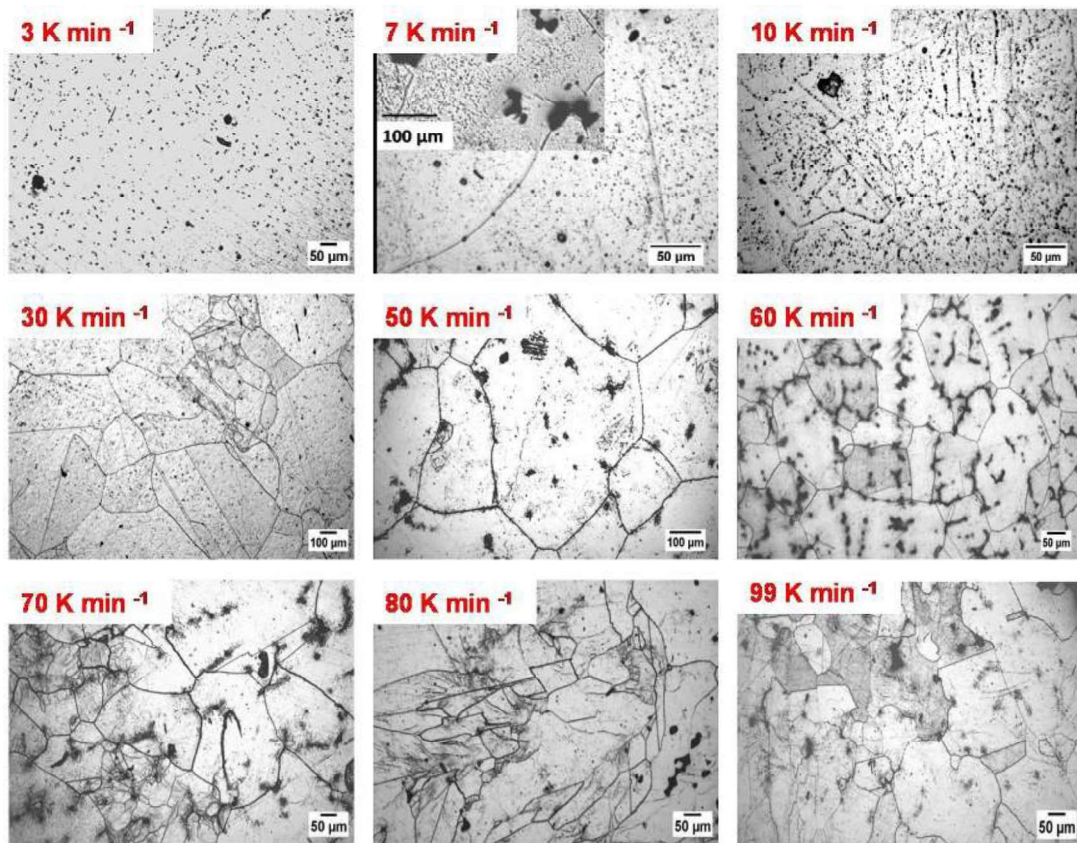


Fig. 4.16. Optical micrographs of samples that are cooled from liquid at different rates. The inset in 7 K min⁻¹ cooled sample marks the intragranular M₂₃C₆ phase.

the primary austenite forms in a massive mode, then there is no (appreciable) segregation of ferrite stabilizing elements in the inter-dendritic liquid. This results in transformation of entire liquid to γ -austenite. However this can be realized only in case of high cooling rates, since it is necessary to undercool the melt below the equilibrium temperature, at which the equality of Gibbs energies of liquid and γ -austenite phase is realized [219]. In view of this, an attempt has been made in this study, to characterize the solidification behavior under varying cooling rates in the range, 3 to 99 K min⁻¹. **Figure 4.15** represents the collage of different solidification thermal arrest DSC profiles obtained at varying cooling rates. It is evident from this figure that with increasing cooling rate, the liquidus temperature decreases and the liquidus-solidus gap (ΔT^{L-S}) shrinks. Further, the separation between the two thermal events: (i) $L \rightarrow \gamma$ and (ii) $\gamma + MX \rightarrow \gamma + MX + \delta$ also decreases with cooling rate. In fact, for 99 K min⁻¹ cooling rate, the two peaks are extremely close to each other. In addition, with increasing cooling rate, the first solidification peak that is $L \rightarrow \gamma$ becomes a little more spread in the temperature domain. This means that the rate of γ -austenite formation from liquid and its growth is extended to lower temperatures, because the diffusion at L/ γ interface is unable to keep pace with the rate of cooling [221]. The transformation onset, finish, and the peak temperatures along with associated enthalpy value for the solidification peaks at various cooling rates are listed in **table 4.5**. For the estimation of enthalpy, pure Iron is used as the standard for the calibration.

observed phase transformations sequence, the transformation temperatures and the solidification enthalpy are listed in **table 4.4**.

Table 4.4

Experimentally determined transformation sequence, transformation temperatures and solidification enthalpy for SS 304H Cu.

Heating Cycle		Cooling Cycle	
<i>Transformation event</i>	<i>Temperature K(°C)</i>	<i>Transformation event</i>	<i>Temperature K(°C)</i>
Cu-dissolution	1167 (894)	L→ γ	1723 (1450)
M ₂₃ C ₆ dissolution	1320 (1047)	L+ γ →L+ γ +MX	1655 (1382)
MX dissolution start	1440 (1167)	L+ γ +MX→ γ +MX+ δ	1607 (1334)
γ → γ +L; Melting start	1653 (1380)	M ₂₃ C ₆ precipitation	1239 (966)
γ +L→L; melting finish	1721 (1448)	Cu- precipitation	962 (689)
Enthalpy of transformation (J g⁻¹)			
Enthalpy of melting			62±7
Total precipitation enthalpy(M ₂₃ C ₆ + Cu)			20±2

As a general remark, it may be said that these solid state transformations are diffusion-driven and occur over a time/temperature range. Hence, these events are not marked by sharp thermal arrests that are characteristic of liquid to solid type or typical first-order transformations; instead they appear as diffuse and spread-out exothermic humps, in an otherwise smooth, baseline-compensated DSC profile.

4.2.6. Effect of cooling rate on solidification in SS 304H Cu

It is a well established fact that for highly alloyed austenitic stainless steels, the cooling rate plays a vital role in deciding the solidification mode [215, 219-221]. In fact, if

Scheil solidification simulation, as seen in **figure 4.12**. The precipitation of MX starts from L+ γ mixture at about 1625 K (1352 °C). Following the precipitation of MX, the exothermic arrest at 1607 K (1334 °C) indicates the formation of some δ -ferrite through $L + \gamma + MX \rightarrow \gamma + MX + \delta$ transformation. The δ -ferrite actually appears at the end of the solidification, that is just before the solidus temperature (1585 K (1312 °C)) of the alloy. The observed temperature of 1607 K (1334 °C) for δ -ferrite nucleation from the liquid is very close to the estimated value from Scheil simulation [1597 K (1324 °C)]. It is also noteworthy that Nb has a high affinity to segregate to the liquid after initial austenite formation. Therefore the extent of non-equilibrium solidification is more prominent with increase in Nb content of the liquid, which favors subsequent δ -ferrite formation [217]. In fact, it is possible that higher Nb-containing steels might solidify through fully ferritic or ferritic- austenitic mode, under suitable cooling conditions [218]. Once δ -ferrite has formed, the local super saturation of liquid in Nb and Cr is relieved to a large extent and the situation is again conducive for further formation of austenite from Nb-lean liquid through the reaction scheme given as, $L + \gamma + MX + \delta \rightarrow \gamma + MX + \delta$. Normally, under slow cooling conditions and at temperatures of the order of 1500 K (1227 °C), it is possible to realize this $\gamma + \delta \rightarrow \gamma$ conversion to reasonable extent, but often, some amount of residual δ -ferrite is found in the final solidified product, if the cooling rate is high [219]. Such a situation is found in SS 304 and 304L welds, which are known to have considerable residual δ -ferrite [219]. In the present DSC analysis, we have not observed any discernible exothermic event for the $\delta \rightarrow \gamma$ transformation. This is attributed to the extremely low-phase fraction of the δ -ferrite phase. Now coming back to the cooling DSC thermogram, the comparatively weaker thermal arrest at 1607 K (1334 °C) stands for the $L + \gamma + MX \rightarrow L + \gamma + MX + \delta$ transformation. Once γ -austenite is formed, the precipitation of $M_{23}C_6$ (1239 K (966 °C)) and finally the elemental copper (962 K (689 °C)) follows one by one. The

solidification starts with the reaction $L \rightarrow L + \gamma$ at 1723 K (1450 °C) followed by precipitation of Nb rich MX carbides at 1655 K (1382 °C). This point also emerges from the results of

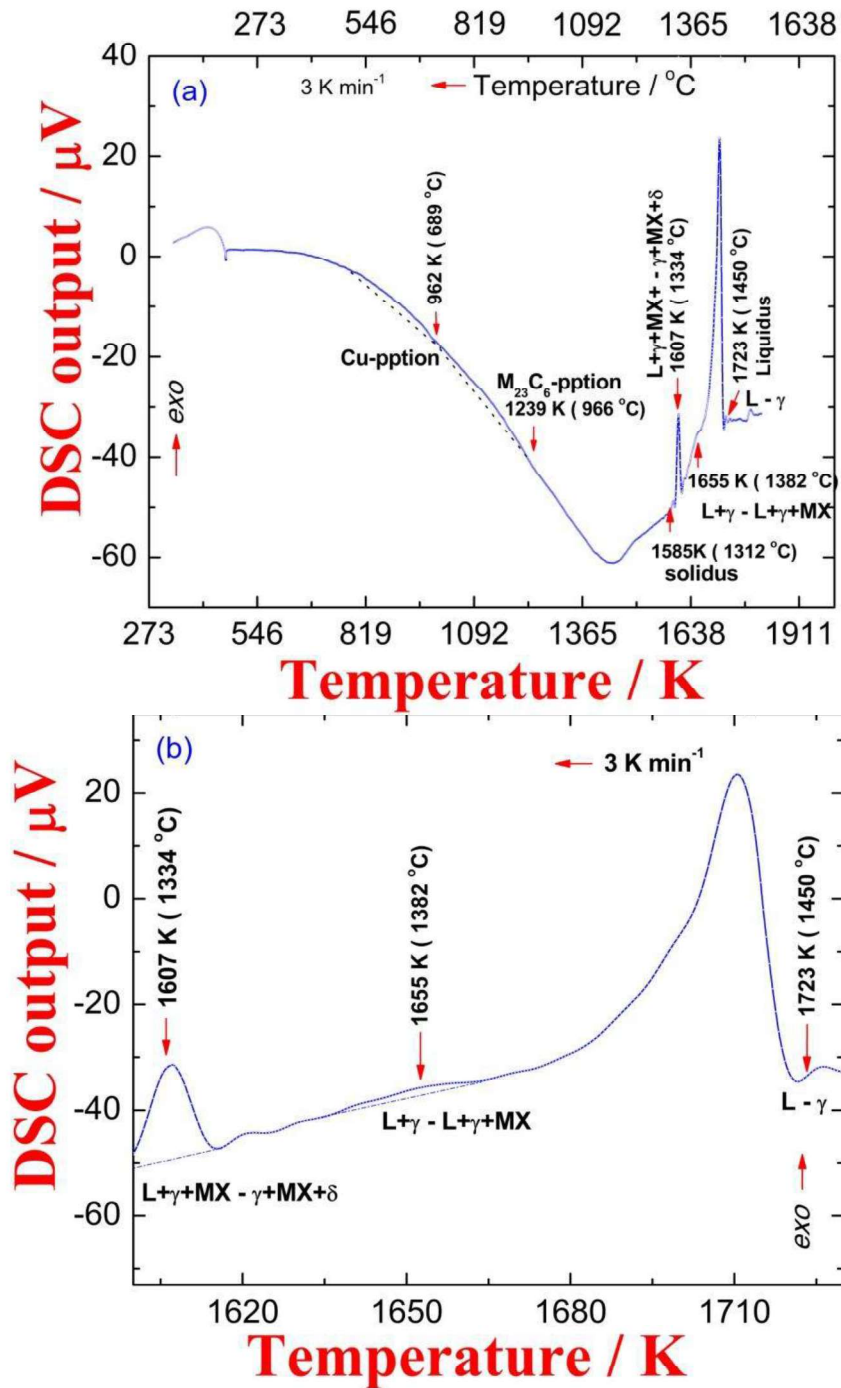


Fig. 4.14. (a) The cooling cycle DSC profile obtained at 3 K min⁻¹, showing various thermal arrests due to phase changes. (b) The expanded view around solidification regime

profile (figure 4.13 (a) and (b)) the solidification in cooling cycle represents two distinct exothermic thermal events. The observed solidification behavior is actually indicative of the Austenite-Ferrite (AF) mode of solidification in SS 304H Cu under slow cooling. The

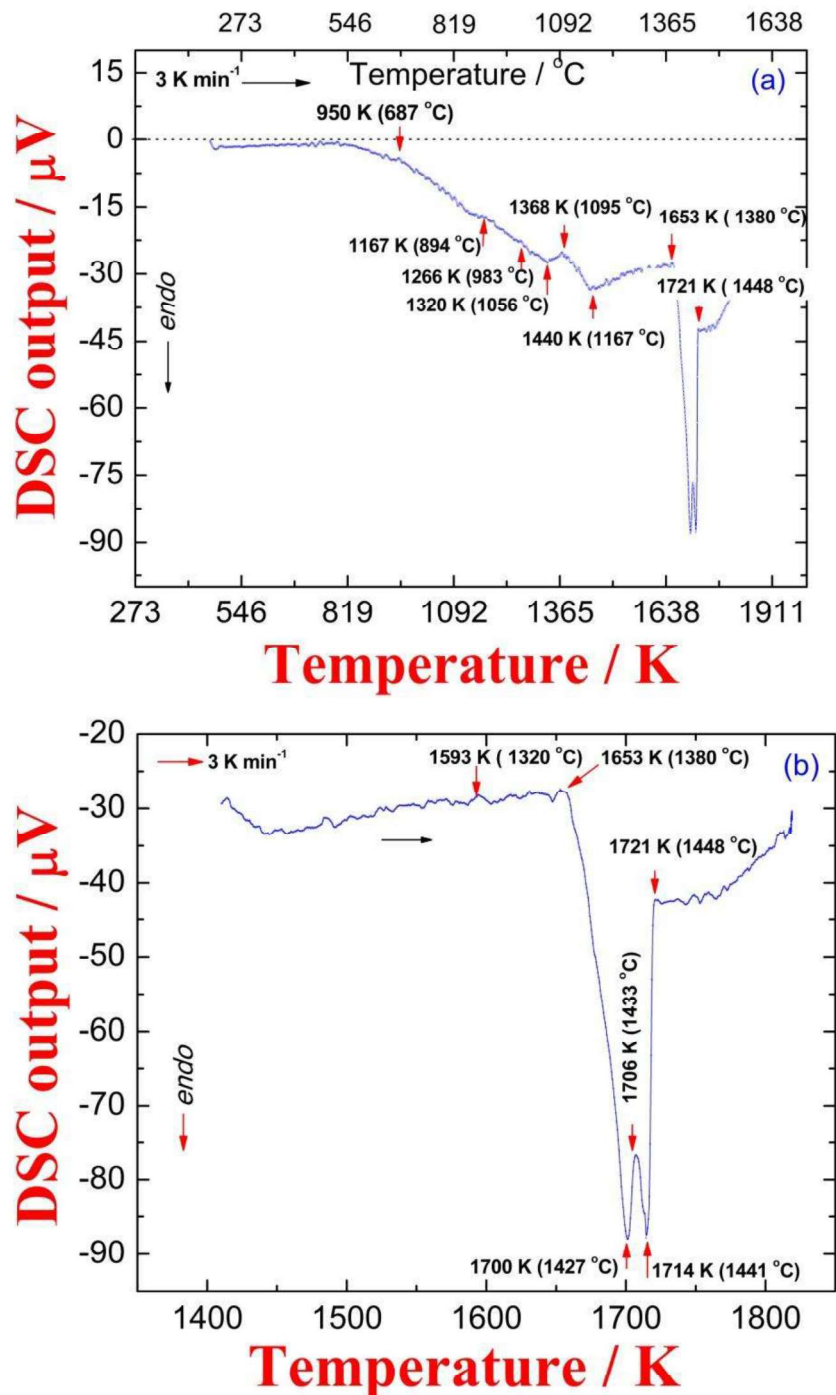


Fig. 4.13 (a). The DSC heating profile obtained at 3 K min^{-1} heating rate, showing various thermal arrests due to phase changes. **(b)** The expanded view around melting regime

(a) for the heating cycle. The expanded view around the melting region is depicted in **figure 4.13 (b)**. The first distinct deviation from the baseline during heating is observed at 950 K (687 °C). This signifies the beginning of the second-phase precipitation or dissolution taking place in the starting microstructure, which is a mixture of γ -austenite+MX+M₂₃C₆+Cu phases. The weak endothermic thermal arrest at 1167 K (894 °C) represents the onset of Cu-dissolution. The dissolution domain of M₂₃C₆ type carbides is in the range 1320 K to 1368 K (1056 °C to 1095 °C). The beginning of MX carbo-nitrides dissolution is indicated by the thermal arrest at 1440 K (1167 °C). However, its full dissolution continues further into high-temperature γ -phase. In fact, the equilibrium *Thermocalc*[®] simulation shows that the full dissolution of MX precipitates occurs only slightly above the solidus temperature, namely, 1650 K (1377 °C). The onset of melting begins at 1653 K (1380 °C) as marked in **figure 4.13 (a)**. A careful observation of the **figure 4.13 (b)** indicates that the melting profile is somewhat split, which actually happens as a result of overlapping of two or more thermal arrests in a narrow temperature domain. This result is in agreement with the *Thermocalc*[®] predicted reaction sequence namely, $\gamma + \text{MX} \rightarrow \text{L} + \gamma + \text{MX} \rightarrow \text{L} + \gamma \rightarrow \text{L}$. Nevertheless, the temperature domain of their occurrence is so close that they appear as split peak instead of separate thermal events. The dissolution of MX-type carbo-nitrides is diffusion-mediated and hence is gradual in nature [212]. The serrated nature of DSC profile observed near the melting region can be attributed to the gradual dissolution of these MX precipitates. The complete dissolution of MX precipitates occurs at 1700 K (1427 °C). Finally, the completion of melting, i.e., $\text{L} + \gamma \rightarrow \text{L}$, occurs at 1721 K (1448 °C).

Figure 4.14 (a) presents 3 K min⁻¹ cooling cycle DSC thermogram for the solution annealed sample. The expanded view around the solidification regime is also shown in **figure 4.14 (b)**. The important point to note is the asymmetry in heating and cooling DSC profiles, which is generic to austenitic stainless steels [213-216]. Therefore in contrast to the heating

The solidification proceeds further up to 1535 K, where the phase fraction of liquid approaches zero. This is the solidus temperature. A critical comparison of Scheil–Gulliver prediction with equilibrium solidification throws up one important point, namely that δ ferrite phase forms invariably at the end of non-equilibrium solidification. This is unlike the case for equilibrium solidification, where the steel solidifies in a fully austenitic mode. The cooling rate plays a vital role in deciding the solidification behavior and the amount and morphology of δ -ferrite. Similar to the case of IFAC-1, a systematic investigation of phase stability has also been carried out in SS 304H Cu using Differential scanning calorimetry (DSC). This is discussed in the next section.

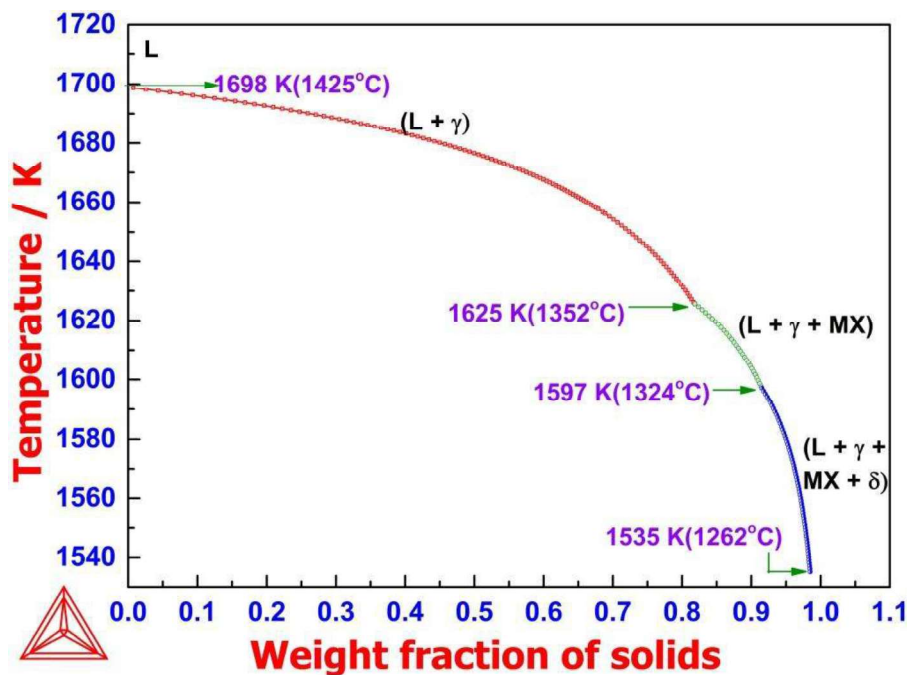


Fig. 4.12. Scheil simulation of the solidification in SS 304H Cu.

4.2.5. DSC investigation of phase stability in SS 304H Cu

In order to carry out a systematic DSC characterization of phase changes, samples of SS 304H Cu annealed at 1473 K/1200 °C for two hours are subjected to controlled heating and cooling at 3 K min⁻¹. The baseline calibrated DSC thermogram is shown in **figure 4.13**

equilibrium path. Therefore an attempt has been made to study the non-equilibrium solidification behavior of SS 304H Cu using Scheil-Guliver solidification module in *Thermocalc*[®]. The weight fraction of solid as a function of temperature during solidification of SS 304 H Cu is shown in **figure 4.12**. It is evident from **figure 4.12** that solidification starts at 1698 K (1425 °C), where the weight fraction of the solids is zero (Liquidus). At 1625 K (1352 °C) the primary MX precipitates out from the mixture of L+ γ , where about 80% of the phase fraction corresponds to γ -austenite. The formation of δ -ferrite occurs at about 1597 K (1324 °C). This confirms the austenitic+ ferritic mode of solidification of SS 304H Cu steel under practical conditions. In case of SS 304H Cu, both Nb and Cr are rejected into the liquid after the nucleation of γ -austenite. Because of this, the Nb-rich Nb (CN) precipitation is favored in SS 304H Cu. However, the liquid supersaturated with Nb and Cr does not relieve its non-equilibrium character fully by the precipitation of Nb (CN). As a result, the δ -ferrite forms from the mixture of L + γ + MX. The formation of δ -ferrite occurs at about 1597 K, where the total phase fraction of the solids amounts to ~91 %.

Table 4.3

Thermocalc[®] predicted phase transformation sequence and corresponding temperature for SS 304H Cu.

Phase Transformation	Temperature(K)/ °C
$L \rightarrow L + \gamma$	1710 / 1437
$L + \gamma \rightarrow L + \gamma + MX$	1650 / 1377
$L + \gamma + MX \rightarrow \gamma + MX$	1640 / 1367
$\gamma + MX \rightarrow \gamma + MX + M_{23}C_6$	1190 / 917
$\gamma + MX + M_{23}C_6 \rightarrow \gamma + MX + M_{23}C_6 + Z\text{-Phase}$	1120 / 847
$\gamma + MX + M_{23}C_6 + Z\text{-Phase} \rightarrow \gamma + MX + M_{23}C_6 + Z\text{-Phase} + Cu$	777 / 504
$\gamma + MX + M_{23}C_6 + Z\text{-Phase} + Cu \rightarrow \alpha' + \alpha'' + \gamma + MX + M_{23}C_6 + Z\text{-Phase} + Cu$	560 / 287

H Cu using equilibrium *Thermocalc*[®] simulation. It has already been mentioned in the previous section that the solidification of a multicomponent alloy does not strictly follow the

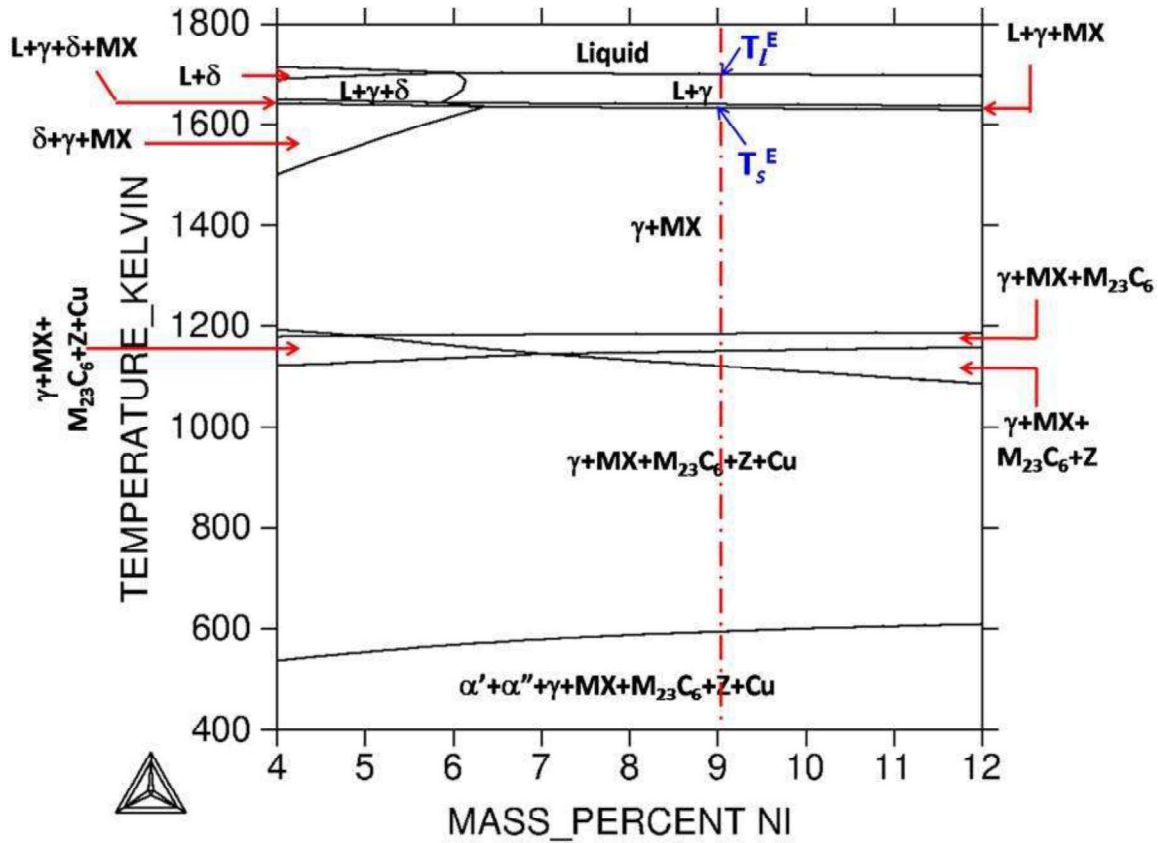


Fig. 4.10. *Thermocalc*[®]-based calculated vertical section as a function of Ni-content for SS 304H Cu. The vertical dotted line corresponds to the Ni content in the steel

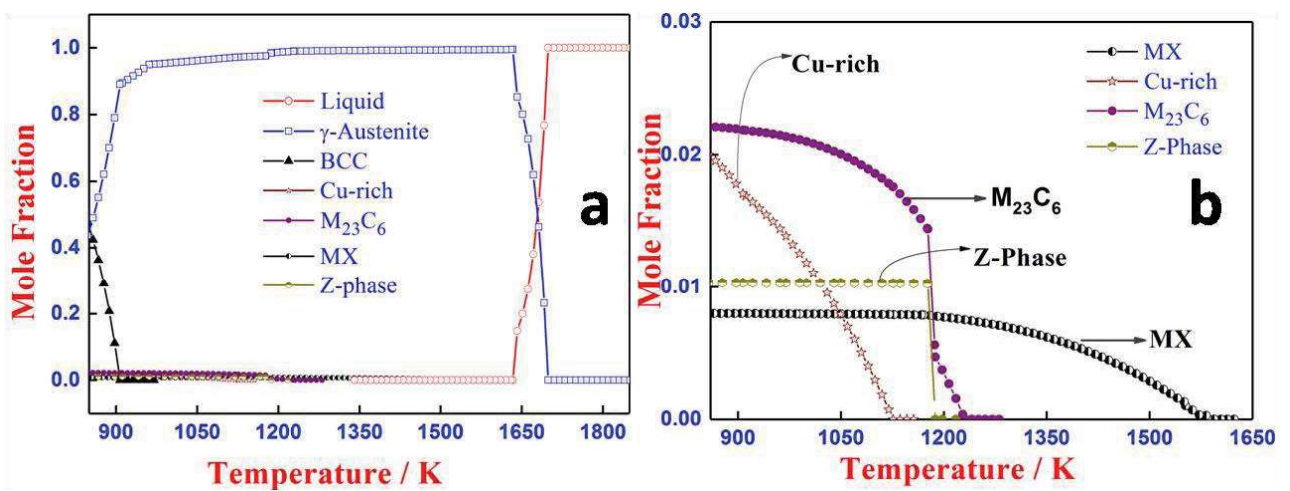


Fig. 4.11. (a) Temperature variation of phase fraction for different phases estimated from *Thermocalc*[®] for SS 304H Cu (b) Magnified view of (a) showing phases with low volume fraction

Table 4.2

Measured transformation temperatures for IFAC-1 using slow scan DSC experiments

Phase Transformation	Temperature (K / °C)
$L \rightarrow L + MX \rightarrow L + MX + \gamma$ (Liquidus)	1684 / 1411
$L + MX + \gamma \rightarrow L + MX + \gamma + \delta$	-
$L + MX + \gamma + \delta \rightarrow MX + \gamma + \delta$	1631 / 1358
$MX + \gamma + \delta \rightarrow MX + \gamma$	1610/1337

4.2.4. *Thermocalc*[®] simulation of phase stability & solidification behavior in 304H Cu

The *Thermocalc*[®] based calculated vertical section for SS 304H Cu is shown in **figure 4.10**. The *fcc*- Cu phase has been considered as one of the active phases in addition to liquid, γ - austenite, δ -ferrite, $M_{23}C_6$, MX and Z-phases. It is clearly evident from **figure 4.10** that SS 304 H Cu containing about 9.3 wt. % Ni should solidify in a fully austenitic mode under equilibrium conditions, that is, $L \rightarrow L + \gamma$. The volume fractions of all the active phases have also been estimated using *Thermocalc*[®] which is shown in **figure 4.11(a)**. The volume fraction of second phase precipitates like $M_{23}C_6$, MX, Cu and Z-phase are illustrated separately in **figure 4.11(b)** as these precipitates constitute only a small fraction as compared to austenite and liquid. From **figure 4.11 (b)** it is evident that, the mole percentage of Cu rich phase and $M_{23}C_6$ is about 2.2; whereas that of MX phase is about 0.75 at 773 K, under equilibrium conditions. The complete dissolution of Cu and $M_{23}C_6$ in γ -austenite matrix occurs at 1127 K and 1220 K respectively. On the other hand, the complete dissolution of Nb rich MX precipitates requires higher solutionizing temperature, around 1585 K, which happens to be just below the equilibrium solidus temperature of this steel. **Table.4.3** lists the sequence of phase transformations and the transformation temperatures obtained for SS 304

solidification peak indicating a primary austenitic mode of solidification. Typical DSC thermogram obtained at 99 K min^{-1} is depicted in **figure 4.9**. It is clear from this figure that only a single thermal arrest is seen during fast cooling. The insets to **figure 4.9** give the

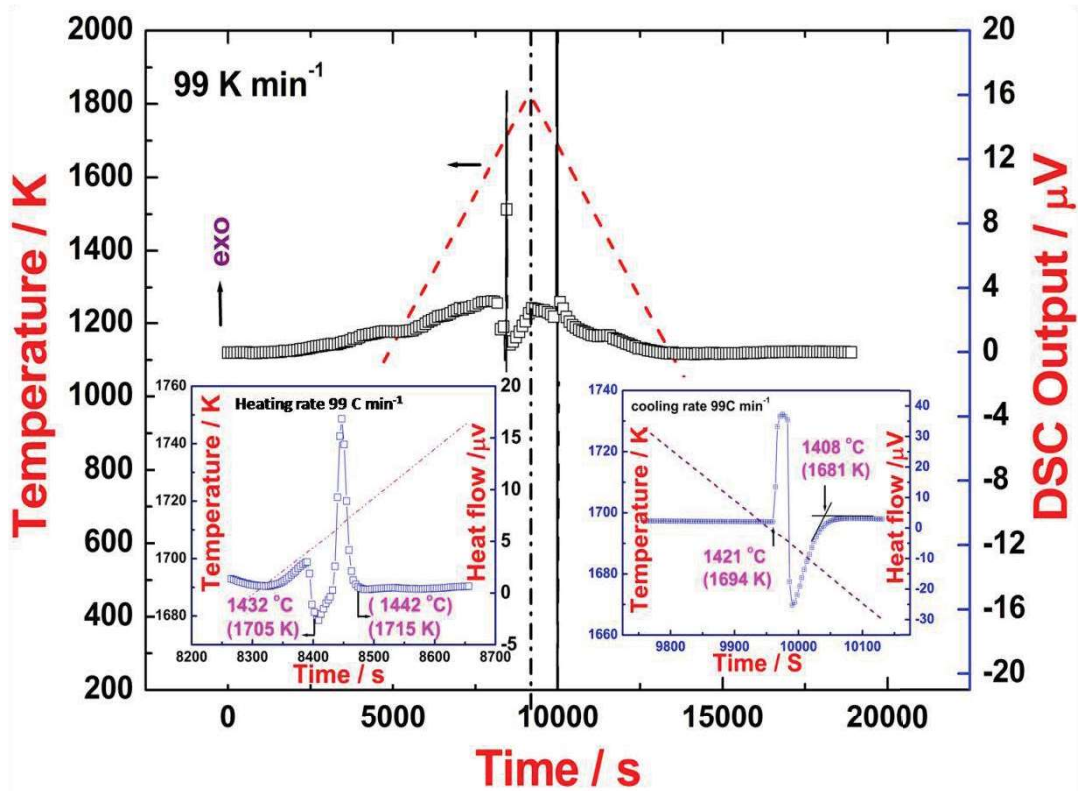


Fig. 4.9. DSC profile obtained at 99 K min^{-1} for IFAC-1 SS. The insets give the expanded view of the melting and solidification region. In contrast to slow 3 K min^{-1} cooling, only one peak is observed under fast cooling condition

expanded views of melting and solidification region. The absence of a second thermal arrest indicates that δ -ferrite has not formed in this case, or its formation has not occurred to any significant extent, so that it is clearly detected by accompanying thermal effects. Therefore the increase in cooling rate alters the solidification mode from (austenitic + ferritic) to fully austenitic mode. The experimental phase transformation temperatures as obtained from slow cooled DSC thermogram are listed in **table 4.2**. The estimated solidification enthalpy or the latent heat of solidification is found to be $200 \pm 15 \text{ J g}^{-1}$.

+MX + γ). **Figure 4.8(c)** shows the expanded view of the cooling cycle DSC thermogram in the solidification region. The solidification onset is found to be quite sharp to peak maximum, followed by a gradual fall in the heat flow as the event is actually caused by overlapping of two or more closely occurring transformation events namely: $L \rightarrow L+MX \rightarrow L + MX + \gamma$ and $L + MX + \gamma \rightarrow L + MX + \gamma + \delta$. The solidus temperature as observed from this figure is 1631 K. However the MX (0.3 wt. %) precipitation and the δ -ferrite nucleation are not observed as separate peaks, since the volume fraction is small. The δ -ferrite subsequently transforms into γ -austenite with the reaction $\gamma + MX + \delta \rightarrow \gamma + MX$ which is represented by the second exothermic peak in **figure 4.8(c)**. It is surprising to observe the formation of δ -ferrite during solidification of IFAC-1 with a 14.9 wt. % Ni. As mentioned before, the equilibrium *Thermocalc*[®] simulation predicts no sign of δ -ferrite formation during the whole solidification regime. This occurs only during non-equilibrium solidification, where the first nucleus of austenite that forms from liquid has a composition different from that of the parent liquid. As a result, the liquid surrounding the freshly nucleated austenite is enriched with ferrite stabilizing elements (Cr, Mo etc.). As the solidification proceeds, the remnant liquid gets richer with Cr and Mo which leads to formation of δ -ferrite phase to relieve the excess Gibbs free energy [209, 210]. It is because of this non-equilibrium segregation effect, IFAC-1 exhibits mixed austenite + ferrite (AF) solidification path. Since the Ni content of the steel is very high, the δ -ferrite formed in this case is metastable and besides its volume fraction is also small. Therefore with subsequent cooling, it is only expected that δ -phase will transform to γ , as attested by the second sharp peak at 1610 K (1337°C) in the cooling DSC profile (**figure 4.8(c)**). It is informative to note here that the rate of cooling from liquid has significant influence on the solidification mode [211]. In this regard the solidification of IFAC-1 has been investigated using DSC for varying cooling rates up to 99 K min⁻¹. It has been observed that for cooling rates exceeding 5 K min⁻¹ the DSC thermogram shows a single

MX→L. Nevertheless the volume fraction of this MX phase is small and therefore the melting quickly proceeds to completion at 1701 K. During the course of cooling cycle, two sharp thermal arrests are clearly evident (**figure 4.8(a)**). Following the results of Scheil solidification simulation using *Thermocalc*[®], the first cooling thermal arrest, with the onset temperature of 1684±5 K represents the nucleation of MX precipitation (L→ L+ MX→L

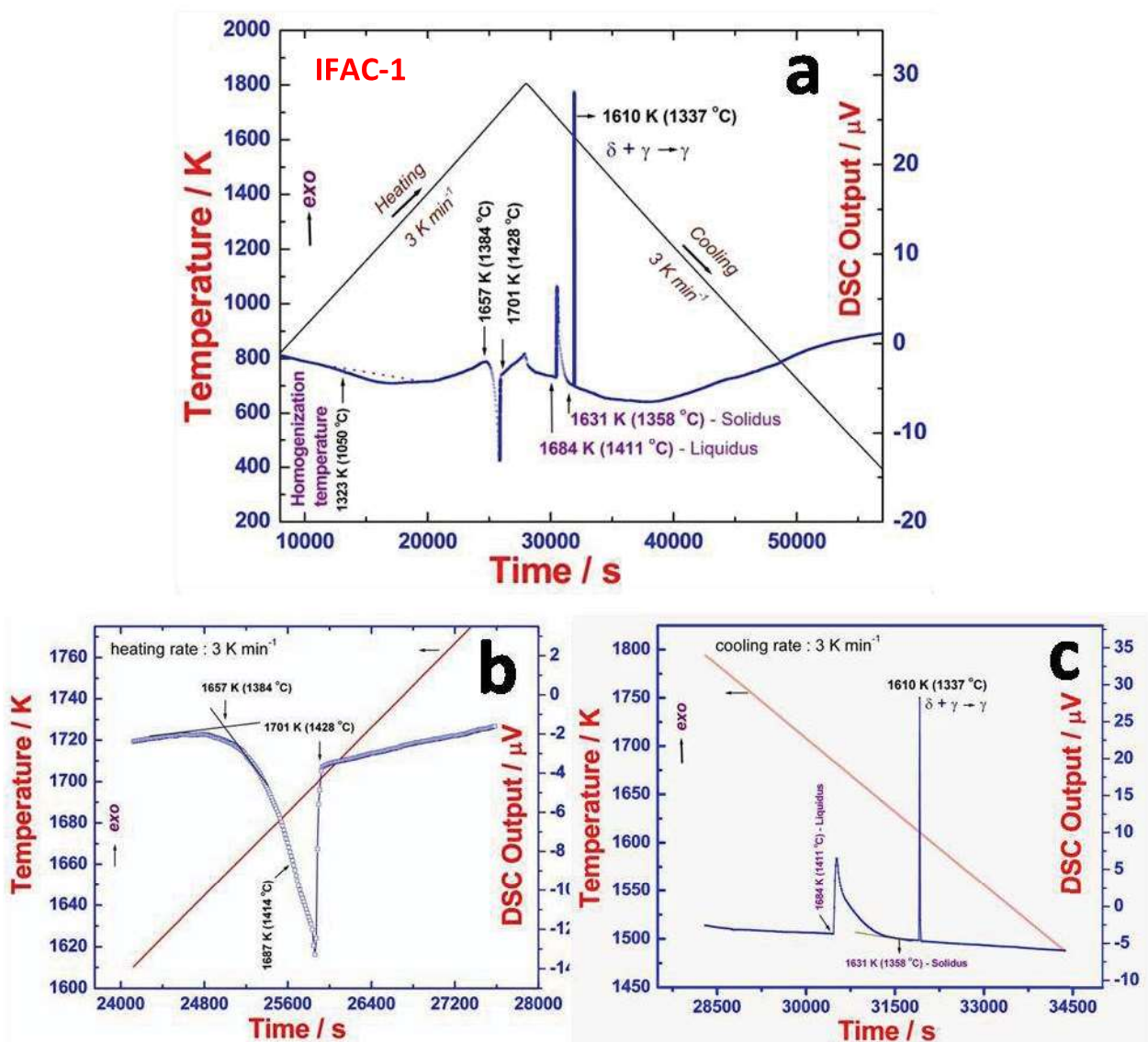


Fig. 4.8. (a) The on-heating and cooling DSC profile of IFAC-1 taken at 3 K min⁻¹ (b). The expanded view of DSC on-heating thermogram around the melting region (c) The expanded view of cooling cycle DSC profile in the solidification region

transformation of the liquid to solid occurs at 1490 K, which is lower than the equilibrium solidus temperature of 1657 K.

As mentioned before, the *Thermocalc*[®] equilibrium simulation can only predict the possibility of formation of different phases and their temperature domain of stability as a function of composition. However, under practical situations, the transformation temperatures, phase compositions, and even the sequence of phase changes solely depends on local kinetic factors prevailing at the transformation front. This in turn depends on composition [40-41, 205].

4.2.3. DSC investigation of phase stability and solidification behavior in IFAC-1 SS

The IFAC-1 sample was subjected to a slow DSC scan with a heating/cooling rate of 3 K min⁻¹. The experiment was conducted starting from room temperature up to 1773 K, which is above the melting regime. The sample was isothermally held for 5 minutes at 1773 K. **Figure 4.8a** shows the on heating and cooling DSC thermogram obtained on IFAC-1 at 3 K min⁻¹. The on heating DSC trace shows an endothermic reaction centered at 1323 K which represents the onset of homogenization reaction in γ -austenite followed by the gradual dissolution of secondary TiC or Ti(C,N) precipitates with more diffused interface. This dissolution occurs by the way of sluggish diffusion in the fcc matrix at relatively lower temperatures. Following the homogenization reaction, a clear evidence of an endothermic peak, representing the melting reaction ($\gamma + MX \rightarrow L$) is observed in the temperature domain, 1657–1701 K. However, it is interesting to note that, the melting thermal arrest is actually associated with a secondary event occurring at 1687 K (1414 °C). This is reflected as a minor shoulder in the expanded view of melting region shown in **figure 4.8 (b)**. In accordance with the equilibrium *Thermocalc*[®] simulation, the secondary peak actually corresponds to the dissolution of MX precipitates prior to the completion of melting, through the reaction $L + \gamma +$

temperature induced phase transformation sequence in an alloy system under full thermodynamic equilibrium, where non-equilibrium segregation is not taken into account. One simple way to account for the non-equilibrium solidification profile is to follow the Scheil–Gulliver scheme, which assumes only local equilibrium at the advancing solidification front [33, 34]. The Scheil–Gulliver solidification can also be simulated with the Scheil

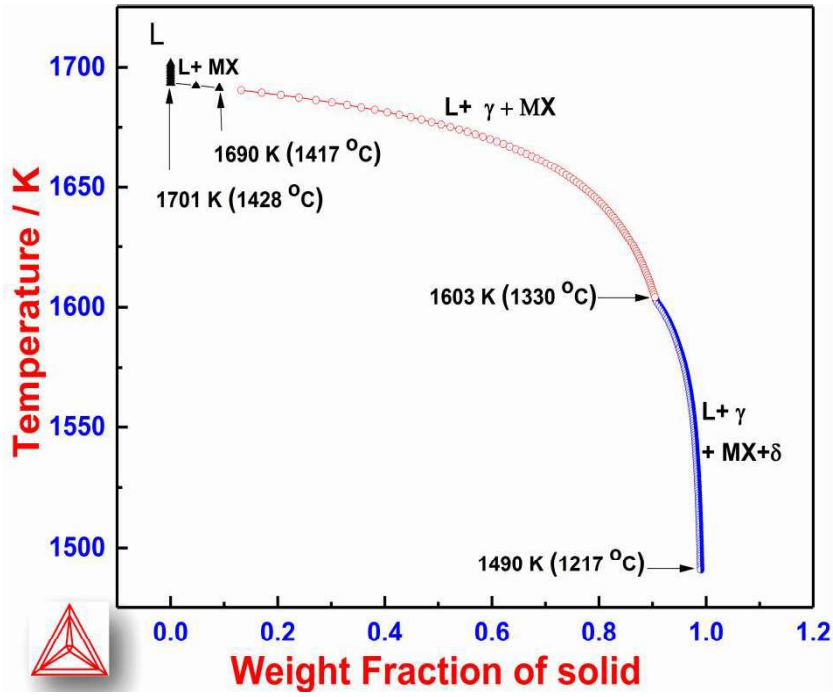


Fig. 4.7. *Thermocalc*[®]-based Scheil simulation of the solidification process for IFAC-1 SS

module using *Thermocalc*[®]. **Figure 4.7** shows the weight fraction of solid as a function of temperature in IFAC-1 using Scheil-Gulliver solidification module. It is observed from **figure 4.7** that, the liquidus temperature during non-equilibrium cooling is found to be 1697 K which is reasonably close to the equilibrium value of 1701 K. In this case, the solidification starts with the precipitation of primary MX phase. This is followed by the nucleation of γ -austenite at 1690 K. The most important fact that emerges from non-equilibrium simulation is the formation of δ -ferrite through the reaction, $L + MX + \gamma \rightarrow L + MX + \gamma + \delta$. This occurs around 1603 K, which is in contradiction with the equilibrium phase formation sequence (**figure 4.6 a**), which suggests a fully austenite mode of solidification. The complete

the predicted transformation sequence as a function of decreasing temperature is listed in **table 4.1**. The δ -ferrite phase in **figure 4.6 (a)** stands for the high temperature nonmagnetic ferrite phase and α -phase represents the low temperature magnetic bcc ferrite, which again separates into α' (Fe rich bcc) and α'' (Cr rich bcc) below about 777 K. However under normal cooling conditions, the low temperature α -ferrite is seldom observed in practical situations due to kinetic considerations [205]. It is clear from the **figure 4.6** that IFAC-1 SS containing about 15.4 wt. % Ni solidifies from the liquid state (L) in a primary

Table 4.1

The *Thermocalc*[®] predicted phase transformation sequence and the transformation temperature for IFAC-1 SS

Phase Transformation sequence	Temperature (K / °C)
$L \rightarrow L+MX$	1701/1428
$L+MX \rightarrow L + \gamma+ MX$	1690/1417
$L + \gamma+ MX \rightarrow \gamma+ MX$	1657/1384
$\gamma + MX \rightarrow \gamma +MX+ \alpha$	860/587
$\gamma +MX+ \alpha \rightarrow \gamma +MX+ \alpha + Z\text{-Phase}$	838/565
$\gamma + MX +\alpha +Z\text{- Phase} \rightarrow \alpha ' + \alpha '' + \gamma +MX+ Z\text{-Phase}$	777/504

austenitic mode under equilibrium. This is given as: $L \rightarrow L+ MX \rightarrow L+ \gamma+ MX \rightarrow \gamma+ MX$. It is noteworthy to mention that, if complete thermodynamic equilibrium were to be followed at the solid–liquid interface during solidification, then the formation of δ -ferrite phase is *not* found during the post solidification cooling. However, this happens only for very slow cooling rates under actual experimental conditions. In the case of highly alloyed steels such as IFAC-1, the segregation tendencies invariably operate even in the liquid phase for finite cooling rates. This will influence the composition of the liquid phase ahead of the solid-liquid interface. Therefore, equilibrium *Thermocalc*[®] simulation predicts only the possible

48, 208]. **Figure 4.6(a)** shows the calculated Ni isopleths (vertical section as a function of Ni composition) for IFAC-1 SS using *Thermocalc*[®]. The mole fractions of various phases under thermodynamic equilibrium as a function of temperature are shown in **figure 4.6(b)**. Further,

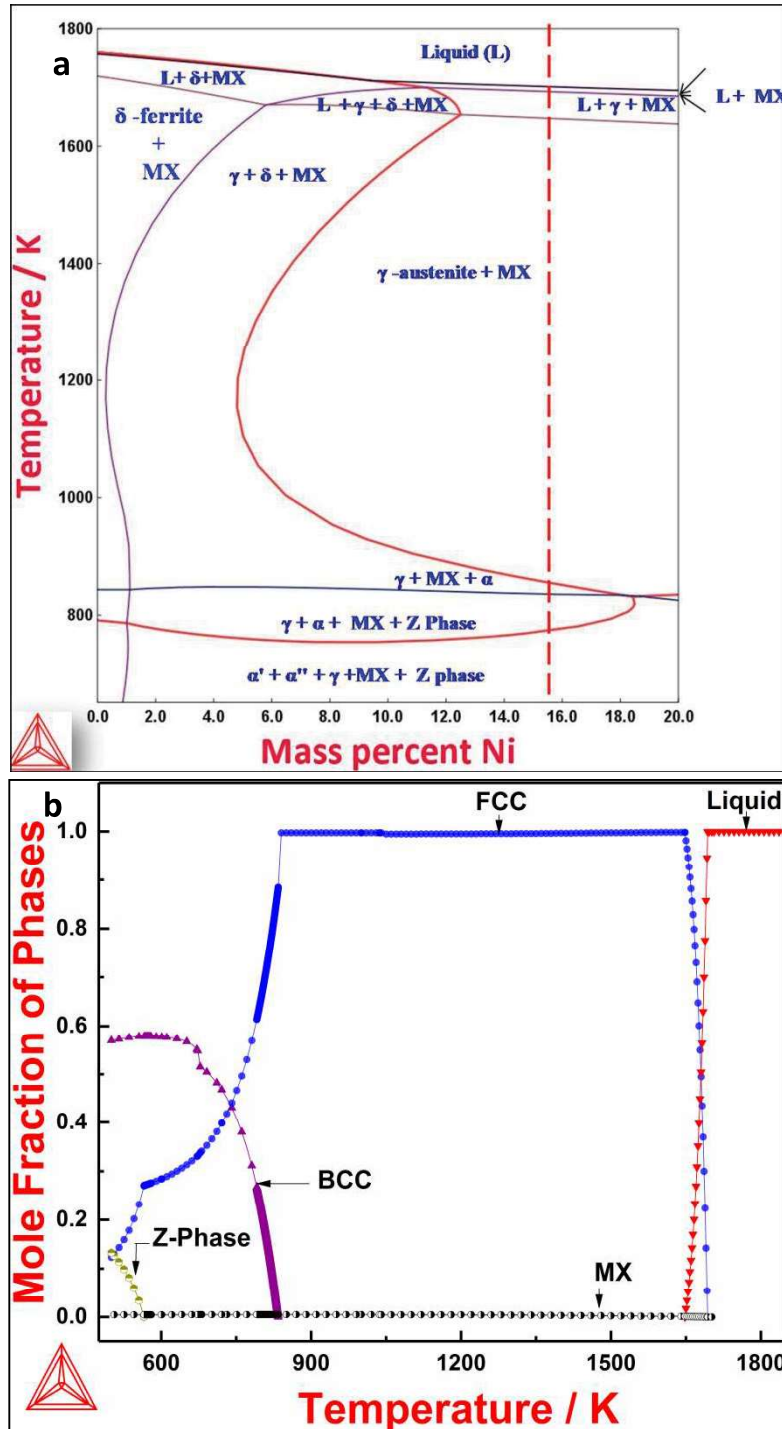


Fig. 4.6. (a) *Thermocalc*[®]-based calculated vertical section for IFAC-1 steel as a function of Ni-content. The vertical dotted line corresponds to the Ni content in the steel. (b) The mole fraction of different phases as a function of temperature

figure 4.5(c) through (g). **Figure 4.5(c)** shows the TEM bright field image of the aged sample which clearly reveals the presence of another coarse precipitate along the austenite grain boundaries, formed during the aging treatment. These are confirmed to be $M_{23}C_6$ type carbides by the selected area diffraction (SAD) pattern (**figure 4.5(d)**). In addition, the presence of fine Cu-rich metallic precipitate has been also identified in the aged sample as shown in **figure 4.5(e)**. It is noted that the distribution of these spherical nano-sized Cu particles are fairly dense and by and large uniformly spread throughout the austenite matrix. The average size of Cu-particles is found to be in the range of 7 to 10 nm. It may be added that the close matching of lattice parameter of the Cu to that of γ -austenite phase gives rise to an SAD pattern that is indistinguishable from γ -austenite matrix. Nevertheless, the EDX spectra confirm the definite presence of Cu-rich particles (**figure 4.5(f) and (g)**). A comparison of these two EDX spectra shows clearly that the spherical nano-sized particles are Cu-rich precipitates. With the basic knowledge of equilibrium phases present in IFAC-1 and SS 304H Cu, obtained through metallography, the next step is to understand the high temperature phase stability and the temperature induced phase transformations in these alloy systems. In order to facilitate such an understanding, a differential scanning calorimetry investigation was carried out in combination with *Thermocalc*[®] simulation of phase equilibrium and Scheil–Gulliver modelling of solidification [33, 34]. This is described in the following sections.

4.2.2. *Thermocalc*[®] simulation of thermal stability & solidification behavior of IFAC-1 SS

This section deals with the equilibrium thermodynamic calculation of phase equilibria in IFAC-1 SS using *Thermocalc*[®] software with TCFE8 steel database. The liquid phase, γ austenite, α -ferrite, MX, $M_{23}C_6$ and Z-phase have been considered as active phases for the evaluation of phase equilibria. The σ phase and Cr_2N are excluded from the calculation as these phases are likely to appear only after long aging durations under applied stress [40, 41,

austenite matrix. However, there was no signature of the $M_{23}C_6$ phase in the solution-annealed sample. This indicates that the solutionizing temperature and time adopted (1473 K (1200 ° C) for 3 hours) are reasonably adequate to dissolve most of the $M_{23}C_6$ phase. Nevertheless, the MX precipitates have not dissolved fully at this temperature and their presence is clearly identified in the bright field TEM image. Further, the solution-annealed samples were aged at 923 K (650 ° C) for 150 hours, followed by furnace cooling. The aging

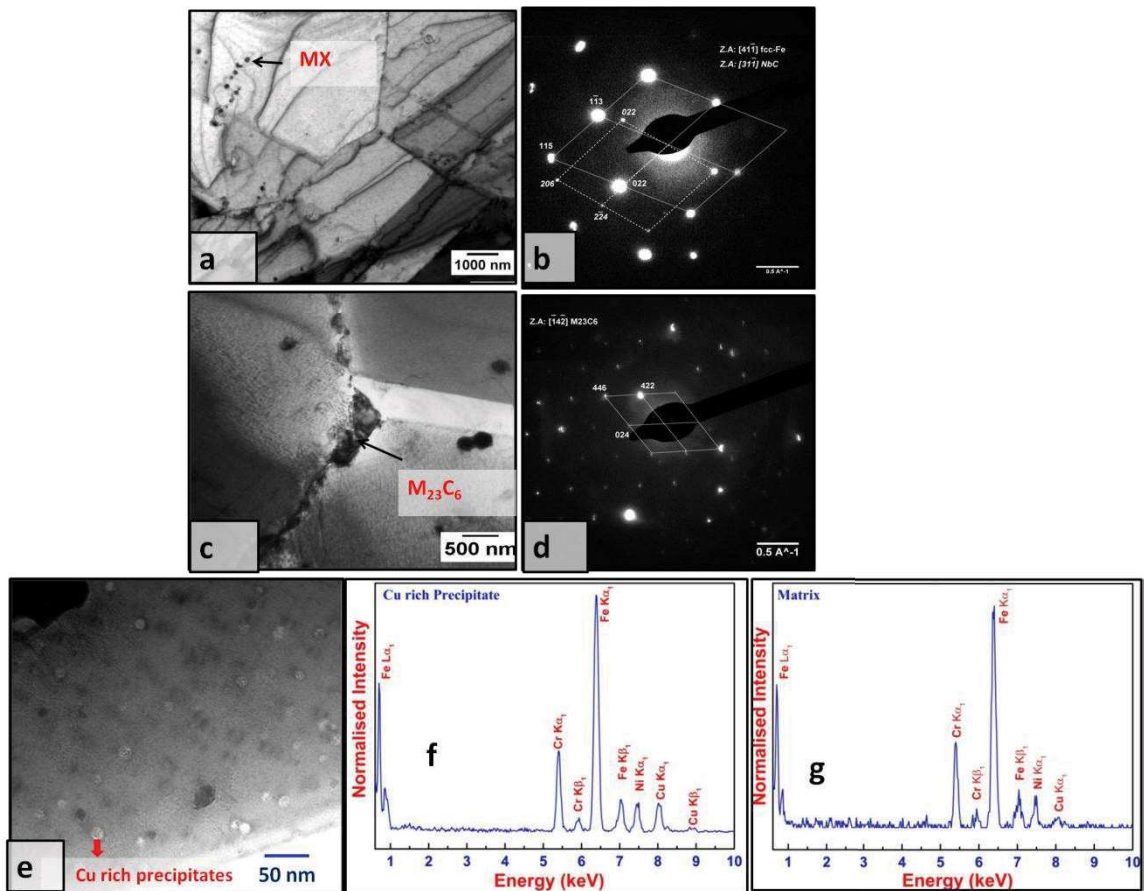


Fig. 4.5. (a) Bright field TEM micrograph of the solution annealed SS 304H Cu showing Nb rich MX phase in austenite matrix (b) SAD pattern from MX phase and austenite matrix in the solution annealed steel (c) TEM image of the aged steel showing $M_{23}C_6$ precipitation along the austenite grain boundary (d) SAD pattern of $M_{23}C_6$ carbide shown in (c) (e) TEM micrograph showing the dense Cu rich metallic precipitates in the aged sample (f) EDX spectrum corresponding to Cu rich phase (g) EDX spectrum of austenite matrix

treatment was intended to facilitate the precipitation of Cu-rich phase in the γ -austenite matrix. These aged samples were then characterized by TEM, and the results are portrayed in

distributed all over the matrix. In order to characterize these second-phase precipitates, a scanning electron microscopy investigation has been carried out. **Figure 4.4** presents the secondary electron micrograph with corresponding EDX spectrum for the solution annealed SS 304H Cu steel sample. It is interesting to note the presence of two separate second-phase precipitates distributed all over the γ -austenite matrix. These are shown by arrow marks in **figure 4.4**. The accompanying EDX spectrum suggests that the coarse grain boundary precipitates are rich in Cr indicating $M_{23}C_6$ type of carbides, while the intragranular precipitates are preferentially rich in Nb, which suggests that they belong to MX-type carbides (Nb (C,N)). The average size of the entire precipitate distribution has been measured using image analysis and is found to be in the range of 1 to 4 μm . However, the preferential distribution of rather coarse $M_{23}C_6$ precipitates situated along the austenite grain boundaries is attributed to their formation by grain boundary nucleation mechanism and subsequent coarsening facilitated during slow furnace cooling. It is useful to mention here that besides $M_{23}C_6$ and MX type carbide phases, the presence of nano-sized Cu-rich metallic precipitates has also been reported in steels containing 3 to 4 wt. % Cu [51]. However, in our present microstructural characterization using SEM, the detection of these fine Cu-rich precipitates was not possible. Therefore, the transmission electron microscopy (TEM) characterization was attempted in aged samples of SS 304 H Cu where the presence of fine Cu-particles is clearly noticed in γ -austenite matrix. **Figure 4.5(a)** and **(b)** show the TEM results for SS 304H Cu sample, which was solution-annealed at 1473 K (1200 °C) for 3 hours followed by water quenching. The water quenching after the solution treatment was meant to restrict the precipitation of the second-phase carbides during cooling. The TEM bright field image for the solution-annealed sample is depicted in **figure 4.5(a)** indicating the presence of second-phase precipitates. Further, the selected area diffraction (SAD) pattern shown in **figure 4.5(b)** taken from these second-phase particles confirmed the MX type of carbides inside the

Figure 4.3 shows the optical micrograph for SS 304H Cu material that is solution annealed at 1473 K for 2 hours. The presence of annealing twins, in addition to well-developed austenite grain structure is observed in SS 304H Cu. The average grain size is estimated to be $46 \pm 4 \mu\text{m}$. Figure 4.3 suggests in addition, the presence of small precipitates

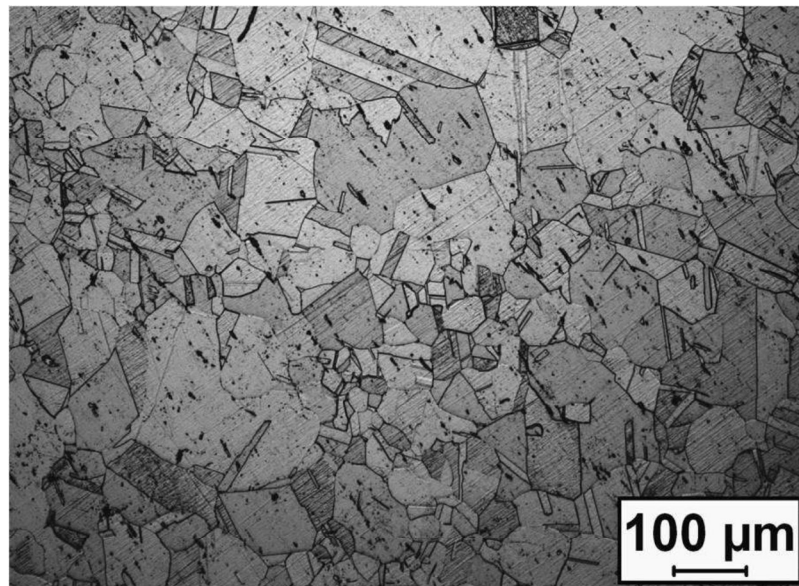


Fig. 4.3. Optical micrograph of SS 304H Cu solution annealed at 1473K for 2h

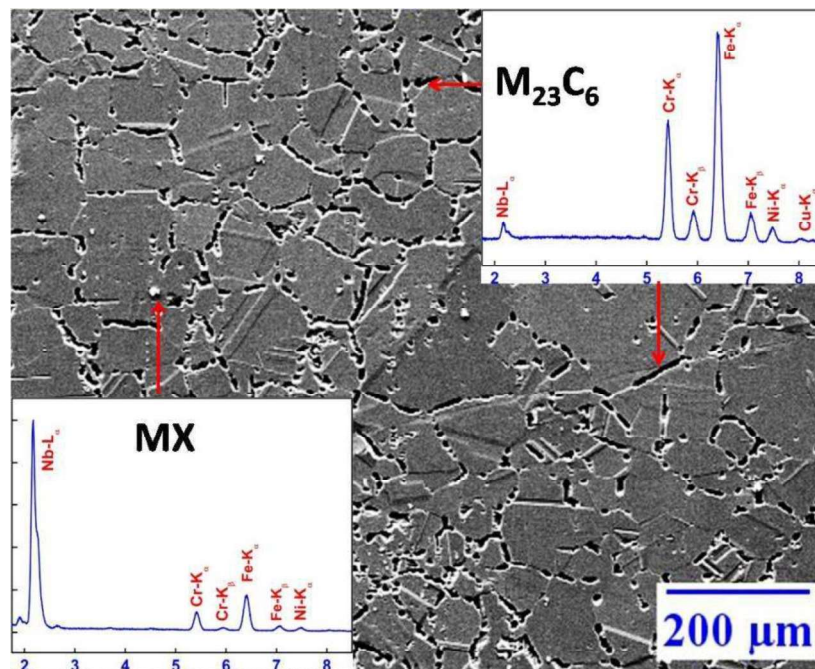


Fig. 4.4. Secondary electron micrograph and associated EDX spectra of a slow-cooled solution-treated SS 304H Cu sample

constant N_A stands for the Avogadro number. The estimated molar volume for IFAC-1 and SS 304 H Cu are: 7.154×10^{-6} and $6.972 \times 10^{-6} \text{ m}^3$ respectively. **Figure 4.2** depicts the optical microstructure for the solution annealed IFAC-1 SS sample containing broad and well developed annealing twins. The average grain size is measured to be $52 \pm 7 \text{ }\mu\text{m}$. It is instructive to mention that, although the formation of Cr rich $M_{23}C_6$ precipitates is anticipated in 300 grade austenitic stainless steels, containing medium to high carbon, the present

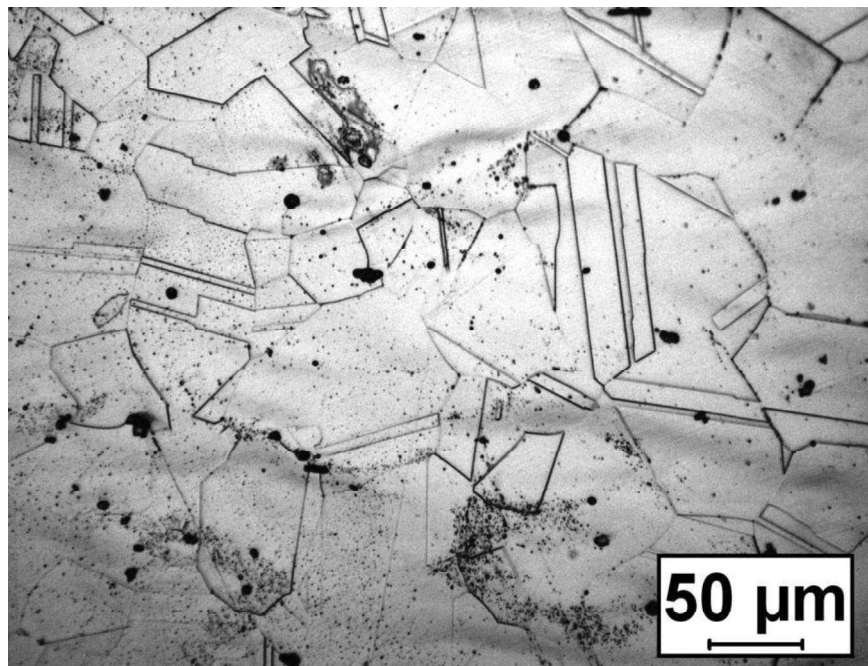


Fig. 4.2. Optical micrograph of IFAC-1 SS solution annealed at 1323 K

candidate IFAC-1 containing only 0.04 wt.% carbon does not contain appreciable $M_{23}C_6$ precipitates [205]. It has been well documented in literature that in cold worked IFAC-1 SS, the presence of Ti promotes the precipitation of fine scale intragranular TiC precipitates during service conditions [206-207]. In this regard, several microstructural investigations have been carried out on IFAC-1 for the identification of nano-scale TiC precipitates using electron microscopy [206]. Hence, this aspect will not be dealt with here any further.

microstructural constituent in both IFAC-1 and SS 304H Cu. The lattice parameters for the γ -austenite phase are estimated from experimental XRD patterns. They are: $a_\gamma=0.3622\pm 0.001$ nm for IFAC-1; and $a_\gamma=0.3591\pm 0.001$ nm for SS 304H Cu steel respectively. The molar volume (V_m) of the γ -austenite phase is estimated using the relation, $V_m^\gamma = (a^3/4) \times N_A$. The

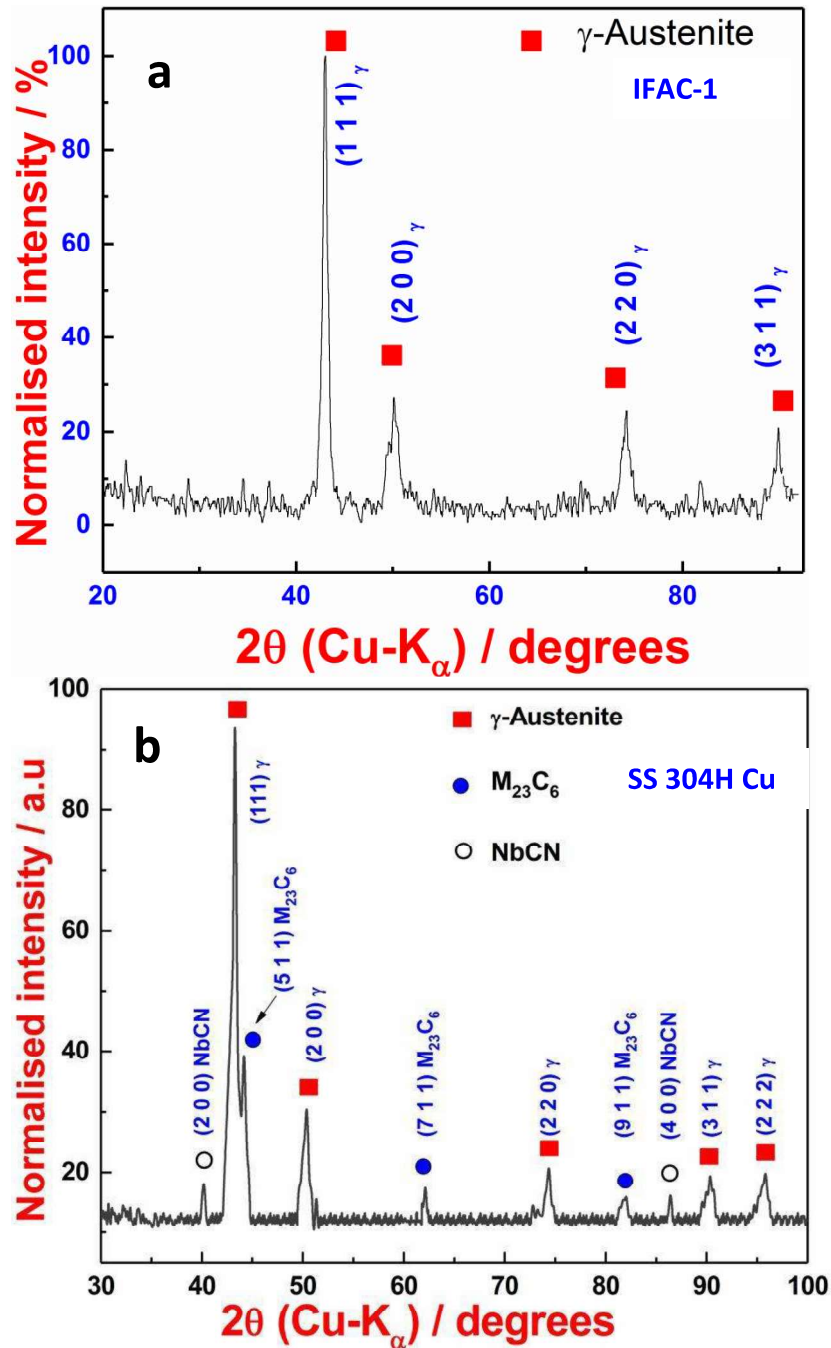


Fig. 4.1. Room temperature X-ray diffraction pattern of (a) IFAC-1 SS and (b) SS 304H Cu showing the diffraction peaks for different phases

void swelling resistance [10, 204]. Therefore the thermal and mechanical properties in these multi component alloys depend on the amount, nature of distribution and stability of these secondary phases. In the light of such situation, the present chapter describes the results of dynamic calorimetry investigation on thermal stability of IFAC-I and SS 304H Cu steels. The experimental results are compared and validated with *Thermocalc*[®] based simulations of thermodynamic phase equilibrium in these alloys. In addition, the melting and solidification behavior has also been studied by in-situ calorimetry under varying heating and cooling rates. This has been done to identify the possible solidification mode and the results are explained based on simple Scheil–Gulliver non-equilibrium solidification modeling. Further, the transformations associated with the precipitation and dissolution of secondary phases have also been discussed. The $M_{23}C_6$ type carbide dissolution has been analyzed using KJMA formalism and relevant kinetic parameters have been estimated. A detailed account of various experimental techniques including sample preparation procedures for calorimetry, X-ray diffraction and metallography investigations has already been presented in chapter 3. The results are presented in the following section.

4.2. Results

4.2.1. Structural and microstructural characterization of initial alloys

The room temperature X-ray diffraction (XRD) profiles of homogenized IFAC-1 SS and SS 304H Cu is shown in **figure 4.1(a)** and **figure 4.1(b)** respectively. As can be seen in **figure 4.1a**, the diffraction peaks for IFAC-1 confirm the presence of only *fcc* γ -austenite phase. However for SS 304H Cu, the diffraction peaks show the presence of γ -austenite, cubic $M_{23}C_6$ and MX type carbo-nitrides. At this point, the possibility of any other phase present in these alloys cannot be completely ignored based on XRD alone, since phases if present in smaller volume fractions cannot be detected using routine X-ray diffraction analysis. The relatively higher intensity of the γ -austenite phase indicates that it is the major

Investigation of Phase Stability in IFAC-1 and SS 304H Cu Stainless Steels

4.1. Introduction

It is well-known that the selection of materials and the associated manufacturing technology depends to a large extent on the availability of reliable and critically assessed thermal, physical and mechanical property data [201]. This requirement is of paramount importance in the case of advanced materials used for high temperature, high pressure and high neutron flux applications in modern fossil fuel and nuclear power sectors [8-10, 14-19, 95]. Appropriate combination of strength coupled to good ductility, oxidation resistance and fabrication capability in terms of standard and advanced manufacturing processes are the desired attributes of advanced engineering materials. The realization of such a desirable combination of properties in any material depends on the ease with which the fundamental structure and microstructure can be tailored by suitable alloying additions and thermomechanical heat treatments [202]. Stated in an alternate fashion, the basic structure and microstructure stability of a material in response to an external stimulus decides the suitability of that material as a potential candidate for the concerned application. Since IFAC-1 and SS 304H Cu have been developed on specific mission mode for tailor made applications, it is necessary to generate a comprehensive knowledgebase on basic physical metallurgy aspects that are concerned with high temperature phase stability. It may be mentioned that SS 304H Cu steel is precipitation strengthened by the addition of small amounts of Cu and Nb, which are dispersed in the γ -austenite matrix [51, 160, 203]. On the other hand, the presence of 2.5 wt. % Ti in IFAC-1 austenitic stainless steel, serves to bind carbon by forming again nano-sized TiC particles which are essential for providing enhanced

Chapter 4

Investigation of Phase Stability in IFAC-1 and SS 304H Cu Stainless Steels

5.6. Conclusion

- I. The high temperature thermophysical properties have been measured for indigenously developed IFAC-1 SS and SS 304H Cu. A comprehensive database has been established for these two materials. Tabulation of values for select temperatures and analytical fit expressions in the temperature range, 298-1273 K are provided
- II. The measured thermophysical properties are compared with available experimental data on similar 300-grade austenitic stainless steels. It is found that data generated in this study compare well; and are certainly in expected order for typical 300-grade austenitic stainless steels
- III. The Debye-Grüneisen quasi-harmonic modelling of heat capacity and thermal expansion have been carried out in the temperature range, 0-1273 K. The model with suitably evaluated model parameters successfully reproduced the observed trend in thermal property data.
- IV. The thermophysical properties of IFAC-1 is found to vary smoothly with temperature, as the steel is a single phase alloy with no transformations involved in the investigated temperature domain. The thermophysical and elastic properties of SS 304H Cu is found to change significantly due to the Cu precipitation.

5.5. Discussion

Austenitic stainless steels as a class of engineering materials have diverse applications. In general, they are known for good high temperature creep and oxidation resistance, and further are known to be amenable to property tailoring by careful compositional control [20, 41]. In literature, the high temperature thermo-physical properties of a wide variety of austenitic stainless steels have been discussed and reliable recommendations have also been made for various thermo-physical properties [54-56]. The present alloys are developed indigenously and as of now there is no existing database on thermophysical properties of these alloys. In this regard a comprehensive database on high temperature thermophysical properties has been established for these alloys through this study. The experimental measurement results show that the heat capacity, the coefficient of linear thermal expansion and thermal conductivity of IFAC-1 SS are similar to the values obtained for other 300 grade austenitic stainless steels. However in case of SS 304H Cu, the heat capacity is slightly lower and the linear thermal expansion is found to be higher above 850 K, as compared to the reported values on 300 grade austenitic stainless steels. Similarly the thermal conductivity for SS 304H Cu is also found to be significantly lower above 850 K. The abnormality observed above 850 K in this alloy is due to the dissolution of second phase Cu rich precipitates. IFAC-1 on the other hand does not undergo any phase transformations in the experimental temperature domain and hence the thermophysical properties indicate a smooth variation with temperature.

The present investigation of elastic properties indicates that both alloys have excellent room temperature strength. With increase in temperature, the modulus softens gradually, which turns out to be nearly 50% of the room temperature value at 1273 K in both alloys. Again, in case of SS 304 H Cu, the Cu precipitation contributes significantly to the high temperature elastic modulus.

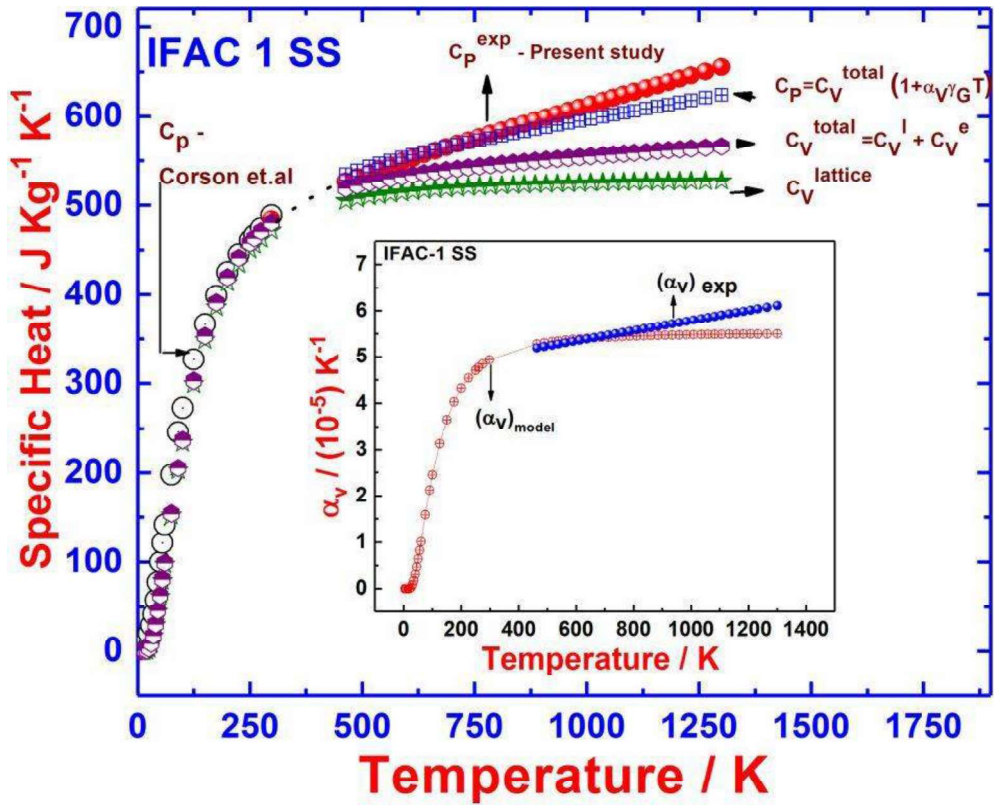


Fig. 5.16. The Debye-Grüneisen model C_p values obtained for IFAC-1 SS are co-plotted with the experimental low temperature data for SS 316 by Corson et al. The measured and model estimated volume thermal expansivity is also shown as an inset to the figure

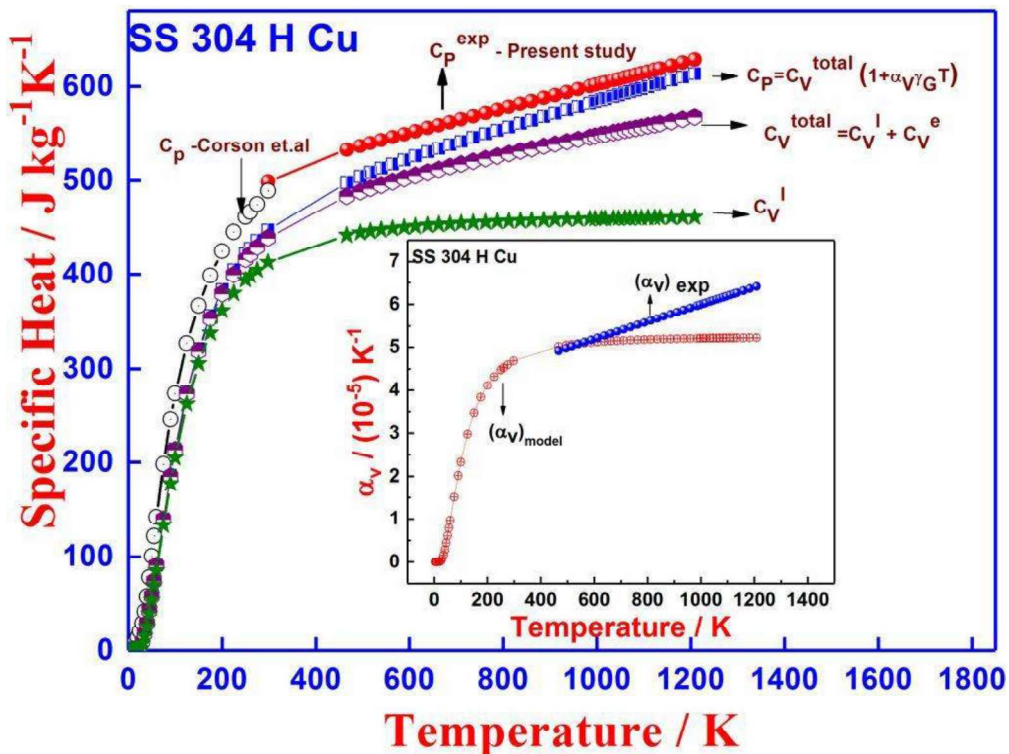


Fig. 5.17. The Debye-Grüneisen model C_p values obtained for SS 304H Cu are co-plotted with the experimental low temperature data for SS 316 by Corson et al. The measured and model estimated volume thermal expansivity is shown as an inset to the figure

Once the total isochoric specific heat (C_V) and the coefficient of thermal expansion are evaluated, the volume thermal expansion (α_V) and the isobaric specific heat (C_P) can be evaluated from the following equation

$$\alpha_V = \frac{\partial V_T}{\partial T} \cong \frac{1}{V_T} \left(\frac{\gamma_0}{B_0} \right) C_V \quad (5.21)$$

$$C_P = C_V (1 + \alpha_V \gamma_G T) \quad (5.22)$$

Figure 5.16 illustrates the individual C_V contributions calculated using Debye-Grüneisen model along with the measured experimental data for IFAC-1 SS. The measured low temperature C_p data for SS 316 [232] has also been co plotted for comparison. The measured and estimated values of volume thermal expansivity are shown as an inset to the same figure in the temperature range 0 K to 1273 K. The measured and model estimated heat capacity for SS 304H Cu is shown in **figure 5.17** where the volume thermal expansivity is again shown as an inset. The model values agree well with the low temperature C_p data of SS 316 for both the steels. However, at high temperature the model predicts slightly lower C_p and this is attributed to the neglect of higher order anharmonicity. However, it is interesting to point out that the deviation of the measured values from the model prediction is relatively higher in case of SS 304H Cu compared to IFAC-1 SS. This deviation is ascribed to the minor contribution arising from the dissolution of second phase particles in case of SS 304H Cu which has not been incorporated in the model. Notwithstanding such limitations, the Debye-Grüneisen scheme presents a reasonable approximation of high temperature thermal property data in a consistent fashion. The model based C_p and α_V values for IFAC-1 SS at $T=298$ K are $484 \text{ J Kg}^{-1} \text{ K}^{-1}$ and $4.93 \times 10^{-5} \text{ K}^{-1}$ respectively. The corresponding values for SS 304H Cu at 298 K are $447 \text{ J Kg}^{-1} \text{ K}^{-1}$ and $4.99 \times 10^{-5} \text{ K}^{-1}$.

In the above equations T is the absolute temperature in Kelvin, p is a constant representing the number of atoms per formula unit of the solid, R is the gas constant and θ is the characteristic temperature. In the case of steel, which contain small amount of dissolved interstitial carbon atoms (0.042 mass %), the value of p exceeds unity by a small amount [236]. In the present estimation, the p value has been chosen to be 1.05 [59]. It must be mentioned here that in evaluating C_v , the characteristic temperature θ is considered as a function of temperature through the following relation.

$$\theta_T = \theta_0 \left(\frac{V_T}{V_0} \right)^{-\gamma_G} \quad (5.20)$$

Where θ_0 stands for the 0 K value and γ_G represents the vibrational Grüneisen parameter. The idea of using a temperature dependent θ is to incorporate the role of lattice anharmonicity in its quasiharmonic approximation [60, 62]. The parameters used in the above equations for the estimation of heat capacity and thermal expansion are listed in **table 5.7**.

Table 5.7

List of input parameters used in Debye–Grüneisen model of thermal properties

Input parameters	IFAC-1	SS 304H Cu
Molecular weight (gram mol ⁻¹)	56.89	55.96
Zero Kelvin Debye temperature	454	470
Zero Kelvin Grüneisen parameter	1.69	1.63
Cp at 298.15 K (J kg ⁻¹ K ⁻¹)	484.4	498.4
Γ_e -the electronic specific heat coefficient (J kg ⁻¹ K ⁻²)	0.464	0.464
Specific volume (m ³ kg ⁻¹)	1.244E-4	1.247E-4
Zero Kelvin adiabatic bulk modulus (GPa)	162	165
Molar volume (m ³)	7.154×10 ⁻⁶	6.972×10 ⁻⁶

5.4.3. Estimation of heat capacity and thermal expansivity

The total isochoric specific heat (C_V) which is taken as the sum of the electronic (C_V^e) and lattice (C_V^l) contributions is expressed by:

$$C_V = C_V^l + C_V^e \quad (5.17)$$

The electronic contribution is a linear function of temperature and is given by relation $C_V^e = \Gamma_e T$, where Γ_e is the electronic coefficient of specific heat, estimated usually from (very) low temperature C_p data [232, 234]. Since, at present, no data is available for the low temperature specific heat of the present steels, the Γ_e value of $0.464 \text{ J Kg}^{-1} \text{ K}^{-2}$ for SS316 is assumed [232]. The lattice contribution to heat capacity is estimated from the internal energy (U_T) which is generally obtained using Debye approximation. However, Debye model does not offer the facility of a single analytical expression for evaluating U_T in the entire temperature range (0–298.15 K). Therefore the better choice is to use Nernst–Lindemann’s analytical approximation (interpolation function) for representing the temperature variation of U_T in this range [59, 235]. This interpolation formula approximates well the Debye model of representing the internal energy as a continuous, analytic and differentiable expression of temperature [235]. The Nernst–Lindemann formulation has been successfully used in modelling the temperature and pressure dependence of thermal and elastic quantities of many minerals and ionic solids [235]. Without going further into details, the governing expression for U_T is given as [59, 235].

$$U_T = \frac{3}{4} pR\theta \left\{ \left[\frac{2}{e^{\theta/T} - 1} \right] + \left[\frac{1}{e^{\theta/T} - 1} \right] \right\} \quad (5.18)$$

$$C_V^l = \left(\frac{\partial U_T}{\partial T} \right)_p = \frac{3}{4} pR\theta \left(\frac{\theta^2}{T^2} \right) \left\{ \left[\frac{2e^{\theta/T}}{(e^{\theta/T} - 1)^2} \right] + \left[\frac{e^{\theta/2T}}{2(e^{\theta/2T} - 1)^2} \right] \right\} \quad (5.19)$$

$$\int dV = V_T - V_0 = \left(\frac{\gamma_G}{B_T} \right) \int C_V dT = \left(\frac{\gamma_G}{B_T} \right) (U_T - U_0) \quad (5.15)$$

Now Eq. (5.15) can be written as:

$$V_T = V_0 + \left(\left(\frac{\gamma_0}{B_0} \right) U_T \right) \quad (5.16)$$

Where U_T is the internal energy of the system and K_0 , γ_0 are the 0 K bulk modulus and Grüneisen parameter respectively. It is important to note from Eq. (5.16) that the constant ($\epsilon = \gamma_0/K_0$) can be estimated from the slope of the plot V_T vs ΔH .

It is an established fact in thermophysical literature that γ_g is basically a weakly temperature dependent parameter for many condensed phases and that in practical calculations the γ_g can be considered as a constant above the Debye characteristic temperature (θ_D) [60]. However, γ_g in the present study is allowed to vary with volume, which for complicated solids like stainless steels is rather difficult to estimate reliably. Nevertheless, the reasonable temperature independence of a composite quantity such as (γ_G/K_s) can be taken to compensate this gap partially as this approximation offers a simple and useful means of incorporating the volume (temperature) dependence of vibrational anharmonicity into practical calculations [233]. The *implicit* temperature dependence of specific volume and enthalpy measured in the present study is shown in **figure 5.15**. From **figure 5.15**, the slope of the plot ($\epsilon = \gamma_0/B_0$) is estimated as: $1.31 \times 10^{-11} \text{ m}^3 \text{ J}^{-1}$ and $1.43 \times 10^{-11} \text{ m}^3 \text{ J}^{-1}$ for IFAC-1 SS and SS 304H Cu respectively. The values of γ_0/B_0 are used to incorporate the vibrational anharmonicity for the estimation of thermal expansion and the heat capacity for the present alloys.

Cu. The γ_G values obtained in the present study are also found to be similar to the reported values for a 15Cr-15 Ni austenitic stainless steel [58].

5.4.2. Correlation of molar volume and enthalpy

The effect of change in volume of a solid on the vibrational properties is generally described by introducing the Grüneisen parameter (γ_g). As a consequence, the effect of

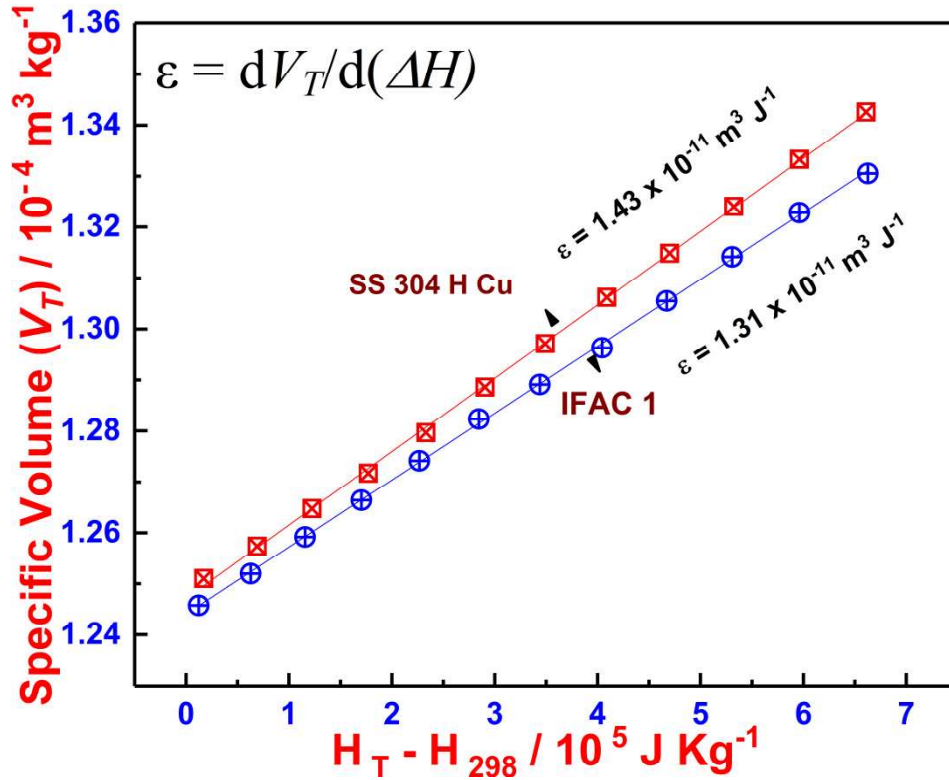


Fig. 5.15. Linear correlation between enthalpy increment and specific volume for IFAC-1 SS and SS 304H Cu

temperature on the lattice dynamics can be described by the parameter γ_g which characterizes the vibrational anharmonicity in the solid [60-62]. From the definition, Grüneisen parameter (γ_g) is generally expressed by the Eq. (5.13). Regrouping the terms in Eq. (5.13) one can obtain:

$$\alpha_V V_T = \left(\frac{\partial V}{\partial T} \right)_p = \frac{\gamma_G C_V}{B_T} \quad (5.14)$$

By integrating the Eq. (5.14) at constant pressure, one can obtain:

In the above relation, h is the Planck's constant; K_B is the Boltzmann constant; N_A is the Avogadro number; V_m is the molar volume; and C_m is the averaged sound velocity, which assuming polycrystalline elastic isotropy, is given by the relation [62, 63].

$$\frac{3}{C_m^3} = \frac{1}{C_l^3} + \frac{2}{C_t^3} \quad (5.10)$$

Here, C_l and C_t stand for acoustic velocities of longitudinal and transverse components respectively. These can be estimated from the values of polycrystalline elastic constants in the following manner [62, 63].

$$C_l = \left(\frac{K + \frac{4}{3}G}{\rho} \right)^{\frac{1}{2}} \quad (5.11)$$

$$C_t = \left(\frac{G}{\rho} \right)^{\frac{1}{2}} \quad (5.12)$$

The room temperature values of molar volume (V_m^{298}), density (ρ_{298}), elastic moduli (E , G , K) observed for the present steels are listed down in **table 5.7**. Using these measured values of parameters, the following estimates of $\theta_D = 454$ K for IFAC-1 and 470 K for SS 304H Cu is obtained for $T=298$ K, which is reasonably close to the reported value of $\theta_D=463$ K for 300 grade austenitic stainless steels [232]. The Grüneisen parameter, γ_G can be obtained using experimental data on volume thermal expansion coefficient α_v , heat capacity C_p , specific volume V_T , and adiabatic bulk modulus, K_s . [62]

$$\gamma_G = \frac{V_T K_s \alpha_v}{C_p} = \frac{V_T K_T \alpha_v}{C_v} \quad (5.13)$$

Here K_T and C_v stand for the isothermal bulk modulus and the isochoric heat capacity respectively. Using the measured data for α_v , C_p , V_T and K_s from the present study, the estimated room temperature γ_G values are found to be *1.89 for IFAC-1* and *1.63 for SS 304H*

5.4. Integrated modelling of thermophysical properties by Debye-Grüneisen formalism

Although austenitic stainless steels are mostly used for high temperature applications, they are also known for their suitability in cryogenic applications [228]. For both IFAC-1 SS and SS 304H Cu, there exist no low temperature thermophysical property data in open literature. Therefore to arrive at a comprehensive description of thermal properties right from zero Kelvin to high temperature, a suitable robust modelling approach, with minimal input data has been adopted. In this context, it must be mentioned that stainless steels are complex systems to model on rigorous first-principles basis, although some attempts have been made in the recent past in this direction [229]. The simultaneous presence of substitutional and interstitial disorder in addition to precipitated carbide or other intermetallic phases, make the *ab initio* theoretical study of phase stability and thermophysical properties of steels a difficult task. Nevertheless, it is possible to carry out an integrated modelling cum assessment of thermal properties of complex alloys on a phenomenological basis, such as Debye-Grüneisen quasiharmonic formalism, which does not invoke the microscopic description of bonding forces and their susceptibility to the influence of external variables like temperature, pressure and alloying additions [60-62]. In the present study an integrated phenomenological Debye-Grüneisen approach has been adopted to model temperature dependent heat capacity and thermal expansivity [59, 230-231].

5.4.1. Estimation of elastic Debye temperature and Grüneisen parameter

It is well known that knowledge of elastic quantities readily enables an approximate determination of the Debye temperature, θ_D through the following relation [62].

$$\theta_D = \left(\frac{h}{K_B} \right) \times \left(\frac{3N_A}{4\pi V_m} \right)^{1/3} \times C_m \quad (5.9)$$

It must be mentioned here that, there exists very few literature data for the high temperature elastic property of the austenitic stainless steels from room temperature up to 1273 K. The room temperature values of E and G for 304 SS reported by H. Ledbetter ($E=200$ GPa, $G=80$ GPa) match reasonably well with the measured values in the present study [65]. The E and G values of SS 304 and SS 316 reported by British stainless steel association [227] are plotted in **figure 5.14** along with the measured values of E and G for IFAC-1 and SS 304H Cu. It can be observed from **figure 5.14** that the temperature variation of elastic moduli for the steels in the present study follow similar trend to that of SS 304 and SS 316. Nevertheless the softening of these advanced austenitic stainless steels (IFAC-1 and SS 304H Cu) is relatively less than that of SS 304 and SS 316 at high temperatures.

Table 5.6

Fit parameters obtained from nonlinear least square fitting of the temperature variation of elastic modulus data to *Eq. (5.8)*.

Fit Parameters	IFAC-1			SS 304 H Cu		
	E /GPa	G /GPa	K /GPa	E /GPa	G /GPa	K /GPa
A (GPa)	224.88 ± 1.6	95 ± 0	178 ± 1.7	254.94 ± 1	102.73 ± 0.59	165.52 ± 1.97
B (GPa K^{-1})	-0.091 ± 0	-0.072 ± 0.001	-0.07 ± 0.003	-0.194 ± 0.004	-0.082 ± 0.002	-0.112 ± 0.009
C (GPa K^{-2})	1.8×10^{-5} $\pm 0.01 \times 10^{-5}$	5.7×10^{-5} $\pm 0.3 \times 10^{-5}$	9.2×10^{-6} $\pm 6.2 \times 10^{-6}$	1.5×10^{-4} $\pm 0.1 \times 10^{-4}$	5.8×10^{-5} $\pm 0.4 \times 10^{-5}$	1.8×10^{-4} $\pm 0.12 \times 10^{-4}$
D (GPa K^{-3})	5.54×10^{-9} $\pm 0.03 \times 10^{-9}$	-2.35×10^{-8} $\pm 0.2 \times 10^{-8}$	1.76×10^{-9} $\pm 0.4 \times 10^{-9}$	-6.5×10^{-8} $\pm 0.3 \times 10^{-8}$	-2.3×10^{-8} $\pm 0.2 \times 10^{-8}$	-1×10^{-7} $\pm 0.01 \times 10^{-7}$
R^2 (fit)	0.99	0.99	0.95	0.99	0.99	0.98

In order to describe analytically the temperature dependence of E , G and K in the temperature domain $298 \leq T \leq 1273$ K, the estimated elastic moduli values are fit to the following equation.

$$E, G, K / GPa = A + BT + CT^2 + DT^3 \quad (5.8)$$

The fit parameters A , B , C , D obtained for E , G , and K are listed in **table 5.6** for both IFAC-1 and SS 304H Cu. As stated earlier, the variation of μ with temperature is dependent on relative changes in both E and G . Therefore the relative softening in E and G for an alloy can be observed qualitatively from the parameter $(d\mu /dT)$. This parameter is evaluated using linear fitting the μ vs T data and found to be $\sim d\mu /dT = -1.33 \times 10^{-6} \text{ K}^{-1}$ for IFAC-1 SS and 6.77×10^{-5} for SS 304H Cu. This abnormality in the temperature dependence of μ requires further investigation.

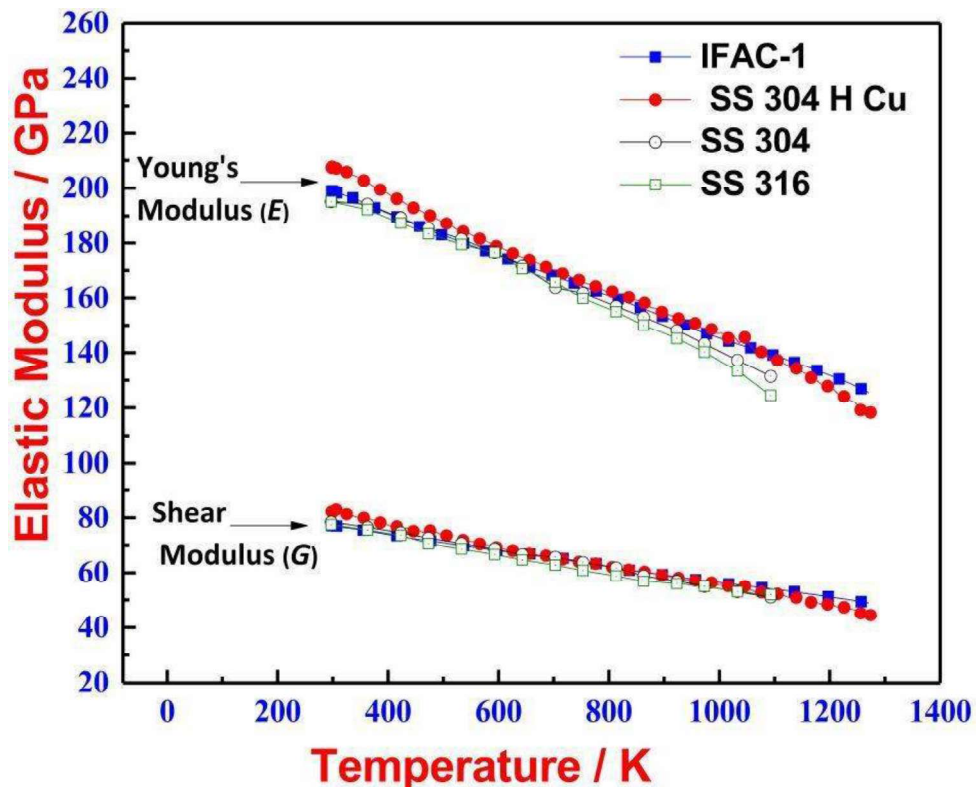


Fig. 5.14. Young's modulus and Shear modulus for IFAC-1 and SS 304H Cu obtained in the present study are compared with literature data on other related austenitic stainless steel

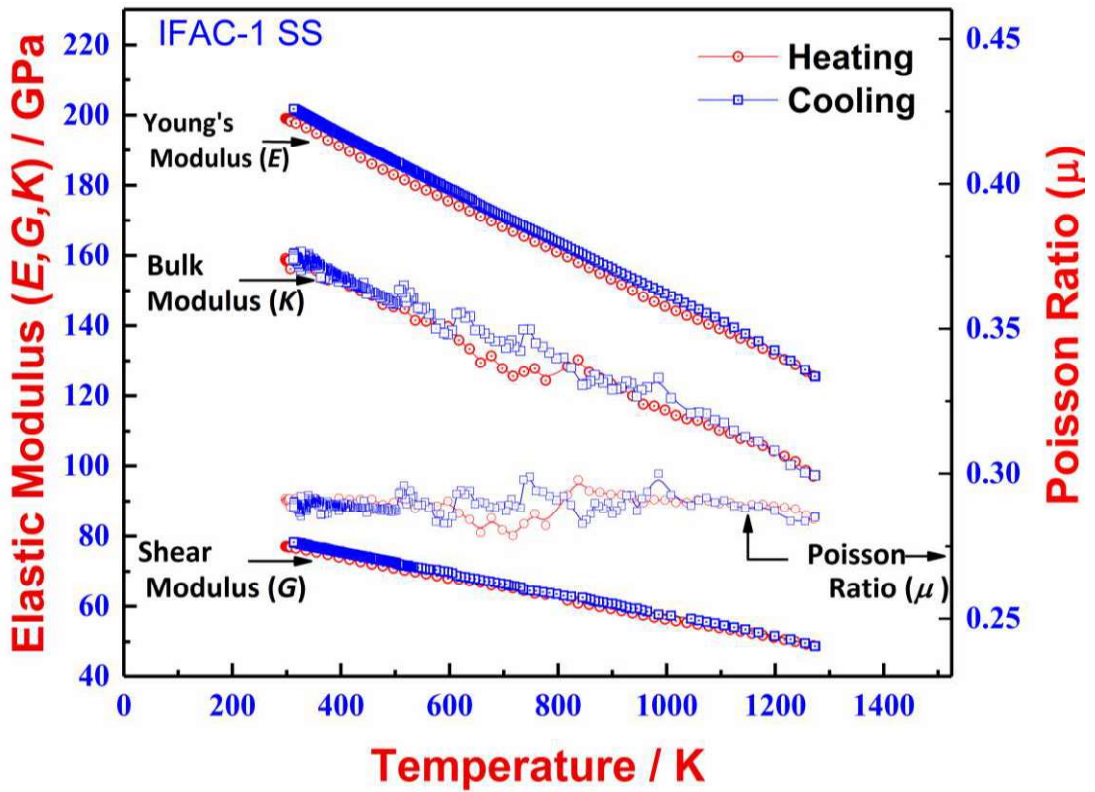


Fig. 5.12. Temperature variation of measured Young's modulus (E), Shear Modulus (G), Bulk Modulus (K) and Poisson's ratio (μ) for IFAC-1 SS

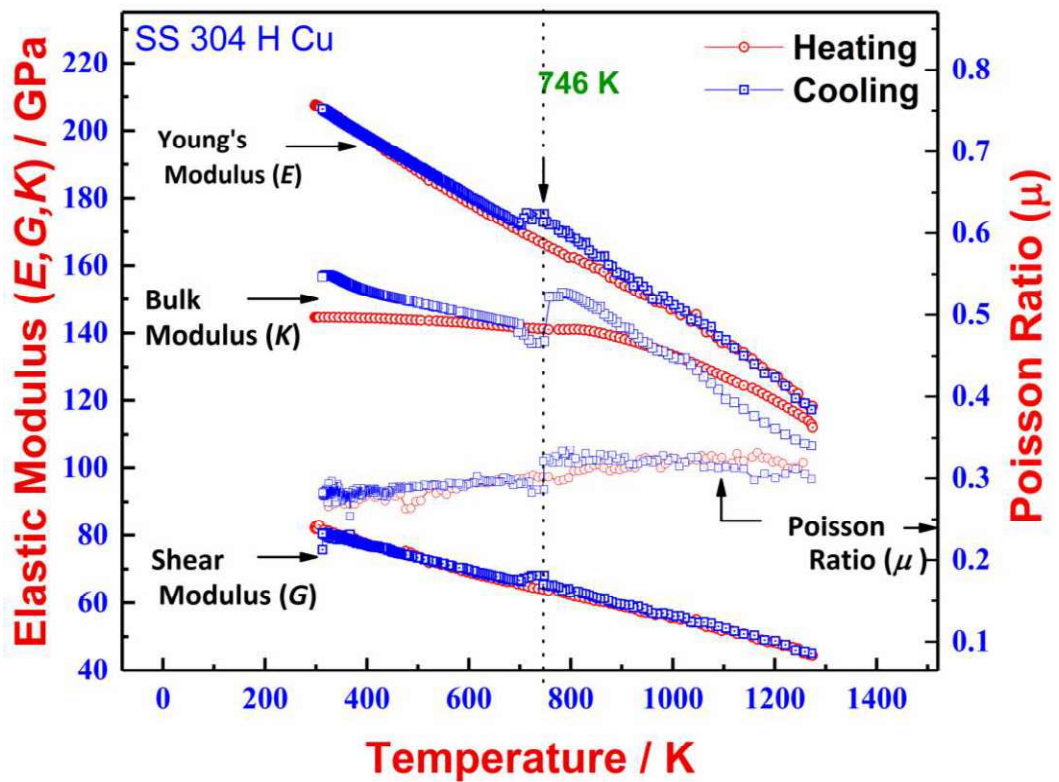


Fig. 5.13. Temperature variation of measured Young's modulus (E), Shear Modulus (G), Bulk Modulus (K) and Poisson's ratio (μ) for SS 304H Cu

the Poisson ratio (μ) are evaluated using standard relations expressed in *Eq. (3.20)* and *Eq. (3.21)* (chapter 3).

Figure 5.10 and **figure 5.11** depict the temperature variation of measured resonant frequency in both flexure and torsion mode for IFAC-1 and SS 304H Cu respectively. It is evident that the variations of resonant frequency in both flexure and torsion modes exhibit qualitatively similar temperature dependence for both heating and cooling cycles in the two steels studied here. The temperature variation of resonant frequency for flexure and torsion modes in IFAC-1 does not show any abnormal change in the temperature range of 298-1273 K. This is expected as the alloy does not undergo any phase transformation in this temperature domain and the elastic softening of the material with increase in temperature is due to thermal expansion effects associated with austenite phase. However, in the case of SS 304H Cu, the resonant frequency for both modes shows a minor inflection at 746 K in cooling cycle, although no abnormality was observed in the heating cycle. The values of elastic (E), shear (G), bulk moduli (K) and Poisson ratio (μ) values for IFAC-1 estimated from flexural and torsional frequencies, using *Eq. (5.9)-(5.15)* are shown in **figure 5.12**. The corresponding values for SS 304H Cu are shown in **figure 5.13**.

It emerges from **figure 5.12** and **figure 5.13**, that elastic moduli E , G and K exhibit a decrease with increasing temperature. It is interesting to note that in case of SS 304H Cu clear inflections are observed at 746 K, in E , G and K moduli (**figure 5.14**). Recalling the results obtained using dynamic calorimetry (*chapter 4*), it is clear that precipitation of Cu rich particles occurs in this alloy in the temperature interval 962-750 K (689-477 °C). The small step in E , G , K and μ in the same temperature range, in which Cu precipitation is found upon continued cooling also supports this observation.

(Eq. (3.15) and Eq. (3.16), chapter 3) [194-196]. In a similar manner, the shear modulus G is estimated from the fundamental torsional frequency f_{tor} using the Eq. (3.17) to Eq. (3.19) (chapter 3). [194-196]. Once the values of E and G are evaluated the bulk modulus (K) and

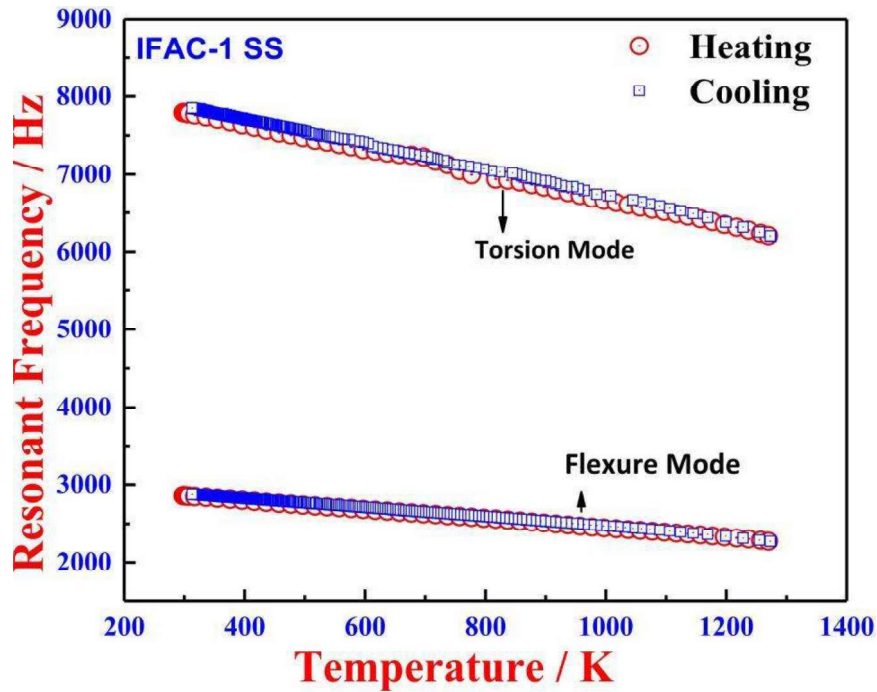


Fig. 5.10. Variation of flexural and torsion mode frequency with temperature for IFAC-1 SS

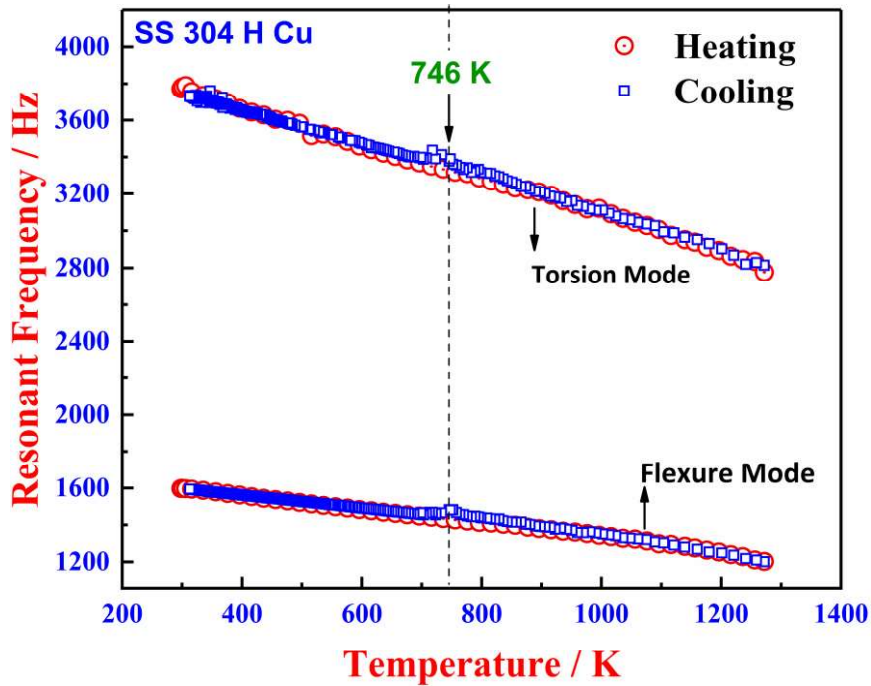


Fig. 5.11. Variation of flexural and torsion mode frequency with temperature for SS 304H Cu

treatments [39, 68]. Further, the composition and distribution of secondary phases also depend strongly on the thermo-mechanical treatments [226].

Therefore the temperature and thermal history play a vital role in thermal conductivity in steels. As observed from the DSC results in Chapter 4, IFAC-1 does not undergo any thermal event in the 298-1273 K temperature domain. Therefore there is no significant contribution from any phase other than the parent γ -austenite. Therefore the thermal conductivity is by and large a monotonically increasing function of temperature. However, in case of SS 304H Cu, the addition of Cu (2.95 wt.%) and Nb (0.58 wt.%) results in second phase precipitates, such as MX, $M_{23}C_6$ and Cu. The presence of these second phases in γ -austenite matrix acts as disturbances in lattice periodicity and influence the total thermal conductivity in a manner that varies depending on the volume fraction and morphology of phases, while it is difficult to quantify their effects. The estimated values of thermal conductivity for SS 304H Cu are similar to values reported by Kim for SS 316L and SS 304 L up to 873 K (see, **figure 5.9**) [55]. The measured values of thermal diffusivity and the thermal conductivity are presented in **table 5.5**.

5.3.4. Measurement of dynamic elastic moduli

The resonant vibrational frequencies corresponding to flexure and torsion modes have been measured using *IET* and *RFDA* software for both IFAC-1 and SS 304H Cu. The measurement was carried out during both heating and cooling cycles. Heating is done at the rate of 7 K per minute, while natural furnace cooling (forced cooling would rupture the ceramic support) is adopted for all experiments. The experimental frequency spectrum measured is Fourier transformed and compared against a simulated one, using the proprietary RFDA software from which the frequencies corresponding to flexure mode (f_{flx}) and torsion mode (f_{tor}) is determined [193]. The Young's modulus, $E(T)$ at the measurement temperature T , is estimated from f_{flx} by the analytical relation that is valid for a rectangular bar specimen

although the thermal conductivity of IFAC-1 reveals reasonable agreement with values reported for 300 grade austenitic steels in the current experimental temperature domain, the values for SS 304H Cu show a substantial drop in the conductivity for temperatures above 873 K. It is a well-known fact that in metallic systems the thermal conductivity is determined from both electron and phonon contributions. Therefore the thermal conductivity in such systems is dependent on electron-phonon interactions. In case of alloys, the lattice distortions created by alloying elements and precipitate phases also act as scattering centers for electrons and phonons and hence play a major role in deciding the transport properties. In steels, different microstructures can be attained for the same composition by adopting different heat

Table 5.5

Measured thermal diffusivity and estimated thermal conductivity data for IFAC-1 and SS 304H Cu are tabulated for different temperatures

IFAC-1			SS 304H Cu		
Temperature (K)	Thermal diffusivity ($10^{-6} \text{ m}^2 \text{ s}^{-1}$)	Thermal conductivity ($\text{W m}^{-1} \text{ K}^{-1}$)	Temperature (K)	Thermal diffusivity ($10^{-6} \text{ m}^2 \text{ s}^{-1}$)	Thermal conductivity ($\text{W m}^{-1} \text{ K}^{-1}$)
293	3.23	13.55	293	3.45	13.78
323	3.34	13.98	323	3.55	14.33
368	3.47	15.02	373	3.71	15.18
423	3.56	16.13	423	3.83	15.92
473	3.65	17.02	473	3.98	16.74
523	3.72	17.58	523	4.12	17.53
573	3.81	18.44	573	4.22	18.20
623	3.89	19.42	623	4.37	19.05
673	3.95	20.07	673	4.47	19.72
723	4.01	20.91	723	4.57	20.36
773	4.08	21.79	773	4.66	21.01
823	4.14	22.60	823	4.73	21.57
873	4.19	22.92	873	4.80	22.10
923	4.25	23.90	923	4.85	22.57
973	4.31	24.85	973	4.89	22.96
1023	4.34	25.16	1023	4.87	23.12
1073	4.41	26.37	1073	5.03	24.10
1123	4.46	26.69	1123	5.11	24.72
1173	4.51	27.91	1173	5.39	26.33
1223	4.58	28.61	1223	5.57	27.47
1273	4.66	29.34	1273	5.66	28.19

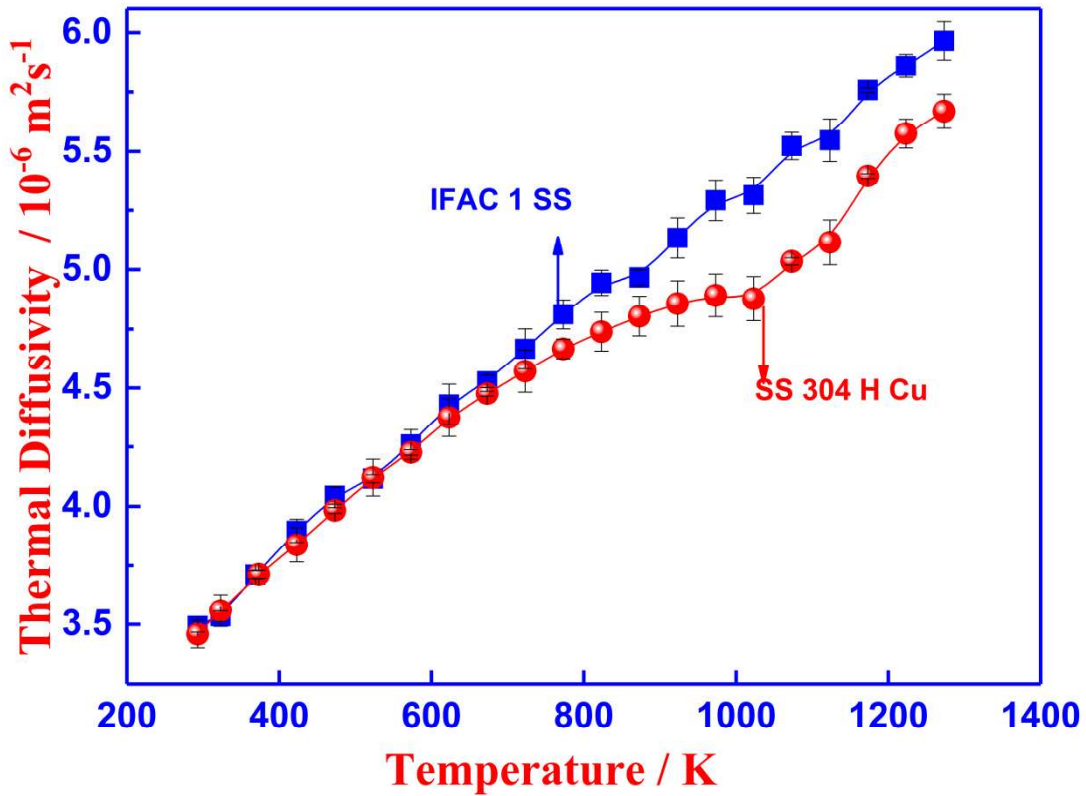


Fig. 5.8. Temperature variation of measured thermal diffusivity for IFAC-1 and SS 304 H Cu

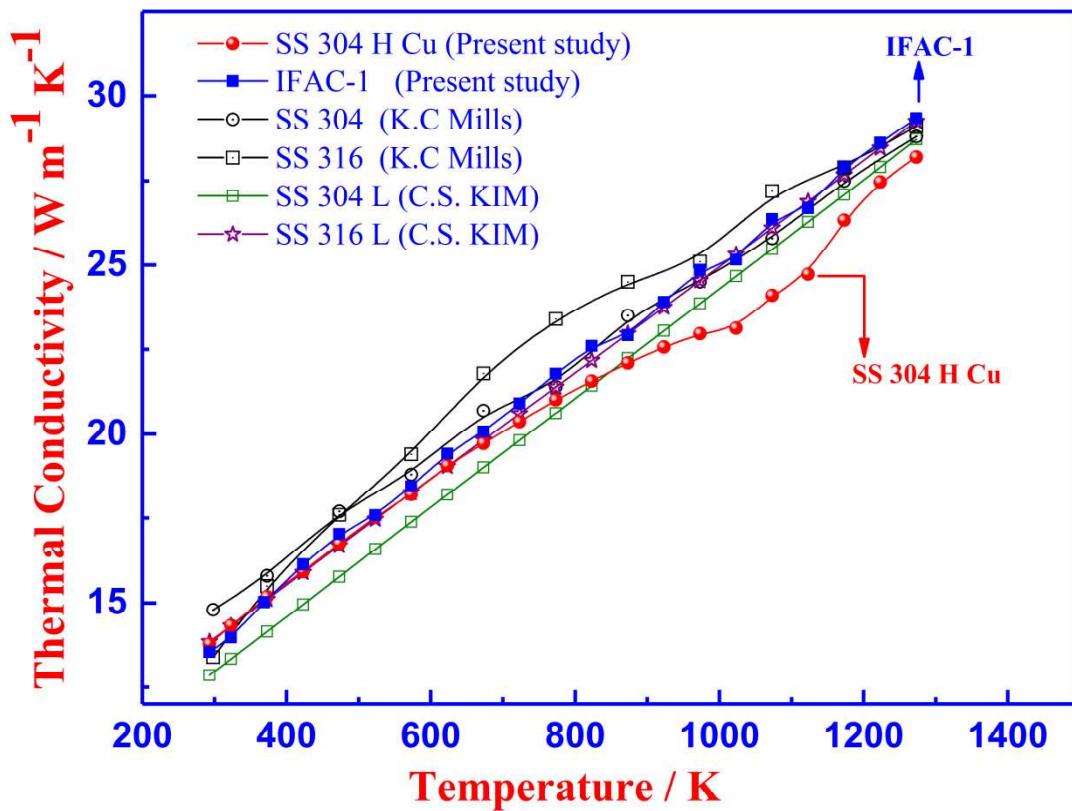


Fig. 5.9 Thermal conductivity for IFAC-1 and SS 304H Cu obtained in the present study are compared with literature data on other related austenitic stainless steels

5.3.3. Thermal diffusivity

The measured values of thermal diffusivity (λ) as a function of temperature for both IFAC-1 SS and SS 304 H Cu are graphically displayed in **figure 5.8**. The standard deviation of five compatible measurements at each temperature is depicted as the error bar in the same figure. It is evident from **figure 5.8** that thermal diffusivity increases nonlinearly with temperature for both the steels in the measured temperature regime. However in case of SS 304H Cu, a clear inflection is noticed in the 873-1123 K temperature region. Above 1123 K, λ again increases almost linearly up to 1273 K. In order to ensure this significant deviation in the measured diffusivity values in case of SS 304H Cu, the measurement was repeated for three different specimens. Similar variation of diffusivity is observed for repeated experiments.

The abnormality in the thermal diffusivity variation for SS 304H Cu in the temperature range of 873-1123 K, is clearly a manifestation due to dissolution of Cu-precipitates, as witnessed in the case of temperature dependence of enthalpy and dilatational strain. The measured diffusivity data, together with density and specific heat have been used to evaluate the bulk thermal conductivity (k) for both IFAC-1 SS and SS 304H Cu using *Eq. (5.7)*, Where K is the thermal conductivity, λ is the thermal diffusivity ρ is the density and C_p is the isobaric heat capacity.

$$K = \lambda\rho C_p \quad (5.7)$$

The temperature variation of density and specific heat estimated in the previous section is used for the evaluation of thermal conductivity using *Eq. (5.7)*. The estimated temperature variations of thermal conductivity for IFAC-1 and SS 304H Cu are portrayed in **figure 5.9** along with literature data on 300 grade austenitic stainless steels [55, 56]. It is clear that

Table 5.4

Values of enthalpy increment, specific heat, linear thermal expansion coefficient and density for SS 304H Cu are tabulated as a function of temperature.

Temperature (K)	H_T-H_{298} (exp) (J g ⁻¹)	H_T-H_{298} (fit) (J g ⁻¹)	Percentage deviation $\delta=100 \times \{\Delta H(\text{exp}) - \Delta H(\text{fit})\} / \Delta H(\text{exp})$ (%)	C_p (J kg ⁻¹ K ⁻¹)	α_l 10^{-5} K ⁻¹	ρ (Kg m ⁻³)
466	91.7	95.5	-7.4	532.53	1.69	7965
495	105.1	108.8	-4.5	536.49	1.71	7954
516	116.6	122.0	-7.0	539.46	1.73	7943
539	126.0	135.3	0.5	542.59	1.74	7932
564	142.2	148.6	-4.3	545.86	1.76	7921
589	151.7	162.3	-6.2	549.19	1.78	7909
613	176.3	175.5	-7.1	552.36	1.79	7898
639	182.1	189.9	-4.0	555.77	1.81	7886
662	191.5	203.3	-1.9	558.80	1.83	7874
686	203.0	217.5	-2.5	561.91	1.84	7862
710	222.3	231.1	-3.6	565.01	1.86	7850
736	241.3	245.8	-1.6	568.39	1.88	7837
762	252.8	259.2	0.1	571.76	1.89	7825
787	264.3	273.8	-0.7	574.94	1.91	7812
811	283.2	287.8	-2.8	578.06	1.93	7799
836	302.8	302.5	-3.7	581.24	1.94	7786
860	314.4	316.6	-4.9	584.29	1.96	7773
886	322.5	331.4	-4.7	587.59	1.98	7759
910	333.4	345.7	-2.3	590.66	1.99	7746
936	343.7	360.6	-6.0	593.86	2.01	7732
960	357.9	374.9	-3.8	596.90	2.03	7719
985	381.4	390.0	-3.0	600.09	2.04	7704
996	374.5	396.8	-2.5	601.53	2.05	7698
1008	390.3	405.0	-0.7	603.23	2.06	7690
1018	397.6	409.7	0.4	604.23	2.06	7686
1034	409.5	419.8	-2.7	606.33	2.08	7676
1046	423.9	426.7	3.4	607.76	2.08	7669
1059	436.8	435.0	1.5	609.48	2.09	7662
1070	429.8	441.4	2.2	610.81	2.10	7655
1083	465.6	450.0	1.2	612.42	2.11	7647
1094	463.6	456.5	0.5	613.91	2.11	7641
1108	475.7	465.2	1.1	615.69	2.12	7633
1123	479.8	474.1	1.2	617.52	2.13	7626
1134	483.6	481.0	-0.0	618.92	2.14	7618
1159	502.0	496.3	-7.4	622.01	2.16	7602
1182	517.4	511.1	-4.5	625.00	2.17	7588
1205	526.9	527.1	-7.0	628.22	2.19	7573

Table 5.3

Values of enthalpy increment, specific heat, linear thermal expansion coefficient and density for IFAC-1 are tabulated as a function of temperature

T (K)	$H_T - H_{298.15}$ <i>exp</i> (J g ⁻¹)	$H_T - H_{298.15}$ <i>(Fit)</i> (J g ⁻¹)	<i>Percentage deviation</i> $\delta = 100 \times \{ \Delta H(\text{exp}) - \Delta H(\text{fit}) \} / \Delta H(\text{exp})$ (%)	C_p <i>(Fit)</i> (J Kg ⁻¹ K ⁻¹)	α_l <i>(Fit)</i> 10 ⁻⁵ K ⁻¹	ρ (Kg m ⁻³)
464	75.32	84.22	-11	526.8	1.69	7966
489	90.44	97.45	-7.8	531.6	1.70	7955
516	105.0	111.9	-6.7	536.6	1.71	7944
539	117.3	124.3	-5.7	540.8	1.72	7934
563	128.9	137.3	-6.5	545.0	1.73	7924
588	138.6	151.0	-9.0	549.2	1.74	7913
613	150.5	164.8	-9.4	553.4	1.75	7902
638	162.6	178.6	-9.7	557.5	1.76	7891
663	180.4	192.6	-6.6	561.5	1.77	7880
687	197.5	206.2	-4.4	565.4	1.78	7869
712	215.2	220.3	-2.4	569.3	1.79	7858
737	227.4	234.6	-3.0	573.2	1.80	7846
761	236.1	248.4	-5.3	576.9	1.81	7835
786	250.4	262.9	-4.9	580.7	1.82	7824
811	262.4	277.5	-5.6	584.5	1.83	7812
836	276.2	292.1	-5.6	588.3	1.84	7801
860	290.7	306.3	-5.3	591.9	1.85	7789
885	310.7	321.1	-3.3	595.6	1.86	7777
910	325.2	336.1	-3.2	599.3	1.87	7766
934	347.8	350.5	-0.77	602.8	1.88	7754
959	371.8	365.6	1.7	606.5	1.89	7742
984	384.5	380.8	1.0	610.2	1.90	7730
1009	400.1	396.1	1.1	613.8	1.91	7718
1036	426.6	412.7	3.3	617.8	1.92	7704
1059	445.1	427.0	4.1	621.1	1.93	7693
1082	455.3	441.3	3.1	624.5	1.94	7682
1106	468.8	456.3	2.8	627.9	1.95	7670
1133	486.6	473.3	2.8	631.8	1.96	7656
1158	499.9	489.2	2.3	635.4	1.97	7643
1182	512.6	504.5	1.6	638.9	1.98	7631
1207	525.7	520.5	1.0	642.5	1.99	7618
1232	550.7	536.6	2.6	646.1	2.00	7605
1264	568.4	557.3	2.0	650.7	2.01	7589

steels has been calculated from the measured values of room temperature density using the expression $\rho = (nM / VN_A)$, where V and N_A represent the unit cell volume and Avogadro's number respectively and n stands for the effective number of atoms in the unit cell. In the present study $n = 4:2$ is assumed in accordance with the requirement that there is a nominal agreement between the measured and approximately estimated density from the chemical composition [59]. Estimated density data for IFAC-1 and SS 304H Cu are graphically portrayed in **figure 5.7** along with literature data on 300 grade austenitic stainless steels [55, 56]. The measured enthalpy increment, heat capacity, average thermal expansion and density values for IFAC-1 SS and SS 304H Cu are presented in **table 5.3** and **table 5.4** respectively. These are obtained using the fit expressions obtained in this study.

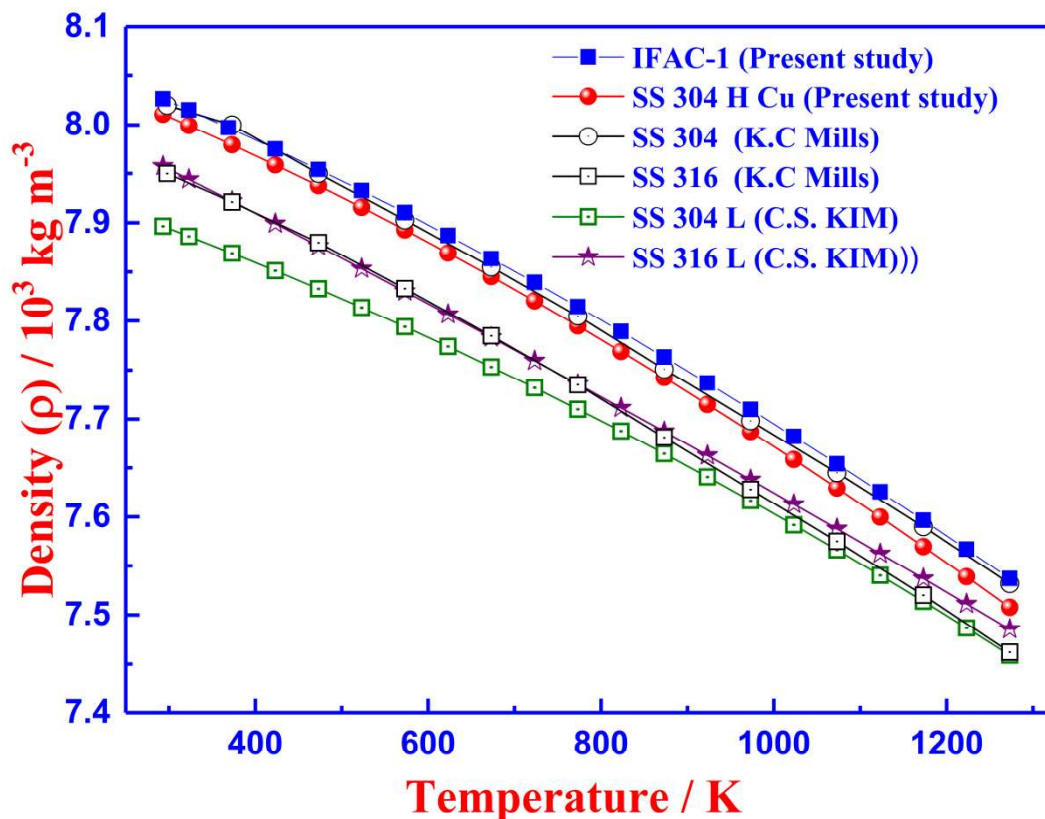


Fig. 5.7. Density versus temperature data on IFAC-1 SS and SS304 H Cu compared with literature values on related austenitic stainless steels

reported by Kim [55] for SS 304 L are found to be lower than the present value for the entire temperature regime.

The thermal expansion data obtained in this study have also been used to obtain bulk density as a function of temperature. The temperature variation of density is given as:

$$\rho(T) = \frac{M}{V_o (1 + 3\alpha_l(T - 298))} \quad (5.6)$$

Where M is the molecular weight, V_o is the molar volume at 298 K and α_l is the linear coefficient of thermal expansion. While evaluating the temperature dependence of density, the value of M and V_o for IFAC-1 are taken to be: 56.01×10^{-3} kg and 6.923×10^{-6} m³ mol⁻¹ respectively [59]. The corresponding values for SS 304H Cu were estimated to be 55.97×10^{-3} kg and 6.973×10^{-6} m³ mol⁻¹ respectively [59]. The average molecular weight (M) for the

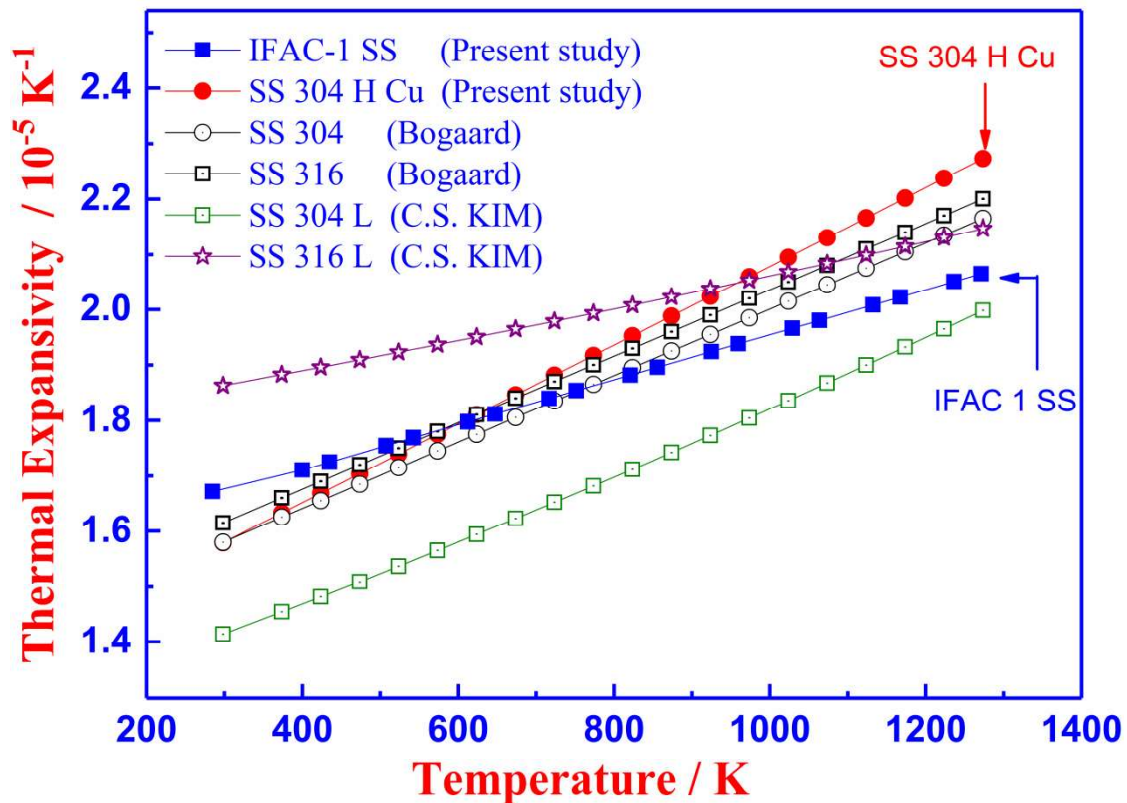


Fig. 5.6. Comparison of measured linear thermal expansion coefficients of IFAC-1 and SS 304H Cu austenitic stainless steel with literature data on 300 grade austenitic stainless steels

It is evident from **table 5.2** that the coefficient for cubic and quartic terms in *Eq.(5.3)* are indeed small and hence for all practical calculations the 3rd order temperature dependence of thermal expansion for both the steels can be ignored. Using the fit expression given in *Eq. (5.3)*, the linear thermal expansivity values have been estimated in the temperature range 373 to 1273 K. The average (α_{avg}) and instantaneous (α_{inst}) linear thermal expansion coefficients are given by *Eq. (5.4)* and *(5.5)*.

$$\alpha_{avg} = \frac{1}{l_{298}} \left(\frac{dl_T}{dT} \right) \quad (5.4)$$

$$\alpha_{inst} = \frac{1}{l_T} \left(\frac{dl_T}{dT} \right) \quad (5.5)$$

Here, l_{298} and l_T represent the length of the sample at $T=298$ K and at any temperature T respectively. The measured values of l_{298} for IFAC-1 and SS 304H Cu are 1750 and 1616.2 μm respectively. The estimated α_{avg} for IFAC-1 and SS 304H Cu are plotted as a function of temperature in **figure 5.6** along with available literature data on AISI 304, 304L, 316 and 316L grade austenitic stainless steels [54, 55]. It is observed that present experimental measurement values for the average thermal expansion of IFAC-1 are close to the reported values for SS 316 in the low temperature domain; but above 800 K, the values are found to be lower than that of SS 316. It must be mentioned that IFAC-1 is basically a low carbon austenitic stainless steel, whose composition is similar to SS 316 L, but with small additions of Ti and Si. In addition, IFAC-1 is compositionally tailored with respect to minor alloying elements like B, P and S. Therefore the thermal expansion characteristics of IFAC-1 and SS 316 are expected to be similar only on broad basis. The present experimental values of the average thermal expansion coefficient for SS 304H Cu is in good agreement with the reported data on SS 304 by Bogaard *et al* [54]. However, for temperatures above 700 K, the α_{avg} data for SS 304H Cu is systematically higher. On the other hand, the thermal expansion data

this temperature region, which marks the dissolution of Cu-precipitates; there is a perceptible oscillation in the corresponding linear thermal expansivity, which is proportional to $(d\Delta l_T/dT)$. In other words, the dissolution of precipitated Cu-particles at high temperatures influences linear thermal expansion coefficient in a subtle manner. But this feature is absent in the cooling cycle, since the time given is inadequate to precipitate Cu from supersaturated austenite matrix. Based on our earlier *ThermoCalc*[®] simulation results on temperature induced phase instabilities in SS 304HCu (see section 4.2.4), the temperature domain where the deviation is observed in the Δl_T versus temperature, matches well with the dissolution temperature of nano-sized Cu-precipitates. Nevertheless, continuous cooling at 7 K min⁻¹ does not result in appreciable Cu-precipitation for kinetic reasons. In fact, an additional isothermal aging step is needed to promote Cu-precipitation. This explains as to why a corresponding cusp is not observed in the cooling dilatometry trace. For the purpose of estimating linear thermal expansivity, the dilatometric strain recorded during heating has been fitted to a third degree polynomial in temperature increment (T-373). Here, T=373 is taken as the reference temperature.

$$l_T = l_1 + l_2(T - 373) + l_3(T - 373)^2 + l_4(T - 373)^3 \quad (5.3)$$

The values of fit parameters estimated for both IFAC-1 and SS 304H Cu by the nonlinear least square regression is listed in **table 5.2**.

Table 5.2

The fit coefficients appearing in Eq. (5.3) of measured dilatational strain as a function of temperature for IFAC-1 and SS 304H Cu.

Fit Parameters	l_1 (μm)	l_2 ($\mu\text{m K}^{-1}$)	l_3 ($\mu\text{m K}^{-2}$)	l_4 ($\mu\text{m K}^{-3}$)	R^2 (fit)
IFAC-1 SS	1750 \pm 0	0.0297 \pm 5.19 $\times 10^{-5}$	(3.55 \pm 0.07) $\times 10^{-6}$	1.07 $\times 10^{-23}$ \pm 0	0.99
SS 304H Cu	1648.1 \pm 0.07	0.026 \pm 0	(5.853 \pm 0.19) $\times 10^{-6}$	2.20 $\times 10^{-24}$ \pm 0	0.99

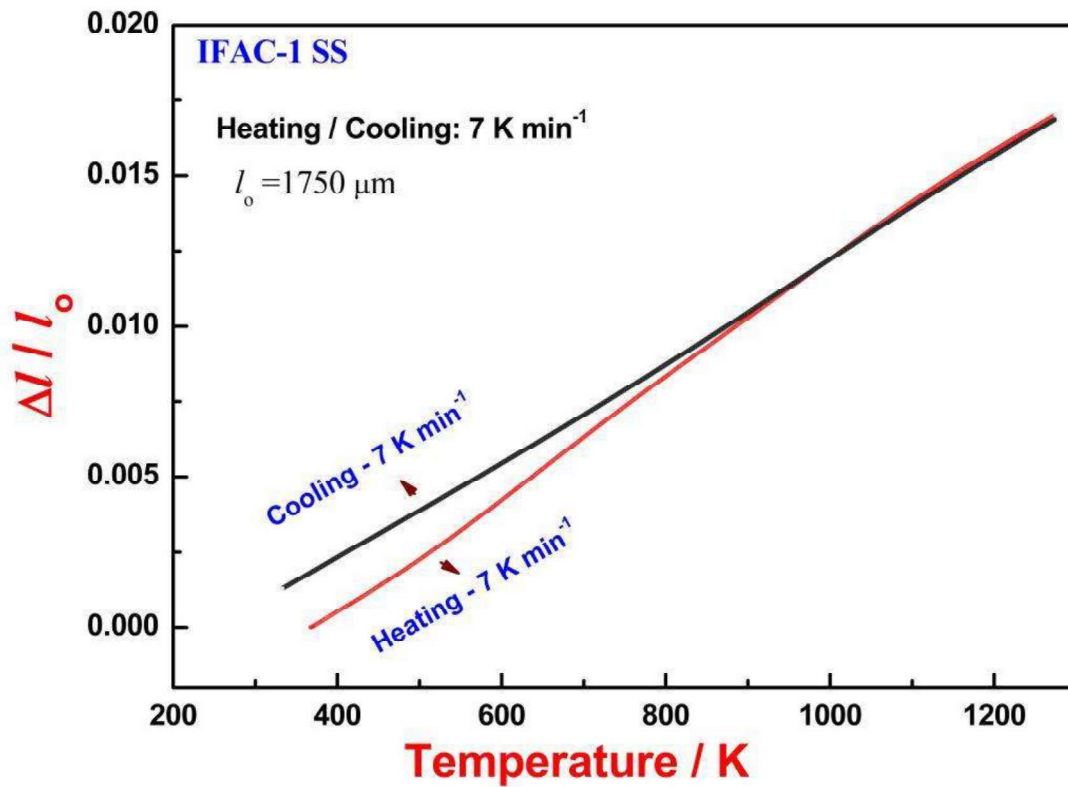


Fig. 5.4. Temperature variation of measured dilatational strain for IFAC-1SS

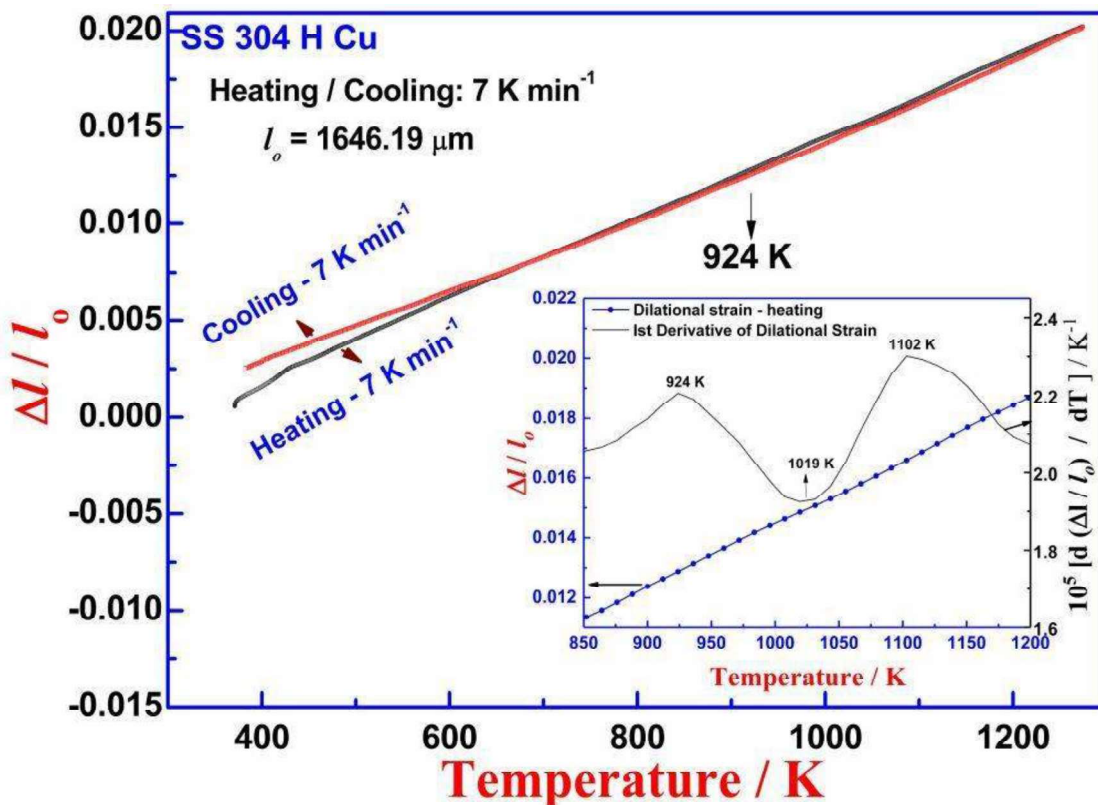


Fig. 5.5. Temperature variation of measured dilatational strain for SS 304H Cu. The inset portrays the enlarged region in the temperature domain 850-1200 K along with the temperature derivative of the dilatational strain. A subtle variation in apparent linear expansion coefficient is observed in this region.

temperatures above 800 K; while below 800 K, the measured values are higher than that of SS 316 [55]. On the other hand, the measured values of heat capacity for SS 304H Cu is similar to that of the SS 304 below about 700 K. As the temperature increases above 700 K, a consistently lower value of C_p is noticed. This discrepancy is due to difference in the chemical composition and hence the microchemistry of various precipitate phases present in these steels, although all of them fall under the 300-series of austenitic stainless steels.

5.3.2. Thermal expansion and density

The thermally induced linear dilatational strain ($\Delta l_T / l_o$) has been measured in the temperature range 373 to 1273 K at 7 K min⁻¹ heating and cooling rate. Here, l_o refers to the starting length of the sample at 298.15 K; Δl_T refers to the measured change in length as a function of temperature. Pure alpha alumina sintered pellet certified by *Setaram* has been employed as calibration standard. **Figure 5.4** and **figure 5.5** depict the experimental dilatometry trace obtained on IFAC-1 and SS 304 H Cu respectively. It is evident from **figure 5.4** that for IFAC-1 steel, the measured displacement Δl_T below 800 K differs between heating and cooling cycle. However for SS 304H Cu, it is found almost to be linear and reversible, except at low temperature region. It is also interesting to note that Δl_T in the case of SS 304H Cu exhibits a minor change of slope at 924 K, as shown by the arrowhead in **figure 5.5**. It is noteworthy that the observed deviation in Δl_T in the low temperature region, for both steels as well as the minute variation at 924 K observed during heating in SS 304H Cu has been found to be repeatable, on three different runs carried out with similar samples under identical experimental conditions. In **figure 5.5**, the first derivative of linear thermal strain ($d\Delta l_T / dT$) for SS 304H Cu material is presented as an inset in the temperature region 924 to 1102 K. Though it might appear that Δl_T varies only by a small value around

Table 5.1

Fit parameters of measured enthalpy data as a function of temperature for IFAC-1 and SS 304H Cu.

Fit Parameters	A (J gm ⁻¹)	B (J gm ⁻¹ K ⁻¹)	C (J gm ⁻¹ K ⁻²)	D (J gm ⁻¹ K)	R ² (fit)
IFAC-I	157.49±1.88	0.475±0	7.02×10 ⁻⁵ ±0	2876±0	0.98
SS 304 H Cu	-144.73 ±2.04	0.478 ±0	6.24×10 ⁻⁵ ±0	789±0	0.99

Cu and IFAC-1 respectively [54, 55]. In this sense, care has been taken to get physically meaningful value of specific heat from empirically arrived at fit function. The comparison of estimated C_p for IFAC-I and SS 304H Cu with reported values for related 300-grade steels, is made in **figure 5.3**. It emerges from **figure 5.3**, that C_p of IFAC-1 is similar to that SS316 for

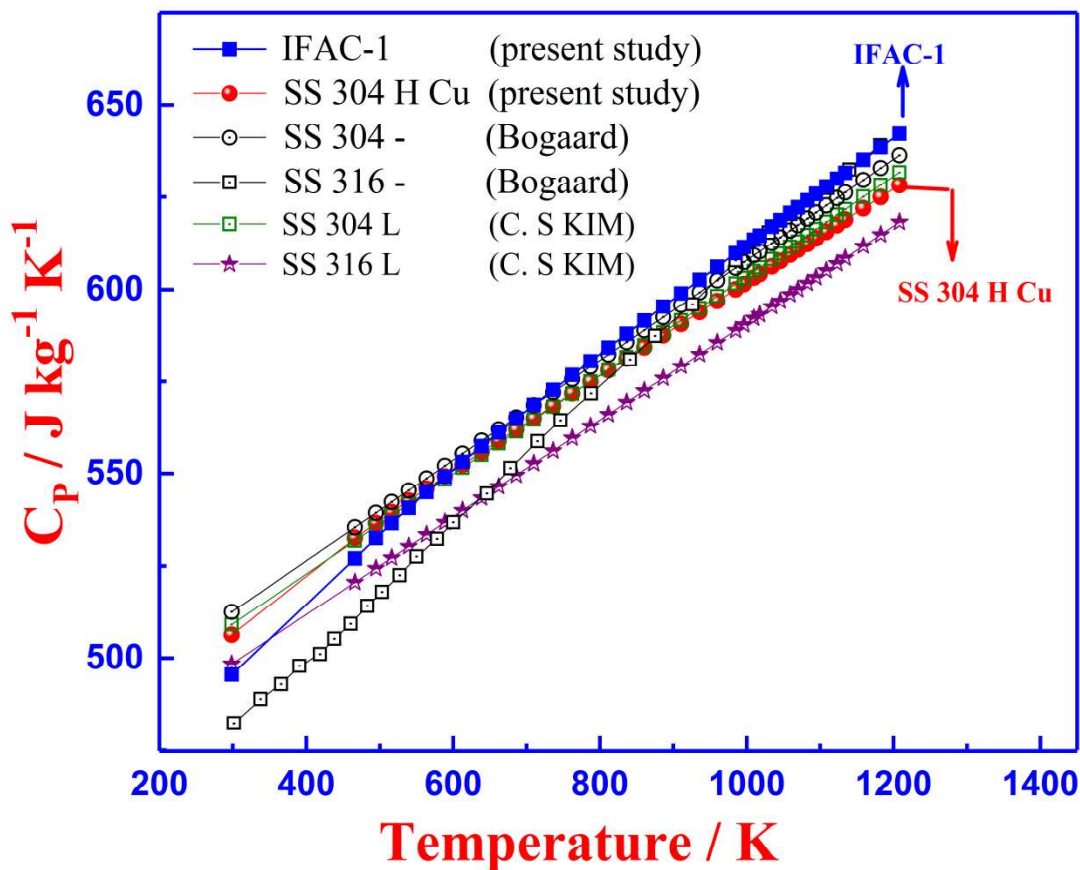


Fig. 5.3. Comparison of measured heat capacity (C_p) values of IFAC-1 and SS304H Cu with the reported data on the related 300 grade austenitic stainless steels [54, 55]

here that the intrinsic anharmonic character of the γ -austenite lattice vibrations can also contribute to enthalpy at high temperatures. But this is a minor effect in the temperature range studied here.

The measured temperature variations of enthalpy in the temperature range 298–1273 K for both IFAC-1 and SS 304 H Cu are fitted to the Maier-Kelly expression (*Eq. 5.1*), using the method of nonlinear least square regression [225].

$$H_T - H_{298} / \text{Jg}^{-1} = A + BT + CT^2 + \frac{D}{T} \quad (5.1)$$

In the above expression, T is temperature in Kelvin; H_{298} is enthalpy at 298.15 K, set equal to 0. In the present study, following standard convention, T=298.15 K is taken as the reference temperature, and H_T is given with respect to T=298.15. The boundary condition that is employed in this fit are: $H_T - H_{298} = 0$ at 298 K; further the calculated specific heat C_p at 298.15 K should agree reasonably well with the value that is typical of SS 304H Cu or related grades of austenitic stainless steels [54-56]. Since no low temperature calorimetry based C_p data are available for both IFAC-I and SS 304H Cu steels, it was not possible to obtain a precise experimental value for C_p at 298.15 K. Nevertheless, a plausible estimate is arrived at based on literature reports on similar grade austenitic stainless steels [58-59]. The fit coefficients are listed in corresponding figures and also tabulated in **table-5.1**. From *Eq. (5.1)*, the heat capacity C_p is estimated as follows.

$$C_p / \text{J Kg}^{-1} \text{K}^{-1} = \left(B + 2CT - \frac{D}{T^2} \right) 1000 \quad (5.2)$$

It is important to mention that in fitting the enthalpy data to *Eq. (5.1)*, the fit was constrained to yield nearly a similar value of room temperature heat capacity (C_p) that is reported for similar grades of austenitic stainless steels. The data of Bogaard for AISI 304; that of Kim for 316L have been considered in making plausible room temperature C_p estimates for SS 304H

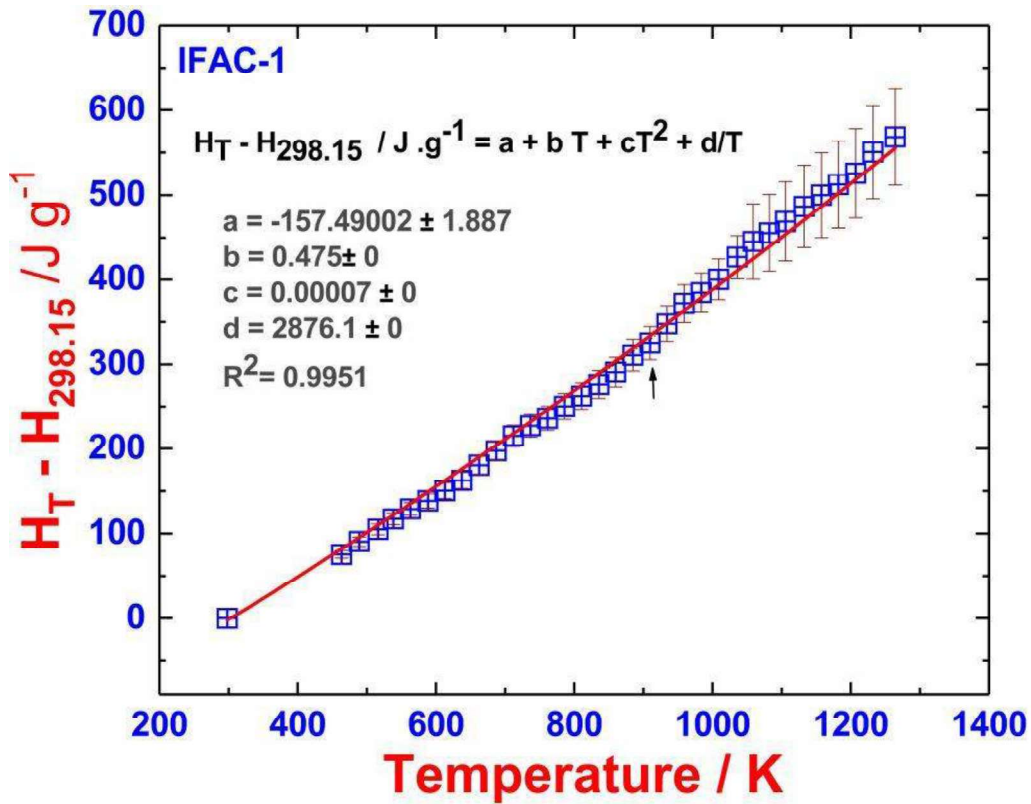


Fig. 5.1. Enthalpy variation with temperature for IFAC-1 SS

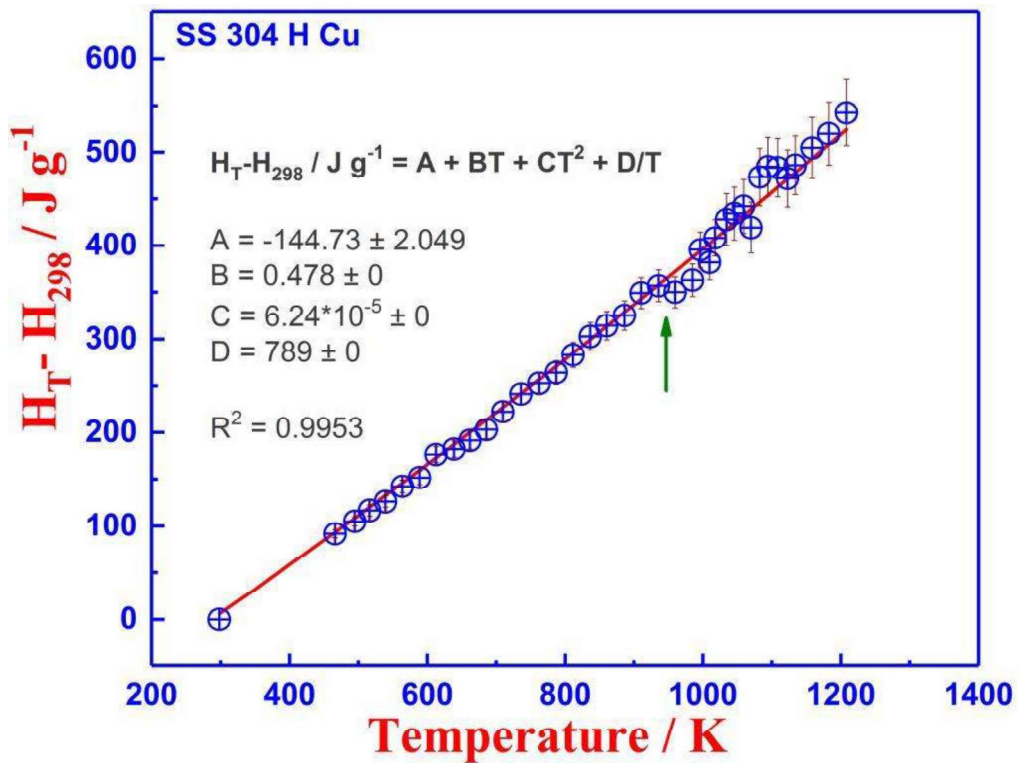


Fig. 5.2. Enthalpy variation with temperature for SS 304H Cu

specimens of known dimensions, as per ASTM practice [194, 195]. The resonance frequencies corresponding to flexure and torsion modes have been measured based on *Impulse Excitation Technique* (IET), using the equipment supplied by IMCE Belgium. The principle, operation and calibration details of the above experimental techniques have been described in detail in Chapter 3. The results, analysis of data and conclusions are presented in the subsequent sections.

5.3. Results

5.3.1. Enthalpy increment measurements and specific heat as function of temperature

The measured enthalpy increment ($H_T - H_{298}$) values as a function of temperature for IFAC-1 SS are displayed in **figure 5.1**. The line through the data points represents the best fit. Similar data on SS 304H Cu are presented in **figure 5.2**. The uncertainty, estimated as the standard deviation of three consecutive measurements on different samples, under the same experimental conditions, is shown as vertical error bar in both figures. It is observed from **figure 5.1** that except for a minor inflection at about 923 K (700°C) in the enthalpy behavior of IFAC-1, no significant change is found in the smooth nonlinear temperature variation of measured enthalpy. Although such nonlinear temperature dependence of enthalpy increment is also observed in SS 304H Cu, a clear dip is observed in the temperature region 886-1045 K, which is marked by the arrow head (**figure 5.2**). Based on the inference drawn from *Thermocalc*[®] based phase equilibria simulations, as well as results obtained from DSC investigations (Chapter 4), it is clear that the above mentioned temperature range characterizes the dissolution of nano-sized Cu-precipitates present in the austenite matrix of SS 304H Cu. Since the estimated volume fraction of these second phase Cu-particles is small; the observed change in enthalpy is only small. Hence this feature does not appear as a discrete step in **figure 5.2**. However, the observed dip is attributed to dissolution of Cu-precipitates and related changes in the microstructure of SS 304H Cu. It is useful to mention

Measurement and Modelling of High Temperature Thermophysical Properties of IFAC-1 & 304H Cu Stainless Steels

5.1. Introduction

The present chapter deals with the measurement and assessment of the high temperature thermophysical and thermomechanical properties of IFAC-1 SS and SS 304H Cu. In particular, the temperature variation of enthalpy increment ($H_T - H_{298}$), dilatational strain ($\Delta l/l_0$), the thermal diffusivity (λ) and elastic moduli have been measured in the temperature range of 298-1273 K. The experimental techniques adopted for this purpose are: (i) drop calorimetry for enthalpy measurements; (ii) dilatometry for thermal expansion measurements; (iii) laser flash method for thermal diffusivity and (iv) impulse excitation technique (IET) for elastic property measurement. In addition, an integrated modelling of measured thermal and elastic properties, based on Debye–Grüneisen formalism has also been presented in this chapter.

5.2. Experimental details

The ‘as received’ IFAC-I and SS 304H Cu samples were annealed for 1 hour at 1473 and 1523 K respectively. SS 304H Cu specimen was further subjected to an aging treatment at 923 K for 150 hours in order to facilitate full precipitation of Cu rich phase in austenite matrix. The details of sample preparation and heat treatment schedules have already been elaborated in chapter 3. The enthalpy increment and dilatational strain measurements were carried out using a *Setaram*[®] inverse drop calorimeter and thermo mechanical analyzer from 298 to 1273 K. The temperature dependence of thermal diffusivity was measured using the *Linseis*[®] laser flash equipment. The determination of elastic modulus is based on accurate measurement of resonant vibrational frequencies in both flexural and torsional modes on

Chapter 5

Measurement and Modelling of High Temperature Thermophysical Properties of IFAC-1 & 304H Cu Stainless Steels

VII. A critical comparison of the estimated activation energy values in these steels suggest that, both recovery and recrystallization in SS 04 H Cu are mostly controlled by grain boundary diffusion. However for IFAC-1 SS the recovery process happens to be controlled by grain boundary diffusion. The recrystallization on the other hand is influenced by bulk diffusion mechanism.

understanding of these individual processes is essential to explain the behavior of Avrami exponent in these steels. In this regard a geometrical simulation approach is adopted in this study to investigate the role of nucleation mode on the kinetics of static recrystallization and microstructure evolution in IFAC-1 SS. This is discussed in the next chapter.

6.5. Conclusion

- I. Dynamic calorimetric recovery and recrystallization processes taking place upon continuous annealing of severely cold worked IFAC-I and SS 304H Cu has been carried out.
- II. The peak recovery and recrystallization temperatures for IFAC-1 SS have been determined to be 815 K and 1070 K respectively. The corresponding temperatures for recovery and recrystallization in SS 304H Cu are found to be 826 and 986 K. These data are also supported by observed temperature variation of hardness measurements carried out on post-anneal specimens.
- III. The average value of the total stored energy release in IFAC-1 is found to be $9.4 \pm 1.4 \text{ J g}^{-1}$. The corresponding value for SS 304 H Cu is $17.3 \pm 1.4 \text{ J g}^{-1}$.
- IV. SS 304H Cu undergoes simultaneous precipitation and recrystallization. Therefore pre-aging treatment is required to avoid the simultaneous occurrence of the two events.
- V. For temperatures exceeding 1273 K/1000°C, partial dissolution of TiC particles in IFAC-1 SS resulted in secondary recrystallization.
- VI. The effective activation energy for recovery and recrystallization for IFAC-1 are estimated to be $198 \pm 7 \text{ kJ mol}^{-1}$ and $336 \pm 9 \text{ kJ mol}^{-1}$ respectively. In case of SS 304H Cu the effective activation energies for recovery and recrystallization are found to be 144 ± 14 and $192 \pm 12 \text{ kJ mol}^{-1}$ respectively.

value of $177.2 \text{ kJ mol}^{-1}$, which he interpreted as suggestive of grain boundary diffusion in austenitic steels [249]. Varin also listed the average value of activation energy for grain boundary diffusion in quite a few austenitic stainless steels in the range, 150 to 195 kJ mol^{-1} . Therefore it appears that the kinetics of static recovery and recrystallization in severely deformed SS 304 H Cu is controlled by grain boundary diffusion phenomenon. Recently, Mohapatra and Sahay modelled the recrystallization kinetics in Fe-25Mn-1Al (wt.%) alloy using an impingement corrected KJMA formalism and obtained an activation energy of about 330 kJ mol^{-1} , which is suggestive of volume diffusion [268]. In the present study, $Q_{eff} = 336$ has been obtained for static recrystallization in IFAC-1. In view of their result it can be said that, recrystallization in IFAC-1 is mostly influenced by bulk diffusion mechanism. It is noteworthy to mention here that, the apparent activation energy for recovery and recrystallization, as evaluated by a particular technique is only indicative of that part of the activation barrier associated with the defect relaxation process. The measured values are meaningful within the specified context of defect relaxation [72]. In this context, since recovery is aided by rearrangement of the defect structure by the movement of low angle boundaries, the DSC based estimation of the apparent activation energy is taken as a measure of the overall activation barrier for the relaxation processes which in the present case is close to the value of activation energy for grain boundary diffusion. Similarly the values obtained for activation energy for the recrystallization is close to the reported activation energy of bulk diffusion in the steel which indicates that the process is controlled by volume diffusion although indirectly

The Avrami exponent obtained for the present steels is smaller than the theoretical prediction of KJMA approach (*see section 2.12.1*). As the Avrami exponent is a function of modes of nucleation, growth as well as the impingement during the transformation, a fundamental

recrystallization steps. The Q_{eff} values for recovery and recrystallization during static recrystallization in austenitic stainless steels have not been explored extensively in the literature. Most of the quoted values of Q_{eff} are obtained from models of dynamic recrystallization at high temperatures, where volume diffusion is the rate controlling step. In a recent study on 50% cold worked Fe-21.6Mn-0.38C (mass %) steel, Lu *et al* estimated a value of 182 kJ mol⁻¹ for the thermally activated recovery step [265]. This was obtained from the analysis of the measured decay in the grain boundary migration rate during the course of recovery which is assumed to follow the classical model put forth by Kuhlmann *et al* [266]. In other words, the recovery process is assumed to be diffusional in nature where the grain boundary diffusion is taken as the rate controlling step. The present value of 198 kJ mol⁻¹ for IFAC-1 steel is of the same order as the one obtained for Fe-21.6Mn-0.38C steel. In his systematic investigation of activation energy for static recrystallization in austenite, Medina *et al* have estimated Q_{eff} for recrystallization in eleven austenitic steels micro-alloyed with Nb and Ti [267]. The activation energy for recrystallization in their study was found to vary between 92 to 293 kJ mol⁻¹. As a general observation, they have found that carbon accelerates the kinetics of recrystallization in austenite whereas other elements either in solution or by forming precipitates, slow down the kinetics. For IFAC-1 SS, low carbon and high alloying element content slow down the kinetics of recrystallization. Therefore the activation energy in case of IFAC-1 is slightly higher, namely 336 kJ mol⁻¹. On the other hand SS 304H Cu, containing nearly 2.5 times more carbon than IFAC-1 SS supports the acceleration of recrystallization kinetics. In addition to this, the extent of alloying is also small as compared to IFAC-1. This might be the reason as to why the activation energy of static recrystallization in SS 304H Cu (192 kJ mol⁻¹) is not too high as is the case with IFAC-1. In an earlier investigation on the change in grain boundary characteristics upon recrystallization of plastically deformed austenitic stainless steels, R. A. Varin obtained an activation energy

corresponding analysis for recovery and recrystallization in SS 304H Cu is shown in **figure 6.15(a) and (b)** respectively. The effective activation energies obtained for recovery and recrystallization processes are listed in **table 6.1** as well as in the corresponding figures. It is interesting to note that Q_{recryst} is higher than that of recovery in both steels. The average value of exponent n remains fairly constant with regard to heating rate variation. It is believed that this constancy of n reflects the fact that both in recovery and recrystallization processes, the fundamental defect structure reorganization mechanisms involved remained robust and did not change significantly during the nonisothermal annealing process. The effective activation energy (Q_{eff}) is one such fundamental parameter which provides some information about the fundamental processes involved in the defect structure reorganization during recovery and

Table 6.1:

Tabulation of kinetic parameters for the recovery and recrystallization processes for IFAC-1 and SS 304H Cu obtained in this study under different heating rates (β)

IFAC-1					SS 304H Cu				
$\beta/$ K min^{-1}	n	$Q/$ kJ mol^{-1}	$k_0/$ 10^{16} s^{-1}	R^2 (fit)	$\beta/$ K min^{-1}	n	$Q/$ kJ mol^{-1}	$k_0/$ 10^9 s^{-1}	R^2 (fit)
Recovery					Recovery				
5	0.60±0.002	198	2.8±0.012	0.99	15	0.77±0.001	144	1.02±0.001	0.99
7	0.64±0.001	198	2.9±0.006	0.97	20	0.9±0.002	144	0.97±0.003	0.99
10	0.60±0.002	198	5.7±0.02	0.97	30	0.72±0.001	144	1.24±0.002	0.99
15	0.56±0.001	198	2.7±0.004	0.98	40	0.94±0.006	144	0.73±0.005	0.94
20	0.60±0.002	198	5.9±0.03	0.99					
30	0.56±0.001	198	4.2±0.02	0.98					
40	0.64±0.003	198	3.0±0.01	0.99					
Recrystallization					Recrystallization				
5	0.48±0.001	336	6.67±0.02	0.99	15	0.73±0.002	192	5.4±0.02	0.99
7	0.56±0.003	336	6.69±0.04	0.99	20	0.72±0.004	192	5.0±0.03	0.99
10	0.48±0.002	336	2.1±0.014	0.98	30	0.69±0.001	192	4.4±0.01	0.99
15	0.56±0.001	336	4.39±0.01	0.97	40	0.84±0.002	192	11±0.03	0.99
20	0.56±0.001	336	2.08±0.06	0.97					
30	0.47±0.001	336	1.06±0.05	0.98					
40	0.49±0.001	336	1.23±0.05	0.99					

scattered points in **figure 6.12** & **figure 6.13** show the curves fitted in accordance with *Eq.* (6.5). The fit parameters obtained from the analysis are listed in **table 6.1**. It must be mentioned here that in the above fitting procedure, Q_{eff} values were kept fixed. This value is estimated by the Kissinger linearization procedure which predicts a more accurate value for the activation energy of the heating rate dependence of peak recovery and recrystallization temperatures. Since the details of these Kissinger and KJMA models have already been discussed in Chapter 2, they are not discussed here. **Figure 6.14(a)** and **(b)** show the Kissinger plot for recovery and recrystallization respectively for IFAC-1 SS. The

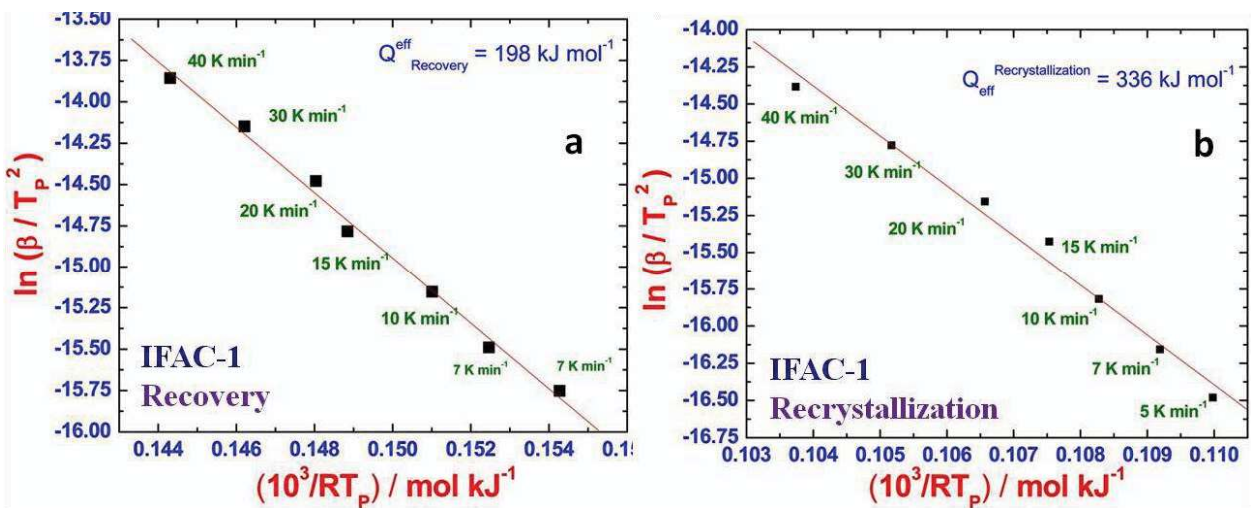


Fig.6.14. Kissinger linearization plots of (a) recovery (b) recrystallization for IFAC-1 SS. T_p represents the peak temperature corresponding to the exothermic hump obtained using DSC.

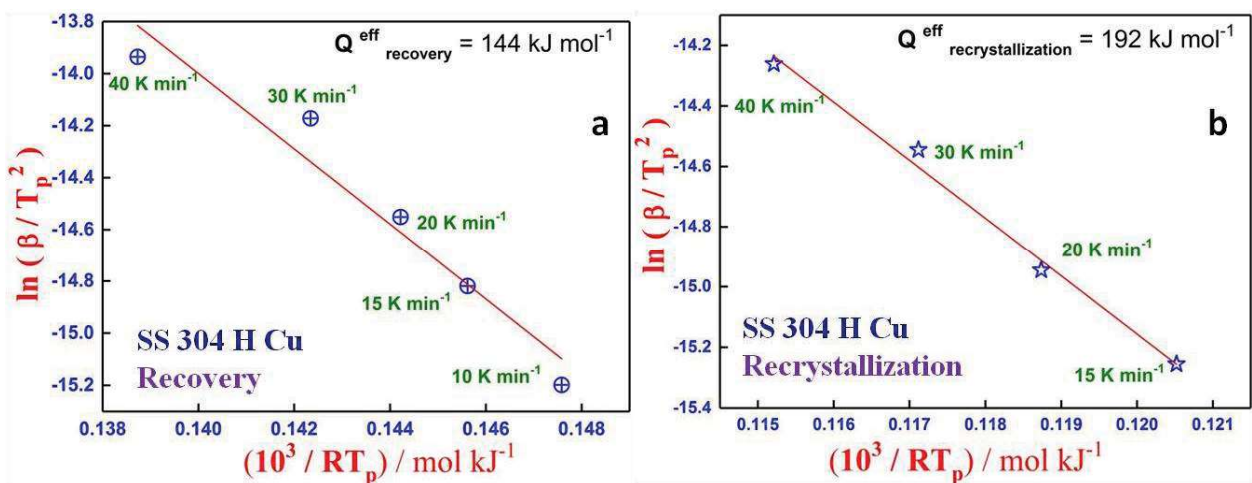


Fig.6.15. Kissinger linearization plots of (a) recovery (b) recrystallization for SS 304H Cu.

somewhat resistant to full recrystallization up to high temperatures, but once the recrystallization event is initiated it proceeds at a rapid pace. The fractional recovery and recrystallization plots for SS 304H Cu are shown in **figure 6.13(a) and (b)**. The onset of recovery is found to be a function of heating rate. For heating rates 15 and 20 K min⁻¹, the fractional recovery curves are very similar. However there is an obvious difference between the fractional recovery curves with heating rate 20 and the 30 K min⁻¹ which is clearly observed from **figure 6.13(a)**. This indicates that there is a certain change in the kinetics of recovery when the heating rate exceeds 20 K min⁻¹. This fact is also observed in case of recrystallization (**figure 6.13(b)**) when the heating rate is changed from 20 to 30 K min⁻¹.

The fractional recovery and recrystallization versus temperature data have been modelled in terms of the site saturation approximation of KJMA formalism [133]. The site saturation approximation is based on the fact that all the potential nuclei for recrystallization are already present in some form or the other in the starting cold worked microstructure itself (see section 2.10.1). Under such assumptions the transformed fraction as a function of temperature under anisothermal conditions can be expressed by the following equation [119, 133] (see section 2.12.1).

$$f(T) = 1 - \exp \left[-k_o^n \exp \left(\frac{-nQ_{eff}}{RT} \right) \left(\frac{R(T - T_s)}{\beta Q_{eff}} \right)^n \right] \quad (6.5)$$

$$k = k_o \exp \left(\frac{-Q_{eff}}{RT} \right) \quad (6.6)$$

In the above expression k is the Arrhenius rate constant for the overall transformation process; n is the effective kinetic exponent, Q_{eff} is the effective or overall activation energy and T_s is the transformation onset temperature. The fractional recovery and recrystallization plots in **figure 6.12 & figure 6.13** were subjected to a nonlinear least square fitting with Eq. (6.5) and the fit parameters (k_o , Q_{eff} , n) are estimated. The solid lines passing through the

recrystallization is reduced in the case of slow annealing processes. Stated in an alternate fashion, the temperature interval between the start and finish of the principal recrystallization event is becoming small for increasing heating rates. This aspect is reflected in **figure 6.12b**,

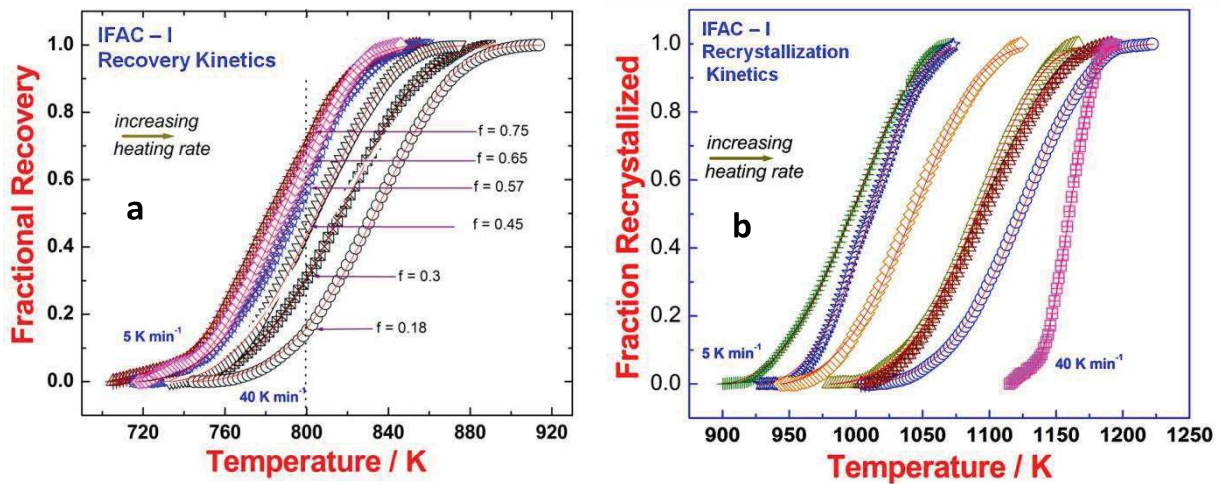


Fig.6.12. The fractional extent of (a) recovery and (b) recrystallization registered as a function of temperature under different heating rates for 85% cold work IFAC-1 SS

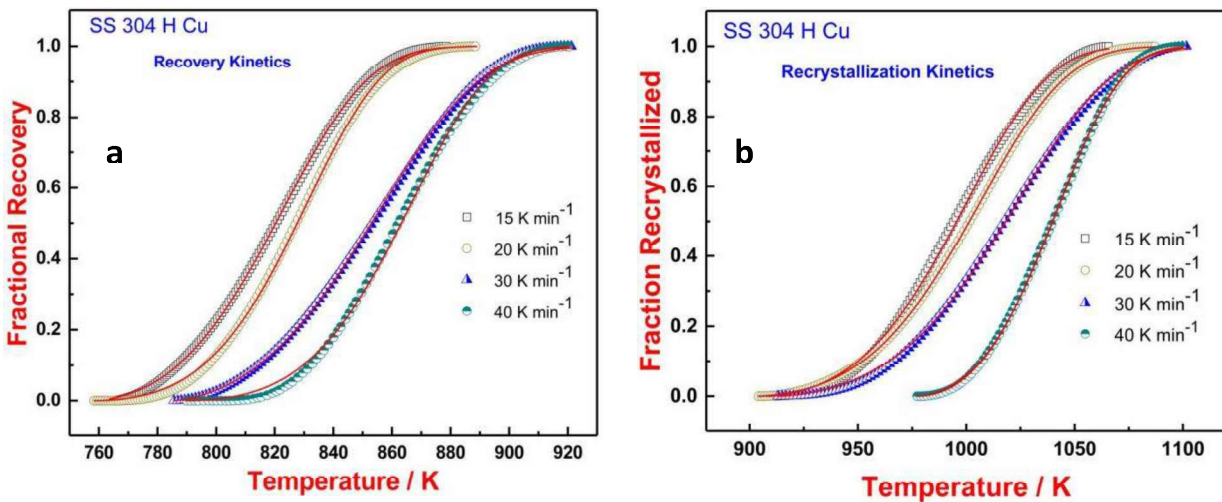


Fig. 6.13. The fractional extent of (a) recovery and (b) recrystallization registered as a function of temperature under different heating rates for 85% cold work SS 304H Cu

wherein, the fractional recrystallization curve is not so steep for small heating rates (5 K min^{-1}); but it is the other way round for 40 K min^{-1} . Further the temperature interval between the start and finish of the principal recrystallization event is becoming small for increasing heating rates. The practical implication of this point is that under fast heating, IFAC-1 is

Therefore, the higher values of stored energy measured in this study are unlikely to be clouded by the countering effect coming from martensite reversion.

6.4.3. Kinetics of recovery and recrystallization in IFAC-1 and SS 304H Cu

In general the recrystallization kinetics is modelled using the empirical model developed by Kolmogorov-Johnson-Mehl-Avrami (KJMA) for diffusional phase transformation kinetics [126-128, 139, 140]. A detailed description on KJMA approach and its limitations are provided in chapter 2 (see section 2.12.1).

In the present study, the fractional extent (f) of recovery and recrystallization as a function of temperature (T) under different heating rates (β) are obtained as the ratio of the partial peak area from T_s to T to that of the total peak area spanning T_s and T_f [261]. Here, T_s and T_f stand respectively for transformation start and finish temperatures.

$$f(T) = \frac{\int_{T_s}^T \phi dT}{\int_{T_s}^{T_f} \phi dT} \quad (6.4)$$

In the above expression $\phi(T)$ is the baseline calibrated DSC output. In **figures 6.12(a) and (b)**, the temperature variation of fractional recovery and recrystallization estimated using Eq.6.4 is plotted for different heating rates for IFAC-1 SS. It is clear that in both cases, the transformation plots are fairly sigmoidal in character, justifying the adoption of KJMA formalism for empirically describing them. In case of IFAC-1 SS, the fractional recovery curves are extremely self-similar for different heating rates and that the heating rate variation of recovery onset temperature also is not very drastic (**figure 6.12(a)**). For a fixed temperature, the fractional recovery increases inversely as the heating rate which indicates that slow heating is conducive for realizing nearly full recovery before it paves way for recrystallization. The consequence of this situation is that the driving force for

251]. Although austenitic stainless steels belong to the typical class of low sfe fcc alloys, the typical composition of P-added IFAC-I steel makes the sfe slightly higher compared to SS 304 and SS 316 grades [83]. In general it is believed that lower sfe makes dislocation cross slip more difficult, and as a result, the dislocation mobility is also kept low. This helps in promoting more homogeneous defect density distribution in the plastically deformed state. In addition, the lower the sfe , the larger could be the stored energy and hence the driving force for recrystallization [83]. The sfe of IFAC-I is estimated to be of the order of 65 to 76 m J m⁻² while the corresponding values for 304 and 316 stainless steels are in the range, 9.2-32.5 m J m⁻² (9.2-41.8 m J m⁻² for 304L) and 34.6-80.7 m J m⁻² respectively [83]. Although there is no reported experimental value of sfe of 304H Cu, an empirical estimation of sfe using a recent thermodynamic model by Curtze *et al* shows that the sfe value for the steel is nearly about 28 m J m⁻² [263]. In essence, the SS 304H Cu with low stacking fault energy possesses relatively high driving force, which is unlike the case for IFAC-1, though it belongs to the category of low to medium sfe material. This is the reason as to why the release of stored energy is relatively high in SS 304H Cu as compared to IFAC-1. It is also important to mention here that simultaneous precipitation and recrystallization can lead to an inhibited recrystallization in several alloy systems [248]. Such a situation is highly probable in SS 304H Cu as well. The pre aging treatment on SS 304H Cu as carried out in this study, produces some Cu-solute clustering at nano-metric scale [51-53]. In view of these facts it can be said that, although SS 304H Cu is a (relatively) low sfe material, the simultaneous precipitation of Cu inhibits recrystallization. This in some sense is responsible for the relatively higher stored energy release during recovery as compared to IFAC-1. It is additionally useful to mention here that, interference from the reversion of strain induced martensite during annealing is absent in medium to high sfe austenitic steels [89]. The addition of Cu in case of SS 304H Cu can significantly suppress the formation of strain-induced martensite during deformation [264].

stored energy values of 1.6 and 7.8 J g⁻¹ for the recovery and recrystallization stages respectively. The corresponding values for SS 304H Cu is found to be 3.4 and 9.45 J g⁻¹ respectively. The measured values of stored energy release for IFAC-1 and SS3 04H Cu for different heating rates are shown as histograms in **figure 6.11(a)** and **(b)** respectively. While

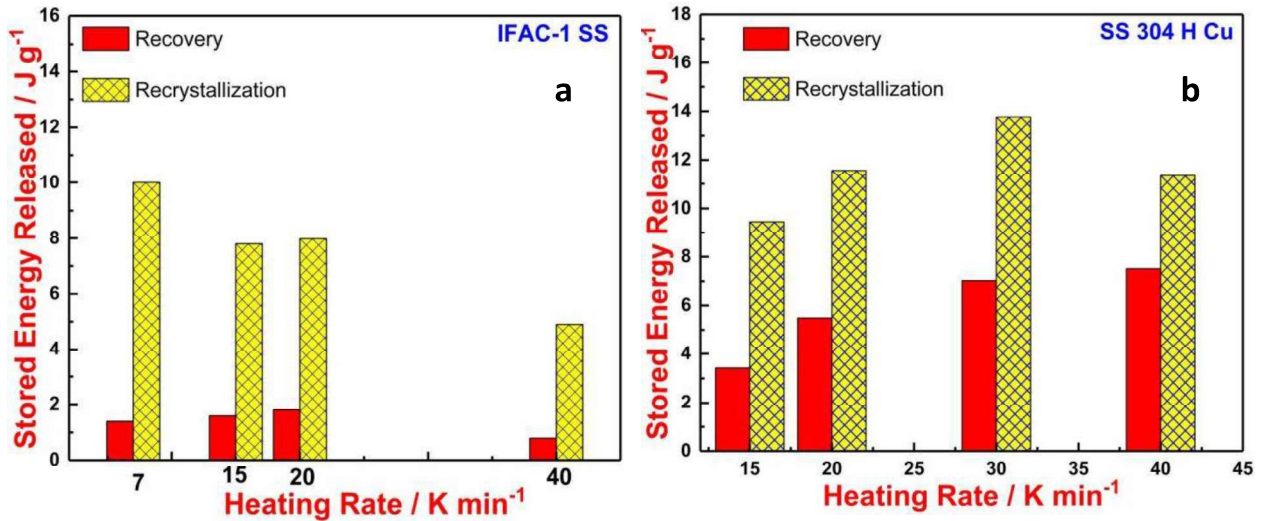


Fig. 6.11. Histogram showing the measured stored energy releases during recovery and recrystallization for **(a)** IFAC-1 SS and **(b)** SS 304H Cu

measuring the stored energy release from the DSC thermograms, it has been observed that the recovery and recrystallization thermal events overlap in certain heating rates, where the stored energy release during individual recovery and recrystallization cannot be separated. Although the measured stored energy due to recovery and recrystallization varies differently with heating rates in both the steels, it is interesting to note that, the total energy released in recovery and recrystallization is slightly higher in case of SS 304H Cu in comparison with IFAC-1 steel. In addition, the ratio of the stored energy release due to recovery and recrystallization is relatively high in SS 304H Cu. This difference in the measured stored energy release is due to the difference in the fundamental mechanism of defect relaxation in both the steels. A major factor that decides the extent of stored energy relaxation mechanisms during thermal annealing in austenitic stainless steels is the stacking fault energy (*sfe*) [83,

following approximation correlating the instantaneous hardness (H_t) at time t with $\rho(t)$ is often employed in literature [260].

$$\rho(t) = \left\{ \frac{1}{3(AGB)} (H_0 - H_t) \right\}^3 \quad (6.2)$$

In Eq. (6.2), A is a constant (~ 0.4) and H_0 is the initial hardness. A typical value b of Burgers vector 2.48×10^{-10} m may be employed in case of austenitic steels [261]. In the case of alloy systems having hard pinning particles of radius $R(t)$ with volume fraction $f_v(t)$ coming out of the supersaturated matrix due to precipitation at high temperatures, the processes of recovery, recrystallization and precipitation may interact in a complicated manner to modify the overall driving force $F(t)$ in the following manner [257, 258].

$$F(t) = \frac{1}{2} \rho G b^2 - 3 \frac{\gamma_{gb} f_v(t)}{R(t)} \quad (6.3)$$

The second term on the right hand side of the above equation is the Zener pressure exerted by fine precipitates to the overall driving force for grain growth. In essence, the models employed to estimate the stored energy release during the process of recovery and recrystallization only provide approximate values without invoking the heterogeneity in stored energy distribution. Calorimetry on the other hand is the only direct method available to make meaningful estimates of the energy released during relaxation from the internally stressed state [68,105,260-262]. Further careful calorimetric investigation of stored energy release can also provide useful supplement in understanding the kinetics of recovery and recrystallization phenomena taking place in plastically deformed alloys [261].

6.4.2. The stored energy release during annealing

The stored energy due to recovery and recrystallization has been estimated from the peak area of corresponding DSC thermal event during different heating and cooling rates. In the case of 85% cold worked IFAC-1 stainless steel, the present DSC experiments yielded

6.4. Discussion

6.4.1. Calorimetry and the strain energy relaxation process

Both recovery and recrystallization belong to the class of strain energy driven, crystal structure and composition invariant phase transformations. In principle the dynamics of these processes are governed by the structure and mobility of grain boundaries [68, 70, 258-259]. The stored energy due to deformation is the driving force which is released upon adequate thermal activation and this culminates in the process of recovery and recrystallization. However the magnitude of the stored energy is relatively small in comparison with typical solid state transformations. Further the process of recovery and recrystallization is a discontinuous transformation (spatially and time wise these phenomenon are localized) due to the heterogeneity in the stored energy distribution. Therefore accurate estimation of stored energy, and hence estimation of kinetics of recovery and recrystallization using dynamic calorimetry needs special attention in planning the experiments and interpreting results.

Assuming that dislocations are the major source of stored-in energy due to plastic work in metals and alloys, the driving force for recrystallization can be approximated as follows [70, 259].

$$E = \frac{1}{2} G b^2 \rho \quad (6.1)$$

In the above expression, G is the shear modulus at the annealing temperature; b is the Burgers vector and ρ is the average dislocation density due to plastic deformation. Thus, it is possible to obtain a reasonable measure of energy release from thermally induced complex reorganization of dislocation networks, if the time dependence of dislocation density $\rho(t)$, can be estimated by measuring changes in the mechanical or physical property such as the variation in hardness or resistivity as a function of time [70, 73]. Thus for example, the

823 K which represents the onset of recrystallization. This fact is in accordance with the DSC observation regarding the onset of recrystallization. The microstructure of the specimen annealed for 1023 K which is above the peak recrystallization temperature shows freshly nucleated strain-free grains.

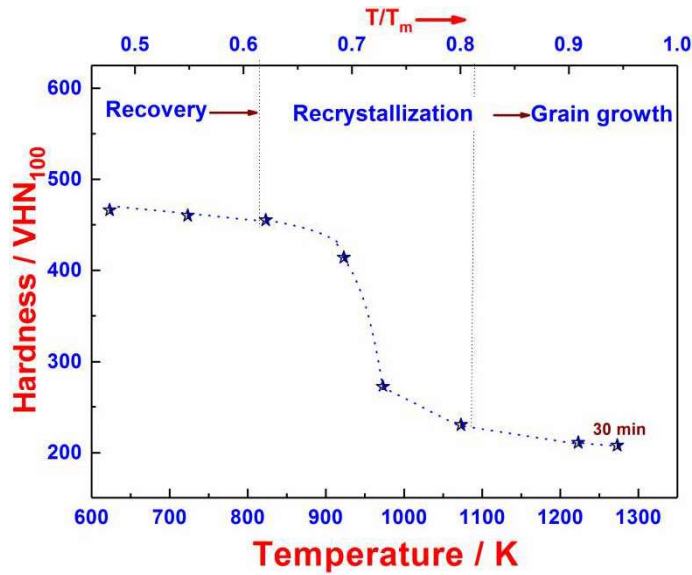


Fig. 6.9. Variation of micro hardness in SS 304H Cu for 30 minutes of annealing at different temperatures. The temperature domains of recovery, recrystallization and grain growth is noted

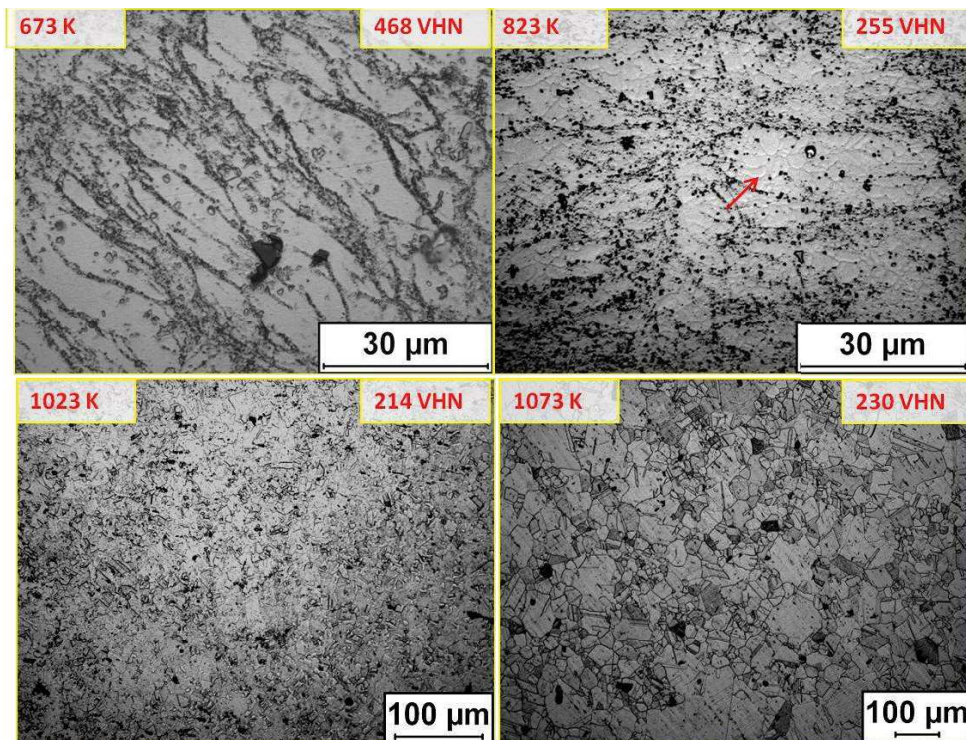


Fig. 6.10. The evolution of microstructure in deformed SS304H Cu samples as a function of annealing temperature for 30 min annealing time.

6.3.6. Microhardness variation and microstructural evolution during strain energy relaxation in SS 304H Cu

The microstructure evolution during static recrystallization and the corresponding microhardness variation in SS 304H Cu have been carried out in a similar fashion to that of IFAC-1 SS. In this regard, 80% rolled specimens of SS 304H Cu were annealed inside a muffle furnace for 30 minutes duration at temperatures starting from 623 K to 1273 K. The variation of microhardness as well as microstructure evolution has been monitored in this experiment. **Figure 6.9** shows the hardness variation as a function of temperature and the corresponding microstructure evolution is depicted in **figure 6.10**. The gradual change in the hardness values up to an annealing temperature of 823 K represents the recovery domain for this steel. The corresponding microstructure changes are illustrated in **figure 6.10** for samples annealed at 673 and 823 K. It is interesting to observe the subgrain structure evolution for the sample annealed at 823 K (*see arrow head*). It is a well-known fact that, the dislocation recovery is not a one step process but proceeds as a series of steps involving different micro mechanisms where the stored energy is gradually released by the restructuring and annihilation of dislocations in each step [68]. The random dislocations in a heavily deformed material gradually reorient themselves to form a cellular structure which gradually coarsens into well-defined subgrain structures. However the subgrain structures are not observed in case of materials with low stacking fault energy as the recrystallization occurs before significant recovery takes place [68, 70, 79]. In the present case for SS 304H Cu the presence of small Cu precipitates inhibits the recrystallization process and hence a significant recovery is achieved; this leads to the formation of well-developed subgrain structure in SS 304HCu. This is expected in case of alloys containing second phase precipitates [68]. The cellular structures are observed in the recovered specimens of SS 304H Cu for specimen annealed at 823 K (**figure 6.10**). The hardness values are observed to fall drastically for annealing above

much solute super-saturation; the driving force is rather small for homogeneous mode of precipitate nucleation to take place [248]. Therefore SS 304H Cu containing only about 3 wt % Cu, exhibits heterogeneous precipitation reaction, due to which several minor humps are actually observed in the DSC output in **figure 6.7** for all the three successive heating cycles. Further the simultaneous occurrence of recrystallization and precipitation in this alloy leads to complex interactions which make it difficult to study the kinetics of recrystallization in an isolated fashion. In view of this, the specimens of SS 304H Cu was aged at 923 K for about 150 hour, prior to cold rolling. This prior aging facilitates the full precipitation of Cu. Subsequently these deformed samples were subjected to heating with moderately higher heating rates for the investigation of kinetics of recovery and recrystallization in this alloy. It is believed that in such samples the interference between concurrent precipitation reaction and recrystallization transformation is minimal.

Figure 6.8 depicts the on-heating DSC thermogram for aged and cold worked specimens for heating rates, 15, 20, 30 and 40 K min⁻¹ respectively. It is interesting to note that there is no sign of a distinct precipitation event noticed in **figure 6.8** except for the two thermal events corresponding to recovery and recrystallization steps. The peak temperatures for these events are also noted in the same figure. With increase in the heating rate, the peak recrystallization is gradually shifted to a higher temperature domain, which is reflective of all transformations mediated through a nucleation and growth process. The rate of variation for the recovery and recrystallization temperatures has been calculated using a linear fitting procedure in manner as explained in **figure 6.4** with respect to IFAC-1 SS. The estimated equilibrium temperatures for recovery and recrystallization are found to be 800 and 965 K by extrapolating the linear fits to 0 K min⁻¹ heating rate.

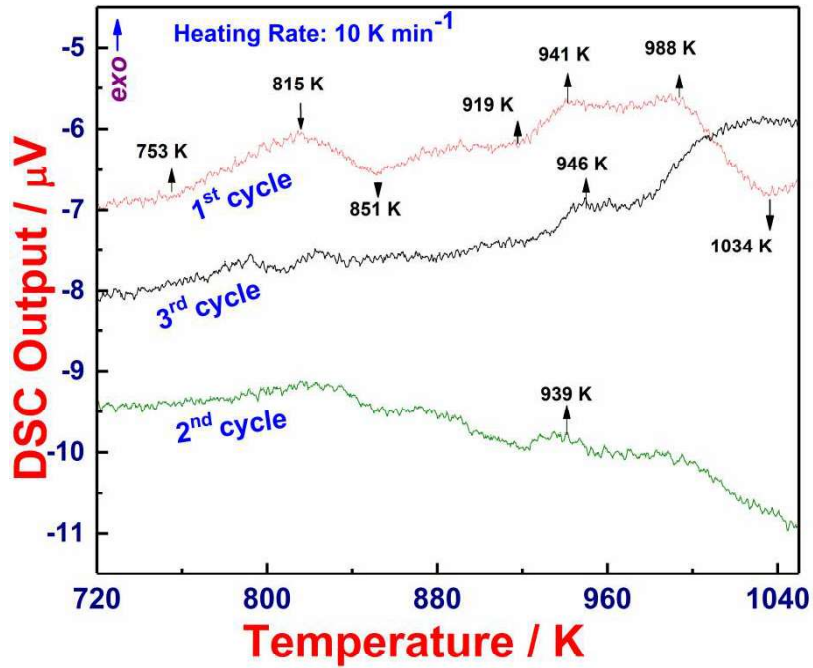


Fig. 6.7. DSC thermogram for the 85% cold rolled SS 304H Cu specimen. The three consecutive runs for the same specimen are denoted as 1st, 2nd and 3rd cycle.

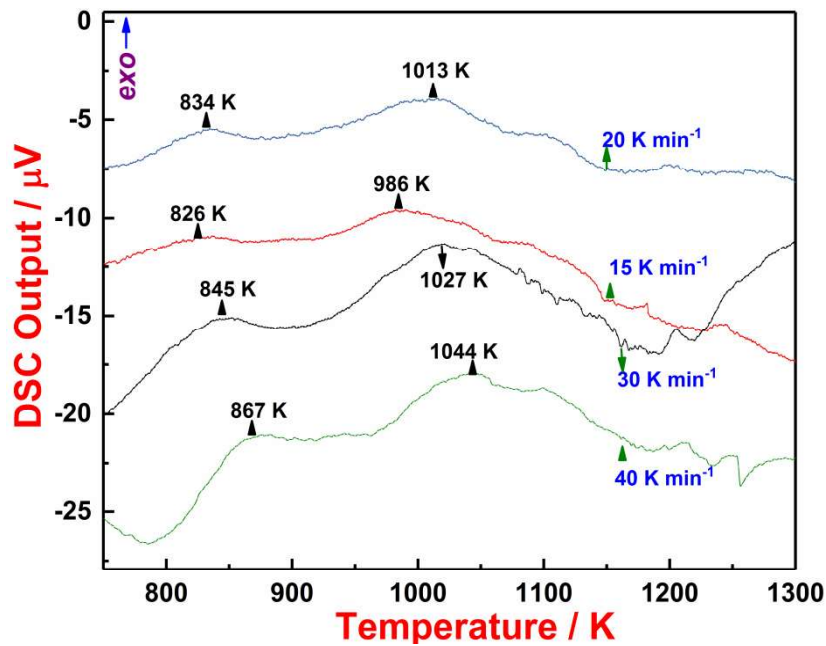


Fig. 6.8. DSC thermogram for 85% rolled SS 304H Cu for different heating rates. The samples were aged at 923 K for 150 h duration prior to deformation in order to avoid the simultaneous precipitation and recrystallization in this steel.

corresponding to the precipitation appears repeatedly in the 2nd and 3rd cycle DSC thermogram at 939 and 946 K respectively. It is a well-known fact that, a large driving force is required for homogeneous precipitation reaction and in the case of dilute alloys with not

recovery and recrystallization as a function of time under anisothermal conditions using a suitable theoretical framework of transformation kinetics, such as Kolmogorov–Johnson–Mehl–Avrami formalism which will be focused in a latter section [133, 252]. The results of DSC studies on SS 304H Cu is taken up next.

6.3.5. DSC investigation of recovery and recrystallization in SS 304H Cu

In order to monitor the temperature domain of recovery and recrystallization, deformed specimens (85% thickness reduction) of SS 304H Cu were characterized using heat flux DSC with different heating rates. **Figure 6.7** depicts three successive on-heating DSC thermogram for a single deformed specimen of SS 304H Cu. The three consecutive runs are denoted as 1st, 2nd, and 3rd cycle in the corresponding figure. It is interesting to note that the exothermic events shown in 1st cycle DSC thermogram in the temperature domain 753-851 K and 919-1034 K, disappear in the 2nd and 3rd cycle. This indicates that these thermal events are obtained as a direct consequence of recovery and recrystallization in this steel where most part of the stored energy is released, in the 1st cycle itself. Nevertheless the exothermic event in the temperature domain 919-1034 K as shown in **figure 6.7** is appearing as two overlapping exothermic events. With inference from the cooling DSC thermogram for the annealed SS 304H Cu (*see figure 4.13a in chapter 4*), the precipitation of Cu occurs in the temperature domain 817-962 K. Therefore the simultaneous precipitation and recrystallization in this alloy appears as two overlapping thermal events in the DSC output. It is also interesting to note here that, the thermal event with the peak temperature denoted at 941 K is appearing repeatedly in the 2nd and 3rd cycle on heating DSC profile. This exothermic event is reflective of the precipitation reaction in this steel. As the precipitation involves long range diffusion of solute particles, generally longer time duration is desired under suitable aging temperature. However in the present case with a heating rate 10 K min⁻¹, complete precipitation doesn't seem to happen in the 1st cycle. Hence the exothermic event

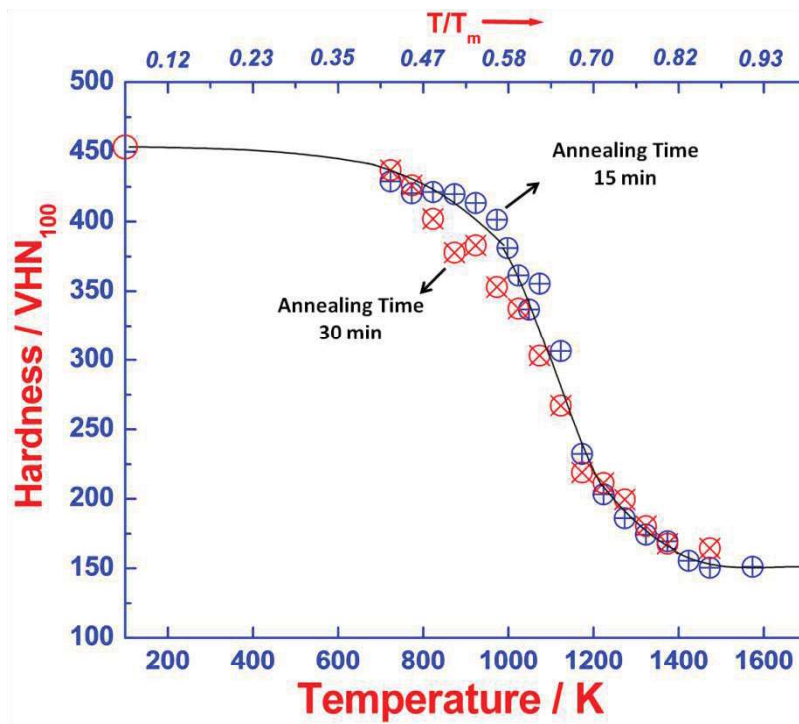


Fig. 6.5. Variation of microhardness with annealing temperature for the 85% cold rolled IFAC-1

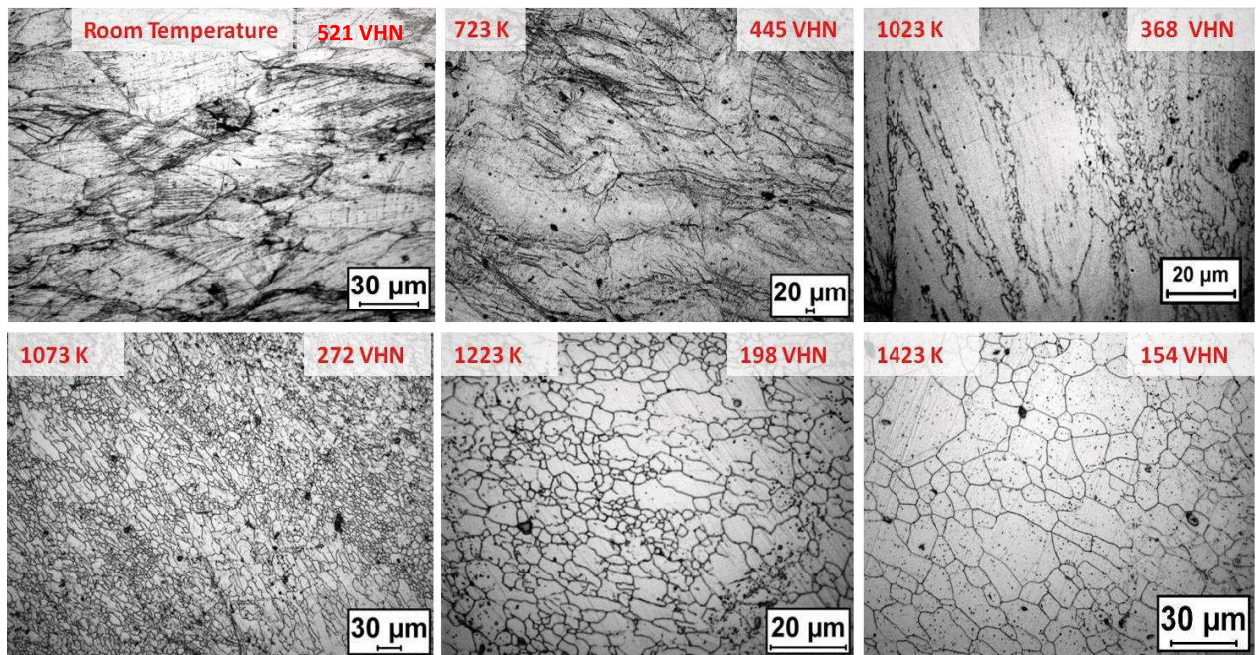


Fig. 6.6. The microstructure evolution during annealing of cold rolled IFAC-1 SS as observed through optical microscopy

morphology decorated by thick rectangular annealing twins. This is typical of the fully annealed microstructure of austenitic stainless steel. The effective activation energies involved in the lattice softening process can be obtained by modeling the fractional extent of

6.3.4. Microhardness variation and microstructural evolution during strain energy relaxation in IFAC-1

In line with the dynamic calorimetric investigation, the recovery and the recrystallization in IFAC-1 have also been investigated using the variation in microhardness values during annealing. A set of specimens were annealed for 15 minutes and 30 minutes duration at 50 K interval in the temperature domain 650 K to 1450 K. The choice of this wide temperature domain of annealing is intended towards clearly identifying the recovery, recrystallization and grain growth domains by the help of both microhardness variation and the microstructure evolution. The samples subsequent to annealing treatment are immediately cooled to room temperature at 100 K min^{-1} .

In **figure 6.5**, the variation of hardness as a function of annealing temperature is graphically portrayed for both 15 and 30 minutes of annealing time. The accompanying changes happening to the microstructure during annealing are also shown in **figure 6.6**. It is clear from **figure 6.5** that the hardness variation with annealing temperature exhibits an inverse sigmoidal character that is typical of diffusional transformations. It is clear that the onset of significant lattice softening as measured by the decrease in hardness sets in at about $0.5T/T_m$, where T_m is the melting point. But the microstructure at the resolution level of optical microscopy does not exhibit any drastic restructuring as yet at this temperature. However with increasing temperature, the rate of lattice softening increases dramatically and reaches its maximum at about $0.6T/T_m$ or 1150 K. This matches well with the peak temperature of the principal recrystallization, as registered in the DSC trace (**figure 6.2a&b**). With further rise in temperature, the rate of hardness change exhibits a gradual decrease, but this stage is attested by pronounced microstructural changes which include the formation of copious amount of small recrystallized grains and their growth with time. The final microstructure seen at the end portion of the annealing cycle is one of regular polygonal grain

and the slope of the fit ($dT/d\beta$) was obtained. The slope is a measure of the incubation time (τ) for the event (either recovery or recrystallization) concerned. In general terms, it may be said that for the recovery process, the heating rate sensitivity of the onset temperature does not exhibit appreciable dependence on the extent of prior cold work ($\tau_{Rc}=83$ s for both 70 and 85% cold work; see, **figure 6.4**). However the heating rate dependence of the recrystallization onset shows a clear decrease with increasing extent of cold work and hence stored energy ($\tau_{Rx}=113$ and 65 s for 70 and 85% cold work). This implies that the incubation time for recrystallization decreases with increase in stored energy. This kinetic asymmetry noticed with regard to the role of prior cold work in influencing the heating rate sensitivity of recovery and recrystallization phenomena is indeed interesting, as it must have some interpretable links with the micromechanics of the unit processes that are responsible for lattice recovery and subsequent recrystallized microstructure development. It is generally held that recovery upon annealing does not entail any incubation time as it is a spontaneous process not requiring long range atom diffusion [68, 70, 75]; but the difficulty in detecting the first measurable trace of recovery in terms of corresponding changes that it induces in parameters like hardness, enthalpy, electrical resistance, *etc.*, always introduces a small time lag in the measurement. But the important point to notice here is that increasing the extent of prior cold work beyond a threshold level does not serve to catalyze the speedy initiation of defect recovery. On the other hand the nucleation of recrystallization which is invariably a heterogeneous process is characterized by definite incubation time that varies inversely as the magnitude of driving force, namely the stored energy [68, 70]. It is believed that the recrystallized nuclei are already present in the heterogeneously cold worked state itself and that their transformation into strain free nuclei occurs through the movement of strain energy driven high angle boundaries [70]. Therefore increasing the severity of plastic strain promotes the initiation of recrystallization event as observed in **figure 6.4**.

kinetics therefore is a function of the heating and cooling rate. In this regard the effect of heating rate on recovery and recrystallization thermal arrests is analyzed using DSC. The results are discussed in the following section.

6.3.3. The effect of heating rate on recovery and recrystallization

IFAC-1 specimens rolled up to 70 % and 85% thickness reduction were subjected to continuous heating at different scanning rates (5 to 40 K min⁻¹) in a heat flux dynamic calorimeter and corresponding on heating DSC thermogram have been recorded. From this the heating rate variations of recovery and recrystallization onset temperatures were obtained.

Figure 6.4 illustrates the variation of recovery and recrystallization peak temperatures for

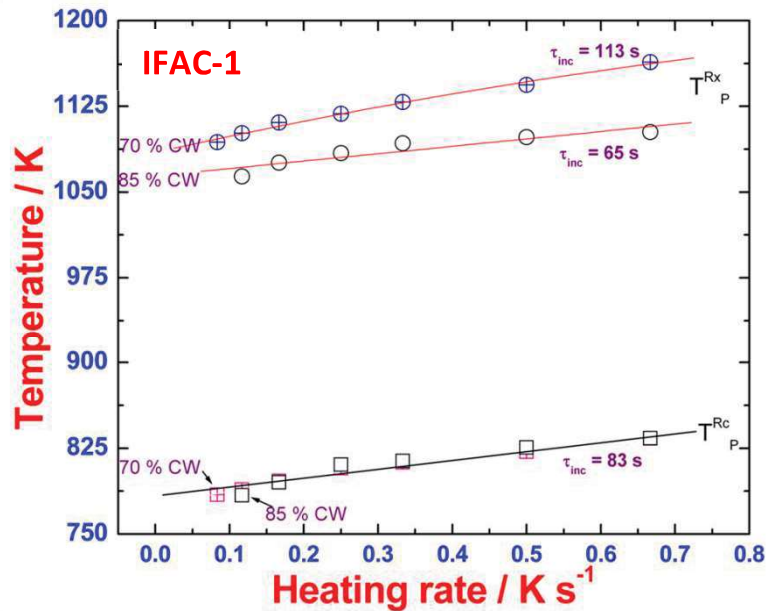


Fig. 6.4. Variation of recovery and recrystallization peak temperatures with heating rate for 70 and 85% cold worked IFAC-1 specimens.

both 70% and 85% rolled IFAC-1 samples. The peak temperatures of both recovery and recrystallization are found to increase with heating rate, but with different slopes. It is also observed that the extent of prior cold work influences the heating rate sensitivity of the peak thermal arrest temperatures. The heating rate (β) dependence of the peak thermal arrest temperature for both recovery and recrystallization was subjected to a linear fitting procedure

In **figure 6.3**, the optical micrograph of the sample quenched from 1323 K is shown. It is clear that the region outlined in dotted rectangle bears evidence for anomalous grain growth. It must be mentioned here that the abnormal grains observed in **figure 6.3** shouldn't be confused with the strain induced boundary migration (SIBM) which generally occurs

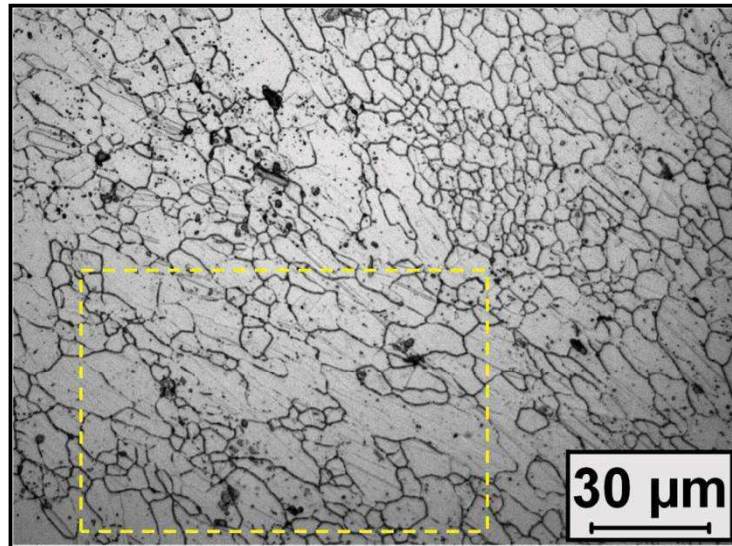


Fig. 6.3. Optical micrograph of the IFAC-1 sample annealed at 1323 K for 15 minutes in DSC and fast cooled to room temperature. The part of the microstructure outlined by the dotted rectangle bears evidence for secondary recrystallization

during recrystallization for low strains [68]. At higher strains, the internal deformation substructure leads to a more homogeneous distribution of the internal deformation energy which leads to discontinuous nucleation due to subgrain coarsening. An important observation is that the microstructures of IFAC-1 SS annealed below 1023 K does not show any signs of abnormal grains. This indicates that the microstructures shown in **figure 6.3** are due to the dissolution of secondary TiC precipitates leading to secondary recrystallization.

It is important to note that the phenomenon of strain energy relaxation in a deformed lattice intrinsically depends on atomic diffusion process. A diffusional transformation normally proceeds with the nucleation and growth of product phase nuclei, once adequate amount of thermal activation is supplied to the system. In such conditions, the transformation

actually the resultant of enthalpy associated with the sequence of unit processes that are responsible for lattice softening and the development of a low energy defect configuration [68, 71]. The tail of this recovery peak is followed by the onset of principal recrystallization thermal arrest peaked at 1070 K. It is interesting to note that recrystallization in this case seems to proceed in discrete bursts, as evidenced by two subsidiary shoulders at 1162 and 1225 K respectively. It is probable that these smaller peaks are associated with secondary recrystallization phenomenon, which occurs following the dissolution of nano-sized secondary TiC particles, which in this class of steels normally occurs in the temperature range of 1323–1373 K [83, 251]. It may be added that the endothermic TiC dissolution event in itself is rather difficult to detect separately in a DSC experiment, as the volume fraction of the precipitate is rather small which is observed in the *Thermocalc*[®] simulation (see section 4.2.2). In fact, we have not observed any evidence of TiC precipitate dissolution in the dynamic calorimetry investigation of a fully annealed specimen which is already reported in chapter 4. However, the dissolution of TiC located on prior dislocations has an indirect effect, in that, the grain boundaries whose mobility was earlier restricted due to pinning by TiC particles, have now been rendered free to undergo migration and thus contribute to secondary recrystallization. It is useful to note that the small post recrystallization exothermic humps seen at 1323 K are still present in 2nd and 3rd cycle DSC scans (**figure 6.2(a)**) with a gradual reduction of intensity. This suggests that some microstructural evolution still continues to be active even after the occurrence of bulk recrystallization process. The gradual dissolution of TiC particles results in unpinning of some of the favorably oriented grain boundaries which promotes secondary recrystallization or anomalous grain growth phenomenon happening at post 1273 K temperature region [83]. In order to observe the secondary recrystallization event in detail, metallographic characterization was carried out on DSC samples quenched directly from 1323 K.

primary heating cycle (1st run), for identifying the minor shoulders associated with the two major exothermic events. The recovery thermal arrest observed at 815 K is found to be associated with a few minor humps in the DSC profile. The recovery thermal arrest is

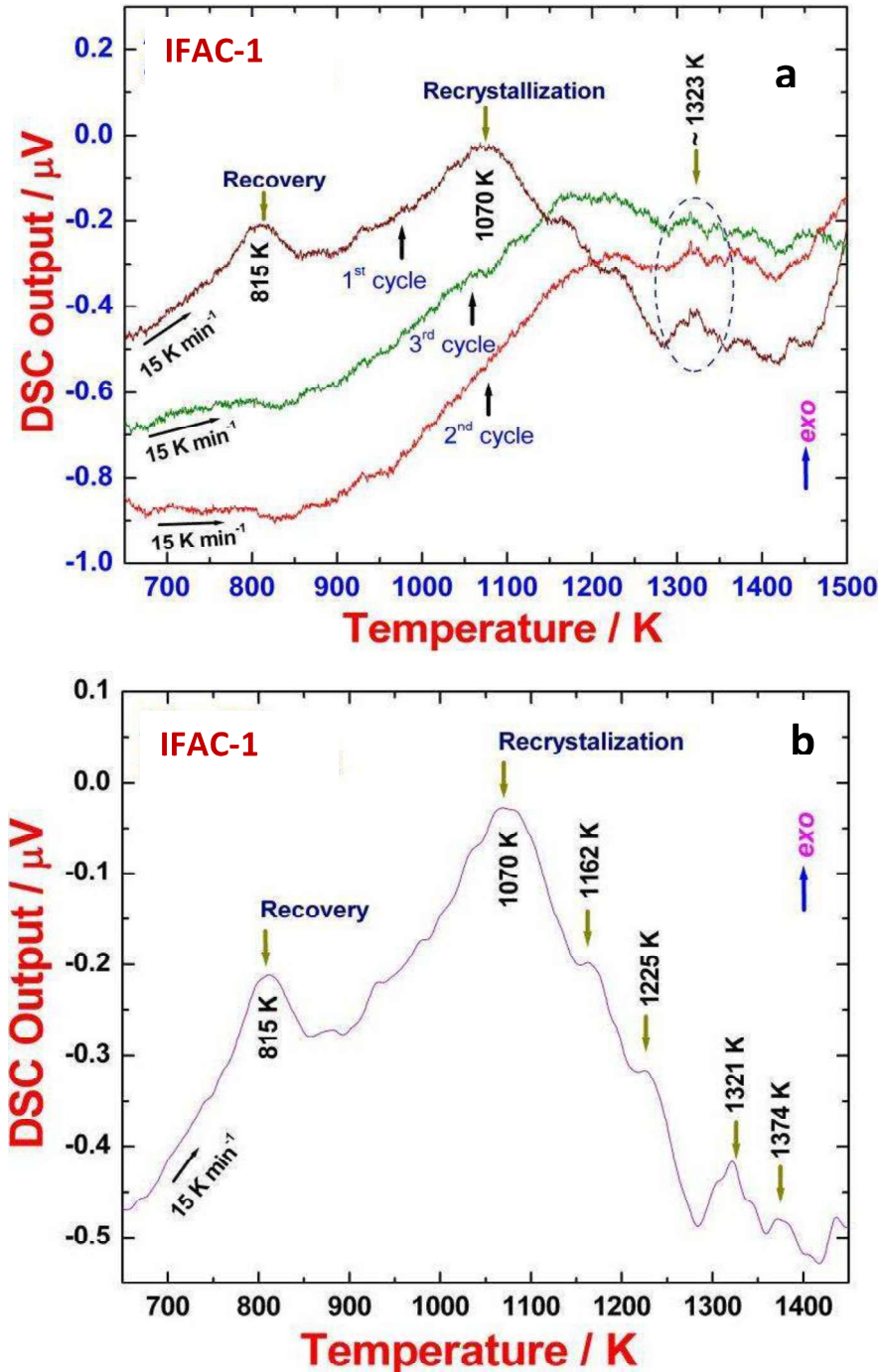


Fig. 6.2. (a) Three successive heating DSC traces of 85 % cold rolled IFAC-1 obtained on same sample under identical experimental conditions (b) The expanded view of the on-heating DSC thermogram for the 1st cycle shown in (a). Distinct thermal arrests due to recovery and recrystallization events are seen.

microhardness value of the cold rolled IFAC-1 SS is found to be in the range 455 (70%)-521 (85%) VHN.

Figure 6.1(b) depicts the optical micrograph for cold rolled SS 304H Cu for 70% thickness reduction. The figure indicates elongated grains in the rolling direction. Unlike IFAC-1, the deformed microstructure of SS 304H Cu shows the presence of a large amount of deformation twins (arrow #I). Further somewhat serrated grain interfaces (arrow #II) are also observed in the deformed microstructure. In addition, the presence of second phase precipitates are also noticed along the deformed grain interfaces. The average microhardness value of the 70% deformed SS 304H Cu is found to be 476 VHN. The observed microhardness values for both IFAC-1 and the SS 304 H Cu are in good agreement with the reported ones for cold worked SS316 austenitic steels [251].

6.3.2. DSC investigation of recovery and recrystallization in IFAC-1 SS

In order to identify recovery and recrystallization temperature domains in IFAC-1 SS, the 85% cold rolled samples were subjected to controlled heating and cooling in a differential scanning calorimeter. **Figure 6.2(a)** depicts the baseline subtracted on heating DSC profile for three successive scans which were carried out for the same sample under identical experimental conditions without removing the sample from DSC cradle. **Figure 6.2(a)** brings out the sequence of major events that accompany the lattice softening behavior in IFAC-1 austenitic stainless steel. The primary heating cycle (1st cycle) constitutes two major exothermic events located at 815 K and 1070 K corresponding to recovery and recrystallization. Further a careful observation of three successive thermal arrests in **figure 6.2(a)** indicates that bulk of stored energy is released during recovery and recrystallization events in the primary heating cycle itself, as there is no clear evidence of any thermal events in the 2nd and 3rd heating cycles, in the temperature domain corresponding to recovery and recrystallization. **Figure 6.2(b)** shows the expanded view of the DSC thermogram for the

6.3. Results

6.3.1. The deformed state

The optical micrograph of the typical deformed microstructure (70% thickness reduction) for IFAC-1 SS is shown in **figure 6.1(a)**. The presence of elongated grains is clearly observed along rolling direction, as marked by the arrow head pointer #1 in **figure 6.1(a)**. In addition, the presence of deformation twins is also found in the microstructure (arrow #2). Further in some parts of microstructure, the presence of macro deformation bands (arrow #3) and numerous crisscrossing slip traces (arrow #4) are also noticed. This appears to be generic of the deformed microstructure in austenitic stainless steels [83, 249-251]. The

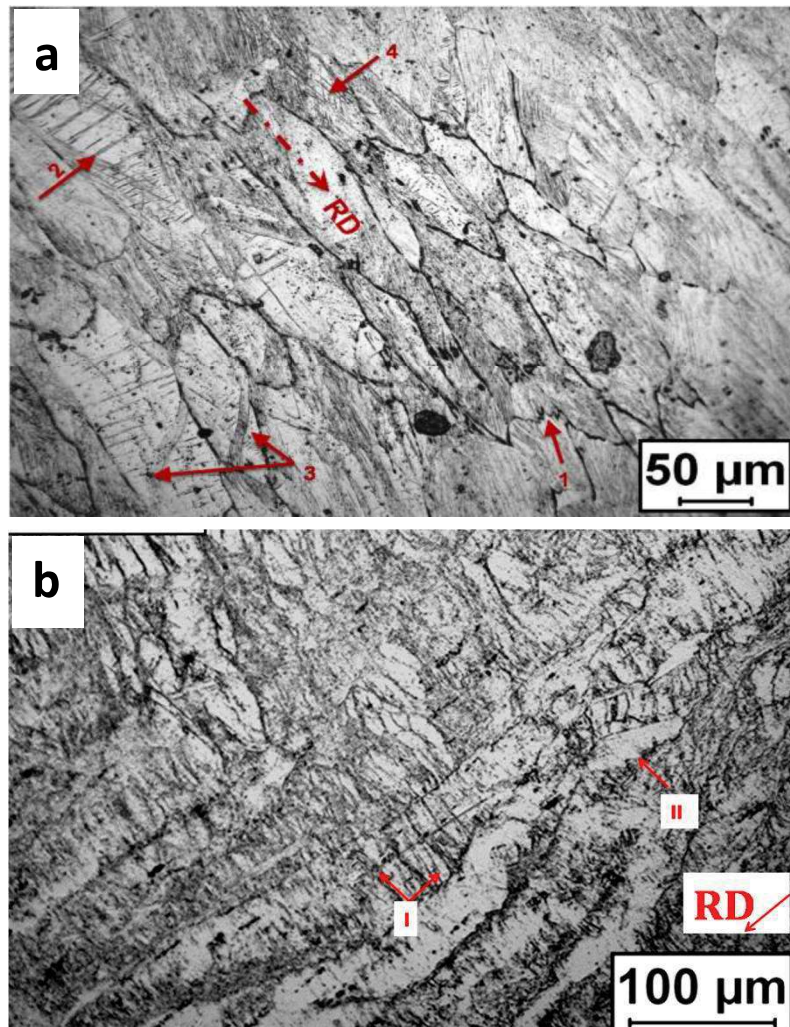


Fig. 6.1. Optical microstructure for 70% deformed (a) IFAC-1 (b) SS 304H Cu austenitic stainless steel

properties. Therefore it is highly essential to monitor both recovery and recrystallization behavior of this material.

In the present study a dynamic calorimetry investigation has been carried out in conjunction with the measurement of microhardness and microscopy studies to monitor the recovery and recrystallization behavior in IFAC-1 and 304H Cu. The recovery and recrystallization temperatures and their dependence on prior cold work have been estimated. The kinetics of recovery and recrystallization has also been characterized using standard analytical formalisms [126-128, 139-140, 157-158]. Before proceeding further, a brief account of experimental details is presented in the next section.

6.2. Experimental detail

The as-received samples of IFAC-1 and SS 304H Cu were annealed at 1573 K for about 30 minutes (which is above the normal homogenization temperature of the steel) and this is followed by furnace cooling to room temperature. This choice of the annealing temperature is based on our DSC results discussed in chapter 4. The annealing temperature of 1573 K is well above the standard homogenization temperature for 300-grade austenitic stainless steels. For SS 304H Cu this temperature is also above the temperature required for complete dissolution of $M_{23}C_6$ and Cu rich metallic precipitates. The annealed plates were subjected to cold rolling to the tune of 70% and 85% thickness reduction at room temperature. These samples are then used in the present calorimetry studies. The cold worked and annealed samples were polished and etched with dilute HNO_3 solution for metallographic characterization and microhardness measurements. The details of DSC, microscopy and microhardness measurement techniques have already been elaborated in Chapter 3. Only the results are presented and discussed in this chapter.

movement. In many cases, overlap of recovery and recrystallization or their simultaneous occurrences cannot be avoided.

In general practice, engineering materials on numerous occasions undergo various thermomechanical processing routes like hot working, cold working, annealing *etc.*, before they achieve a stable topology of microstructure that is suitable for the end use. In such a scenario, recrystallization is an inevitable phenomena which needs to be controlled carefully to obtain suitable grain size, shape, orientation and distribution in the final microstructure [238]. The mechanism and the kinetics of recrystallization have been widely investigated in a variety of materials, especially, the austenitic stainless steels [239-247]. However, in the case of alloys where recrystallization can occur simultaneously with second phase precipitation, the actual mechanism and kinetics of recrystallization are largely affected by precipitate characteristics [237, 248]. Depending on initial microstructure, composition and processing conditions, the precipitation can either precede, follow or occur simultaneously with the recrystallization. Therefore the final microstructure is actually decided by the interaction between recrystallization and the precipitation kinetics. Alternately, the deformed state of a material can also influence the nature of precipitation and in turn, the precipitation influences the mechanism and kinetics of recrystallization to a large extent. In this way there operates a synergy between these two solid state transformation processes.

In the present study, the recrystallization processes occurring in two austenitic stainless steels, namely IFAC-1 and SS 304H Cu are investigated. Since the details of choice of material and the service condition have already been presented in chapter 1 and chapter 2, these will not be elaborated in this chapter. Nevertheless, it is important to mention that IFAC-1 SS, which is the candidate structural material for the fast breeder reactor in India, will be used under 20% cold worked condition for improved irradiation swelling resistance

Investigation of Recovery and Recrystallization Processes in IFAC-1 & SS 304H Cu Stainless Steels using Dynamic Calorimetry

6.1. Introduction

It is a well-known fact that a material when subjected to an external load undergoes both elastic and plastic deformation depending on the magnitude of applied stress. When it is deformed plastically, a part of the mechanical energy supplied to the system is dissipated in the form of heat and the remnant portion is stored inside the bulk as internal energy [68, 70, 87, 237]. The internal energy increase due to plastic deformation is retained inside the material in the form of complex defect networks. The magnitude of the stored energy depends on several factors, namely the magnitude of deformation, the rate of application of applied strain, the temperature of deformation, the initial microstructure and the thermophysical characteristics of material i.e. elastic moduli and thermal conductivity etc. The stored energy of deformation is an essential feature of the deformed state of the material, which develops certain degree of thermodynamic instability under the action of external stress. Under adequate thermal activation, a deformed material can therefore undergo a restoration process in the form of recovery and recrystallization to achieve a new strain free microstructure, and during which process, the stored energy is fully or partially released [70, 73-74, 79, 238]. The process of recovery which generally occurs prior to recrystallization involves defect reorganization at microscopic level; which ultimately ends up with a low energy defect structure in the material. During recrystallization, new strain free grains nucleate in the recovered material and grow towards the deformed regions. The deformation induced defects are also getting swept away in the process along with the advancement of interface. It is the strain energy gradient that is the primary driving force for interface

Chapter 6

***Investigation of Recovery and
Recrystallization Processes in
IFAC-1 & SS 304H Cu
Stainless Steels using Dynamic
Calorimetry***

- VII. The grain size distribution as well as the average grain size in the simulated microstructure for AN mode is found to be similar to the experimentally observed grain size distribution for the IFAC-1 SS.
- VIII. The algorithm presented here to monitor the grain size distribution under different nucleation modes can be further extended to check the nature of grain size distribution for arbitrary mixing of pure SSN and CN modes.

for intermediate nucleation modes, the parameters are found to vary continuously depending on the individual contribution from pure SSN and CN mode.

- II. Due to the limited availability of nucleation sites in a heterogeneous recrystallization in comparison to a homogeneous one, the rate of increase or decrease in the Avrami exponent in a mixed or Avrami nucleation mode is always more for the heterogeneous recrystallization. However, the variation of Avrami exponent is sensitive to the nucleation rate for both mixed and Avrami modes of nucleation.
- III. The variation of kinetic parameters (q , m) in the MPM model behaves similarly to the Avrami exponent (n) irrespective of nucleation modes.
- IV. The experimental results for Avrami exponent in IFAC-1 show a minor deviation at the end of the transformation which is similar to the simulation results for Avrami nucleation mode.
- V. The grain size distribution due to static recrystallization is found to be sensitive to the nucleation mode. In case of CN, MN and AN mode, the size distributions are found to be lognormal whereas for SSN mode the observed distribution is normal. The grain size distribution observed in the present simulation for the MN mode is a mixture of large grains and a continuous band of smaller grains. For AN mode, the grain size distribution can differ widely depending on the nucleation rate.
- VI. The grain size distribution in pure site saturation and continuous nucleation is unique. But the average grain size depends on both the nucleation rate and the number of preexisting nuclei. However both average grain size and the size distribution can be controlled for Mixed and Avrami nucleation modes by suitably adapting the initial microstructure as well as the time-temperature path of annealing.

experimental results by fitting with appropriate analytical expressions for various nucleation and growth modes. These parameters are then used in the simulation to monitor the kinetics and grain size distribution for different nucleation modes to obtain an optimized initial microstructure and the time-temperature path to reach at a desired average grain size and size distribution. It is important to mention here that the interface energy, curvature as well as the presence of impurities have a finite effect on the kinetics and the grain size distribution in the final microstructure, which is not introduced explicitly in the present model. However, by incorporating these factors, the current approach can be extended to study the combined effect of nucleation and growth using more sophisticated modes such as cellular automata and phase field modelling etc. Nevertheless, the final grain size distribution in IFAC-1 SS is qualitatively similar to the simulation results observed for Avrami nucleation mode although a quantitative agreement cannot be claimed only on the basis of nucleation mode.

7.8. Summary and conclusions

An algorithm is proposed to study the role of nucleation modes on the kinetics of static recrystallization under isothermal annealing conditions. The kinetic parameters are evaluated from the simulation using KJMA and MPM formalism to verify the validity of isokinetic assumption in case of pure site saturation, pure continuous nucleation modes as well as a mixture of these two pure nucleation modes. The model also provides considerable insight into the microstructure evolution as governed by the intricacies of various nucleation possibilities and delivers a logical approach to control the average grain size and their size distribution under different conditions of nucleation.

The salient results of the present study are listed as follows.

- I. The kinetic parameters (n , q , m) for pure site saturation and continuous nucleation modes are found to follow the isokinetic assumptions of KJMA approach. However

of preexisting nuclei under SSN mode. For CN mode, the available time for growth is small for those nuclei which appear at a later stage of transformation, as compared to those which appear rather early. But the same growth time is available for all the nuclei that appear at the same instant during the transformation. Therefore the statistical grain size distribution consists of a continuous band of grains (**figure 7.15 (b)**). Nevertheless, the average grain size in CN mode depends on the nucleation rate. Further, in the MN mode, the grain size distribution is a mixture of large grains due to preexisting nuclei and a continuous band of smaller grains due to continuous nucleation (**figure 7.15 (c)**). Hence, the grain size distribution and the average grain size are functions of both N^* and N_o . Similarly for AN mode, as the nucleation rate varies continuously, the individual grain sizes also differ widely (**figure 7.15 (d)**). Therefore both the grain size distribution and the average grain size depend on the nucleation rate (λ_o). In essence, for intermediate nucleation modes, both grain size distribution and average grain size can be controlled by controlling the parameters N^* and λ_o . Based on present results, the grain sizes can be controlled by the choice of the temperature of annealing for SSN and CN modes; but the size distribution cannot be altered. However, for intermediate nucleation modes, both grain size and its distribution can be modified for a suitable choice of annealing temperature and time.

The observed variation of the kinetic parameters in this study during an isothermal transformation provides a fundamental insight to identify the nucleation mode from complex experimental results. A gradual increase and decrease in the kinetic parameters during the transformation in a mixed and Avrami nucleation mode straightaway differentiates the two intermediate modes. However, a prior knowledge of the growth mechanism is absolutely necessary, as different combinations of nucleation and growth can lead to a change in the transformation kinetics and hence the final grain size distribution. Once the growth mechanism is known, the nucleation and growth parameters can be obtained from

explaining the varying kinetic parameters during the transformation. The estimated Avrami exponent in the present experimental investigation is found to be 2.4 for an isothermal annealing at 1073K. This value also leads to the inference that the nucleation mode for the IFAC-1 in this study follows an intermediate mode of nucleation.

The algorithm presented in this study is also employed to demonstrate the development of grain morphology during static recrystallization for different nucleation modes. Several attempts have been made previously to study the microstructure evolution during primary recrystallization for SSN and CN modes with different growth models [273-276]. Although the grain size distributions obtained by simulation did not agree with the experimental observations, most of them were found approximately to be lognormal. This disagreement was attributed to the inadequacy of the computer model to incorporate the complexity of the recrystallization phenomena. In general the grain size distribution depends on several factors like the mode of nucleation, the mechanism of atomic diffusion for interface migration, the grain boundary energy as well as the presence of impurities and second phase precipitates [284, 285]. All these factors need to be suitably introduced in the model to understand fully the nature of grain size distribution in a real material. Alternatively, the individual aspects can also be studied separately to point out the role of different factors on the final grain size distribution. In this spirit, in analyzing the role of nucleation modes alone, the present study reveals that the size distribution and the average grain size of the recrystallized microstructure are very sensitive to the nucleation mode. For SSN mode, all the nuclei are subjected to grow for the same time duration until completion of transformation. Therefore the individual grain sizes depend only on the impingement between the recrystallized grains which results in a normal grain size distribution (**figure 7.15 (a)**). However, increase in the number of preexisting nuclei leads to the cessation of growth at an early stage of the transformation. Therefore the average grain size is a function of the number

It has been observed that the grain size distribution for SSN mode fits the normal distribution function with better accuracy. However, for CN, MN and AN mode, the grain size is found to follow a lognormal distribution. The grain size distribution for the experimental specimen is also found to be lognormal with the average grain size similar to the simulated one with Avrami nucleation mode.

7.7. Discussion

Although the model presented here is introduced in the context of static recrystallization, it is applicable for any solid state transformation, that is governed by nucleation and growth processes. In general, the kinetic parameters are often derived by linear fitting of the measured data from appropriate experiments using KJMA and MPM formalism. However, these models are based on isokinetic approach, valid only for pure SSN and pure CN mode. In case of transformations mediated through a mixture of pure SSN and CN modes, this linear fitting procedure can produce a unique value for the parameters (n , q , m) which leads to imprecise information about the nucleation and growth modes. Due to this inadequacy of the KJMA approach, various models are developed in order to correctly describe the transformation kinetics and the grain size distribution during static recrystallization [119, 270, 282-283]. The present simulation results demonstrate that, if the nucleation rate (λ_0) in AN mode and the number of preexisting nuclei (N^*) in MN mode are large enough, the contribution from the pure SSN mode is higher. Therefore the estimated kinetic parameters are also close to that of the pure SSN mode. Similarly, for low values of λ_0 in AN mode and higher values of N_0 in the MN mode, the kinetic parameters are close to a pure CN mode. In addition, the homogeneous and heterogeneous choice of nucleation sites is also responsible for the relative contribution of pure SSN and CN modes in case of intermediate modes. Therefore it is possible to estimate the relative contribution of pure SSN and CN modes towards the intermediate modes using the present model, which helps in

recrystallized. This is shown in **figure 7.15 (e)**, where the grain size is normalized to the average grain size of the experimental deformed microstructure (R) in rolling direction (**figure 7.1 (a)**). In order to verify the nature of the grain size distribution under different nucleation modes, the distribution plots in **figure 7.15** are subjected to non-linear fitting with normal and lognormal distribution functions expressed as in *Eq. (7.10)* and *Eq. (7.11)* respectively.

$$Y = Y_0 + \frac{A}{\sqrt{\pi/2} w} \exp\left(-2 \frac{(X - X_c)^2}{w^2}\right) \quad (7.10)$$

$$Y = Y_0 + \frac{1}{\sqrt{2\pi} wX} \exp\left[-\frac{\left(\ln\left(\frac{X}{X_c}\right)\right)^2}{2 w^2}\right] \quad (7.11)$$

Where Y is the distribution function, X_c is the average grain size and w is the full width at half maxima of the distribution. Y_0 and A are constants. The solid lines shown in **figure 7.15** illustrate the fitted distribution function for grain size distributions and the corresponding fit parameters are listed in **table 7.4**.

Table 7.4

The fit parameters obtained from the grain size distribution fits (*Eq. (7.10 & 7.11)*) for simulated (different nucleation modes) and experimental microstructures

Nucleation mode	Grain size distribution function	Y_0	A	X_c (Average grain size)	w	R^2 (fit)
Site saturated Nucleation	Normal	0.012	0.327	$0.35R_0$	$0.25 R_0$	0.96
Continuous Nucleation	lognormal	0.014	0.353	$0.24R_0$	$0.67 R_0$	0.84
Mixed Nucleation	lognormal	0.013	0.439	$0.305R_0$	$0.731 R_0$	0.97
Avrami Nucleation	lognormal	0.051	0.201	$0.192R_0$	$0.510 R_0$	0.9
Experimental	lognormal	0.022	0.224	$0.186R$	$0.514 R$	0.97

corresponding to $f=1$ (complete recrystallization) for all the four different nucleation modes. The grain size(r) for the recrystallized microstructures, in this case is defined as the diameter of a circle with the same area as that of a grain and then normalized with respect to the diameter of the circle with an average grain area of the parent deformed microstructure (R_0) in the rolling direction (**figure 7.5 (b)**). The normalized grain size distribution for the simulated microstructures is illustrated in the **figure.7.15 (a-d)** for SSN, CN, MN and AN modes respectively. In order to compare with experimental results, the grain size distribution is also measured in the experimental sample (**figure 7.1 (c)**) which was completely

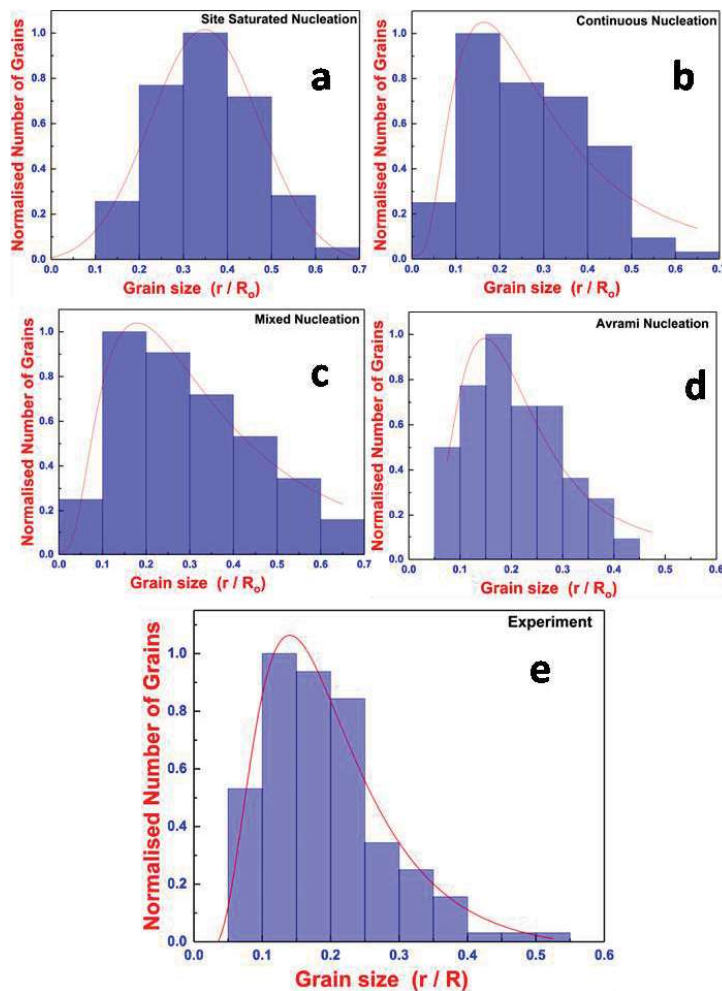


Fig. 7.15. A comparison of grain size distribution in the fully recrystallized microstructure from simulation and experiment for different nucleation modes.(a) Site saturation (b) Continuous nucleation (c) Mixed nucleation (d) Avrami nucleation.(e) from experiment. The grain size is normalized to the average grain size of the corresponding deformed microstructure for both simulation (R) and experiment (R_0).The solid lines in (a) is fitted to Eq. (7.10) and for (b), (c), (d) and (e) is fitted to Eq.(7.11).

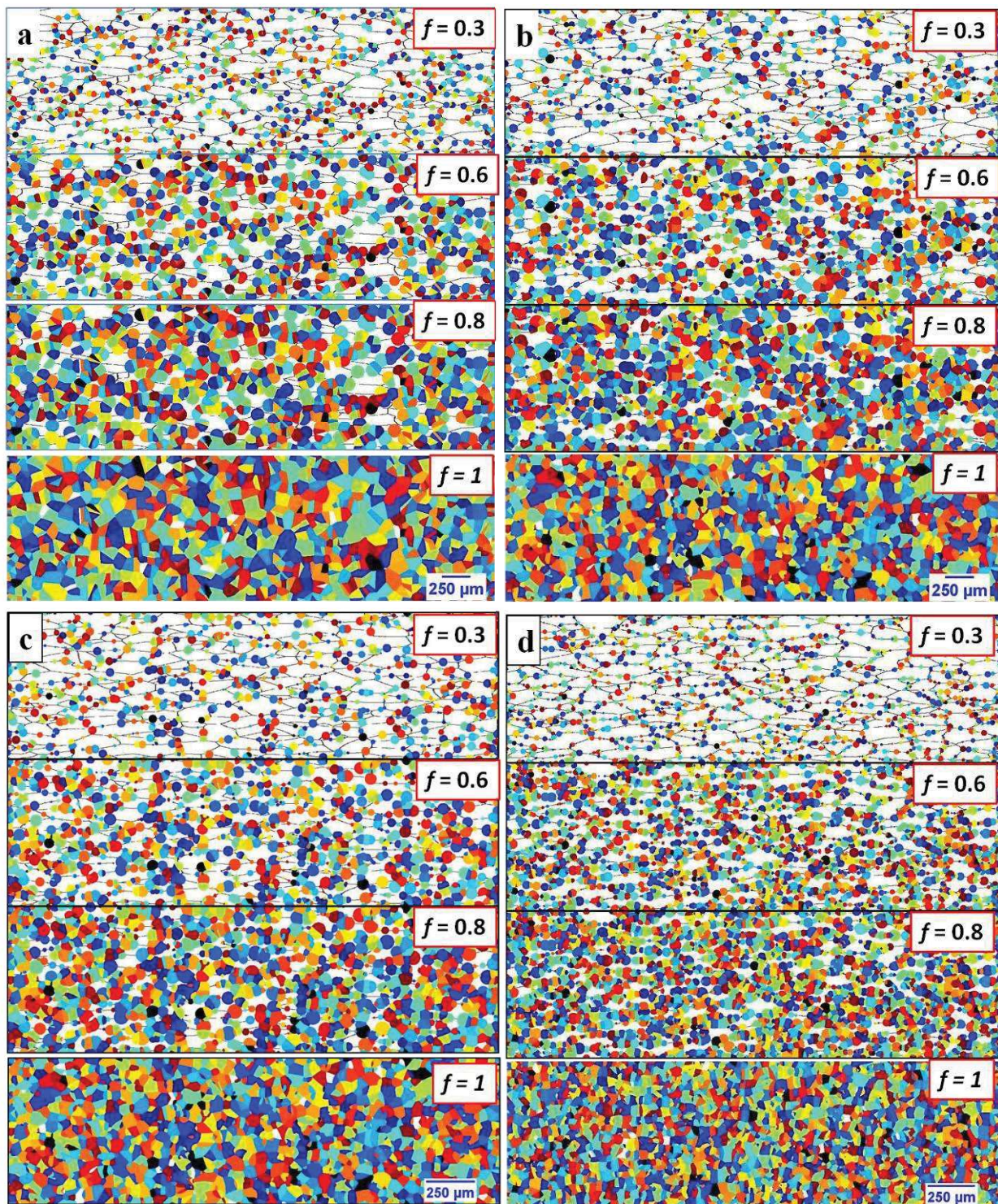


Fig. 7.14. Snapshots of microstructure evolution in (a) Site saturation (SSN) (b) continuous nucleation (CN) (c) Mixed nucleation (MN) and (d) Avrami Nucleation (AN) mode for heterogeneous recrystallization

of λ_o . In the present case, the transformation seems to complete well before all the sites are saturated for nucleation. Therefore Avrami exponent for homogeneous recrystallization in AN mode is found to be constant and similar to that of CN mode throughout the transformation (**figure 7.8 (a)**). In order to further investigate the effect of λ_o on the variation of Avrami exponent, simulations were carried out with varying λ_o under heterogeneous recrystallization module. **Figure 7.13** depicts the variation of Avrami exponent during the transformation for different values of λ_o ($\lambda_o/2$, $\lambda_o/4$, $1.5\lambda_o$, $2\lambda_o$). It can be clearly noticed that with doubling the value of λ_o the n value approaches quickly towards the n value of SSN mode whereas changing the value of λ_o to $\lambda_o/4$, the Avrami exponent remains almost constant which is the characteristics of CN mode. Further **figure 7.9 (a)** and **figure 7.9 (b)** clearly establish a higher value of S_v for AN mode compared to other modes for both homogeneous and heterogeneous recrystallization, which is attributed for the higher nucleation rate. The behavior of q and m parameters is found to be similar to that of n for obvious reasons (**figure 7.10** and **figure 7.11**).

7.6. Simulated and experimental grain size distribution: A comparison

This section deals with the role of nucleation mode in dictating the microstructural evolution under isothermal annealing conditions. **Figure 7.14 (a)-(d)** depict the time evolution of the simulated microstructure under isothermal annealing at 1073 K for SSN, CN, MN and AN mode with heterogeneous recrystallization. The microstructures are chosen for four different transformed volume fractions ($f=0.3, 0.6, 0.8$ and 1) in both cases. In general, higher nucleation rate and/or preexisting nuclei leads to severe impingement between the product phase and the nuclei cease to grow even at a relatively early stage of transformation. Therefore the final grain size distribution and the average grain size are also explicit functions of the nucleation parameters N_o , N^* and λ_o . In order to understand the role of these parameters, the grain size distribution has been measured from the simulated microstructures

(b)). However, as the transformation proceeds, the n value for homogeneous recrystallization remains practically constant whereas for heterogeneous recrystallization the value of n decreases gradually. This can be explained on the basis of individual contributions from pure

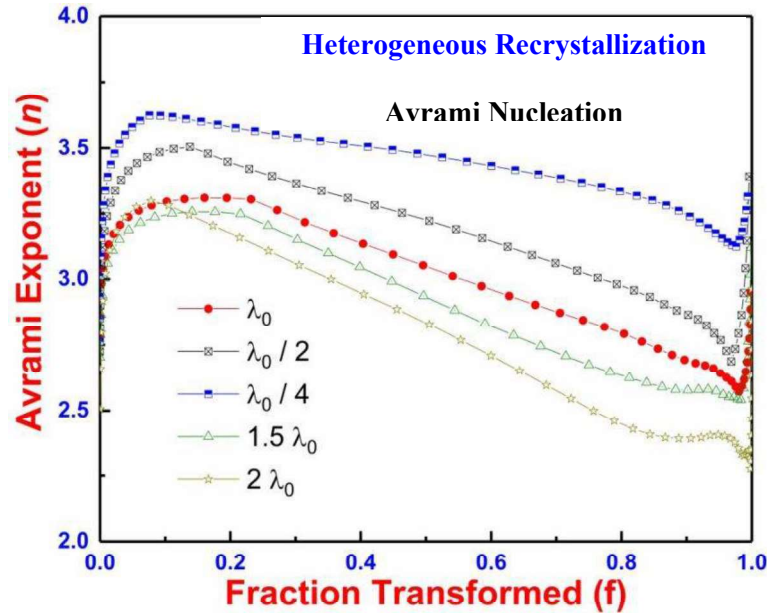


Fig. 7.13. Variation of Avrami exponent for varying (λ_0) in the Avrami nucleation mode with heterogeneous recrystallization. ($\lambda_0=6.4 \times 10^8$ Nuclei m^{-2})

SSN and CN mode which is basically decided by the value of λ_0 . Pure SSN and CN modes are extreme cases of AN mode with very high and very small value of λ_0 . In other words, the parameter λ_0 actually decides the rate of saturation of the available nucleation sites. Therefore with identical values of λ_0 , the AN mode under heterogeneous recrystallization approaches faster towards the SSN mode compared to homogeneous recrystallization, as the number of available nucleation sites is comparatively very small in the heterogeneous case. This explains why the observed n value gradually approaches towards the n value of SSN mode during heterogeneous recrystallization (**figure 7.8(a)**). In the present simulation for AN mode, the complete transformation occurs before all the heterogeneous sites are saturated which results in an n value of 2.5 at the end of the transformation. In a similar line of argument for homogeneous recrystallization, the AN mode approaches towards the SSN mode as all the sites are saturated for nucleation which is only possible for a very large value

in the Avrami exponent in a MN mode actually depends on the nucleation rate (N_0). In order to monitor the dependence of Avrami exponent on the nucleation rate in MN mode, simulations were carried out under heterogeneous nucleation module by altering the values of

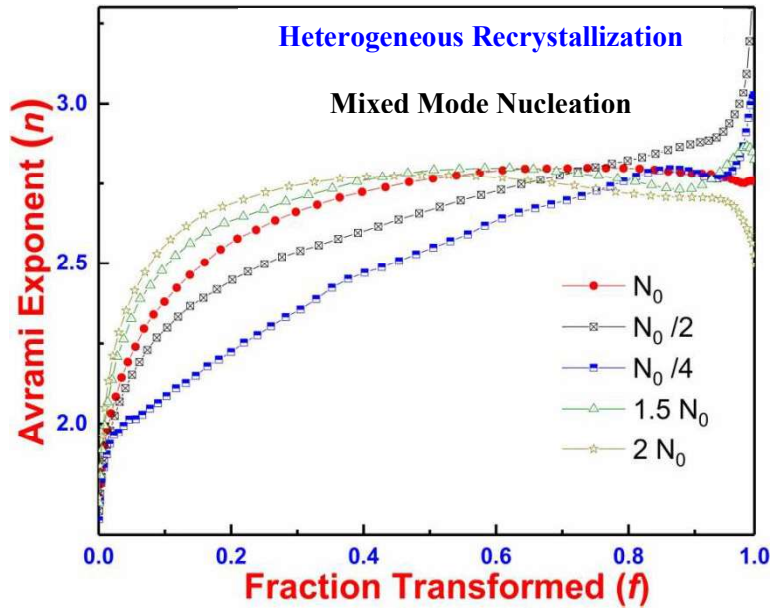


Fig. 7.12. Variation of Avrami exponent for varying nucleation rate (N_0) in the mixed mode nucleation for heterogeneous recrystallization. ($N_0=2.1 \times 10^{16}$ Nuclei m^{-2})

N_0 with the same value for N^* . These results are shown in **figure 7.12** with nucleation rates ($N_0/2$, $N_0/4$, $1.5N_0$, $2N_0$). It can be noticed from **figure 7.12** that by doubling the nucleation rate from N_0 to $2N_0$ the Avrami exponent quickly attains a maximum value and behaves similar to a continuous nucleation mode. On the other hand, if the nucleation rate is changed from N_0 to $N_0/4$, a gradual increase in the Avrami exponent is observed which attains its maximum value nearly at the end of the transformation. The values of q and m for MN mode behave in an identical manner to that of Avrami exponent and vary continuously (**table 7.3**) between the corresponding values of q and m for pure SSN and CN mode in both homogeneous and heterogeneous recrystallization.

7.5.3. Avrami nucleation mode

In contrast to MN mode, the Avrami exponent in case of AN mode is observed to start with an initial value of 3 at the beginning of transformation (**figure 7.8 (a)** and **figure 7.8**

boundary area per unit time) adopted in the present study. This lower nucleation rate in CN mode leads to a slightly higher value of q and m ($q=0.82$ and $m=2.44$) in comparison to the reported values of Goetz and Seetharaman ($q=0.67$ and $m=2$) for homogeneous recrystallization with a nucleation density of 3×10^{-4} nuclei per unit grain boundary area per unit time [150]. The observed q and m values for SSN mode (**table 7.3**) are in good agreement with the predicted values of q and m by Goetz and Seetharaman [150]. Similar observations have been obtained for heterogeneous recrystallization under both SSN and CN modes.

7.5.2. *Mixed nucleation mode*

The Avrami exponent for the MN mode (**figure 7.8 (a)** and **figure 7.8 (b)**) starts with a value of 2 at the beginning of the transformation where the contribution is purely from SSN mode. However as the transformation proceeds, nuclei add up continuously and the Avrami exponent gradually approaches towards the theoretical values of CN mode ($n=3$). This is because the MN mode is actually a mixture of pure SSN and CN modes depending on the values N_0 , and N^* (*Eq. (2.5)*). Therefore the overall kinetics is also decided by individual contributions from pure SSN and CN modes. Although this happens in both homogeneous and heterogeneous recrystallization, the Avrami exponent is found to increase rapidly in heterogeneous recrystallization as compared to homogeneous one. This is because; the availability of total nucleation sites in case of a heterogeneous recrystallization is small, when compared with homogeneous recrystallization. Therefore with identical nucleation rate for both homogeneous and heterogeneous recrystallization, the rate at which the available nucleation sites are filled up during continuous nucleation is higher in case of a heterogeneous recrystallization. This fact can also be witnessed from **figure 7.9 (b)** for heterogeneous recrystallization, where the difference in S_v for MN and CN mode is less in comparison to homogeneous recrystallization (**figure 7.9 (a)**). Therefore the rate of increase

continuously for which it was evaluated for several domains of transformed fraction and the variation in the range of q is evaluated. Further, the m values for different nucleation modes are also estimated in a manner similar to that of q from the slope of the plot $\ln(S_v/(1-f))$ vs $\ln(t)$ (see **figure 7.11 (a)** and **figure 7.11 (b)**). The estimated values of n , q , m from the simulation are listed in **table 7.3**.

Table 7.3

The variation of kinetic parameters calculated from the simulation using KJMA and MPM model [Hom. Rxtn. (Homogeneous Recrystallization), Het. Rxtn. (Heterogeneous Recrystallization)]

Nucleation Mode	n		q		m	
	Hom. Rxtn	Het. Rxtn	Hom. Rxtn	Het. Rxtn	Hom. Rxtn	Het. Rxtn
SSN	1.98	1.77	0.47	0.46	0.88	0.86
CN	2.98	2.83	0.82	0.78	2.44	2.13
MN	2-3	2-2.83	0.48-0.83	0.52-0.67	0.86-2.42	1-1.7
AN	3.15	3.2 - 1.5	0.79	0.77-0.53	2.42	2.01-1.41

7.5. Analysis of kinetic parameters under different nucleation modes

7.5.1. Site saturation and continuous nucleation mode

The observed value of n during heterogeneous recrystallization for SSN mode ($n=1.77$) and CN mode ($n=2.83$) is slightly lower than the KJMA model prediction ($n=2$ for SSN and $n=3$ for CN) whereas a good agreement is observed for the case of homogeneous recrystallization. This can be explained with the Cahn's modification of KJMA approach for heterogeneous recrystallization which states that the n value in a heterogeneous recrystallization comes down due to the reduced dimensionality of growth [281]. Further the delayed occurrence of $S_v = (S_v)_{\max}$ observed for the CN mode, in contrast to SSN mode (**figure 7.9 (a)** and **figure 7.9 (b)**) can be ascribed for the reduced impingement between the product phases resulting due to the lower nucleation rate (1.7×10^{-5} nuclei per unit grain

different for each nucleation mode depending on the number of preexisting nuclei and the nucleation rate. **Figure 7.10 (a)** and **figure 7.10 (b)** show the plot of $\ln (S_v (1-f))$ vs $\ln (-\ln (1-f))$ for all the nucleation modes in homogeneous and heterogeneous recrystallization respectively. The data points were subjected to a linear fit with *Eq. (2.24)*, excluding the nonlinearity part observed above ($f > 0.97$) and the slope of the linear fit (q) is estimated for SSN and CN mode. For MN and AN nucleation mode, the slope is observed to vary

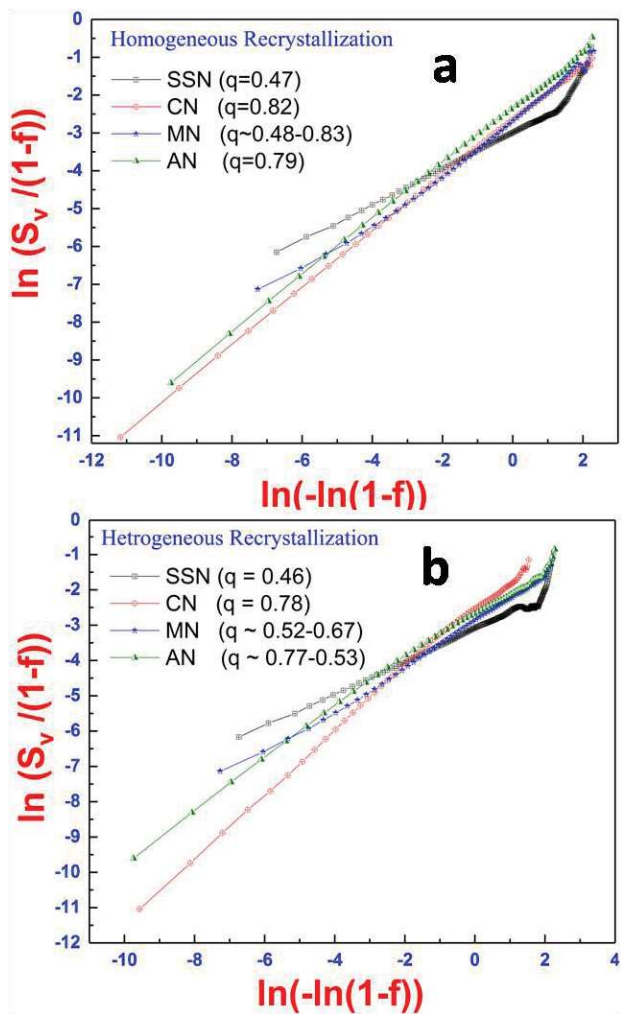


Fig. 7.10. Plots of $\ln (S_v/(1-f))$ vs $\ln (-\ln(1-f))$ for different nucleation modes under (a) homogeneous recrystallization (b) heterogeneous grain boundary recrystallization. The slope of the plots (q) is estimated using *Eq. (2.24)* excluding the nonlinear region observed at the end of the transformation. The q values are listed in the figure for corresponding nucleation modes

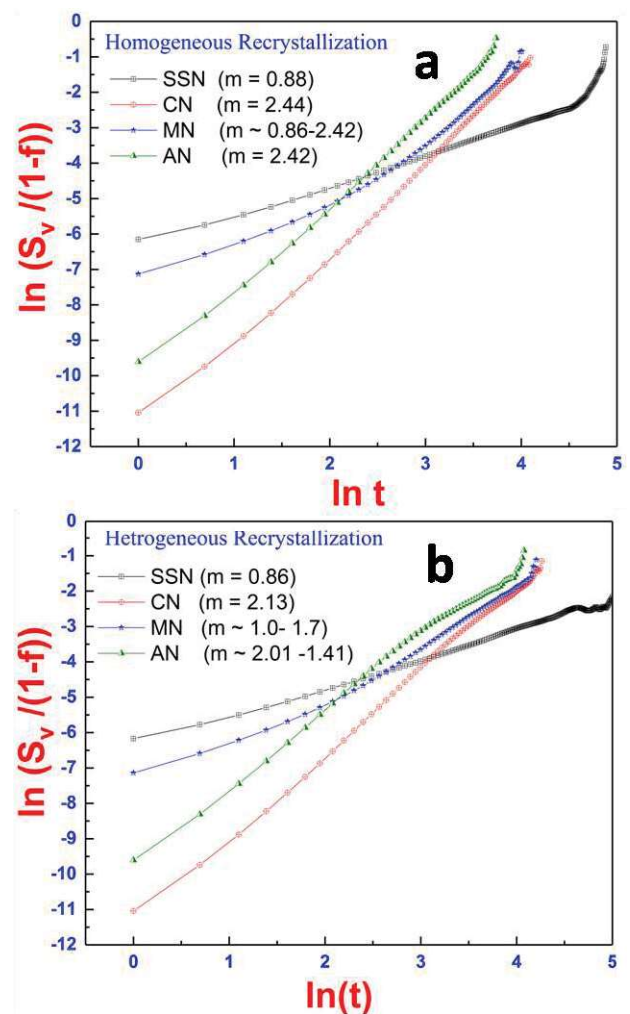


Fig. 7.11. Plots of $\ln (S_v/(1-f))$ vs $\ln (t)$ for different nucleation modes under (a) homogeneous recrystallization (b) heterogeneous grain boundary recrystallization. The slope of the plots (m) is estimated using *Eq. (2.23)* excluding the nonlinear region observed at the end of the transformation. The m values are listed in the figure for corresponding nucleation modes

volume because only a few growing nuclei are available at the very beginning and also at the end of the transformation [280]. **Figure 7.9 (a)** and **figure 7.9 (b)** show the variation of (S_v) as a function of recrystallized fraction (f) for homogeneous and heterogeneous recrystallization respectively. It can be clearly observed that the value of S_v is always higher in case of homogeneous recrystallization as compared to the heterogeneous one; because of less impingement taking place in the former case. Therefore the variations of S_v are also

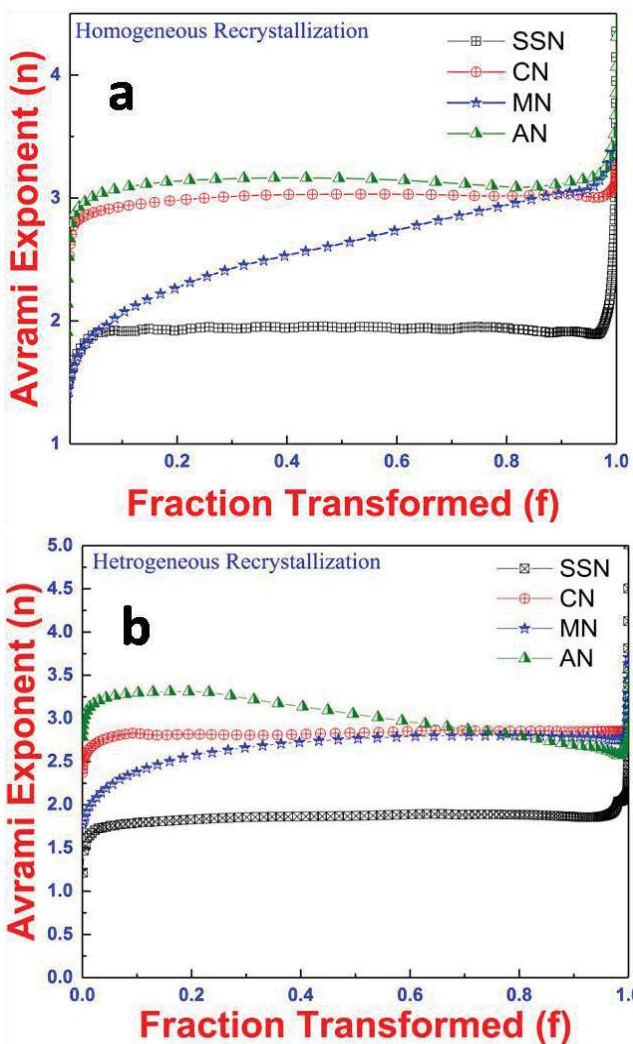


Fig. 7.8. Variation of Avrami exponent with transformed fraction for different nucleation modes (a) homogeneous recrystallization (b) heterogeneous recrystallization

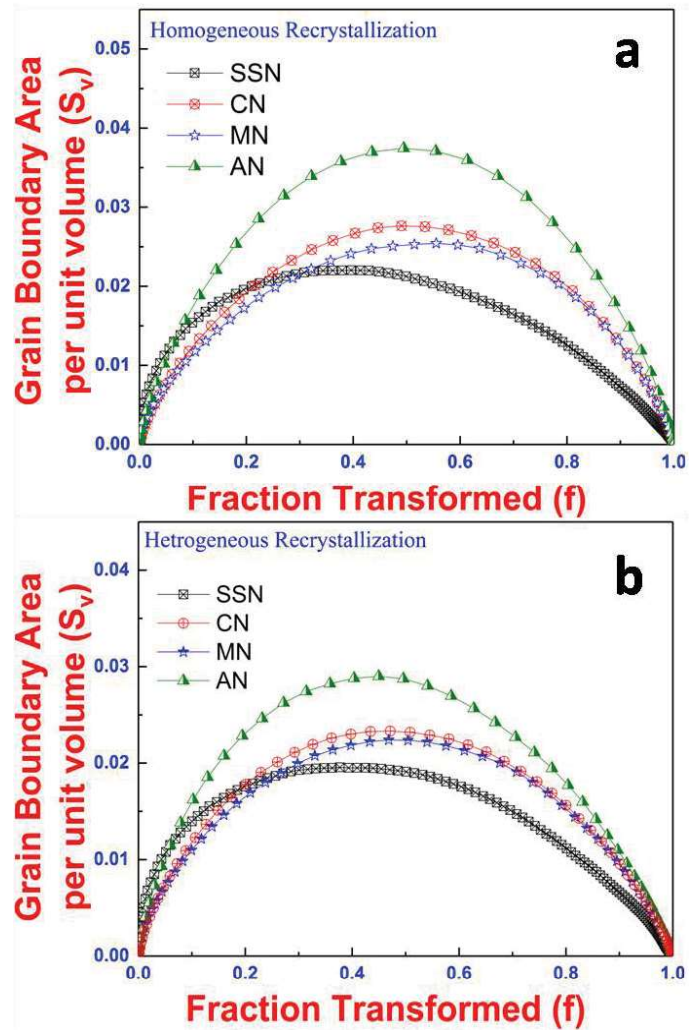


Fig. 7.9. Variation of Grain boundary area per unit volume as a function of transformed fraction estimated from the simulation for different nucleation modes (a) Homogeneous recrystallization (b) Heterogeneous recrystallization

actual transformed fraction estimated from the microstructural parameters using *Eq. (7.6)*; whereas the solid lines through these points are based on Avrami model derived using *Eq. (2.14)* and *Eq. (7.7)*. The observed difference in the KJMA model prediction and the actual transformed fraction is within 3%. This signifies that the present algorithm has high accuracy. The major source of error in this model arises primarily from space discretization scheme. In general, the ratio of the size of simulation volume to that of a single cell should be as high as possible, to achieve more accurate results. In this context, in the present model, the area of a single cell is assumed as $0.25 \mu\text{m}^2$ to enhance the accuracy. The actual transformed fraction estimated from *Eq. (7.6)* is used in the kinetic analysis of static recrystallization in this study which is described in the next section.

7.4. Results

7.4.1. Evaluation of kinetic parameters from simulation

In general, the Avrami exponent (n) can be estimated from the transformed fraction data by taking the double logarithm of *Eq. (2.15)*.

$$\ln(-\ln(1-f)) = n \ln K_o - \frac{nQ}{RT} + n \ln t \quad (7.8)$$

The Avrami exponent n is the slope of the plot $\ln(-\ln(1-f))$ vs $\ln(t)$ and can be obtained by differentiating *Eq. (7.8)*.

$$n = \frac{\partial [\ln(-\ln(1-f))]}{\partial \ln t} \quad (7.9)$$

The values of n estimated using *Eq. (7.9)* as a function of the transformed fraction are plotted in **figure 7.8 (a)** and **figure 7.8 (b)** for homogeneous and heterogeneous recrystallization respectively. Comparison of **figure 7.8 (a)** and **figure.7.8 (b)** clearly reveals that the Avrami exponent deviates from the normal trend below 3% and above 97% of transformation for both homogeneous and heterogeneous recrystallization in a similar fashion. This deviation, as pointed out by Hesselbarth and Gobel, occurs in all simulations with discrete space in a finite

7.2) for different nucleation modes for an isothermal annealing at 1073 K is illustrated in figure 7.6. Figure 7.7 represents the variation of transformed fraction estimated for different nucleation modes under homogeneous recrystallization. The scattered points represent the

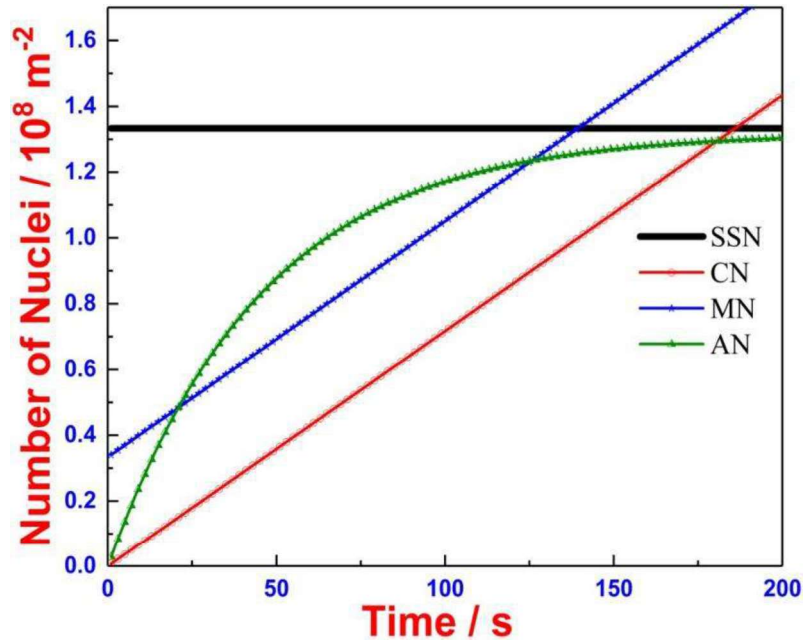


Fig. 7.6. Time evolution of number of nuclei per unit volume for different nucleation modes considered in the present simulation

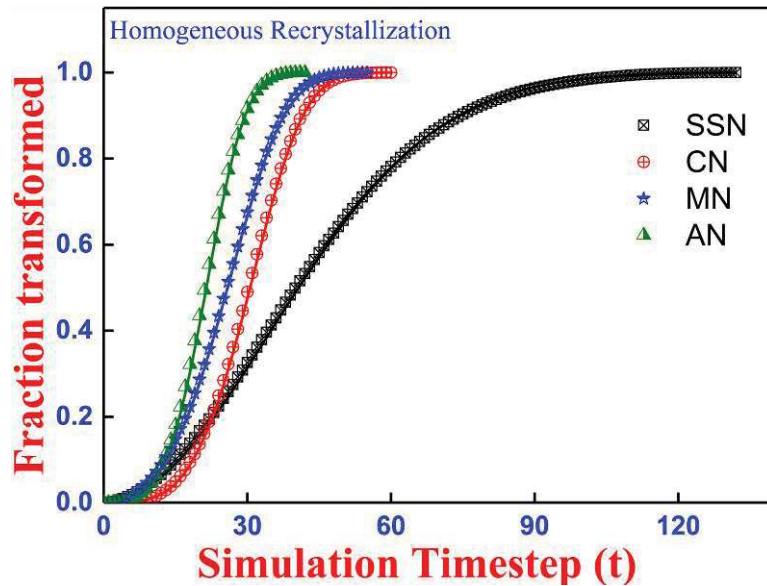


Fig. 7.7. The time evolution of recrystallized fraction as calculated from the microstructure evolution from the simulation for different nucleation modes in homogeneous recrystallization. The solid lines represent the transformed fraction calculated from KJMA model

7.3.3. Evaluation of actual and extended transformed fraction

Once the recrystallization is initiated, the fraction of the recrystallized volume $f(t_i)$ is estimated at each time step by taking the ratio of the number of recrystallized cells to the total number of cells in the initial volume.

$$f(t_i) = \frac{\text{No of cells with state variable } (\varphi > 0)}{\text{Total no of cells in the initial volume}} \quad (7.6)$$

In the present scheme, we have also calculated the time evolution of the extended volume fraction ($f_{ext}(t)$) using the following expression.

$$f_{ext}(t_i) = \frac{\Omega}{V} \sum_{i=1}^{t_i} N_{t_i-i+1} (Gi)^s \quad (7.7)$$

Where, N_r is the number of nuclei appearing in the r^{th} simulation time step, calculated from Eq. (2.3 - 2.7), V stands for the total simulation volume and Ω is the geometrical factor which depends on the shape of the evolving grain. In the case of isotropic growth, Ω takes a value π or $4\pi/3$ for two and three-dimensions respectively. The parameter s stands for the growth dimensionality and has a value of 2 and 3 for two and three dimensional growth respectively. For the calculation of total interfacial boundary cells at each time step, the total number of deformed cells with ($\varphi=0$) was found out which have at least one neighboring recrystallized cell ($\varphi>0$). This number was then divided by the total simulation volume to estimate the interfacial area between recrystallized and non-recrystallized regions (S_v) (see section 2.12.2).

7.3.4. Accuracy of the algorithm

The relationship between actual and extended transformed fraction in Eq. (2.14) is exact, although the applicability of KJMA model is limited to certain conditions of nucleation and growth [279]. Therefore, the actual transformed fraction calculated from the present simulation (Eq. (7.6)) is compared with values estimated analytically from Avrami model using (Eq. 2.14) & (Eq. 7.7) to check the accuracy of the present algorithm. The time evolution of the number of nuclei per unit volume, calculated (using the parameters in table

appearing during the time step $t = t_{i-1}$ to $t = t_i$ will be allowed to grow with a constant growth velocity calculated using *Eq. (2.13)*. The radial increment ($\Delta x(t_i)$) during the growth of these nuclei in the time span of $t = t_{i-1}$ to $t = t_i$ is estimated from the following equation.

$$\Delta x(t_i) = \int_{t_{i-1}}^{t_i} G_v d\tau \quad (7.4)$$

Where G_v stands for the growth velocity. For all the previous nuclei appeared before time t_{i-1} having radii $x(t_{i-1})$, will grow into the deformed region with an updated radius $x(t_i)$ at time t_i .

$$x(t_i) = x(t_{i-1}) + \Delta x(t_i) \quad (7.5)$$

In accordance with the Avrami model, the radius calculated from *Eq. (7.5)* is called as the extended radius of the nuclei. For the calculation of actual growth, only those cells are identified at the i^{th} time step, whose distance from the center of the nuclei lies between $x(t_{i-1})$ and $x(t_i)$. These cells are then checked to verify their state variables, to ensure that they belong to the deformed state. If this condition is satisfied, the identified cells are assigned the same state variable $\varphi = p_1$ as that of the center cell. Otherwise, those cells are left unattended without a change in the state variable. The capillary pressure arising from the grain boundary curvature is neglected in the present algorithm. The entire simulation was carried out at an annealing temperature of 1073 K in the defined simulation volume under periodic boundary conditions. Once the state variable of all the deformed cells in the simulation volume changes their state from $\varphi = 0$ to $\varphi > 0$, the time loop ends with a 100% transformation. A minimum of five such simulations was performed for each nucleation mode to check the accuracy of the algorithm. The entire code for the simulation has been developed in-house based on this algorithm.

7.3.2. Algorithm for simulation of static recrystallization

The size of each cell was arbitrarily chosen as $\Delta x=0.5 \mu m$ in the deformed volume which represents the spatial resolution of the model. With this choice of cell length, the average grain size along the rolling direction (R_o) in the deformed microstructure, shown in **figure 7.5 (b)**, is found to be $157 \mu m$. Every individual cell in the grid is defined by an integer coordinate and is assigned one state variable (ϕ) that physically represents the orientation information in the scalar form. The state ($\phi=0$) represents a deformed state and ($\phi>0$) represents a fully recrystallized state inside the simulation volume. For the homogeneous nucleation module, nucleation sites are picked randomly from all cells in the simulation volume. However, under heterogeneous nucleation module, the integer coordinates of all the cells along the grain boundaries are identified and saved in a separate array from which heterogeneous nucleation sites are chosen randomly. The number of nucleation sites appearing during time step $t= t_{i-1}$ to $t=t_i$ is evaluated from the following equation.

$$\Delta N(t_i) = V \left[\int_0^{t_i} \dot{N} d\tau - \int_0^{t_{i-1}} \dot{N} d\tau \right] \quad (7.3)$$

Where \dot{N} is the nucleation rate per unit volume calculated from Eq. (2.3) - (2.7), for SSN, CN MN and AN modes respectively and V is the simulation volume. Once a new nucleus has appeared in one cell, it is assigned with a specified state variable $\phi=p_1$, chosen randomly in the range, 1-90. This cell serves as the center of the strain-free grain during the isotropic growth in subsequent time. The state variable $\phi=p_1$ assigned to a nucleated cell actually separates the cell from its surrounding cells which either belongs to a deformed state ($\phi=0$) or another strain-free grain with a different state variable ($\phi >0$). If nuclei appear at a cell that belongs to a strain-free grain, it is considered as phantom nuclei, as termed by Avrami. A phantom nucleus is not allowed to appear in the simulation volume although they are included for the calculation of extended volume fraction. The $\Delta N (t_i)$ number of nuclei

deformed region. Additionally, the interface is assumed to move with a constant isotropic velocity, until and unless they impinge with another interface. At first sight, the assumption on constant and isotropic interface velocity appears to oversimplify the model because it is known that in practical situations the interface moves with varying velocity depending on the orientations of the neighboring sites. However, for the present purpose of evaluating the kinetic parameters under different possible nucleation modes and compare with the theoretically predicted values from KJMA and MPM method, this assumption can be justified. To serve this purpose, the present model is formulated in tune with the KJMA model which assumes random nucleation and constant isotropic growth for the product phase nuclei.

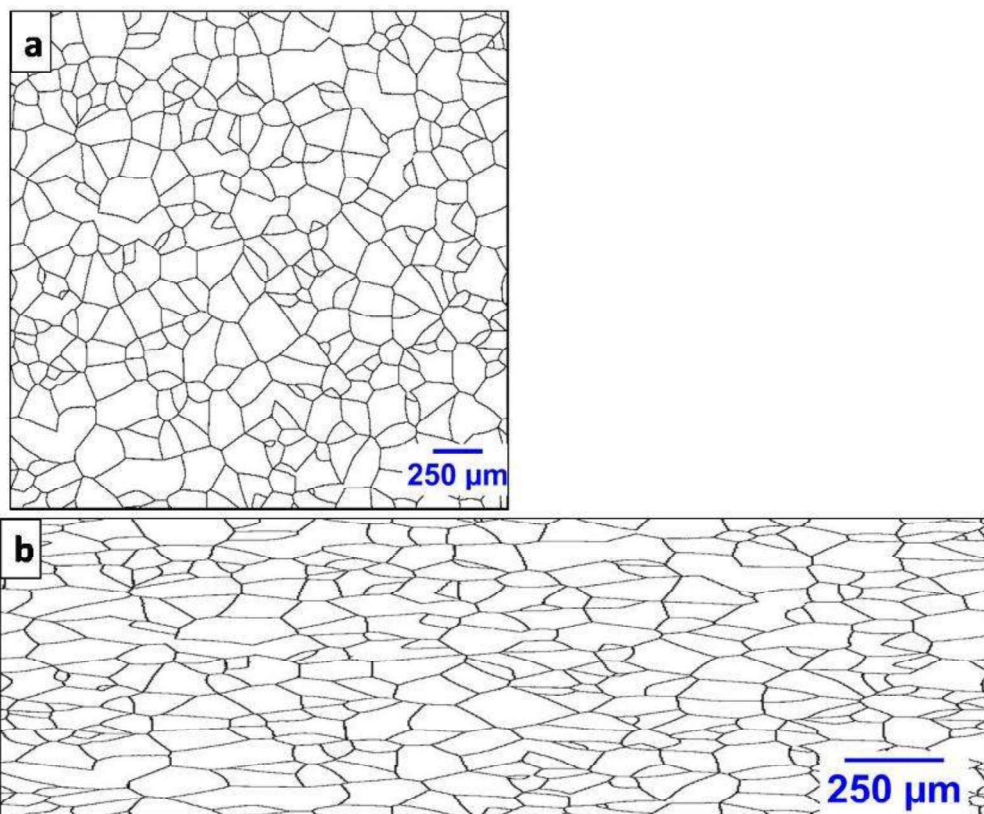


Fig. 7.5. (a) The initial microstructure generated using the present algorithm **(b)** The 70% rolled microstructure generated from microstructure shown in (a) by uniform compression in one direction

and Q_G values. Similarly, a systematic deviation of 2% in the measured f curves results in a maximum of 22 % error in the original values of Q_N and Q_G . It is noteworthy to mention here that the estimated activation energies for nucleation and growth (Q_N and Q_G) are valid only for CN, MN, AN modes of nucleation. In case of SSN mode, $Q_{eff} = Q_G$. The estimated values of Q_N , Q_G as well as the numerical values of the parameters figuring in Eq. (2.3-2.7) and Eq. (2.13) are listed in **table 7.2** [119, 126]. These values serve as inputs for the simulation component of this study. This is discussed next.

7.3. Simulation method

7.3.1. Setup of the deformed microstructure

The initial microstructure was generated on a (5000 × 5000) grid of square cells by simulation of homogeneous recrystallization with continuous nucleation mode under periodic boundary conditions. This has been generated using the algorithm (*Appendix-A*) which has also been used to obtain the microstructures that evolve during recrystallization. The details of the algorithm are described in the succeeding section. In the next step, the initial microstructure generated is deformed homogeneously to the extent of 70% (thickness reduction) by simulations of plane strain compression test which is used in industrial rolling to produce genuine descriptions of microstructures [278]. This compressed grid of cells (5000 × 1500) generated by the above procedure serves as the deformed volume for the nucleation and growth of strain-free grains in all the simulations carried out in this study. The basic purpose of this thickness reduction procedure is to compare the grain size distribution of the recrystallized grains under different nucleation modes as a function of the average grain size of the deformed structure in the rolling direction. **Figure 7.5 (a)** and **figure 7.5 (b)** show the initial and the subsequent deformed volume generated in the above procedure. Before proceeding further, it is worthy of mentioning here that the stored energy due to deformation, which is the driving force for recrystallization is assumed to be uniform throughout the

in **figure 7.4** (scattered points) and fitted to *Eq. (7.2)* (solid line) to obtain the fit parameters $Q_N=215\pm 20$ and $Q_G=280\pm 6$ kJmol⁻¹.

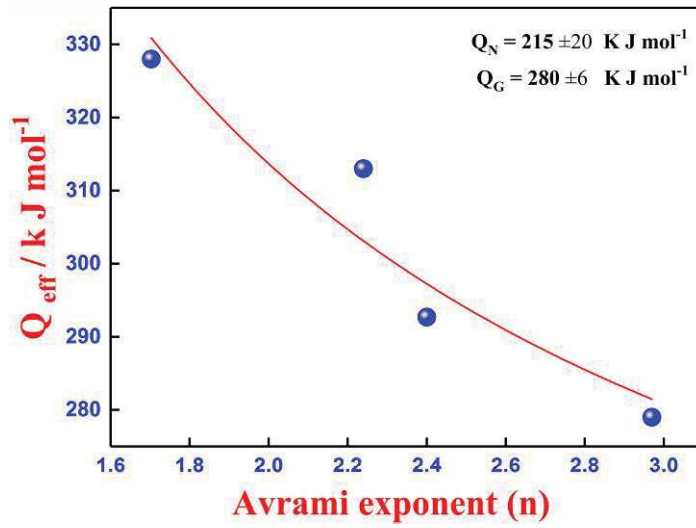


Fig. 7.4. Effective activation energy (Q_{eff}) as a function of Avrami exponent. The solid line represents the fitted curve according to *Eq. (7.2)*

Table 7.2

Numerical value of the parameters in *Eq. (2.3-2.7)* and *Eq. (2.13)* used in the computer simulation [119, 126]. The activation energy for nucleation (Q_N) and growth (Q_G) is estimated from the experimental data.

Nucleation Mode	Pre-exponential Term (Nucleation) Nuclei m ⁻²	Q_N kJ mol ⁻¹	Q_G kJ mol ⁻¹	Preexponential Term (Growth) m s ⁻¹
Site Saturated Nucleation (SSN)	$N^* = 1.332 \times 10^8$	0	292	$G_o = 8.55 \times 10^7$
Continuous Nucleation (CN)	$N_o = 2.1 \times 10^{16}$	215	280	
Mixed mode Nucleation (MN)	$N^* = 3.3 \times 10^7$ $N_o = 2.1 \times 10^{16}$	215	280	
Avrami Nucleation (AN)	$\bar{N} = 1.32 \times 10^8$ $\lambda_o = 6.4 \times 10^8$	215	280	

In order to observe the robustness of the fit parameters, a sensitivity analysis was carried out to monitor the effect of the experimental error. It has been observed that a systematic deviation of 2 K in the temperature produces up to 10 % variation in originally estimated Q_N

comes down slightly at the end of the transformation. It is important to mention here that, the concept of constant kinetic parameters is indeed a coarse approximation, which is valid only in the case of pure SSN and CN mode [126, 134, 137]. However, for transformations taking

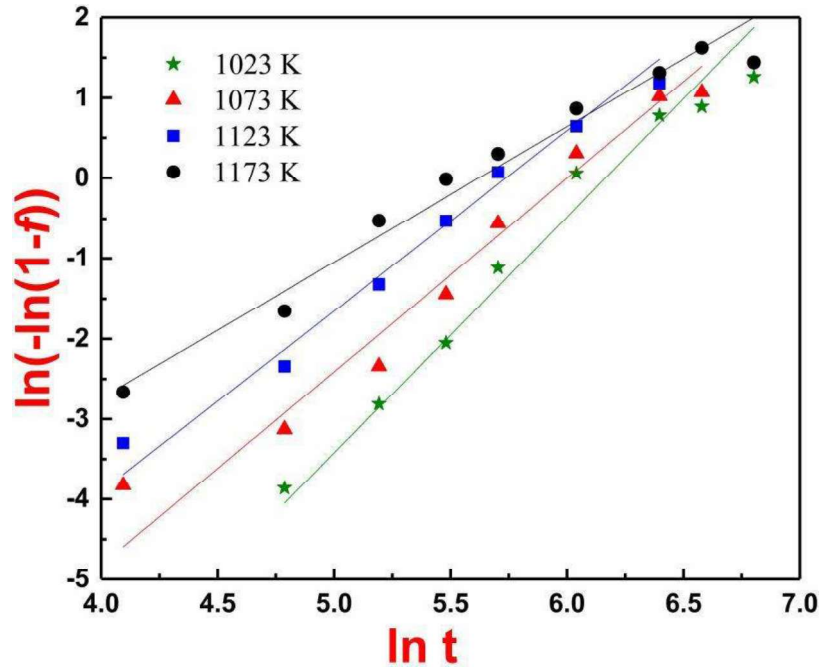


Fig. 7.3. The Avrami plot for isothermal static recrystallization at four different temperatures

place with intermediate nucleation modes, the effective activation energy can be represented as a sum of individual contributions arising independently from nucleation and growth using the following equation [126, 134, 137].

$$Q_{eff} = \frac{\frac{d}{m_G} Q_G + \left(n - \frac{d}{m_G} \right) Q_N}{n} \quad (7.2)$$

Where d and m_G stand for the dimensionality of growth and the mode of growth respectively. The parameter m_G has the value of 1 and 2 for interface and diffusion controlled growth modes respectively. The parameter n is the Avrami exponent which has the value (d/m_G) for pure site saturation and (d/m_G+1) for continuous nucleation. In the present experimental conditions, the value of (d/m_G) is 3. The parameters Q_N and Q_G stand for individual activation energies for nucleation and growth. The estimated values of Q_{eff} and n (table 7.1) are plotted

correspond to the experimental values while the line depicts the fitted curve using KJMA model given in Eq. (2.15). By using similar procedures for different annealing temperatures of 1023, 1073, 1123, 1173 K, the effective activation energy and Avrami exponent are estimated. These parameters (n , Q_{eff} , k_o) are listed in **table 7.1**. **Figure 7.3** depicts the so-called Avrami plot obtained from the time variation of the measured transformed fraction (scattered points) along with the linear fits (solid lines) under isothermal annealing at the

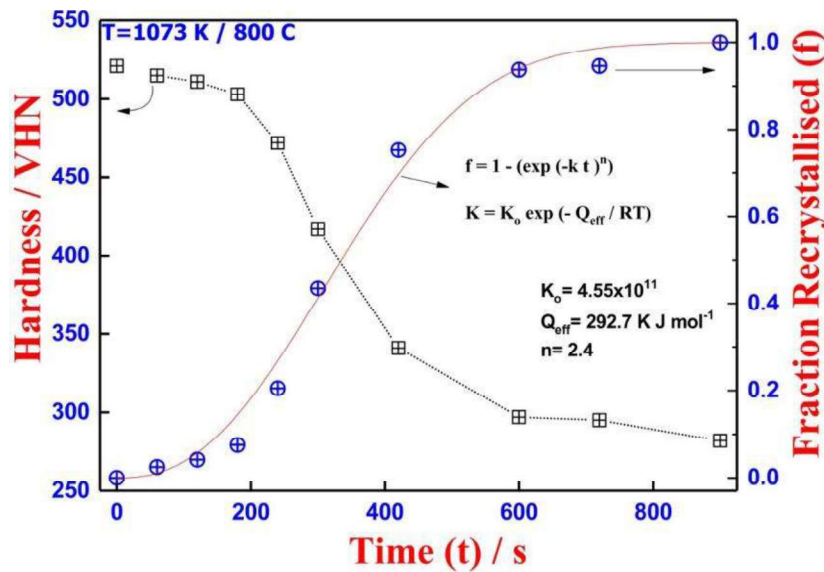


Fig. 7.2. Variation of microhardness and the recrystallized fraction with annealing time for IFAC-1 austenitic stainless steel at annealing temperature 1073 K

Table 7.1

Experimentally measured kinetic parameters (n , Q_{eff} and k_o) for static recrystallization in IFAC-1 at different annealing temperatures in accordance with KJMA model

Temperature of Annealing (K)	Avrami Exponent(n)	Effective Activation Energy (Q_{eff}) / kJ mol ⁻¹	k_o / s ⁻¹	R ² /fit
1023	2.97	279	2.62x10 ⁶	0.99
1073	2.4	293	1.08x10 ⁸	0.99
1123	2.24	313	2.08x10 ⁹	0.99
1173	1.703	328	8.07x10 ¹⁰	0.99

above-mentioned temperatures. It is interesting to note here that the Avrami exponent which is the slope of the plots in **figure 7.3** is almost constant during the transformation although it

521±12 VHN, which gradually decreases to 294±8 and 282±10 VHN after isothermal annealing for 600 and 900 s respectively. Complete recrystallization is observed after 900 s of annealing at 1073 K. The extent of recrystallization as a function of time has been calculated from hardness data under isothermal annealing using the expression given below.

$$f = 1 - \frac{(H_t - H_f)}{(H_0 - H_f)} \quad (7.1)$$

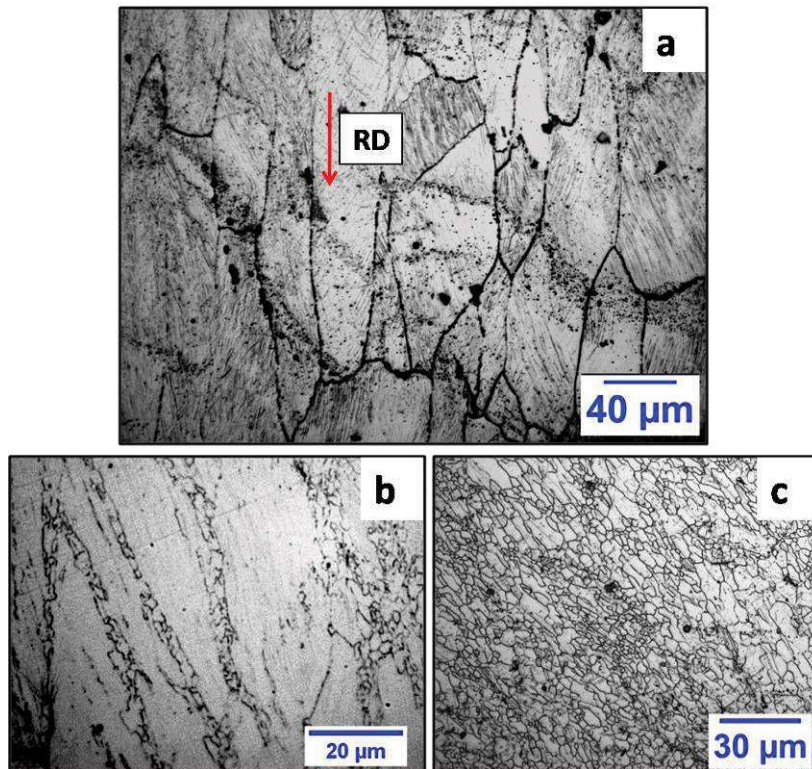


Fig. 7.1. (a) The optical micrograph for 70% rolled austenitic stainless steel showing elongated grains in the rolled direction (b) Nucleation of strain-free grains along the grain boundary of the deformed austenitic stainless steel after annealing for 240 s at 1073 K (c) microstructure showing complete recrystallization for annealing time 600 s at 1073 K

Where f is fraction transformed, H_t corresponds to hardness value for a typical annealing time t , H_0 stand for starting hardness of the deformed sample and H_f is the hardness of sample annealed for the maximum time duration (900 s). This is depicted in **figure 7.2**, where the left Y-axis stands for the measured hardness values and the right Y-axis represents the fraction transformed at an annealing temperature of 1073 K. In **figure 7.2** the scattered points

parameters is analyzed to examine the applicability of isokinetic approach for different nucleation modes. In addition, the grain size distribution under different nucleation modes has also been evaluated from the simulated microstructures and compared with experimental results.

7.2. Experimental study

Samples of size (5x5x2) mm were prepared from 70% cold rolled IFAC-1 SS plate and isothermally annealed in a muffle furnace at four different temperatures (1023, 1073, 1123 and 1173 K) in the time span ranging from 0 to 15 minutes. The annealed samples were water quenched in order to retain the microstructure that is representative of the annealing temperature. The selection of the above temperatures is based on the fact that they are well above the onset temperature of recrystallization for this steel [277]. The microstructural characterization and the micro-hardness measurements of deformed and annealed samples were performed using optical microscopy and *Leitz* microhardness tester. At least 8 to 12 indentations were made for each sample and the average of all the measurements is accepted as the representative hardness value.

7.2.1. Estimation of activation energy

Figure 7.1(a) illustrates the optical microstructure of the 70% rolled IFAC-1 showing elongated grains in the rolling direction. The average grain size is found to be $124 \pm 7 \mu\text{m}$ along the rolling direction. **Figure 7.1(b)** and **figure 7.1(c)** illustrate the optical microstructures after isothermal annealing of the deformed steel at 1073 K for a time span of 240 s and 600 s respectively. Partial recrystallization is observed for the sample annealed for 240 s with the appearance of new strain-free grains (**figure 7.1(b)**) nucleated preferentially along the grain boundary regions of the deformed grain structure. The microstructure of the sample annealed for 600 s (**figure 7.1(c)**) shows a fully recrystallized structure with very fine grains. It is observed that the average microhardness value for the 70% cold rolled IFAC-1 is

272]. A detailed description on the possible nucleation and growth modes during diffusional phase transformations is provided in chapter 2 (*see section 2.10*).

Several analytical and computational methods have been employed in the past to study the kinetics and microstructure evolution during recrystallization [273-274]. The grain size distributions in static recrystallization, resulting due to different nucleation and growth rates have been addressed by Saetre *et al* and Marthinsen *et al* using geometrical models [273-274]. Latter Srolovitz *et al* observed minor deviations of Avrami exponent from KJMA prediction for site saturated and constant nucleation modes using Monte Carlo simulation technique [275, 276]. The systematic variation of n , q , and m was demonstrated by Goetz *et al* using a cellular automata model and found reasonable agreement with the theoretical values of KJMA and MPM model [150]. However, the nucleation modes adopted in all these studies are either pure site saturation or continuous. In actual practice, the nucleation can occur in an intermediate mode i.e. a mixture of pure site saturation and continuous mode such as mixed or Avrami mode where the KJMA kinetics may not be applicable (*see section 2.10.1*) [120-122]. It is important to mention here that, altering the nucleation mode to examine the effect of nucleation on the overall kinetics of recrystallization is almost an impossible task by experiment. In this regard the present chapter deals with an algorithmic approach that provides for accurate prediction of the time evolution of parameters f , f_{ext} , and S_v during the process of thermally activated static recrystallization, following plastic deformation. The static recrystallization in IFAC-1 has been experimentally studied to obtain the activation energies which are used as the input parameters for the simulation. The kinetic parameters (n , q , m) are explicitly evaluated from the simulation for pure *site saturation* (*SSN*), *pure continuous nucleation* (*CN*) and *intermediate modes like mixed nucleation* (*MN*) and *Avrami nucleation* (*AN*) in both *homogeneous* (spatially random nucleation) and *heterogeneous* (grain boundary nucleation) recrystallization. Further, the variation of kinetic

Role of Nucleation Mode on Kinetics of Static Recrystallization & Grain Structure Development: A Mesoscopic Simulation Approach

7.1. Introduction

The kinetics of recrystallization has drawn substantial attention not only due to its technical importance in controlling the grain morphology to design materials with improved properties, but also to develop a fundamental understanding of the underlying mechanism of the process itself. The overall kinetics of recrystallization is basically decided by the cooperative dynamics of individual processes like nucleation, growth and impingement as pointed out by Kolmogorov-Johnson-Mehl-Avrami (KJMA) model [126-128, 139, 140]. The detailed description on the KJMA formalism is elaborated in Chapter 2 (*see section 2.12.1*). The kinetic parameters n , Q_{eff} , and k_0 in the classical KJMA model depend solely on the dynamics of individual processes involved in the transformation and therefore the accurate estimation of these quantities provides an insight into the underlying mechanism of transformation, which in turn helps in controlling the final grain structure. However the general KJMA model is based on the isokinetic approach which implies that the kinetic parameters n , Q_{eff} , and k_0 remain constant during the entire course of transformation [133-137]. Similarly the microstructural path method (MPM) developed by Vandermeer and co-workers (*see section 2.12.2*) to study the kinetics of transformation that is governed by nucleation and growth processes is also based on the isokinetic approach from KJMA formalism and the kinetic parameters q and m are again constant throughout the transformation [144-149]. It has been observed that experimentally measured kinetic parameters often deviate from *ideal* KJMA and /or MPM model predictions which are attributed to the simplified assumptions for the mechanism of nucleation and growth [269-

Chapter 7

Role of Nucleation Mode on Kinetics of Static Recrystallization & Grain Structure Development: A Mesoscopic Simulation Approach

Appendix-A

Algorithm for the generation of initial microstructure

The initial microstructure was generated on a (5000x5000) grid of cells with periodic boundary conditions, assuming homogeneous nucleation and constant isotropic growth of the product phase. All the cells in the grid were assigned one state variable $\phi=0$ before the onset of nucleation. The nucleation sites (individual cells) were selected randomly from the grid of cells assuming continuous nucleation mode. The number of nuclei appearing at each time step was estimated using *Eq. (2.4)* and *Eq. (7.3)*. The state variable of these selected nucleation sites was changed to an integer value chosen randomly in the range ($1 \leq \phi \leq 90$). These nucleation sites appearing at each time step served as the center of one grain and were allowed to grow with a constant velocity in the subsequent time. The growth velocity was estimated using *Eq. (2.13)* at an annealing temperature 1073 K. The incremental radius for each individual nucleus was calculated at each time step using *Eq. (7.5)* and the cells within this incremental radius were checked to ensure that they do not belong to another grain. The state variable of the cells inside the incremental radius with $\phi=0$ was changed to the state variable of the center cell. Otherwise, the state variable of the cells inside the incremental radius was left with their previous state variable. The simulation was allowed to proceed until none of the cells in the entire simulation volume was left with a state variable $\phi=0$. The microstructure evolved in this procedure was used as the initial microstructure (**figure 7.5 (a)**) in the present study which was subsequently deformed to carry out the simulations of static recrystallization.

- I. CALPHAD based phase stability assessment based on the experimentally measured data on the solidus, liquidus together with corresponding enthalpy of phase change in IFAC-1 and SS 304H Cu
- II. Rationalization of the experimentally generated thermophysical properties of these advanced steels based on lattice dynamics to obtain a fundamental understanding of the nature of variation of these properties. For example the effect of Cu which significantly affects the thermal conductivity, linear thermal expansivity as well as the elastic moduli in SS 304H Cu needs to be addressed from a theoretical ground.
- III. Extension of the thermo-kinetics analysis in the present study to obtain reliable values for interface energy and mobility which are currently unavailable in these advanced steels
- IV. Investigation on evolution of microstructure and texture during recovery and recrystallization using advanced electron microscopy techniques.
- V. Evaluation of valuable kinetic parameters for grain growth for these steels which is presently lacking, with special emphasis on the role of secondary phase precipitates on the kinetics of grain growth.
- VI. Extension of the present simulation study on the role of nucleation mode on the kinetics of static recrystallization by incorporating the heterogeneous stored energy distribution using crystal plasticity finite element method to predict the evolution of recrystallization texture.
- VII. Extension of the computer simulations carried out for IFAC-1 SS to SS 304H Cu by incorporating the effect of second phase precipitates.

Further a geometrical simulation approach has been adopted to study the role of nucleation mode on the kinetics of static recrystallization and the development of grain structure in IFAC-1. It has been observed that the rate of increase or decrease in the Avrami exponent in a mixed or Avrami nucleation mode is always higher for the heterogeneous recrystallization. However, the variation of Avrami exponent is sensitive to the nucleation rate for both mixed and Avrami mode of nucleation. The variation of kinetic parameters (q , m) in the MPM model behaves similarly to the Avrami exponent (n) irrespective of nucleation modes. The grain size distribution due to static recrystallization is found to be sensitive to the nucleation mode. In case of continuous nucleation (CN), mixed nucleation (MN) and Avrami nucleation (AN) mode, the size distributions are found to be lognormal whereas for site saturation nucleation (SSN) mode the observed distribution is normal. The grain size distribution for the mixed mode nucleation is a mixture of large grains and a continuous band of smaller grains. For the Avrami mode, the grain size distribution differs widely depending on the nucleation rate. The average grain size and the size distribution can be controlled for both, MN and AN mode by suitable selection of the initial microstructure as well as the time-temperature path of annealing. On the other hand the grain size distribution in pure site saturation and continuous nucleation is unique although the average grain size depends on both the nucleation rate and the number of preexisting nuclei.

8.2. Further avenues of research

The present thesis reports an extensive characterization of phase stability, measurement of high temperature thermophysical properties as well as the recovery and recrystallization aspects of two advanced austenitic stainless steels i.e. IFAC-1 SS and SS 304H Cu. This opens up numerous avenues for further research, a few of which are listed below.

K) have been established. Although both the steels undergo austenitic + ferritic mode of solidification under slow cooling conditions, the amount of δ -ferrite formation in case of SS 304H Cu is appreciable in comparison to IFAC-1 SS. Further the thermophysical properties of both have been measured and compared with the available literature data on AISI 300 grade austenitic stainless steels. It has been observed that, in case of IFAC-1 SS, the measured thermophysical properties vary smoothly with temperature whereas the thermophysical and elastic properties of SS 304H Cu are found to change significantly due to the Cu precipitation. The heat capacity and the volume thermal expansivity have also been estimated for both the steels from 0 to 1273 K using quasi-harmonic Debye Grunissen formalism.

The peak recovery and recrystallization temperatures for IFAC-1 SS have been determined to be 815 and 1070 K respectively. The corresponding temperatures in SS304H Cu are found to be 826 and 986 K. The average value of the total stored energy release in IFAC-1 and SS 304H Cu is found to be $9.4 \pm 1.4 \text{ J g}^{-1}$ and $17.3 \pm 1.4 \text{ J}$ respectively. In case of IFAC-1, at temperatures exceeding 1273 K, partial dissolution of TiC particles resulted in secondary recrystallization. On the other hand SS 304H Cu undergoes simultaneous precipitation and recrystallization. Therefore pre-aging treatment is required to avoid the simultaneous occurrence of the two processes. The effective activation energies for recovery and recrystallization for IFAC-1 are estimated to be $198 \pm 7 \text{ kJ mol}^{-1}$ and $336 \pm 9 \text{ kJ mol}^{-1}$ respectively. In case of SS 304H Cu the effective activation energies for recovery and recrystallization are found to be 144 ± 14 and $192 \pm 12 \text{ kJ mol}^{-1}$ respectively. These activation energy values suggest that, both recovery and recrystallization in SS 304H Cu are primarily controlled by grain boundary diffusion. However for IFAC-1 SS, the recovery process is controlled by grain boundary diffusion and the recrystallization is influenced by bulk diffusion mechanism.

Summary and Further Avenues of Research

8.1. Summary of the present study

The scope of the present thesis is to investigate the high temperature phase stability, thermophysical properties as well as the recovery and recrystallization behavior of two advanced austenitic stainless steels that are candidate materials for fast breeder nuclear reactors (IFAC-1 SS) and advanced ultra-supercritical thermal power plants (SS 304H Cu). This study has been carried out using experimental techniques, modelling tools as well as computer simulation to evaluate several thermokinetic and thermodynamic data which not only provides a comprehensive database for the design engineers but also provides an insight into the physical metallurgy of these steels. Although dynamic calorimetry has been used as a major experimental technique in association with metallography and hardness measurements to study the phase stability and the recovery, recrystallization behavior of these steels, there are several other state of the art techniques such as drop calorimetry, dilatometry, laser flash thermal diffusivity and impulse excitation technique that have been employed to establish a comprehensive database on the thermophysical properties in the two advanced steels. The salient results of the thesis are summarized as follows.

The IFAC-1 SS constitutes γ -austenite with fine scale TiC/N (MX) precipitates whereas in case of SS 304H Cu, the initial microstructure consists of a mixture of γ -austenite +MX + $M_{23}C_6$ + Cu. The homogenization of IFAC-1 is found to be initiated at 1323 K (1050 °C). Similarly the dissolution of Cu and $M_{23}C_6$ precipitates in SS 304H Cu are found to initiate at 1167 K (894 °C) and 1320 K (1047 °C) respectively. The complete dissolution of MX precipitates occurs near melting temperatures for both the steels. The liquidus and solidus temperatures for IFAC-1 (1684 K and 1631 K) and SS 304H Cu (1723 K and 1607

Chapter 8

Summary & Further Avenues of Research

271. Z. Liu, R. O. Olivares, Y. Lei, C. I. Garcia and G. Wang, *J Alloys Comp.*, **679** (2016) 293.
272. J. Wang, S. Niu, T. Guo, H. Kou and J. Li, *J Alloys Comp.*, **710** (2017) 144.
273. T. O. Saetre, O. Hunderi and E. Nes, *Acta Metall.*, **34** (1986) 981.
274. K. Marthinsen, O. Lohne and E. Nes, *Acta Metall.*, **37** (1989) 135.
275. D. J. Srolovitz, G. S. Grest and M. P. Anderson, *Acta. Metall.*, **34** (1986) 1833.
276. D. J. Srolovitz, G. S. Grest, M. P. Anderson and A. D. Rolet, *Acta. Metall.*, **36** (1988) 2115.
277. H. Tripathy, S. Raju, A. K. Rai and T. Jayakumar, *Steel Res. Int.*, **84** (2013) 1046.
278. T. Furu, H. R. Shercliff, G. J. Baxter and C. M. Sellars, *Acta Mater.*, **47** (1999) 2377.
279. A. A. Burbelko, E. Fras and W. Kapturkiewicz, *Mater.Sci. Eng.*, **A413–414** (2005) 429.
280. H. W. Hesselbarth and I. R. Göbel, *Acta. Metall. Mater.*, **39** (1991) 2135.
281. J. W. Cahn, *Acta Metall.*, **4** (1956) 449.
282. P. R. Rios and E. Villa, *Acta Mater.*, **57** (2009) 1199.
283. E. Villa and P. R. Rios, *Acta Mater.*, **58** (2010) 2752.
284. A. M. Gokhale, *Metall Trans.*, **A15** (1985) 559.
285. C. S. Pande, *Model. Simul. Mater.Sci. Eng.*, **23** (2015) 035009.

247. M. Naghizadeh, and H. Mirzadeh, *Metall and Mat Trans.*, **A47** (2016) 4210.
248. M. J. Jones and F.J. Humphreys, *Acta. Mater.*, **51** (2003) 2149.
249. R. A. Varin, *Mater. Sci. Engg.*, **66** (1984) 97.
250. N. Hirota, F. Yin, T. Inoue and T. Azuma, *ISIJ International*, **48** (2008) 475.
251. Y. Mandiang, D. Azilinson, M. Adj and G. Cizeron, *Mater. Sci. Tech.*, **16** (2000) 399.
252. J. Farjas and R. Roura, *Acta mater.*, **54** (2006) 5573.
253. M. Verdier, Y. Brecheta and P. Guyot, *Acta Mater.*, **47** (1999) 127.
254. F. J. Humphreys, *Acta mater.*, **45** (1997) 4231.
255. P. R. Rios, *Scripta mater.*, **34** (1996) 1185.
256. P. R. Rios, *Metall. Met Trans.*, **A28** (1997) 939.
257. F. J. Humphreys, *Mater. Sci. Tech.*, **15** (1999) 37.
258. H. S. Zurob, C. R. Hutchinson, Y. Brechet and G. Purdy, *Acta mater.*, **50** (2002) 3075.
259. H. S. Zurob, Y. Brechet and J. Dunlop, *Acta mater.*, **54** (2006) 3983.
260. R. J. Contieri, M. Zanotello and R. Caram, *Mater. Sci. Engg.*, **A527** (2010) 3994.
261. N. Gao, M. J. Starink and T. G. Langdon, *Mater. Sci. Tech.*, **25** (2009) 667.
262. S. S. Hajra, A. A. Gazder and E. V. Pereloma, *Mater. Sci. Eng.*, **A524** (2009) 158.
263. S. Curtze, V. T. Kuokkala, A. Oikari, J. Talonen and H. Hänninen, *Acta. Mater.*, **59** (2011) 1068.
264. I. T. Hong and C. H. Koo, *Mat. Sci. Engg.*, **A393** (2005) 213.
265. Y. Lu, D. A. Molodov and G. Gottstein, *Acta mater.*, **59** (2011) 3229.
266. D. Kuhlmann, G. Masing and J. Raffelspeper, *Z. Metallkunde*, **40** (1949) 235.
267. S. F. Medina and P. Fabregue, *JMS.*, **26** (1991) 5427.
268. G. Mohapatra and S. S. Sahay, *Mater. Sci. Tech.*, **27** (2011) 377.
269. A. Calka and A. P. Radlinski, *Acta Metall.*, **35** (1987) 1823.
270. P. Krüger and E. Woldt, *Acta Metall. Mater.*, **40** (1992) 2933.

227. The British Standards Institution report: BS EN 10088-1:2014
(<http://www.bssa.org.uk/topics.php?article=139>)
228. Materials for cryogenic services, *Engineering properties of austenitic stainless steels*.
Publication no: 4368, INCO data books. (1974). <http://www.nickelinstitute.org/>
229. H. Pitkanen, M. Alatalo, A. Puisto, M. Ropo, K. Kokko, M. P. J. Punkkinen, P. Olsson,
B. Johansson, S. Hertzman and L. Vitos, *Phys. Rev.*, **B79** (2009) 4108.
230. A. K. Rai, H. Tripathy, B. Jeyaganesh and S. Raju, *J. Nucl. Mater.*, **427** (2012) 378.
231. A. K. Rai and S. Raju, *J. Therm. Anal. Calorim.*, **112** (2013) 73.
232. J. M. Corson and N. I. Mitchem, *Cryogenics*, **19** (1979) 11.
233. S. Raju and A. K. Rai, *J. Nucl. Mater.*, **408** (2011) 40.
234. V. Arp, J. H. Wilson, L. Winrich and P. Sikora, *Cryogenics*, **2** (1962) 230.
235. P. I. Dorogokupets. *Am. Mineral.*, **85** (2000) 329.
236. A. Jablonka, K. Harste and K. Schwerdtfeger, *Steel Res.*, **62** (1991) 24.
237. M. B. Be Ver, D. L. Holt and A. L. Titchener, *Prog. Mat. Sci.*, **17** (1973) 5.
238. M. Bhatia, *Prog. Mater. Sci.*, **42** (1997) 59.
239. M. Jin, *J. Iron & Steel Res. Int.*, **20** (2013) 67.
240. Y. C. Lin and M. S. Chen, *J. Mater. Sci.*, **44** (2009) 835.
241. P. Kratochvil, B. Smola, L. Stulikovi and P. Vostr Czech, *J. Phys.*, **B35** (1985) 257.
242. T. V. Vikhareva, O. V. Fomina. and G. Y Kalinin, *Metallurgist*, **60** (2016) 281.
243. F. Chen, D. Sui and Z. J. Cui, *J. of Materi. Eng and Perform.*, **23** (2014) 3034.
244. X. Yang, An. He, C. Wu, S. Li, H. Zhang and X. Wang, *J of Materi Eng and Perform.*,
24 (2015) 4346.
245. A. V. Chastukhin, D. A. Ringinen, G. E. Khadeev and L. I. Efron, *Metallurgist*, **59**
(2016) 1180.
246. B. R. Kumar, and S. Sharma, *Metall and Mat Trans.*, **A45** (2014) 6027.

208. V. Vodarek, *Metall. Mater. Trans.*, **29** (1991) 229.
209. A. Hunter and M. Ferry, *Scr. Mater.*, **46** (2002) 253.
210. T. Koseki, H. Inoue, H. Morimoto and S. Ohkita, *Nippon Steel Tech. Report.* **65**, (1995) 33.
211. N. Suutala, *Metall. Trans.*, **A14** (1983) 191.
212. A. R. Jones and B. Ralph, *Metallography*, **10** (1977) 469.
213. H. Tripathy, S. Raju, A. K. Rai, G. Panneerselvam, and T. Jayakumar, *Nucl. Eng. Des.*, **255** (2013) 86.
214. R. M. Boothby, *Mater. Sci. Tech.*, **2** (1986) 78.
215. J. W. Elmer, S. M. Allen and T.W. Eager, *Metall. Trans.*, **A20** (1989) 2117.
216. J. A. Brooks and A. W. Thompson, *Int. Mater. Rev.*, **36** (1991) 16.
217. J. Miettinen, *Metall. Mater. Trans.*, **B28** (1997) 281.
218. J. N. Dupont. *Weld Res Suppl.*, **7** (1999) 253.
219. J. W. Fu, Y. S. Yang, J. J. Guo, and W.H. Tang, *Mater. Sci. Tech.*, **24** (2008) 941.
220. J. C. Ma, Y. S. Yang, W. H. Tomg, Y. Fang, Y. Fu, and Z. Q. Hu, *Mater. Sci. Eng.*, **A444** (2007) 64.
221. M. Bobadilla, *J. Cryst. Growth*, **89** (1988) 531.
222. K. Rajasekhar, C. S. Harendranath, R. Raman and S.D. Kulkarni, *Mater. Charact.*, **38** (1997) 53.
223. O. Hammar and U. Svensson, *Solidification and Casting of Metals*, The Metals Society, London, (1979) 401.
224. G. El. Nayal and J. Beech, *Mater. Sci. Tech.*, **2**(1986) 603.
225. C. G. Maier and K. K. Kelley, *J Am Chem Soc.*, **54** (1932) 3243.
226. M. J. Peet, H. S Hasan and H. K. D. H. Bhadeshia, *Int J Heat Mass Tran.*, **54** (2011) 2602.

194. *ASTM E1876-15: Standard Test Method for Dynamic Young's Modulus, Shear Modulus, and Poisson's Ratio by Impulse Excitation of Vibration*, ASTM International, West Conshohocken, PA, (2015).
195. *ASTM C1259-15: Standard Test Method for Dynamic Young's Modulus, Shear Modulus, and Poisson's Ratio for Advanced Ceramics by Impulse Excitation of Vibration*, ASTM International, West Conshohocken, PA (2015).
196. J. Etcheverry, G. Sanchez, N. Bonades and L. I. Raggu, *IV Congreso Iberoamericano de Acoustica*, FIA A025 (2008).
197. NPL *Measurement Good Practice Guide No. 98* (2006) 59.
198. L. E. Samules, *Metallographic Polishing by Mechanical Methods*, (4th edition) ASM International, Materials Park, USA (2003).
199. G. F. Vander Voort, *Metallography Principles and Practice*, Mc-Graw- Hill book Company (1984).
200. User guide for imageJ, <https://imagej.nih.gov/ij/docs/guide/user-guide.pdf>.
201. S. Sharafat, G. R. Odette and J. Blanchard, *J. Nucl. Mater.*, **386–388** (2009) 896.
202. R. L. Plauta, C. Herrera, D. M. Escriba, P. R. Rios and A. F. Padilh, *Mat Res.*, **10**, (2007) 453.
203. Y. Sawaragi, K. Ogawa , K. S. A. Natori and S. Hirano. *Sumitoma Search (Jpn)*, **48** (1992) 50.
204. S. Venkadesan, A. K. Bhaduri, P. Rodriguez and K. A. Padmanaban, *J. Nucl. Mater.*, **186** (1992) 177.
205. K. H. Lo, C.H. Shek and J. K. L. Lai, *Mater. Sci Eng.*, **R 65** (2009) 39.
206. S. Balaji, S. Mohan, S. Amirthapandian, S. Chinnathambi, C. David and B. K. Panigrahi, *J. Nucl. Mater.*, **467** (2015) 368.
207. B. Raj and B. K. Choudhary, *Trans IIM.*, **63** (2010) 75.

178. Setsys Evolution-TMA 16/18, *Installation Guide and Manual* (2010).
179. R. G. Munro, *J. Am. Ceram. Soc.*, **80** (1997) 1919.
180. N. Manoj , D. Jain, J. K. Gautam, K. C. Thomas, V. Sudarsan, C. G. S. Pillai, R. K. Vatsa and A. K. Tyagi. *Measurement*, **92** (2016) 318.
181. G. Mohapatra, F. Sommer and E. J. Mittemeijer, *Thermochim Acta*, **453** (2007) 31.
182. W. J. Parker, R. J. Jenkins, C. P. Butler and G. L. Abbott, *J. Appl. Phys.*, **32** (1961) 1679.
183. F. Righini and A. Cezairliyan, *High Temp. High Press.*, **5** (1973) 481.
184. S. Min, J. Blumm, and A. Lindemann, *Thermochim. Acta*, **455** (2007) 46.
185. LFA 1000 HT manual, *Thermal Diffusivity Thermal Conductivity*. www.linseis.com
186. W. M. Steen, *Laser Materials Processing*, (3rd edition), Springer, London; (2003) 70-74
187. R. F. Speyer, *Thermal analysis of Materials*, Marcel Dekker, Inc, New York;(1993) 242-247.
188. R. P. Tye and D. Hume, *J. Therm. Anal. Calorim.*,**131** (2018) 289.
189. G. Roebben, B. Bollen, A. Brebels, J. Van Humbeeck and O. Van der Biest, *Rev. Sci. Instrum.*, **68** (1997) 4511.
190. G. Roebben, R. G. Duan, D. Sciti and O. Van der Biest, *J. Euro Ceram Soc.*, **22** (2002), 2501.
191. J. D. Lord and R. Morrell, *NPL: Measurement Good Practice Guide: Elastic Modulus Measurement*, NPL Report, Teddington, U. K., (2006).
192. M. Radovic, E. Lora-Curzio and L. Riester, *Mater. Sci. Engg.*, **A368** (2004).56.
193. A. Brebels and B. Bollen, *Non destructive evaluation of materials properties as a function of temperature*, NDE India-2014, Conference Proceedings, 20 (2015) No.6, 1-10.

163. M. E. Brown, *Introduction to Thermal Analysis, Techniques and Applications*, (2nd edition) Kluwer Academic Publishers, The Netherlands, (2001).
164. K. Gallagher, *Handbook of Thermal Analysis and Calorimetry*, (edited by M.E. Brown) Elsevier, Amsterdam, (1998).
165. K. D. Maglic, A. Cezairliyan and V. E. Peletsky (Eds.), *Compendium of Thermophysical Property Measurement Techniques, vol. 2*, Plenum Press, New York, (1992).
166. S. M. Sarge, E. Gmelin, G. W. H. Hohne, H. K. Cammenga, W. Hemminger and W. Eysel, *Thermochim. Acta*, **247** (1994) 129.
167. <http://www.setaram.com/SETSYS-Evolution-DTA-DSC.htm>.
168. R. Sabbah, An Xu-wu, J.S. Chickos, M.L. Planas Leitão, M.V. Roux and L.A. Torres, *Thermochim. Acta*, **331** (1999) 93.
169. L. Richardson and E. L. Charsley, *Calibration and Standardisation in DSC*, in *Handbook of Thermal Analysis and Calorimetry. Vol. 1: Principles and Practice*, M. E. Brown (editor), Elsevier Science B.V. (1998).
170. E. Gmelin and St. M. Sarge, *Pure Appl. Chem.*, **67** (1995) 1789.
171. B. Wunderlich, *Thermal Analysis*, San Diego, CA, Academic Press, (1990).
172. M. Brown, *Introduction to Thermal Analysis*, Chapman and Hall, London, (1988).
173. G. W. H. Höhne, W. Hemminger, and H. J. Flammersheim, *Differential Scanning Calorimetry: An Introduction for Practitioners*, Berlin, Springer-Verlag, (1996).
174. Multi HTC-96, *Setaram Installation Guide and Manual* (1997).
175. Y. Takahashi and Y. Kohsaka, *J. Nucl. Mater.*, **130** (1985) 109.
176. D. G. Archer, *J. Phys. Chem. Ref. Data*, **22** (1993) 1441.
177. J. D James, J. A Spittle, S. G. R. Brown and R. W. Evans, *Meas. Sci. Technol.*, **12** (2001) 1.

138. M. J. Starink, *Int. Mater. Rev.*, **49** (2004) 191.
139. W. A. Johnson and R. F. Mehl, *Tranz AIME.*, **135** (1939) 416.
140. A. N. Kolmogorov, *Izv. Akad. Nauk SSSR Ser. Mat.*, **3** (1937) 355.
141. N. S. Mohan and R. Chen, *J. Phys. D: Appl. Phys.*, **3** (1970) 243.
142. W. Tang, Y. Liu, H. Zhang and C. Wang, *Thermochim. Acta*, **408** (2003) 39.
143. Y. Jiang, F. Liu and S. Song, *Thermochim Acta.*, **515** (2011) 51.
144. R. A. Vandermeer and B. B. Rath, *Metall. Trans.*, **A20** (1989) 391.
145. R. A. Vandermeer, R. A. Masumura and B. B. Rath, *Acta Metall. Mater.*, **39** (1991) 383.
146. R. A. Vandermeer and A. Masumura, *Acta Metall. Mater.*, **40** (1992) 877.
147. R. A. Vandermeer and D. Juul Jensen, *Acta Metall. Mater.*, **42** (1994) 2427.
148. R. A. Vandermeer and D. Juul. Jensen, *Metall. Mater. Trans.*, **A26** (1995) 2227.
149. R. A. Vandermeer and B. B. Rath, *Metall. Mater. Trans.*, **A27** (1996) 1513.
150. R. L. Goetz and V. Seetharaman, *Metall. Mater. Trans.*, **A29** (1998) 2307.
151. J. H. Flynn and L. A. Wall, *J. Res. Natl. Bur. Standards* **A70** (1966) 487.
152. T. Ozawa, *Bull. Chem. Soc. Jpn.*, **38** (1970) 1881.
153. C.D. Doyle, *J. Appl. Polym. Sci.*, **5** (1961) 285.
154. D. Doyle, *J. Appl. Polym. Sci.*, **6** (1962) 693.
155. H. L. Friedman, *J. Polym. Sci.*, **6** (1964) 183.
156. C. R. Li and T. B. Tang, *Thermochim. Acta*, **325** (1999) 43.
157. H. E. Kissinger, *Anal. Chem.*, **29** (1957) 1702.
158. T. Akahira and T. Sunose, *Res. Rep. Chiba Inst. Technol. (Sci. Technol.)*, **16** (1971) 22.
159. P. Murray and J. White, *Trans. Brit. Ceram. Soc.*, **54** (1955) 204.
160. F.S. Lin, S.C. Cheng, and X.S. Xie, *Energy Mater.*, **3** (2009) 201.
161. A. Tohyama, M. Miyauchi and Y. Minami, *Trans. ISIJ.*, **25** (1985) 495.
162. Lee D. Hansen and R. S. Criddle, *Thermochim. Acta.*, **160** (1990) 173.

116. H. P. Stuwe, A. F. Padilha and F. Siciliano. Jr, *Mater. Sci. Engg.*, **A 233** (2002) 361.
117. S. Vyazovkin, and C. A. Wight, *Annu. Rev. Phys. Chem.*, **48** (1997) 125.
118. J W Christian, *The theory of transformation in metals and alloys, vol I*, Pergamon Press, Oxford (2002).
119. F. Liu, F. Sommer, C. Bos and E. J Mittemeijer, *Int. Mater. Rev.*, **52** (2007) 193.
120. F. Liu, F. Sommer and E. J. Mittemeijer, *J. Mater. Res.*, **19** (2004) 2586.
121. F. Liu, F. Sommer and E. J. Mittemeijer, *Acta Mater.*, **52** (2004) 3207.
122. V. I Tkatcha, A. I Limanovskii and V. Y. Kameneva, *J. Mater.Sci.*, **32** (1997) 5669.
123. A. T. W. Kempen, F. Sommer and E. J Mittemeijer, *J. Mater. Sci.*, **37** (2002) 1321.
124. F. Liu, S. J Song, J. F. Xu and J. Wang, *Acta Mater.*, **56** (2008) 6003.
125. Y. Jiang, F. Liu and S. J. Song, *Trans. Nonferrous. Met. Soc. China*, **22** (2012) 1176.
126. M. Avrami, *J. Chem. Phys.*, **7** (1939) 1103.
127. M. Avrami, *J. Chem. Phys.*, **8** (1940) 212.
128. M. Avrami, *J. Chem. Phys.*, **9** (1941) 177.
129. D. R. Allen, J. C. Foley and J. H. Perepezko, *Acta Mater.*, **46** (1998) 431.
130. T. Pradell, D. Crespo, N. Clavaguera and M. T. C. Mora, *J. Phys. Condens Matter.*, **10** (1998) 3833.
131. D. E. Coates, *Metall. Trans.*, **3** (1972) 1203.
132. K. N. Lad, R. T. Savalia, A. Pratap, G. K. Dey and S. Banerjee, *Thermochim. Acta.*, **473** (2008) 74.
133. E. J. Mittemeijer, *J. Mater. Sci.*, **27** (1992) 3977.
134. A. T. W. Kempen, F. Sommer and E. J. Mittemeijer, *J. Mater. Sci.*, **37** (2002) 1321.
135. A. T. W. Kempen, F. Sommer and E. J. Mittemeijer, *Acta Mater.*, **50** (2002) 1319.
136. E. J Mittemeijer and F. Sommer, *Z Metallkd.*, **93** (2002) 352.
137. F. Liu, F. Sommer and E. J. Mittemeijer, *J. Mater. Sci.*, **39** (2004) 1621.

95. S. J. Zinkle and J. T. Busby, *Mater. Today*, **12** (2009) 12.
96. O. Hunderi and N. Ryum, *J. Mater. Sci.*, **15** (1980) 1104.
97. T. Gladman, *JOM.*, **44** (1992) 21.
98. P. R. Roy, *Phase Transitions*, Pergamon Press, New York (1973).
99. A. K. Jena and M. C. Chaturvedi, *Phase Transformations in Materials*, Prentice Hall, New Jersey (1991).
100. V. Raghavan, *Solid State Phase Transformations*, Prentice-Hall of India, New Delhi (1992).
101. A. Desalvo and F. Zignani, *J. Nucl. Mater.*, **20** (1966) 108.
102. G. F. Missiroli, D. Nobili and F. Zignani, *J. Nucl. Mater.*, **21** (1967) 199.
103. S. Takamura, R. Hanada and S. Okuda, *J. Phys. Soc. Jpn.*, **30** (1976) 1360.
104. G. Gottstein, H. Steffen and H. Wollenberger, *Scripta Metall.*, **7** (1973) 451.
105. R. K. Stout and C. R. Brooks, *Scripta Metall.*, **10** (1976) 741.
106. A. M. Guereanu, F. Ariziti and I. Gutierrez, *Acta mater.*, **52** (2004) 3665.
107. A. Borbely and J. H. Driver, *Mater. Sci. Engg.*, **A387-389** (2004) 231.
108. E. Schafner, M. Zehetbauer, A. Borbely and T. Ungar, *Mater. Sci. Engg.*, **A234-236** (1997) 445.
109. T. L. Richards, S. F. Pugh and H. J. Stokes, *Acta Metall.*, **4** (1956) 75.
110. M. J. Luton, R. A. Petkovic and J. J. Jonas, *Acta Metall.*, **28** (1980) 729.
111. X. T. Wang, Z. L. Lu, T. Siwecki, G. Engberg and Z. Q. Sun, *Mater. Sci. Forum*, **561-565** (2007) 1953.
112. D. Juul Jensen, *Mater. Sci. Tech.*, **21** (2005) 1365.
113. K. J. Kurzydowski, B. Ralph, A. Chojnacka and J. Bucki, *Acta mater.*, **44** (1996) 3005.
114. P. L. Orsetti Rossi and C. M. Sellars, *Acta mater.*, **45** (1997) 137.
115. A. J. Porter and B. Ralph, *Mater. Sci. Engg.*, **59** (1983) 69.

80. J. E. Bailey and P. B. Hirsh, *Phil. Mag.*, **5** (1960) 485.
81. J. L. Lytton, K. H. Westmacott and L. C. Potter, *Trans. Metall. Soc. AIME*, **233** (1965) 1757.
82. T. Hasegawa and U. F. Kocks, *Acta Metall.*, **27** (1979) 1705.
83. A. F. Padilha, R. L. Plaut and P. R. Rios, *ISIJ International.*, **43** (2003) 136.
84. J. Cuddy and M. N. Bassim, *Mater. Sci. Eng.*, **A113** (1989) 421.
85. D. G. Cram, H. S. Zurob, Y. J. M. Brechet and C. R. Hutchinson, *Acta Metall.*, **57** (2009) 5218.
86. H. Hallberg, M. Wallin and M. Ristinmaa, *Mater. Sci. Eng.*, **A527** (2010) 1126.
87. R. W. Cahn, *Recovery and Recrystallization*, in: *Physical Metallurgy*, Vol. 3,(Eds: R. W. Cahn and P. Haasen) Elsevier, North-Holland, Amsterdam (1996), 2400-2492.
88. P. Haasen, *Metall. Trans.*, **24A** (1993) 1001.
89. R. D. Doherty, I. Samajdar, C. T. Necker, H. E. Vatne and E. Nes, *Microstructural and Crystallographic Aspects of Recrystallization* 16 in: *Risø International Symposium on Materials Science* (Eds: N. Hansen, D. Juul Jensen, Y.L. Liu, B. Ralph), Risø National Lab, Roskilde, Denmark, (1995) 1.
90. A. Duggan and C. Y. Chung, *Mater. Sci. Forum*, (edited by H. J. Bunge) *ICOTOM 10*, **157–163** (1994) 1765.
91. N. Hansen, D. Juul Jensen, T. Leffers and B. Ralph, *Annealing Processes-Recovery, Recrystallization and Grain Growth*, Risø National Laboratory, Roskilde, (1986).
92. R. Sandstrom, *Zeitschrift Fuer Met. Res. Adv. Tech.*, **71** (1980) 741.
93. F. J. Humphreys. M. Ferry, C. Johnson and P. Paillard, *Proc. 16th Risø Int. Symp: Microstructural and Crystallographic Aspects of Recrystallization*, Risø National Laboratory, Roskilde, Denmark, Denmark, (1995) 87.
94. F. J. Humphreys, *Acta Metall.*, **25** (1977) 1323.

66. R. W. Cahn, *Physical Metallurgy, Vol. 1*, (Eds: R. W. Cahn, P. Haasen,) Elsevier, North-Holland, Amsterdam (1996).
67. D. A. Porter and K. E. Easterling, *Phase Transformations in Metals and Alloys*, Chapman & Hall, New York (1992).
68. F. J. Humphreys and M. Hatherly, *Recrystallization and Related Annealing Phenomenon*, Pergamon Press, Oxford (1995).
69. G. Dieter, *Mechanical metallurgy*, McGraw-Hill, New York (1986).
70. R. D. Doherty, D. A. Hughes, F. J. Humphreys, J. J. Jonas, D. J. Jensen, M. E. Kassner, W. E. King, T. R. McNelly, H. J. McQueen and A. D. Rollet, *Mater.Sci. Eng.*, **A238** (1997) 219.
71. J. Gil Sevillano and E. Aernoudt, *Mater. Sci. Engg.*, **86** (1987) 35.
72. P. R. Rios, F. Siciliano Jr, H. R. Z. Sandim, R. L. Plaut and A. F. Padilha, *Mater. Res.*, **8** (2005) 225.
73. H. J. McQueen and J. J. Jones, *Recovery and recrystallization during high temperature deformation*, in *Treatise on Materials Science and Technology, Vol. 6, Plastic deformation of Materials* (edited by R. J. Arsenault), Academic Press, (1975).
74. K. Lucke, *Mater. Sci. Eng.*, **A 25** (1976) 153.
75. E. Nes, *Acta Metall. Mater.*, **43** (1995) 2189.
76. R. W. Cahn, *J. Inst. Metals.*, **76** (1949) 121.
77. J. C. M. Li, *Recovery process in metals recrystallization, grain growth and texture*, AIME Metals Park, Ohio (1965) 45-97.
78. W. Carrington, K. F. Hale and D. Mclean, *Proc. R. Soc.*, **A 259** (1960) 203.
79. H. Hu, B. B. Rath and R. A. Vandermeer, *An historical perspective and overview of the annealing studies of cold worked metals, in Recrystallization*, 90 (edited by T. Chandra), TMS, Warrendale (1990) 3–16.

50. A. S. Grot and J. E. Spruiell, *Metal. Mater. Trans.*, **A6** (1975) 2023.
51. I. Sen, E. Amankwah, N. S. Kumar, E. Fleury, K. Ohishi, K. Hono, and U. Ramamurthy, *Mater. Sci. Eng.*, **A258** (2011) 4491.
52. S. Takaki, M. Fujioka, S. Aihara, Y. Nagataki, T. Yamashita, N. Sano, Y. Adachi, M. Nomura and H. Yaguchi, *Materials Transactions*, **45** (2004) 2239.
53. M. E. Fine and D. Isheim, *Scr. Mater.*, **53** (2005) 115.
54. R. H. Bogaard, P. D. Desai, H. H. Li and C. Y Ho, *Thermochim Acta*, **218** (1993) 373.
55. C. S. Kim, *Thermo physical Properties of Stainless Steel*, Technical Report, Argonne National Laboratory, Argonne, **ANL75-55**. (1975) 1-24.
56. K. C. Mills, Y. Su, Z. Li and R. F Brooks, *ISIJ Int.*, **44** (2004) 1661.
57. L. Leibowitz and R. A. Blomquist, *Int J Thermophys*, **9** (1988) 873.
58. A. Banerjee, S. Raju, R. Divakar, E. Mohandas, G. Panneerselvam and M. P. Antony, *J. Nucl. Mater.*, **347** (2005) 20.
59. R. Jose, S. Raju, R. Divakar, E. Mohandas, G. Paneerselvam, M P. Antony and K. Sivasubramanian, *J. Nucl. Mater.*, **317** (2003) 54.
60. O. L. Anderson, *Equation of state of solid for Geophysics and Ceramic Science*, Oxford University press, New York (1995).
61. D. C. Wallace, *Thermodynamics of Crystal*, Wiley, New York (1972).
62. G. Grimvall, *Thermo physical Properties of Materials*, (1st edition) Elsevier science: North Holland, Amsterdam (1986).
63. H. Ledbetter, *Elastic Properties*, in: *Materials at low temperatures*, (Eds: R. P. Reed and A. F. Clark), *Amer. Soc. Metals*, Metals Park, Ohio (1983).
64. H. M. Ledbetter, N. V. Frederick, and M. W. Austin, *J. Appl. Phys.*, **51** (1980) 305.
65. H. Ledbetter, *J. Appl. Phys.*, **52** (1981) 1587.

29. M. Asta, V. Ozolins, and C. Woodward, *JOM*, **53** (2001) 16.
30. L. Q. Chen, *Annu. Rev. Mater. Res.*, **32** (2002) 113.
31. K. Thornton, J. Agren and P. W. Voorhees, *Acta Mater.*, **51** (2003) 5675.
32. I. Steinbach, *Model. Simul. Mater. Sci. Eng.*, **15** (2009) 17.
33. G. H. Gulliver, *J. Inst. Met.*, **9** (1913) 120.
34. E. Scheil, *Z. Metallkd.*, **34** (1942) 70.
35. P. Guiraldenq and O. H. Duparc, *Metall. Res. Technol.*, **114** (2017) 1.
36. M. F. McGuire, *Stainless steels for design engineers*, ASM International, (2008).
37. D. T. Llewellyn and C. R. Hudd, *Steels: Metallurgy and Applications*, (3rd edition) Butterworth-Heinemann (1998).
38. A. J. Sedriks, *Corrosion of stainless steel*, (2nd. edition) John Wiley and Sons, Inc., New York, United States, (1996).
39. H. Bhadeshia and R. Honeycombe, *Steels: Microstructure and Properties*”, (3rd edition) Elsevier (2006).
40. T. Sourmail, *simultaneous precipitation reactions in creep resistant austenitic stainless steels*, Doctoral thesis, University of Cambridge, (2001).
41. T. Sourmail, *Mater. Sci. Tech.*, **17** (2001)1.
42. M. H. Lewis and B. Hattersley, *Acta Metall.*, **13** (1965) 1159.
43. H. Tanaka, M. Murata, F. Abe and K. Yagi, *Mater. Sci. Eng.*, **A234–236** (1997) 1049.
44. D. H. Jack and K. H. Jack, *JISI.*, **209** (1972) 790.
45. P. W. Robinson and D. H. Jack, *Heat Treating.*, **4** (1985) 69.
46. J. K. L. Lai, *Mat. Sci. Engg.*, **A61** (1983) 101.
47. H. J. Beattie and W. C Hagel, *JOM.*, **9** (1957) 911.
48. J. Barcik, *Mater. Sci. Technol.*, **4** (1988) 5.
49. L. P. Stoter, *J. Mater. Sci.*, **16** (1981) 1039.

12. B. Raj, *Bull. Mater. Sci.*, **32** (2009) 271.
13. F. Masuyama, *Low-alloyed steel grades for boilers in ultra-supercritical power plants*, in: *Materials for Ultra-Supercritical and Advanced Ultra-Supercritical Power plants*, edited by A. D. Gianfrancesco, Woodhead Publishing (2017) 53-76.
14. R. Viswanathan and W. Bakker, *J. Mater. Eng. Perform.*, **10** (2001) 81.
15. R. Viswanathan and W. Bakker, *J. Mater. Eng. Perform* **10** (2001) 96.
16. R. Viswanathan, J. F. Henry, J. Tanzosh, G. Stanko, J. Shingledecker, B. Vitalis, and R. Purgert, *J. Mater. Eng. Perform.*, **14** (2005) 281.
17. V. Viswanathan, R. Purgert and P. Rawls, *Adv. Mater. Processes*, **166** (2008) 47.
18. R. Viswanathan, J. Sarver, and J.M. Tanzosh, *J. Mater. Eng. Perform*, **15** (2006) 255.
19. R. Viswanathan, K. Colemana and U. Rao, *Int J Pressure Vessels Piping*, **83** (2006) 778.
20. D. Peckner and I.M. Bernstein, *Handbook of stainless steels*, McGraw-Hill (1977).
21. M. D. Mathew, K. A. Gopal, S. Murugan, B. K. Panigrahi, A. K. Bhaduri and T. Jayakumar, *Adv. Mat. Res.*, **794** (2013) 749.
22. S. Latha, M. D. Mathew, P. Parameswaran, M. Nandagopal and S. L. Mannan, *J. Nucl Mater.*, **409** (2011) 214.
23. G. S Was, *Fundamentals of Radiation Materials Science: Metals and Alloys*, Springer-Verlag, Berlin/Heidelberg (2007).
24. Y. Tateishi, *J. Nucl. Sci. Technol.*, **26** (1989) 132.
25. V. Foldyna, J. Purmensky and Z. Kubon, *ISIJ Int.*, **41** (Suppl.) (2001) S81.
26. J. A. Elliott, *Int. Mater. Rev.*, **56** (2011) 207.
27. E. J. Mittemeijer, *Fundamentals of Materials Science*, Springer, Berlin (2010).
28. S. Raju, *A study on the role of thermo-kinetic measurements and modelling in materials design*, Doctoral thesis, Homi Bhabha National Institute, (2013).

References

1. K. Ummel, *CARMA Revisited: An Updated Database of Carbon Dioxide Emissions from Power Plants Worldwide*. CGD Working Paper 304. Washington D. C. Center for Global Development (2012). <http://www.cgdev.org/content/publications/detail/1426429>
2. M. M. Majoumerd, H. Raasc, K. Janad, S. Ded and M. Assadib, *Energy Procedia.*, **114** (2017) 6478.
3. C. Song, M. Li, F. Zhang, Y. He and W. Tao, *Energy Procedia.*, **61** (2014) 904.
4. *World Energy Council, Resources* (2016). www.worldenergy.org/publications/2016/world-energy-resources-2016
5. *CO₂ emissions from Fuel combustion Highlights*, Report Iea (2017). [http://www.iea.org/bookshop/757-CO₂ Emissions from Fuel Combustion 2017](http://www.iea.org/bookshop/757-CO2_Emissions_from_Fuel_Combustion_2017)
6. S. C. Chetal, P. Chellapandi, P. Puthiyavinayagam, S. Raghupathy, V. Balasubramaniyan, P. Selvaraj, P. Mohanakrishnan and B. Raj, *Energy Procedia.*, **7** (2011) 64.
7. P. Puthiyavinayagam, P. Selvaraj, V. Balasubramaniyan, S. Raghupathy, K. Velusamy, K. Devan, B. K. Nashine, G. Padmakumar, K. V. Sureshkumar, S. Varatharajan, P. Mohanakrishnan, G. Srinivasan and A. K. Bhaduri, *Prog. Nucl. Energy*, **101** (2017) 19.
8. S. Banerjee and H. P. Gupta, *Prog. Nucl. Energy*, **101** (2017) 4.
9. S. C. Chetal, V. Balasubramaniyan, P. Chellapandi, P. Mohanakrishnan, P. Puthiyavinayagam, C. P. Pillai, S. Raghupathy, T. K. Shanmugham and C. S. Pillai, *Nucl. Eng. Des.*, **236** (2006) 852.
10. T. Jeyakumar, M. D. Mathew, K. Laha and R. Sandhya, *Nucl. Eng. Des.*, **265** (2013) 1175.
11. B. Raj, S. L Mannan, P. R. V. Rao and M. D. Mathew, *Sadhana*, **27** (2002) 527.